NTNU – Trondheim
Norwegian University of
Science and Technology

The Oxygen Evolution Reaction at Iridium-Ruthenium Oxide Catalysts for PEM Water Electrolysis

Heidi Thuv

Materials Technology
Submission date: June 2015
Supervisor: Svein Sunde, IMTE
Co-supervisor: Anita Reksten, IMT

Norwegian University of Science and Technology
Department of Materials Science and Engineering

PREFACE

This report has been written in the course TMT4905 – Materials Technology , Master's Thesis, spring 2015. This master thesis is the final submission to complete the Masters Degree Program in Materials Technology at the Department of Materials Science and Engineering at the Norwegian University of Science and Technology. The work has been performed during the spring semester in 2015. The part of this master thesis concerning detection of by-products by ring-disk electrodes is a continuation of a preliminary project work named "Characterisation of catalysts for oxygen evolution in PEM water electrolysis". The project work was conducted by the author of this master during the autumn of 2014. The results from this project will be summarised in this master thesis, and it will be clearly stated if figures etc. used in this master are obtained from the preliminary project. Most of the experiments and analysis provided in this report have been conducted by the author, with the exception of the XRD analysis that was conducted by Anita Reksten.

I would like to express my gratitude towards my main supervisor Prof. Svein Sunde for the valuable guidance and discussions throughout the work. Further, I want to thank my co-supervisor PhD candidate Anita Reksten for lab advices, and for answering all kinds of questions throughout the project. Both supervisors general willingness to help has been invaluable. Magnus Bertzen Følstad also deserves many thanks for always ready to help with issues in the lab. I also want to thank Mariia Stepanova for helping me with the salt bridges, and Espen Vinge Fanavoll for the introductory potentiostat training.

Last, but not least, I want to thank Mads Simonsen for keeping my spirits up throughout this semester. Thank you!

ABSTRACT

A sustainable method for hydrogen production can be achieved with PEM water electrolysers. These are considered important for the transition to a society based on renewable energy production as they can be coupled with intermittent power sources like wind and solar power. One major challenge with this technology is the sluggish oxygen evolution in combination with the harsh conditions at the anode, requiring expensive catalyst materials. Mixed iridium-ruthenium oxides are promising electrocatalysts for the oxygen evolution reaction (OER) in these environments.

The aim of this thesis was to study the reaction mechanism of the OER and the by-products of this reaction at $Ir_xRu_{1-x}O_2$ materials, and to investigate how the composition influenced these factors. Four oxide powders (IrO_2, $Ir_{0.6}Ru_{0.4}O_2$, $Ir_{0.3}Ru_{0.7}O_2$ and RuO_2) were synthesised by hydrolysis. These were characterised by XRD, cyclic voltammetry and polarisation in the oxygen evolution potential region.

Polarisation experiments in perchlorate solutions of pH 0, 1, 2 and 3 were used to measure two kinetically significant parameters, namely the Tafel slope and the reaction order with respect to H^+. Tafel slopes of approximately 40 mV and reaction orders of -1.5 were established for all oxides, and suggests that the OER take place with the same mechanism at all oxide compositions. The rate limiting step of the OER at these oxides appears to be the transition of OH_{ads} to O_{ads}. Small variations in the Tafel slopes between the material compositions were ascribed to different intermediate coverage.

Ring-disk electrodes under hydrodynamic control were employed for detection of by-products of the reaction. The ring-disk experiments were performed under dynamic potential control to simulate the intermittent nature of renewable energy sources. The disk electrode was coated with the catalyst material to be studied, and potential step or potential sweep voltammetry was performed at this electrode while the ring electrode was held at a constant potential for detection of the reaction by-products. In addition, the electrolyte flow rate was varied, which revealed that parts of the detected ring current originated from features probably caused by the instrumentation. These features and a variable background current contribution at the ring complicated the interpretation of the ring-disk measurements. The identity of the products produced at the ring could therefore not be established. However, strong indications that at least two products other than oxygen were produced at the disk were found. One specie giving rise to a reduction at the ring and the other giving rise to oxidation. As no conclusion could be drawn concerning the identity of the by-products, the results from the ring-disk experiments could not elucidate the reaction mechanism further.

Potential sweep and potential step voltammetry at the disk resulted in different ratios of the two by-products. This demonstrates that the production of by-products depends on the potential dynamics of the oxygen electrode. It seems that different operating conditions of the electrolyser can favour different by-products and also different ratios of these two products.

SAMMENDRAG

PEM vannelektrolysører kan benyttes til bærekraftig hydrogenproduksjon og er viktige for overgangen til et samfunn basert på fornybar energiproduksjon da disse kan kobles til periodisk kraftproduksjon som f.eks. vind- og solenergi. En utfordring med denne teknologien er den langsomme oksygenutviklingen og de sterkt oksiderende forholdene ved anoden. Dette nødvendiggjør bruk av kostbare katalysatorer på denne elektroden. Blandede oksider basert på iridium og rutenium har vist seg å være lovende katalysatorer for oksygenutvikling i surt miljø.

Formålet med denne oppgaven var å studere reaksjonsmekanismen for oksygenutvikling og eventuelle biprodukter til denne reaksjonen på materialer av typen $Ir_xRu_{1-x}O_2$, samt å undersøke hvordan materialsammensetningen påvirket disse faktorene. Fire ulike oksidpulver (IrO_2, $Ir_{0.6}Ru_{0.4}O_2$, $Ir_{0.3}Ru_{0.7}O_2$ og RuO_2) ble tilberedt ved hydrolysesyntese. Disse ble så karakterisert vha. røntgen, syklisk voltammetri og polarisasjon i potensialområdet hvor oksygenutviklingen finner sted.

Polarisasjonsforsøkene ble utført i perkloratløsninger med pH 0, 1, 2 og 3 og ble brukt til bestemmelse av to viktige kinetiske parametere, nemlig Tafelhelning og reaksjonsorden med hensyn på H^+. For alle oksidene ble Tafelhelningene bestemt til å være ca. 40 mV og reaksjonsordenene til -1.5, noe som indikerer at samme reaksjonsmekanisme er gjeldende på alle materialene. Det hastighetsbestemmende trinnet for oksygenutviklingen på disse oksidene ser derfor ut til å være oksidasjon av adsorbert OH til adsorbert O. Små variasjoner i Tafelhelningene mellom de ulike materialene ble tilskrevet ulik dekningsgrad av adsorbater.

Ring-disk-elektroder under hydrodynamisk kontroll ble bruk for deteksjon av biprodukter av oksygenutviklingen. Ring-disk-eksperimentene ble utført under dynamiske potensialforhold for å simulere den varierende spenningen fra fornybare energikilder. Diskelektroden ble belagt med katalysatormaterialet som skulle undersøkes, og potensialtrinn- eller potensialsveip-voltammetri ble utført på denne elektroden mens ringelektroden ble hold på et konstant potensiale for deteksjon av biprodukter fra disken. I tillegg ble strømningshastigheten til elektrolytten variert. Dette avslørte at noe av den detekterte ringstrømmen sannsynligvis ble forårsaket av instrumenteringen heller enn biprodukter fra disken. Dette, i tillegg til en variabel bakgrunnsstrøm på ringen, gjorde det vanskelig å tolke disse målingene. Identiteten til biproduktene kunne derfor ikke bestemmes. Imidlertid ga målingene sterke indikasjoner på at minst to andre produkter enn oksygen ble produsert på disken, ett som ga opphav til reduksjon på ringen og ett som ga opphav til oksidasjon på ringen. Siden identiteten av biproduktene ikke ble bestemt, kunne ikke resultatene fra ring-disk-målingene belyse reaksjonsmekanismen ytterligere.

Forsøkene med potensialtrinn og potensialsveip på disken resulterte i ulike forhold mellom de to biproduktene. Dette demonstrerer at produksjonen av biprodukter avhenger av dynamikken til diskpotensialet. Det ser ut til at forskjellige driftsbetingelser for vannelektrolysøren kan favorisere forskjellige biprodukter og også ulike forhold mellom de to biproduktene.

LIST OF CONTENTS

1 INTRODUCTION

There is a growing need for renewable power sources in order to reduce emissions from fossil fuels, as well as sustain the increasing energy demand. However, energy production from renewable power sources is often varying over time, and the power production is often stationary. Therefore, there is a need for methods of storing and transportation of the energy after production. Water electrolysis offers a solution for this by converting electrical energy into hydrogen, which thereafter can be stored or transported, and used as a fuel when and where the energy is required, either for electricity production or directly as a fuel in transportation. The combustion of hydrogen has no carbon emissions, and pure water is the only product. This ideal energy cycle is often referred to as the "hydrogen economy", and is illustrated Figure 1-1. [2]

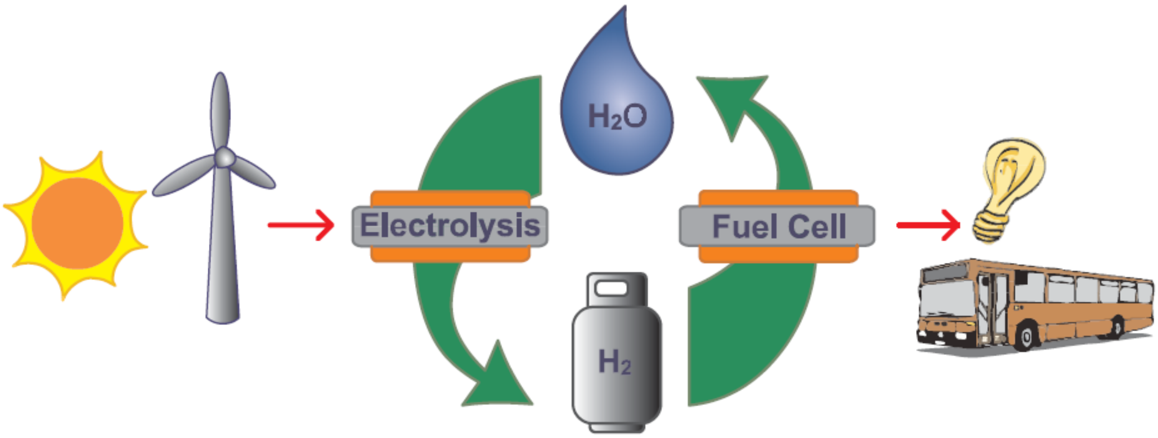

Figure 1-1: The hydrogen economy. Electricity is produced by renewable power sources and utilised for hydrogen production through water electrolysis. The hydrogen is subsequently used as fuel in fuel cells. [3]

Water electrolysis is a technology where electricity is used to split water into hydrogen and oxygen gas. There are three different technologies for water electrolysis: alkaline, solid oxide (SOEC) and polymer electrolyte membrane (PEM) electrolysis. Alkaline water electrolysis is the most used technology industrially, but development of the PEM technology is attractive as it shows many advantages, including higher current densities, higher purity hydrogen, compact system design, low degradation and easy maintenance. However, there are still many challenges to overcome in order to make the process efficient enough for commercialisation. One major problem is the large losses for the oxygen evolution reaction (OER) at low pH conditions. This requires the use of expensive catalyst materials that can also withstand the highly corrosive acidic environment at the oxygen electrode in PEM electrolysers. For PEM electrolysers these catalysts are mainly based on the rutile type materials iridium and ruthenium oxides. RuO_2 exhibits the highest activity of the OER, while IrO_2 is more stable.[4] Mixed iridium-ruthenium oxides has proved efficient to stabilise the catalyst material without compromising the activity of RuO2.[5, 6]

In acidic media the electrochemical generation of oxygen involves four electrons per mole of O_2:

$$2H_2O \rightarrow O_{2\,(g)} + 4H^+ + 4e^- \qquad (1\text{-}1)$$

This reaction is catalytically demanding due to the involvement of high-energy intermediates with complex molecular structure and complicated reaction pathways. As a consequence of this, the reaction mechanism and the oxygen evolution rate depend strongly on the electrode material. The reaction mechanism determines the kinetics of the OER and thus influences the efficiency of water electrolysis. Elucidation of the reaction mechanism at the different catalysts can therefore provide useful insight for energy saving purposes.

Due to the complexity of the OER, the reaction is not completely understood and several mechanisms have been proposed.[7, 8] Some of the most commonly proposed mechanisms involves adsorbed O, OH and OOH as intermediates at the surface of the electrode. These intermediates can possibly react electrochemically at the electrode to form other products than oxygen. Another possibility is that the intermediates desorb from the surface and go into the solution where they can result in a number of reactions. The identity and surface coverage of the reaction intermediates depends on the reaction mechanism and potential conditions. Thus, different materials and operating conditions of the electrolyser is expected to influence the identity and ratio of by-products. This also demonstrates that the OER mechanism, and thus the choice of catalyst material, is intimately linked with the by-products of the reaction. It is therefore believed that the generation of the by-products can be suppressed by choice of catalyst material and operating conditions.

Electrolysers connected to intermittent power sources, like solar or wind energy, will experience fluctuating voltage conditions, and it is therefore important to know how the catalyst materials are influenced by this. Recently, it was discovered that fluctuating voltage conditions give rise to concurrently evolution of possibly volatile species as by-products of the OER on rutile type catalysts. Kusnetzova et. al.[9] found strong evidence that one of these species was hydrogen peroxide, and suggested that another by-product might be ozone. Both these species can cause degradation of the polymer membrane, and thus decrease the lifetime of the electrolyser.[10, 11] It is therefore important to identify these species.

The aim of this work is to study the mechanism of the OER and by-products of this reaction at IrO_2, RuO_2 and mixed Ir-Ru oxides, and to investigate how the catalyst composition will influence these factors. Four different rutile material powders are synthesised by hydrolysis (IrO_2, $Ir_{0.6}Ru_{0.4}O_2$, $Ir_{0.3}Ru_{0.7}O_2$and RuO_2). The catalysts powders are analysed by X-ray diffraction, and electrochemically characterised by cyclic voltammetry and linear sweep voltammetry.

Information about the reaction mechanism is sought obtained by the classical electrochemical approach of obtaining Tafel slopes and reaction orders of the OER at these materials. Polarisation curves of the four different catalysts are recorded in electrolytes with four different H^+ concentrations. From these curves, the Tafel slopes and the reaction orders with respect to H^+ at each of the catalyst is determined.

Further, it is attempted to detect by-products of the OER by the use of ring-disk electrodes under varying potential conditions. Detection of by-products by ring-disk electrodes was attempted in the preliminary project work related to this thesis.[12] The results of this project were, however, difficult to interpret. It is therefore sought to improve the experimental conditions as well as to vary other experimental parameters in this thesis.

The first chapter of this thesis gives a brief introduction to PEM water electrolysis and the relevant thermodynamics and kinetics for this technology. Further, reaction mechanisms and electrocatalysis for the OER is explained, and possible by-products of the reaction are introduced. This is followed by a chapter introducing the theories behind the experimental techniques used in this work, as well as how these techniques can be used to obtain the information sought in this thesis. The experimental procedure, the results obtained and the discussion of the results are given in the last three chapters.

2 PEM WATER ELECTROLYSIS AND THE ELECTROCATALYSIS OF THE OXYGEN EVOLUTION REACTION

In this chapter, a brief introduction to the principles and technology of PEM water electrolysis is given. A major drawback for this technology is the energy demanding oxygen evolution reaction. The electrocatalysis of this reaction and catalyst materials for this reaction is described. Possible by-products of the reaction is also given, and in the end of this section it is described how such by-products have been detected by the use of ring-disk electrodes.

2.1 PEM WATER ELECTROLYSIS

A short introduction to the principles and technology of water electrolysis is given in this section, including the major challenges. This is followed by a brief presentation of the electrochemical thermodynamics and kinetics that are important for these systems and the oxygen evolution reaction.

2.1.1 Principles and technology of PEM water electrolysis

The principle behind water electrolysis is that by supplying energy to an electrochemical cell containing water, water is split into hydrogen at the cathode and oxygen at the anode. A schematic presentation of this process in PEM electrolysers is shown schematically in Figure 2-1. In this technology, the water is supplied at the anode side of the membrane, and is oxidised to oxygen at this electrode. The electrons released at this point go through an external circuit which is connected to the external power supply of the electrolyser. The polymer membrane acts as an electrolyte which selectively conducts cations, so that only protons can pass through to the cathode side of the membrane. There, the protons are reduced to yield hydrogen gas.[4]

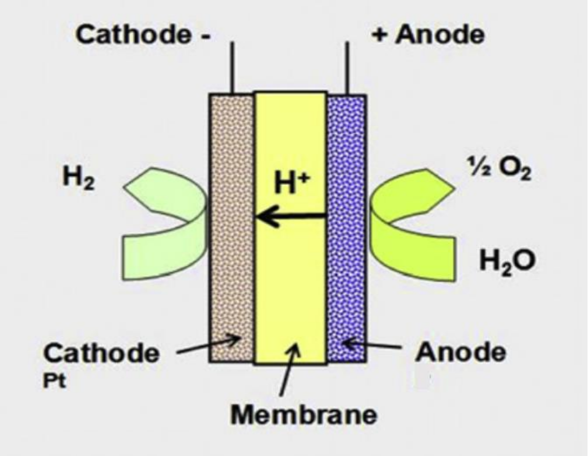

Figure 2-1: Ref: Schematic presentation of the PEM electrolyser. [4]

Design and durability

The anode material in PEM water electrolysers is typically titanium coated by an active layer of transition metal catalysts, commonly IrO_2- and RuO_2- based. The cathode consists of a graphite current collector and a noble metal catalyst (typically Pt). The polymer membrane exhibits low ohmic resistance, is acidic in nature and is proton selective due to the functional sulfonic groups. Several cells are stacked together, separated by graphite based separator plates. The PEM electrolyser can operate under variable power feeding regimes due to the fact that the proton transport across the membrane responds quickly to power fluctuations. This is a significant advantage for integration with renewable energy production.[13]

In addition to the problems with high overvoltage at the anode and the expensive catalysts, another major problem with PEM water electrolysis is the low durability compared to alkaline water electrolysis. The environment in the electrolyser is harsh due to strong oxidising conditions, high temperature, reactive intermediate products, high currents and large potential gradients.[14]

Operational conditions such as potential cycling, start/stop cycling and changes in temperature and pressure, are known to affect the durability of the electrolysers. However, the integration of electrolysers with intermittent energy sources requires electrolysers that can endure dynamic potential loads. Thus, information about operation of the catalytic materials under potential cycling conditions is needed. It is important to know whether they degrade, and if the activity and mechanisms are affected by these conditions.[13]

The membrane is sensitive for chemical degradation, which can be caused by hydrogen peroxide, radicals and other by-products that are possibly formed during the oxygen evolution reaction during electrolysis. These can attack the membrane directly or in combination with certain metal ions present present in the solution. [11, 15, 16] It is therefore important to know which radicals can be present, and under which conditions these are produced, in order to limit the membrane degradation. This can be done by developing a more durable membrane for these species, by introducing measures that inhibit these species to react with the membrane, e.g. an additional layer of hydrogen peroxide decomposition or radical traps [17], or by avoiding operational regimes where these products are formed if feasible.

2.1.2 Thermodynamics of acidic water electrolysis

The electrode and cell reactions in the PEM electrolyser, as well as the standard potentials (25 °C, 1 atm and activity of species at unity) are given below[18]:

$$\text{Total reaction: } \mathrm{H_2O_{(l)}} \rightarrow \mathrm{H_{2\,(g)}} + \frac{1}{2}\mathrm{O_{2\,(g)}} \qquad E^0 = 1.23\ V \qquad (2\text{-}1)$$

$$\text{Cathode reaction: } \mathrm{2H^+ + 2e^-} \rightarrow \mathrm{H_{2\,(g)}} \qquad E^0 = 0\ V \qquad (2\text{-}2)$$

$$\text{Anode reaction: } \frac{1}{2}\mathrm{O_{2\,(g)}} + \mathrm{2H^+ + 2e^-} \leftarrow \mathrm{H_2O_{(l)}} \qquad E^0 = 1.23\ V \qquad (2\text{-}3)$$

The reversible potential for the reaction can be found using Nernst equation [19]:

$$E^{rev} = E^0 - \frac{RT}{nF}\ln\left(p_{H_2}p_{O_2}^{\frac{1}{2}}\right) \qquad (2\text{-}4)$$

Where E^0 is the standard potential of the reaction, R is the gas constant, T the operating temperature, n the number of electrons involved in the total reaction, F the Faraday constant and p_{H_2} and p_{O_2} the partial pressures of the hydrogen and oxygen gas, respectively. The standard potentials of the chemical reactions are valid for standard conditions at 1 atm and 298 K. Nernst equation can be used to calculate the reversible potential for temperatures and activities/pressures other than standard conditions. Applying this for the oxygen evolution reaction (OER) only, it can be seen that the potential for the OER will decrease with 0.059 V per integer increase in pH. However, the hydrogen reaction will have the same pH dependency, and the total thermodanymical cell voltage will therefore be the same for all pH values.

The total reaction is endothermic and consumes heat. The isothermal voltage of the reaction is 1.48 V, which means that the process occurs adiabatically at this potential. If the cell potential is higher than this value, the cell loses heat to the system, whereas lower cell potential results in absorption of heat from the surroundings.[20]

2.1.3 The effect of reaction kinetics and ohmic losses on the operating potential [21, 22]

Thermodynamics give only the minimum potential requirement for a process. Due to kinetics of the reactions, a higher potential is required for the reactions to proceed. This is called overpotential, and can be divided into a cathodic and an anodic component, η_c and η_a, corresponding to the cathodic and anodic electrode reactions. In addition, there will always be ohmic voltage drops in the electrolyte as well as in the electron conducting circuit of the cell. Thus, the minimum cell voltage required to perform water electrolysis, E_{cell}, is given by the sum of these voltage components.

$$E_{cell} = E^{rev} + \eta_c + \eta_a + \Delta V_{ohm} \tag{2-5}$$

Where ΔV_{ohm} is the sum of the ohmic losses in the system.

Both the overpotentials and the ohmic losses varies with current density. The ohmic losses are given by Ohm's law, and thus increase linearly with the applied current. The overpotentials depend on reaction kinetics which can arise due to both slow mass transfer of reactants or products in the electrolyte and electron transfer limitations. A schematic figure of the variation in total applied voltage required for one electrode, ΔV, as a function of current is shown in Figure 2-2.

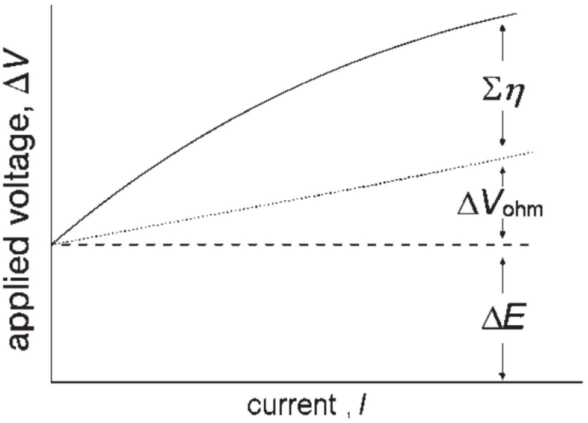

Figure 2-2: Schematic representation of how the applied voltage, ΔV, varies with total current in a cell. [23]

It is desirable to keep both the ohmic potential drop as well as the overpotentials as low as possible. The ohmic drop is mainly a problem of cell engineering, while minimising the overpotentials due to slow electron transfer at the electrodes is a problem for electrocatalysis, and these overpotentials will depend on the choice of electrode material.

The net current on an electrode is the sum of the anodic and cathodic currents. When electron transfer is determining the kinetics of the reaction, implying that mass transfer is negligible for the reaction rate, the net current is given as a function of the overpotential by the Butler-Volmer equation:

$$i_{tot} = i_a + i_c = i_0 \left\{ e^{\frac{\alpha_a nF}{RT}\eta} - e^{-\frac{\alpha_c nF}{RT}\eta} \right\} \tag{2-6}$$

Where α is the charge transfer coefficient, which often lies between 0.4 and 0.6, and the subscripts a and c refers to anodic and cathodic, respectively. For large overpotentials, the smaller of the anodic or cathodic currents can be neglected. For the cathodic reaction, the total current can then be written as:

$$i_{tot} = i_c = -i_0 e^{-\frac{\alpha_c nF}{RT}\eta} \tag{2-7}$$

Which can be simplified to:

$$\eta = b \log \left| \frac{i}{i_0} \right| = a + b \log|i| \tag{2-8}$$

Which is the Tafel equation, and the constant *b* is the Tafel slope, which has the magnitude $\left(\frac{\ln(10)RT}{-\alpha_c nF}\right)$, as seen from the equations above. Analogous, the anodic overpotential can be expressed in the same way, but should give a positive value for η as well as for b ($\left(\frac{\ln(10)RT}{\alpha_a nF}\right)$. As seen from equation (2-8), the Tafel slope can easily be determined by plotting the potential as a function of the logarithm of the current density, as this should give a linear region when the Tafel equation is valid.

If polarisation curves are measured close to the reversible potential of the reaction, where neither the anodic or cathodic overpotentials are sufficiently large that one of the terms in the Butler-Volmer equation can be excluded, the current response will not be linear, but show an exponential behaviour as given by the Butler-Volmer equation. At sufficiently high currents, the electrode transfer will no longer determine the kinetics of the reaction, and mass transfer cannot longer be disregarded. Then, the current response is no longer linear, and will eventually give a limiting (maximum) current value for all potentials further away from the reversible potential.

The Tafel equation implies that a low value of *b* results in lower overpotentials for a given current. The exchange current density, i_0, is the current density at equilibrium (i.e. at E^{rev}) when the reaction rate of the anodic and cathodic direction is equal. i_0 is also a measure of the catalytic activity, with high i_0 corresponding to high electrocatalytic activity. The value of i_0 can also be found from the Tafel relationship if b is known. However, this is not always appropriate, and can in some cases be difficult to determine. Nevertheless, both the Tafel slope, b, and the i_0 can be used for comparing different catalyst materials. The Tafel slope can also give an indication of reaction mechanisms and what is the rate determining step for a reaction. This is described in section 2.2.2.

For water electrolysis, the OER is much more demanding than the hydrogen evolution, and the OER thus gives a significantly higher contribution to the total required overpotential to drive the process. The major challenge with PEM water electrolysis is to find an anodic OER catalyst offering fast kinetics and at the same time is stable in the harsh oxidising environment at the anode.

2.2 ELECTROCATALYSIS OF THE OXYGEN EVOLUTION REACTION

It is often encountered that an electrochemical reaction does not take place close to its thermodynamic potential, or only at a very small rate. However, by changing or modifying the electrode material, the reaction rate can be significantly increased. A reaction behaving in such a way is referred to as an electrocatalytic reaction, and the electrode material enhancing the reaction rate is an electrocatalyst. A catalyst shall provide a lower energy of activation path for the reaction, and should not be consumed in the overall reaction. Often the catalyst is the electrode material itself, particularly for reactions involving adsorption of reactant or intermediates, as these processes represent a high degree of interaction between the reacting electrochemical species and the electrode surface. If the electrode material is the catalyst, the catalytic effect may be a result of chemical or structural modifications of the electrode surface, e.g. changes in the electronic state at the surface or by variation in the geometric nature (crystal planes, alloys, defects etc.) For electrochemical reactions, which occur on electrolyte/electrode interfaces, all electrode surfaces are in principle catalysts, seeing that the reaction would not occur without the electron conducting electrode. Hence, no zero-activity electrode exist, and electrocatalysis is thus based on relative data. The role of the catalyst is to either increase the current density at a fixed potential, or reduce the overpotential at a fixed current density.[24p. 339] [25]

The oxygen evolution and reduction reactions are two of the most studied electrochemical processes as they are of great technical importance in fuel cells and electrolysers, as well as in corrosion processes of metals. Yet, the reaction mechanisms are far from fully understood. The reactions are complex and demanding, resulting in high overvpotentials (usually at least 0.4 V). The reason for the complexity is partly owing to the fact that four electrons are required for the total reaction, resulting in many possible reaction paths. The possible reaction mechanisms also involve high energy intermediates with complex molecular structure that further complicates the reaction path due to the necessity of adsorption and desorption in the reaction steps. In addition, the OER requires high potentials, which can result in dramatic changes in the electrode materials that further can change the reaction kinetics over time. Because of the complexity of the reaction, the kinetics is highly dependent on the catalytic properties of the electrode surface at which it occurs. [22, 26]

The most straightforward way to compare different catalyst materials, is to compare their polarisation curves. A good catalyst will show higher current values, i.e. be more active, at the potentials desired for the electrode process. As seen in the Tafel equation, the activity at a given potential depends on both the exchange current density, i_0, and the Tafel slopes, b. i_0 is an extensive property that depends on many factors in addition to the electrode material (e.g. electrolyte composition, electrode geometry, etc.), and can only be compared for different materials in the same conditions. The Tafel slope is, however, an intensive property, and depends only on the reaction mechanism. A good catalyst for the reaction will show low Tafel slope values, and high exchange current densities.[21, 27]

In this section, catalysis and catalysts for the OER will be introduced. Further, an introduction to reaction mechanisms and kinetics is given. It will be shown how this relates to Tafel slopes and reaction orders. The most popular reaction mechanisms encountered for the OER at oxide materials are further presented. Possible by-products of the OER at oxide catalysts are presented in at the end.

2.2.1 Catalysts for the oxygen evolution reaction

The main purpose of a catalyst is to improve the electrocatalytic activity of wanted reactions, and depress the activity of any unwanted reactions. However, other qualities are also important for technological applications. Requirements for electrocatalysts for oxygen and chlorine gas evolution were summarised by Trasatti in 1984 [28]:

- High surface area
- High electrical conduction
- Good electrocatalytic properties
- Long-term mechanical and chemical stability at the support/active layer and at the active layer/solution interface
- Minimized gas bubble problems
- Enhanced selectivity
- Availability and low cost
- Health and safety

For the OER in PEM electrolysers, the conditions at the anode are harsh, with low pH and high anodic potentials. This limits use of most metals, as they will be oxidised, whereas conductive oxides is a promising alternative. The OER requires adsorption and desorption of reaction intermediates, which involves formation and breakage of bonds between the electrode surface and the reaction intermediates. The electrode surface can therefore influence the activation energy for the electrochemical reaction by modulating the bond strength between active sites and adsorbed intermediates. The adsorption of oxygenated intermediates at an oxide surface is equivalent to oxidation of the active site to a higher valence state. A good catalyst for the OER should therefore be able to change easily between lower and higher oxidation states, to enhance both adsorption and desorption. This property can be quantified by the enthalpy of formation, ΔH_f^0, from a lower to a higher oxidation state in the material.[22] Constructing a plot of the electrocatalytic activity as a function of ΔH_f^0 for different materials yields so-called Volcano plots, where the materials with intermediate enthalpies exhibit the highest catalytic activities. The catalytic activity on the vertical axis is typically represented as the negative of the overpotential or the current at a given overpotential. Figure 2-3 shows the volcano plot for different metal oxides.

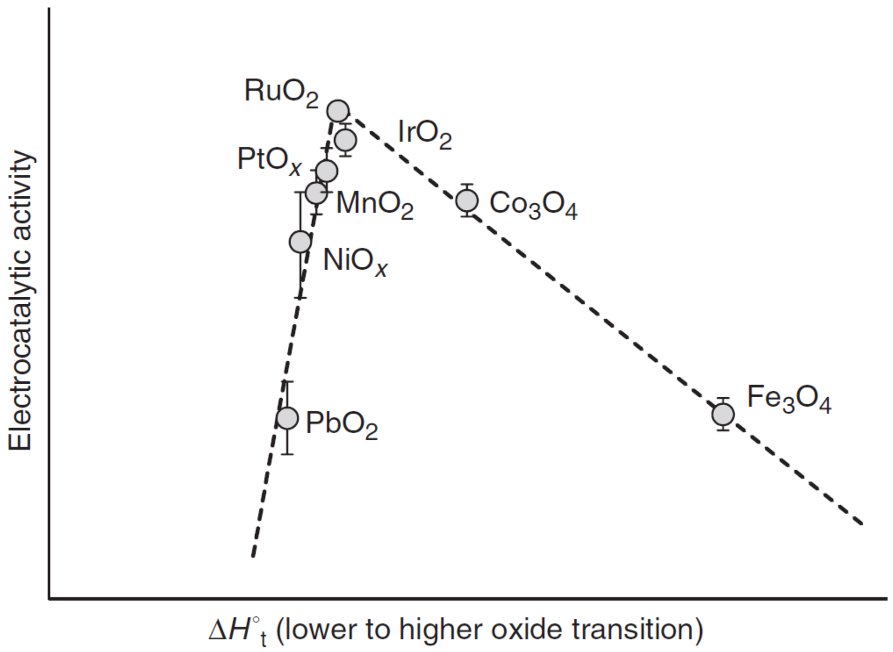

Figure 2-3: Volcano plot of the electrocatalytic activity for the OER against ΔH_f^0 of lower to higher oxide transition for different materials.[22]

The materials to the left of the peak show a small tendency to be oxidised to a higher valence state, which hinders the adsorption of the intermediates and thus results in higher overpotentials. The materials to the right exhibit very high ΔH_f^0 of formation of higher valence oxide states and are oxidised easily, binding intermediates too strongly and by this hinders desorption of the products, thus becoming catalytically inactive. Close to the apex of the curve are RuO_2 and IrO_2, and by experiments these are also found to be the most active materials among single-transition metal oxides for the OER in acidic media.[5, 28] RuO_2 is the most active catalyst, but is unfortunately unstable under the conditions of the PEM electrolyser. If ruthenium oxide is oxidised to Ru(VIII) it can be lost by formation of volatile RuO_4.[22] IrO_2 exhibits lower activity, but is far more stable.[6, 29]

A volcano plot has also been obtained by deriving catalytic activities of the metal oxides from the binding energy of atomic oxygen to the surface by density functional theory (DFT) modelling. It was found that there is a linear relation between the binding energy of O to the metal oxide and the binding energy between HO and HOO to the metal oxide. Thus, oxide surfaces that bind O strongly also binds HO and HOO strongly, and the activity of the OER on oxide surfaces can thus be calculated as a function of only the oxygen-metal oxide binding energy. These DFT calculations also resulted in curves that are qualitatively similar to the volcano plot above, with RuO_2 being the best catalyst, and IrO_2 as number two. These calculations further showed that RuO_2 binds oxygen a little too weakly, while IrO_2 binds oxygen too strongly. [30]

Mixing IrO_2 and RuO_2 has proved efficient to stabilise the catalyst material without compromising the activity of RuO_2.[5, 6] This might be due to the surface segregation of IrO_2, giving a surface that is enriched with iridium that is more stable, and thus protecting the most unstable sites of the ruthenium.[31] The preparation and pre-treatment of the oxides also affects the stability towards corrosion. It is generally accepted that high-temperature oxides with a higher degree of crystallinity are less active but more stable than low-temperature (more amorphous) oxides, which exhibits the opposite relation.[32]

Both IrO_2 and RuO_2 have rutile structures, and possesses metal-like conductivities. The high metallic conductivity reduces the ohmic losses in the material. RuO_2 has slightly smaller lattice parameters compared to IrO_2. [33] Tafel slopes for IrO_2 and RuO_2 found by various authors have been summarised by Matsumoto and Sato.[34] For polycrystalline RuO_2 in acidic media, Tafel slopes between 0.035 V and 0.04 V has been found at low overpotentials, increasing to 0.055 V at high overpotentials. For IrO_2, slightly higher Tafel slopes are obtained, between ca. 0.05 – 0.056 V.

2.2.2 Oxygen evolution reaction mechanisms

Before the mechanisms of the OER are presented, a general introduction to reaction kinetics is given.

General theory on reaction kinetics and definitions of Tafel slopes and reaction orders

The Butler-Volmer equation (2-6) gives the current for the total electrochemical reaction (cathodic – anodic current). Most electrode reactions, however, take place through complicated mechanisms involving a number or consecutive steps. Generally, a total reaction involving transfer of multiple electrons will occur through a stepwise transfer of single electrons. For the OER, the overall reaction consists of a sequence of different electron transfer steps, where one electron is transferred in each step and where each of the steps can have distinctive symmetry factors, exchange currents and equilibrium potentials.[21]

The net rate of any electrochemical reaction is given by:

$$r_{tot} = r_a - r_c \tag{2-9}$$

The net rate determines the net electron generation, and is thus proportional to the current. The rates of the anodic and cathodic directions is proportional to the activity of all reactants, products, adsorbates/surface sites and electrons (i.e. the electrode potential). The general rate expression for a reaction step in the anodic direction is:

$$r_a = k_a \prod_{i=1}^{n} a_{a,i}\, e^{\frac{(1-\beta)zFE}{RT}} \tag{2-10}$$

And analogous for the cathodic direction:

$$r_c = k_c \prod_{i=1}^{n} a_{c,i}\, e^{\frac{-\beta zFE}{RT}} \tag{2-11}$$

Where k_a and k_c are the rate constants in the anodic and cathodic directions, respectively, and β is the symmetry parameter. a_a and a_c are the activities of the reactants for the anodic and cathodic directions, respectively, and available surface sites is comprised by the definition of reactants. The activities of ions can be exchanged by their respective concentrations. The activity of adsorbates and surface sites can be exchanges by the surface concentration of adsorption sites, Γ, multiplied with the fraction of the available surface that is occupied by the adsorbate *i*, θ_i or $(1 - \theta_i)$, respectively.[35]

The exponential factors can be regarded as the activity of the electrons at each side of the reaction. For simple surface reactions with no electron transfer, these factors are omitted.

The symmetry parameter, β, is similar to the charge transfer coefficient, α, but α is applicable for the overall multi-step reaction, whereas β is used only for single reaction steps in a specific reaction scheme. The relation between these two factors is given by:

$$a_a = \frac{n - s}{v} - r\beta \qquad (2\text{-}12)$$

Where *n* is the total number of electrons transferred in the total anodic reaction, *s* is the number of electrons transferred after the so-called rate determining step (rds), *v* is the number of times the rds has to occur for the total reaction to occur once (the stoichiometric number of the reaction mechanism) and *r* is the number of electrons transferred in the rds. The sum of the anodic and cathodic symmetry parameters is unity, where both are usually close to 0.5, and it does not depend significantly on the potential. The symmetry factor is only concerned with the physical chemistry of the elementary electron transfer step, while the transfer coefficient depends on the mechanism of the overall reaction.[36]

Generally, only the concentration of the products and reactants of the total reaction can be known, and it is necessary to eliminate the activity of intermediate species from the total rate expression. One commonly employed technique to achieve this, is the so-called pseudo-equilibrium method, where it is assumed that one reaction step is the rate limiting or rate determining step (rds) and thus controls the rate of the overall reaction. All the other steps are assumed to be at equilibrium, meaning that the rate of reduction and oxidation are equal (i.e. the total rate is zero). If the intermediate products do not diffuse into the bulk of the solution, expressions for the activities of the intermediates can then be obtained and inserted into the total rate expression (rate of the rds) until this total rate expression contains only known quantities. By setting each of the steps as rds, the expression for the total reaction rate, and thus the expression for the total current for the half-cell reaction, can be obtained. Each of these scenarios will result in a theoretical value for the Tafel slope and the reaction order, which are defined by equations (2-13) and (2-14), respectively.

$$b = \left(\frac{\partial \eta}{\partial \log|i|}\right) \qquad (2\text{-}13)$$

$$z_i = \left(\frac{\partial \ln|i|}{\partial \ln a_i}\right)_{E,T,p,a_j \neq a_i} \qquad (2\text{-}14)$$

The theoretical values for the Tafel slopes and reaction orders can be obtained from these equations and compared to values obtained experimentally.[36] Thus, these two quantities plays an important role in the determination of reaction mechanisms.

As described in section 3.2.3, the Tafel slopes can be obtained experimentally from polarisation curves. From the definition of the reaction order, it can be seen that this value equals the slope of a curve of $\ln|i|$ vs. $\ln c_i$, if the activity can be approximated with the concentration. This slope can be obtained experimentally if polarisation measurements are carried out in different electrolytes where the concentration of a specie taking part in the overall electrode reaction is changed. The reaction orders should be obtained from the currents in the electron-transfer-limited region of the polarisation curve (i.e. the Tafel region), if they are to be combined with Tafel slopes for determination of reaction mechanisms.

For the case of the OER in acidic media, the most evident concentration to vary is that of the proton, as it can easily be controlled by varying the pH of the electrolyte. Thus, the anodic reaction order of the proton can be used for mechanistic insight of the OER.

Mechanistic paths for the oxygen evolution reaction

Due to the complexity of the oxygen evolution reaction, many mechanisms have been proposed, many of them including molecular details that are hard to confirm experimentally. The three most popular mechanisms are given in Table 2-1, written for acidic solutions. The table also includes the Tafel slopes and reaction orders assuming the respective step is rds. These values are calculated for zero surface coverage of adsorbed species ($a_s = 1$), and assuming that the symmetry factor is 0.5. S denotes an active surface site. The Tafel slope of 15 mV has unfortunately never been reported for the OER on any material. Intermediate values for the Tafel slopes are often rationalised in terms of mixed mechanisms or intermediate coverage of adsorbed species. [22]

The first step of all three mechanisms is necessarily the discharge of water, resulting in an adsorbed OH intermediate, which is unstable and must be converted into something more stable before further oxidation. Therefore, it is expected that surface rearrangement will take place, and the adsorbed OH intermediate will move to a more active site before further oxidation to an adsorbed oxygen atom and finally O_2 liberation. From these mechanisms we can thus conclude that O_2 is evolved through decomposition of unstable higher oxides, and can be summarised as [22]:

$$\mathrm{MO_x + H_2O \rightarrow MO_{x+1} + 2xH^+ + 2xe^-} \tag{2-15}$$

$$\mathrm{MO_{x+1} \rightarrow MO_x + \frac{x}{2}O_2} \tag{2-16}$$

Table 2-1: The three most popular mechanisms for oxygen evolution, including the Tafel slope and reaction orders when assuming each respective step as the rds.

Reaction step	**Tafel slope, b$_a$**	**b$_a$ [mV] when $\boldsymbol{\beta = 0.5}$**	$\boldsymbol{Z_{a,H^+}}$
The chemical oxide path [7]			
$\boldsymbol{S + H_2O \rightleftharpoons S - OH + H^+ + e^-}$	$\frac{\ln(10)\,RT}{(1-\beta)F}$	118	0
$\boldsymbol{2S - OH \rightleftharpoons S - O + H_2O}$	$\frac{\ln(10)\,RT}{2F}$	30	-2
$\boldsymbol{2S - O \rightleftharpoons O_2 + 2S}$	$\frac{\ln(10)\,RT}{4F}$	15	-4
The electrochemical oxide path [7]			
$\boldsymbol{S + H_2O \rightleftharpoons S - OH + H^+ + e^-}$	$\frac{\ln(10)\,RT}{(1-\beta)F}$	118	0
$\boldsymbol{S - OH \rightleftharpoons S - O + H^+ + e^-}$	$\frac{\ln(10)\,RT}{(2-\beta)F}$	39	-1
$\boldsymbol{2S - O \rightleftharpoons O_2 + 2S}$	$\frac{\ln(10)\,RT}{4F}$	15	-4
Oxide decomposition path [37]			
$\boldsymbol{S + H_2O \rightleftharpoons S - OH + H^+ + e^-}$	$\frac{\ln(10)\,RT}{(1-\beta)F}$	118	0
$\boldsymbol{S - OH \rightleftharpoons S - O^- + H^+}$	$\frac{\ln(10)\,RT}{F}$	59	-1
$\boldsymbol{S - O^- \rightleftharpoons S - O + e^-}$	$\frac{\ln(10)\,RT}{(2-\beta)F}$	39	-2
$\boldsymbol{2S - O \rightleftharpoons O_2 + 2S}$	$\frac{\ln(10)\,RT}{4F}$	15	-4

The reaction mechanisms for the OER on rutile surfaces is still poorly understood, but it is generally accepted that the formation of the oxygen-oxygen bond is a central step. This bond can be formed either by the so-called mononuclear or by the binuclear path. The binuclear path is similar to the electrochemical oxide mechanism proposed by Bockris.[38] This path involves a surface redox reaction where two neighbouring S-O groups form a bridge bonding that yields the intermediate S-O-O-S, which in turn release O_2. This imply that two proximate active catalytic sites are required. This mechanism has been modelled for transition metals other than Ir and Ru.[38, 39]

The mononuclear path does not involve a bridge bonding, but rather an O-O bond formation between the adsorbed oxygen intermediate (S-O) and a water molecule, giving rise to an S-OOH intermediate prior to the final release of O_2. The steps of the mononuclear path, along with the respective Tafel slopes and reaction orders for each step as rate determining step is given in Table 2-2.[30]

The mononuclear path was used in DFT calculations for the OER at rutile (110) surfaces, and it was found that the OER on both RuO_2 and IrO_2 was very similar, and the formation of S-HOO was the rate limiting step on both oxides. The overpotential was found to be slightly larger at IrO_2 compared to RuO_2. [30]

Table 2-2: Mononuclear path proposed for OER on oxide surfaces, with the corresponding Tafel slopes and reaction orders assuming each respective step as rds.[30]

Mononuclear path	**Tafel slope, b$_a$**	**b$_a$ [mV] when $\boldsymbol{\beta = 0.5}$**	$\boldsymbol{Z_{a,H^+}}$
$\boldsymbol{S + H_2O \rightleftharpoons S - OH + H^+ + e^-}$	$\frac{\ln(10)\,RT}{(1-\beta)F}$	118	0
$\boldsymbol{S - OH \rightleftharpoons S - O + H^+ + e^-}$	$\frac{\ln(10)\,RT}{(2-\beta)F}$	39	-1
$\boldsymbol{S - O + H_2O \rightleftharpoons S - OOH + H^+ + e^-}$	$\frac{\ln(10)\,RT}{(3-\beta)F}$	24	-2
$\boldsymbol{S - OOH \rightleftharpoons S + O_2 + H^+ + e^-}$	$\frac{\ln(10)\,RT}{(4-\beta)F}$	17	-3

For the mechanistic path modelled by Rossmeisl et.al., with the formation of S-HOO as the rate limiting step, the rate expression leading to the Tafel slope and reaction order given in Table 2-2 can be deduced as follows by employing the procedure described above. This is provided as an example, and the Tafel slopes and reaction orders for the other steps as rds can be found by the same approach. In these calculations it is assumed that the activity of water and surface sites are unity and that the activity of protons equals the concentration of protons.

The rate of the anodic direction of the rds (step 3) is given as:

$$r_{3,a} = k_{3,a} a_{O_{ads}} a_{H_2O} e^{\frac{(1-\beta)FE}{RT}}$$

Where $a_{O_{ads}}$ is unknown. Expressions for this quantity can be found from the other steps, which are assumed to be in equilibrium:

$$r_{2,a} = r_{2,c}$$

$$k_{2,a} a_{OH_{ads}} e^{\frac{(1-\beta)FE}{RT}} = k_{2,c} a_{O_{ads}} c_{H^+} e^{\frac{-\beta FE}{RT}}$$

$$a_{O_{ads}} = \frac{k_{2,a}}{k_{2,c}}\, a_{OH_{ads}} c_{H^+}^{-1} e^{\frac{FE}{RT}}$$

$$r_{1,a} = r_{1,c}$$

$$k_{1,a} a_s c_{H_2O} e^{\frac{(1-\beta)FE}{RT}} = k_{1,c} a_{OH_{ads}} c_{H^+} e^{\frac{-\beta FE}{RT}}$$

$$a_{OH_{ads}} = \frac{k_{1,a}}{k_{1,c}}\, a_s c_{H^+}^{-1} e^{\frac{FE}{RT}}$$

$$a_{O_{ads}} = \frac{k_{2,a}}{k_{2,c}}\, a_{OH_{ads}} c_{H^+}^{-1} e^{\frac{FE}{RT}}$$

$$a_{O_{ads}} = \frac{k_{2,a}}{k_{2,c}} \frac{k_{1,a}}{k_{1,c}}\, a_s c_{H^+}^{-2} e^{\frac{2FE}{RT}}$$

Inserting the expression for $a_{O_{ads}}$ into the total rate expression for the anodic reaction:

$$r_{3,a} = k_{3,a} a_{O_{ads}} e^{\frac{(1-\beta)FE}{RT}} = k_{3,a} \frac{k_{2,a}}{k_{2,c}} \frac{k_{1,a}}{k_{1,c}}\, a_s c_{H^+}^{-2} e^{\frac{(3-\beta)FE}{RT}}$$

The rate of the reaction is thus expressed in terms of activities and concentrations of reactants and products of the total anodic reaction. As the total anodic reaction rate is proportional to the anodic current, the partial derivatives giving the Tafel slope and reaction order can be found directly from this rate expression:

$$b_a = \left(\frac{\partial \eta}{\partial \log|i|}\right) = \frac{ln(10)\, RT}{(3-\beta)F} = 24\ mV$$

$$z_{a,H^+} = \left(\frac{\partial \ln i}{\partial \ln c_{H^+}}\right)_{E,T,p,a_j \neq a_{H^+}} = -2$$

Thus, the mononuclear path with reaction step 3 as rds should result in Tafel slopes equal to 24 mV/dec and the reaction order with respect to protons should be -2.

2.2.3 By-products of the oxygen evolution reaction at rutile materials

The proposed reaction mechanisms for the OER suggests that adsorbed O, OH and OOH can be reaction intermediates of the OER. Adsorbed OOH (hydroperoxy species) has been identified at gold surfaces as an intermediate of the OER by using in situ surface-enhanced Raman spectroscopy [40], as well as on an IrO_2 surface during photocatalytic water electrolysis.[41] OOH has also been detected as a by-product of the OER by potential modulated reflectance spectroscopy (PMRS) on anodic iridium oxide films.[9]

Hydroperoxyl can form water or hydrogen peroxide (H_2O_2) through electrochemical reduction in acidic media[18]:

$$HO_2 + 3H^+ + 3e^- \rightarrow 2H_2O \qquad E^0 = 1.65\,V \tag{2-17}$$

$$HO_2 + H^+ + 3e^- \rightarrow H_2O_2 \qquad E^0 = 1.44\,V \tag{2-18}$$

Hydrogen peroxide is thus another possible by-product of the OER. H_2O_2 can also be formed by the decomposition of HOO radicals in protic media[42]:

$$2HO_2^{\cdot} \rightarrow H_2O_2 + O_2 \tag{2-19}$$

H_2O_2 can also be formed directly at the anode by oxidation of water through reaction (2-20) at high overpotentials of the OER:

$$H_2O_2 + 2H^+ + 2e^- \rightarrow 2H_2O \qquad E^0 = 1.76\,V \tag{2-20}$$

or by chemical recombination of O_2 and any H_2 from the cathode (e.g. due to crossover of gas in the PEM membrane):

$$H_2 + O_2 \rightarrow H_2O_2 \tag{2-21}$$

Clear evidence of H_2O_2 as a by-product of the OER on IrO_2 electrodes under dynamic potential conditions has been demonstrated by the use of UV-vis spectroscopy of a $KMnO_4$ solution, employing the principle that H_2O_2 will reduce the permanganate to a colourless product.[9]

Hydroperoxyl can also chemically recombine to oxygen or ozone by the chemical reactions (2-22) and (2-23).[18]

$$2HO_2 \rightarrow H_2O + O_3 \tag{2-22}$$

$$2HO_2 \rightarrow H_2O_2 + O_2 \tag{2-23}$$

Ozone might thus also be a by-product at the anode during water splitting. Ozone can also be formed directly at the anode through a 6-electron oxidation of water:

$$O_3 + 6H^+ + 6e^- \rightarrow 3H_2O \qquad E^0 = 1.51\ V \tag{2-24}$$

The formation of both O_3 and H_2O_2 has been reported as by-products of the OER on boron-doped diamond anodes.[43]

2.3 BY-PRODUCTS OF THE OER DETECTED ON RING-DISK ELECTRODES

Rotating ring-disk electrodes or ring-disk electrodes placed in flow cells (see section 3.3) can be used for detection of electroactive (by-)products of electrode reactions. Such experiments are relevant for the investigation of the OER under dynamic potential conditions that can be encountered in PEM electrolysers. The material to be studied can be employed at the inner disk electrode, while the encircling ring electrode is held at a constant potential where the by-products are electrochemically active, and thus might be reduced or oxidised.[9] If the products are to give rise to a current at the ring, they must be stable enough in the solution to reach the ring before decomposing, and additionally they must be electrocatalytically active on the ring electrode material at the chosen potentials. Experiments like this with the ring at 0.6 V and 1.2 V were performed in the preliminary project work.[12]

Considering HO_2, H_2O_2 and O_3 as possible by-products of the OER, and the two different ring potentials 0.6 V and 1.2 V, the thermodynamically possible reactions that can give rise to oxidation and reduction on each of these are given in Table 2-3. Oxygen is also included in the table, as this will obviously also be present at the ring. Further, the potentials given in the table are for standard conditions with activities of all involved species at unity. This is clearly not the case for all by-products at the ring-disk electrode, and it is difficult to know the actual activity of these products at the electrode surface under the dynamic conditions.

From table Table 2-3 it can be seen that hydroperoxyl might give rise to reduction currents at the ring electrode. However, as pointed out in [9] the recombination of HO_2 to H_2O_2 is so fast that it is highly unlikely that a significant portion of these radicals can reach the ring before recombination.

Both H_2O_2 and O_3 can, however, exist in acidic solutions long enough to reach the ring electrode. Ozone is generally accepted to be ca. 10 times more soluble in acidic solutions than O_2.[44] Ozone can decompose in solution by reaction with cations and anions that are capable of being oxidised to higher valent states (Fe^{2+}, Mn^{2+}, I^-, NO_2^-).[45] The stability of O_3 increases with decreasing pH, and in the absence of the chemicals ions listed above, ozone will be stable enough to traverse the distance from the disk to the ring electrode in RDE experiments. [46] However, the presence of H_2O_2 has shown to decrease the stability of O_3 in acidic solutions, catalysed by glass.[47] Other radicals can also increase the decomposition rate of O_3. [48] The decomposition of H_2O_2 into H_2O and O_2 is also catalysed by a variety of materials that can be present in electrochemical solutions (i.e. glass, Pt, dust etc.).[45] The situation is complex, but O_3 and H_2O_2 are in principle products that are possible to detect by ring-disk electrodes

Table 2-3: Thermodynamically possible reactions of potential by-products from the OER at a ring electrode, and the currents that can be detected at the ring when it is held at 0.6 V or 1.2 V.

Reaction	**Standard potential**		**Current on ring**	
			At 0.6 V	At 1.2 V
Hydroperoxyl				
$\boldsymbol{HO_2 + 3H^+ + 3e^- \rightarrow 2H_2O}$	$E^0 = 1.65\ V$	(2-17)	Reduction	Reduction
$\boldsymbol{HO_2 + H^+ + 3e^- \rightarrow H_2O_2}$	$E^0 = 1.44\ V$	(2-18)	Reduction	Reduction
Hydrogen peroxide				
$\boldsymbol{O_2 + 2H^+ + 2e^- \rightarrow H_2O_2}$	$E^0 = 0.695\ V$	(2-25)	Reduction	Oxidation
$\boldsymbol{H_2O_2 + 2H^+ + 2e^- \rightarrow 2H_2O}$	$E^0 = 1.76\ V$	(2-20)	Reduction	Reduction
Ozone				
$\boldsymbol{O_3 + 6H^+ + 6e^- \rightarrow 3H_2O}$	$E^0 = 1.51\ V$	(2-24)	Reduction	Reduction
$\boldsymbol{O_3 + 2H^+ + 2e^- \rightarrow O_2 + H_2O}$	$E^0 = 2.07\ V$	(2-26)	Reduction	Reduction
$\boldsymbol{2O_2 + 2H^+ + 2e^- \rightarrow O_3 + H_2O}$	$E^0 = -0.383\ V$	(2-27)	Oxidation	Oxidation
Oxygen				
$\boldsymbol{O_2 + 4H^+ + 4e^- \rightarrow 2H_2O}$	$E^0 = 1.23\ V$	(2-3)	Reduction	Reduction

Although both H_2O_2 and O_3 can be present at the ring electrode, their electrochemical activity is highly dependent on the ring electrode material chosen for the investigation. This can be utilised as an advantage during ring-disk studies of reaction intermediates, as different ring materials might give rise to different reactions at different potentials. Attempts of this were made in the preliminary project, were the chosen ring materials were gold and platinum.[12] The background for this choices are given below.

Katsounaros et.al. established the potentials where O_2 and H_2O_2 are electrochemically active at platinum electrodes in acidic media.[49] They cycled Pt between 0 V and 1.5 V and showed that oxygen with an activity of unity could not be oxidised within this potential range, and could only be reduced at potentials below ca. 1 V. In acidic solutions containing 10^{-3} M H_2O_2, it was found that H_2O_2 oxidation was the only possible reaction above 0.95 V, and H_2O_2 reduction the only possible reaction below 0.8 V. Analogous experiments on both platinum and a gold electrode in 0.5 M H_2SO_4 solutions were performed in the preliminary project work.[12] The same results were obtained for the platinum electrode, and the activity range of O_2 and H_2O_2 at Au was established in addition. For the potential range 0 V to 1.6 V, O_2 reduction was seen only at potentials lower than 0.5 V at gold electrodes. H_2O_2

showed no activity at gold in the potential range 0.35 V to 1.05 V. Above 1.05 V, H_2O_2 was oxidised at gold. These considerations imply that different current responses are expected for Au and Pt ring electrodes, and further that different responses are expected at 0.6 V and 1.2 V at each of the electrodes.

Kuznetsova et. al. employed a RDE in a flow cell to study the by-products of the OER on both iridium oxide and mixed iridium-ruthenium oxide.[9] The disc electrode was coated with the rutile catalyst and was cycled between 0.6 V and 1.9 V, which is typical potentials encountered at the anode in PEM water electrolysers.[13] The ring electrode was of platinum and was held at a constant potential of 1.2 V. For the positive sweep form 0.6 V to 1.9 V, a reduction current was detected at the ring for potentials higher than the onset of the OER (approx. 1.5 V). When the potential sweep was reversed, the reduction currents observed on the ring were replaced quite instantaneously by an oxidation current, showing some hysteresis. The oxidation current was ascribed to oxidation of H_2O_2, but the reduction current could not be explained. However, it was proposed that ozone might be a probable candidate by-product of the OER for explaining the reduction currents observed.

The hypothesis of ozone being the cause of the observed reduction currents was studied further in the preliminary project work. In this work the different electrocatalytic activity of ozone reduction at Pt and Au was utilised. Ozone reduction is expected to have a higher activity at Au than at Pt.[50] Further, ozone reduction is expected to increase significantly at decreasing potentials at gold electrodes. In particular, the current detected in [50] at a gold electrode at 0.6 V was approximately five times higher than at 1.2 V for similar amounts of ozone. Cyclic voltammetry studies on a *mixture* of H_2O_2 and O_3 ($3 \cdot 10^{-4}\ \mathrm{M}\ O_3$ and $7 \cdot 10^{-4}\ \mathrm{M}\ H_2O_2$) has also indicated that the reduction currents of this mixture will be higher at 0.6 V than at 1.2 V.[51] Ozone does not give rise to oxidation currents below approximately 1.5 V.[50, 51]

It the preliminary project work [12], similar experiments to those published by Kuznetsova et.al.[9] were performed, but the experiments were performed with a gold ring electrode in addition to a platinum electrode, in order to investigate the difference in catalytic activity at these two ring materials. Further, the ring electrodes were held at 0.6 V in addition to 1.2 V, which was the only employed ring potential in the work of Kuznetsova et.al. Thus, it could be studied whether the reduction current increased for lower potentials at the gold electrode, as expected for ozone reduction. It was, however, discovered that the reduction currents were not higher at the gold ring than at the platinum ring. Furthermore, the reduction currents at the gold ring at 0.6 V were not higher than those observed at gold at 1.2 V. This also contradicted the hypothesis of ozone being the cause of the reduction current. In addition, an oxidation current was observed at 0.6 V at the gold ring electrode. This was not likely to be caused by either H_2O_2 or O_3, as these were not expected to be oxidised at gold at this potential, as explained above. This suggested that an additional specie, also resulting from the OER at the disk, caused this oxidation current.

It is believed that there might be a correlation between electrocatalytic activity and amount of by-products created, and thus that a mixed Ir-Ru oxide, which is more active for the OER, will produce less by-products than pure Ir oxide. This was also found in the ring-disk studies of Kuznetsova et.al.[9] and in the preliminary project work [12]. Possible explanations for this were also proposed. If it is assumed that there is no interaction between the sites and that the reaction proceeds by the mononuclear mechanism, two different active sites will be available, one with Ir oxide and one with Ru oxide. It is expected that the bonding of intermediates at the Ru sites is weaker, and thus the OER is more favourable on these sites. This will result in a decrease in the production of intermediates the more Ru that is added. If the OER proceeds by the binuclear mechanism where the bridge bonding is a central step, the OER will be more favourable on both neighbouring Ir-Ru sites and neighbouring Ru-Ru sites compared to the Ir-Ir sites in pure Ir oxide, due to stronger adsorption in the latter case.[9]

3 THEORY BEHIND EXPERIMENTAL METHODS

This chapter provides an overview of the theory and application of experimental methods employed in this thesis. First, a general overview of electrochemical cells is given, then an introduction to the electrochemical characterisation techniques used. Special attention is given to ring-disk electrodes, and the use of these for detection of reaction intermediates. A short introduction to catalyst synthesis procedures is given in the end.

3.1 ELECTROCHEMICAL CELLS

3.1.1 The potentiostat

Generally, it is desired to study a reaction that occur at only one electrode, referred to as the working electrode (WE). To measure the potential of the WE, this electrode is coupled with an electrode of known potential, called the reference electrode (RE).

In order to obtain the potential of the WE from the potential difference between the WE and the RE, it must be required that the RE maintains a constant potential, independent of the current, so that the changes in the measured potential difference corresponds to the same changes in the potential of the WE. This can be achieved by using a non-polarisable electrode as RE. A non-polarisable electrode is an electrode whose potential does not vary with current, and is often referred to as a reversible electrode. There are no ideal reversible electrodes, but non-polarisable behaviour can be attained for some electrodes in a potential range close to their reversible potentials. Two examples of such electrodes are described in the following subsection (the reversible hydrogen electrode and the silver/silver chloride electrode). Another requirement for the circuit between the WE and the RE is that the potential drop in the electrolyte between these electrodes is negligible. This is achieved by the high-impedance connection between these electrodes, and by placing the electrodes as close as possible.

The potential of the WE can be changed by controlling the current to/from the electrode, as shown by the Butler-Volmer equation (2-6). This requires another electrode in connection with the WE. Often, the RE cannot be employed for this purpose, as high currents will give a substantial potential drop between the electrodes. Therefore, a counter electrode (CE) is often dedicated for this purpose.

All three electrodes are electrically connected through the potentiostat. In addition there must be ionic contact between the electrodes. If the electrodes must be placed in different electrolytes or compartments, an extra ionic conductor between the solutions can ensure the ionic contact. This could typically be a salt bridge or a membrane.

A bi-potentiostat is capable of controlling two working electrodes, and this is required for a four electrode setup like the one used in ring-disk measurements (see section 3.3).

3.1.2 Reference electrodes

Two commonly employed reference electrodes are the reversible hydrogen electrode and the silver/silver chloride electrode. Both are described below.[19]

In a reversible hydrogen electrode, the reference electrode reaction is:

$$2\mathrm{H}^+ + 2\mathrm{e}^- \rightleftharpoons \mathrm{H}_2 \qquad \mathrm{E}^0 = 0\,V \tag{3-1}$$

At standard conditions, the reversible potential is zero, and the reversible hydrogen electrode (RHE) is then equal to the standard hydrogen electrode (SHE). At other conditions, the reversible potential is given by Nernst equation:

$$E_{RHE} = E^0 - \frac{RT}{nF}\ln\frac{a_{H^+}^2}{a_{H_2}} \tag{3-2}$$

If the reference electrode can keep a hydrogen pressure of 1 atm above a proton containing solution with a hydrogen concentration, c_{H^+}, and assuming that $a_{H_2} = p_{H_2}$ and $a_{H^+} = c_{H^+}$, the equation can be simplified to:

$$E_{RHE} = 0 - 0.0951pH \tag{3-3}$$

In the lab, a RHE can be made by using platinum as electrode material in a glass chamber filled with a mixture of pure H_2 gas and a H^+ containing solution with known concentration. Using 0.5 M H_2SO_4 as the solution, will give a pH close to zero. H_2SO_4 is a diprotic acid, and is a strong acid in the first dissociation step and has $pK_a = 1.99$ for in the second step. This should give the total H^+ concentration of 0.576 M, corresponding to a pH value of 0.246. This gives the following potential:

$$E_{RHE} = 0 - 0.0951 \cdot 0.25 = -0.0145\,V \tag{3-4}$$

A silver/silver chloride electrode is another type of reference electrode commonly employed. This electrode relies on the redox reaction:

$$\mathrm{AgCl}\ (\mathrm{s}) + \mathrm{e}^- \rightleftharpoons \mathrm{Ag(s)} + \mathrm{Cl}^- \qquad \mathrm{E}^0 = 0.22\,V \tag{3-5}$$

Assuming $a_{Cl^-} = c_{Cl^-}$:

$$E^{rev} = E^0 - \frac{RT}{nF}\ln c_{Cl^-} \tag{3-6}$$

This electrode can be made from a silver wire coated with a thin layer of AgCl, for instance achieved by electroplating in a suitable chloride containing electrolyte (e.g. KCl). [52, 53] The solid Ag/AgCl electrode is placed in a compartment containing a known concentration of chloride ions, and the potential depends on this concentration. For a saturated solution, the potential of the Ag/AgCl electrode is 0.197 V vs. SHE. However, if the wire is placed directly in a solution with no chloride, the potential can be estimated by using the solubility constant of reaction (3-5) and equation (3-6):

$$E^{rev} = 0.22V - \frac{8.314\frac{J}{K \cdot mol}298\,K}{1 \cdot 96485\frac{C}{mol}}\ln\sqrt{K_{sp}} = 0.508\,V \tag{3-7}$$

3.1.3 Liquid junction potentials [19]

If a reference electrode is placed in another compartment than the working electrode, and the two compartments contain different electrolytes, a liquid junction potential (LJP) will be established across the phase boundary between the two electrolytes (the liquid junction). The origin of this potential difference is the different chemical potentials of the ions in each solution. The ions will experience a diffusional driving force in the direction of the more dilute solution, giving rise to a flux across the interface. Anions and cations will at first diffuse independently of each other and at different speeds due to the different mobilities. Due to the unequal diffusion speed, there will arise an excess of cations on one side of the interface, and anions at the other side, giving rise to a potential difference across the junction. This potential establishes an electric field that will accelerate the slowest moving ions, and retard the fastest moving ions. Eventually a steady state is reached, and the junction potential then has a value such that both types of ions are transported at an equal rate. The liquid junction contributes to the overall measured cell potential, and must be subtracted from this value to find the real potential at the working electrode vs. the reference.

$$E_{measured} = E_{real} + LJP$$

The sign of the LJP depends on the relative mobilities of the ions, and it will increase with increasing difference in mobilities between the two solutions.

The liquid junction potential can be calculated by the Henderson equation:

$$E_{LJ} = -\frac{RT}{F} \cdot \frac{\sum_i \frac{(a_i(II) - a_i(I))u_i|z_i|}{z_i}}{\sum_i (a_i(II) - a_i(I))u_i|z_i|} \cdot \ln \frac{\sum_i a_i(II)u_i|z_i|}{a_i(I)u_i|z_i|} \tag{3-8}$$

This equation is derived with the assumptions that concentration and activity is interchangeable when transport numbers are calculated, that the activities of ions vary linearly with fractional distance across the interface, and that the ionic mobilities are independent of activities. Given all other approximations in this equation, it is sufficient to replace activities with concentrations for aqueous solutions of strong 1:1 electrolytes. The Henderson equation has proved to be in very good accordance with experimentally obtained values for these types of solutions, even with all approximations above considered.

Liquid junction potentials can be in the order of a few to a few tens of millivolts and should be sought minimised during experiments and/or corrected for afterwards. From the Henderson equation, it can be seen that the LJP can be reduced if a solution is brought in contact with a solution with an electrolyte with ions with ionic mobilities as close as possible to each other, as this will reduce the pre-logarithmic term since the two contributions then will cancel each other to a high extent. The LJP will also be minimised if the concentration of the electrolyte with ions of the lowest mobility is much higher than the concentrations in the electrolyte with ions of high mobility. A salt bridge between the two solutions can reduce the total LJP considerably by exploiting these facts. If the salt bridge contains a solution of high concentration and ions of equal mobility, the LJP between the salt bridge and both solutions can be reduced.

3.2 ELECTROCHEMICAL CHARACTERISATION

3.2.1 Cyclic voltammetry

Cyclic voltammetry is frequently used, as it offers a wide range of experimental information, and can give insight into both kinetic and thermodynamic parameters of many chemical systems. Due to significant advances in the theoretical understanding of the technique, also complex systems can be studied quantitatively. Cyclic voltammetry is often the preferred experiment to start with to begin a new study, as it gives a "fingerprint" of the material, and can indicate which potential regions show activity.[1, 54]

In cyclic voltammetry, the electrode potential is swept linearly between a lower potential, E_1, and an upper potential, E_2, and the current response is simultaneously recorded. When the potential reaches E_2, the scan is reversed, and a cycle is completed when E_1 is reached again. This is illustrated in Figure 3-1. Usually, the cycle is repeated several times, and the potential limits can be kept constant of all cycles or changed for later cycles. Important information can also be obtained by repeating the experiments for different sweep rates.[55]

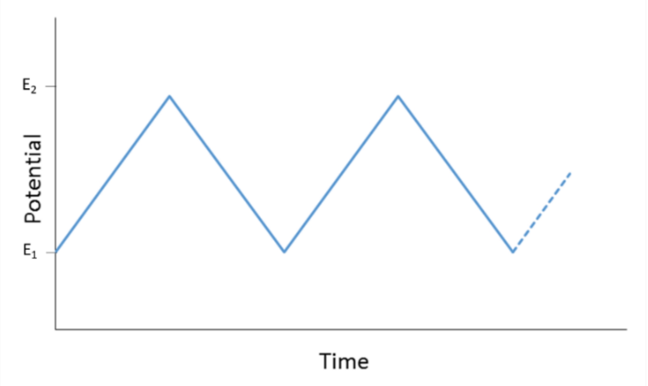

Figure 3-1: Typical variation of potential as a function of time during cyclic voltammetry.

Cyclic voltammetry with electroactive species in solution

Cyclic voltammetry is normally a non-steady state technique, and experiments are therefore usually performed in unstirred solutions, where diffusion is ideally the only significant contribution to mass transport. The experiments take place while the diffusion layer is developing, meaning that the concentration of reactants, intermediates and products are a function of both time and distance from the electrode. Usually, the conditions are chosen such that it can be assumed that Fick's laws of diffusion in one dimension can be applied for description of mass transport.[56]

A textbook example of a cyclic voltammogram for a redox process is shown in Figure 3-2, presenting the current as a function of potential. I_{pf} and I_{pb} are the peak currents observed on the forward and backward sweeps, respectively. E_{pf} and E_{pb} are the potentials corresponding to the peak currents.

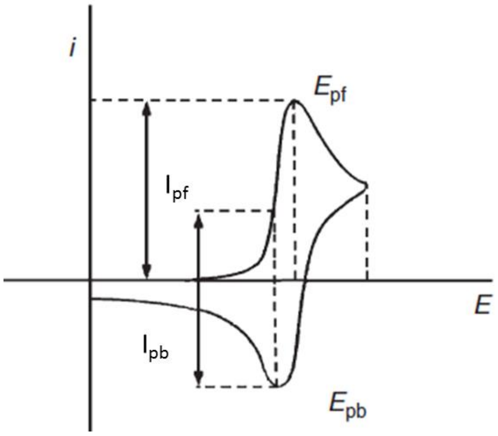

Figure 3-2: A textbook example of a cyclic voltammogram.[1]

For each electrode reaction where the current is determined by both diffusion to the electrode and an electron transfer process, a peak current will be observed in the voltammogram. The potential scan usually starts where no faradaic current flows. As the potential is swept closer to the standard potential of the reaction, electron transfer is initiated. This results in a decrease of the concentration of the reactant at the surface, and a concentration gradient between the bulk and the surface is developed. The concentration gradient results in an increased flux of reactant to the surface, and thereby causes an increase in current. The thickness of the layer where the concentration gradient is set up is called the diffusion layer thickness, δ. This thickness will increase with time according to $\delta = \sqrt{\pi D t}$, where *D* is the diffusion coefficient of the reactant and *t* is time. As the potential is increased further, the current will increase further and will eventually reach the limiting current. Then, the concentration profile can only increase by expanding the thickness of the diffusion layer. This will cause the current to decrease again, thereby giving a peak in the voltammogram. If the sweep rate, *v*, is increased, the diffusion layer will have less time to grow and the concentration gradient will thus be larger, resulting in higher currents.[55, 56]

The peak current, I_p, for a reaction involving reversible electron transfer is given by the following equation (at 298 K)[56]:

$$I_p = 2.69 \cdot 10^5 n^{3/2} A D^{1/2} c v^{1/2} \tag{3-9}$$

Where *n* is the number of electrons involved in the electrode reaction, *c* is the concentration given in mol/cm^3, A is the area given in cm^2, D is in cm^2/s, *v* in V/s and I_p in amperes.

Cyclic voltammetry is normally a non-steady state technique, but can also be performed on systems where the diffusion layer thickness is controlled. The shape of the voltammograms will then look different. As for non-steady state conditions during the positive sweep, the current will gradually increase in the regions of the voltammogram where the reactions are not limited by diffusion. When the concentration at the surface eventually is zero, the limiting current is reached. However, as the diffusion layer thickness cannot expand into the solution, both the concentration gradient and current will now be constant for the rest of the positive sweep, as well as for the reversed sweep until the region with mixed diffusion and electron transfer control is again reached. The current will thus remain at the peak value for the rest of the sweep, as long as the same reaction is occurring.[56] The limiting current is a function of the diffusion layer thickness. This relation is described in section 3.3.1, as well as means for controlling the diffusion layer thickness by rotating the electrode.

Cyclic voltammograms for characterisation of materials (as unique electrochemical spectra)

If there are no redox-active couples in an aqueous solution at the potential interval where the cyclic voltammetry is performed, the observed current-potential behaviour will correspond to the formation and dissolution of chemisorbed hydride and oxide layers on the electrode surface, in addition to the current for double layer charging. A typical voltammogram of platinum is given in Figure 3-3, here in 0.5 M H_2SO_4. There are mainly three different regions in this voltammogram: the hydrogen region, the double layer region and the oxide region. Following the changes in the anodic (positive) sweep, starting at about 0.4 V vs. RHE and continuing until the onset of the surface oxidation, is a double layer region. The only current that flows is that required to charge the double layer when the potential is swept at the rate, v. The current in this region is given by $i_{dl} = C_{dl} \cdot v$. At higher potentials is the oxide region, where oxygen chemisorption begins. Two peaks can be seen in this region, and has been attributed to the reaction occurring by discharge of water in two stages at the Pt surface. First one half of the monolayer of water is discharged, and at higher potential the second half, which experiences stronger interfacial interactions with the surface, is discharged.[57] If the potential is increased above ca. 1.6 V, oxygen evolution will take place, and at even higher potentials, an oxide phase may form on the surface. By "oxide phase" it is referred to an oxide with thickness significantly larger than a monolayer, as opposed to the thin layer formed in the oxide region between 0.8 and 1.4 V. On the reverse scan (cathodic), the chemisorbed oxide layer is reduced, and a reduction peak is observed. Moving towards more negative potentials on the reverse scan, the double layer region is again encountered, and at potentials below 0.35 V is the hydrogen region, where hydrogen is adsorbed to the platinum surface, and desorbed again on the anodic sweep.[55]

A typical voltammogram for gold in the same electrolyte (0.5 M H_2SO_4) is given in Figure 3-4. It can be seen that the curves for the different metals has distinct features, and these are characteristic of the particular metal.[58] This is why these cyclic voltammograms are often referred to as unique electrochemical spectra for each material. For gold, we can see that the double-layer region is much larger than for platinum, which allows for investigations over a wide potential range without any formation of oxide or hydride layers.

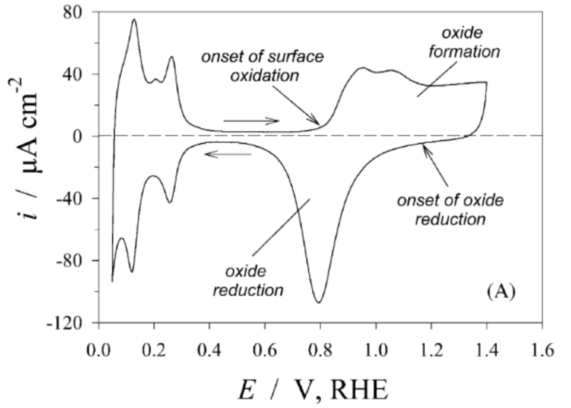

Figure 3-3: Typical voltammogram of the platinum electrode, here in 0.5 M H_2SO_4.[57]

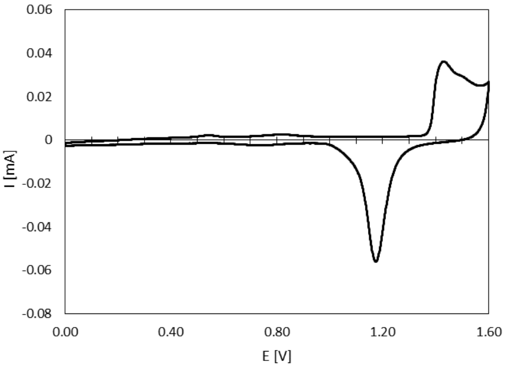

Figure 3-4: Typical voltammogram of the gold electrode, here in 0.5 M H_2SO_4 purged with N_2.[12]

If there are electrochemically active species in the solution, the current curve will always be the sum of the curve for the electrode film processes that occur in solution without these species, and the current for the electrode reactions of the species in solution. It may therefore be convenient to subtract the blank response of the electrode from the total curve when the reaction of solution species are studied.

Limitations for cyclic voltammetry

The recorded current is a sum of the faradaic and the capacitive currents. i_F is proportional to $v^{1/2}$ while i_{dl} is proportional to v ($i_{dl} = C_{dl} \cdot v$). As typical values for the capacitive current lies between 2 and 4 mA/cm^2, i_{dl} is negligible at low sweep rates. However, the effect of this current contribution increases with increasing *v*, and this is one of the major limitations for the maximum sweep rates that can be applied.[59] The limits for the minimum sweep rates that can be applied should be at least such that the diffusion layer is still growing, in order to avoid steady-state conditions. The limit will thus depend on the system studied, but typically at least a few mV/s should be applied.[54]

IR drop also influences the CV. Due to IR drop between the working and reference electrodes, the applied voltage is changed from the desired value, E, to E minus IR. Since I varies during a scan, the sweep will not be linear. This will result in decreased peak heights and increased peak separations, and can thus result in a CV that resembles quasi-reversible behaviour even though the process is reversible.[59]

Cyclic voltammetry on Ir and Ir-Ru oxides

Typical voltammograms for iridium and ruthenium oxides are given in Figure 3-5 a) and b), respectively. The materials in these figures were prepared by standard DSA technique and recorded in 0.5 M H_2SO_4 and cycled within the stability ranges of the electrolyte. The standard DSA technique involves coating a dimensionally stable substrate with the metal oxide precursors, and subsequently heating these at 350 °C to 600 °C. This results in thermal decomposition of the precursors into the respective metal oxides. [60]

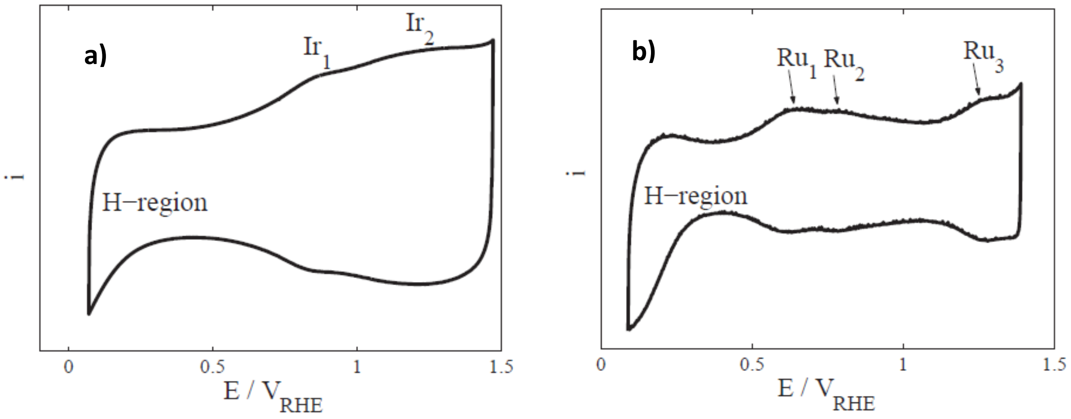

Figure 3-5: Typical cyclic voltammograms of a) IrO_2 and b) RuO_2.[60]

The hydrogen region is found at potentials below 0.4 V vs. RHE, and here hydrogen is adsorbed and desorbed as described above for Pt and Au. Above 0.4 V vs. RHE, OH is adsorbed on the oxide surfaces, and for more positive potentials oxides are formed. The peaks observed above 0.4 V are consequences of the redox transitions of the metal ions as oxygen species are adsorbed on the surface, which leads to ejection of protons and electrons. The voltammograms show symetrical anodic and cathodic peaks for oxide formation and dissolution, which implies that these redox transitions are reversible.[61]

A surface reversible redox process gives rise to the peaks of iridium oxide, and can in the simplest form be written as [61]:

$$\mathrm{IrO_a(OH)_b \rightleftharpoons IrO_{a+x}(OH)_{b-x} + xH^+ + xe^-} \qquad (3\text{-}10)$$

The peaks in the oxide region of the ruthenium oxide voltammogram is given by analogous reactions[62]:

$$\mathrm{RuO}_{a-x}(\mathrm{OH})_{b+x} \rightleftharpoons \mathrm{RuO_a(OH)_b + xH^+ + xe^-} \qquad (3\text{-}11)$$

The two peaks in the iridium oxide voltammogram corresponds to the transitions Ir(III)/Ir(IV) at about 0.93 V, and to Ir(IV)/Ir(VI) at ca. 1.35 V.[63] For ruthenium, the first peak (Ru_1) corresponds to the transition Ru(II)/Ru(III), the second (Ru_2) to Ru(III)/Ru(IV) and the third to Ru(IV)/Ru(VI).[64, 65]

If x = 1 in equations (3-10) and (3-11) above, this will give a Nernstian dependence of the peaks in the voltammograms, implying that the peaks of the voltammograms will shift 59 mV in the negative direction for each integer increase in the pH value. This means that the peaks will have the same position when the potential is given with reference to a reversible hydrogen electrode.

It has, however, been found that the intercalation process also can involve other cations, anions and water from the surrounding solution[66, 67]. A reaction equation including these parameters has been proposed for the intercalation reaction for the Ir(III)/Ir(IV) transition for anodically grown iridium films[67]:

$$\mathrm{IrO_2} \cdot n\mathrm{H_2O} + (1+\delta)\mathrm{H^+} + \delta A^- + \mathrm{e^-} \rightleftharpoons \mathrm{IrO(OH)}_{1+\delta}A_\delta^- \cdot m\mathrm{H_2O} + (n-m)\mathrm{H_2O} \qquad (3\text{-}12)$$

The peak positions and the pH dependence will therefore depend on the anion of the electrolyte, as different anions exhibit different extents of adsorption. Na^+ and Li^+ has also been found to intercalate into the iridium oxide in non-aqueous electrolytes.[68]

Further, the peak positions and shape can vary depending on the preparation procedure of the oxide (e.g. hydrous or anhydrous oxide), especially for iridium oxide.[66, 69] In the voltammograms for thermal iridium oxide (anhydrous) the peaks are generally more broad and less pronounced than for hydrous oxides.[69, 70] Further, the pH dependence of hydrous and anhydrous oxides are found to be different. The pH sensitivity (mV change of reduction potential of the intercalation reaction per pH unit) of differently prepared iridium oxides has been compared in [71]. Generally, the pH dependence was found to be ca. 59 mV/pH for thermally prepared iridium oxide, whereas electrochemically grown oxide films was found to exhibit higher and more scattered values. The super-nernstian behavior found for the anidically grown oxides has been explained by the assumption that more than one proton is involved per electron in the intercalation process.[72] The large variation of the pH sensitivity for these oxides is ascribed the differences in fabrication that leads to differences in oxidation state and extent of hydration.[71, 72]

The differences described above between differently prepared oxides show that the intercalation process is complex and that it is difficult to predict the behavior of differently prepared oxides in different electrolytes. Variations in preparation procedure can affect the voltamograms for the oxides in the same electrolytes, even with the same nominal composition. Further, the voltammograms of the same material can look different in different electrolytes.

3.2.2 Potential step voltammetry [56]

In potential step voltammetry the potential of the working electrode is stepped instantaneously from a value E_1 to E_2 as show in Figure 3-6 a) and the resulting current is measured as a function of time. Usually, the initial potential, E_1, is chosen to such that no faradaic current flows, and E_2 in the potential range where a reaction can occur. When the potential of the electrode is stepped from E_1 to E_2 , a faradic currents starts to flow at the same time as the double layer is charged. The recorded current is a sum of these faradaic capacitive processes, and can typically look like the curve in Figure 3-6 b).

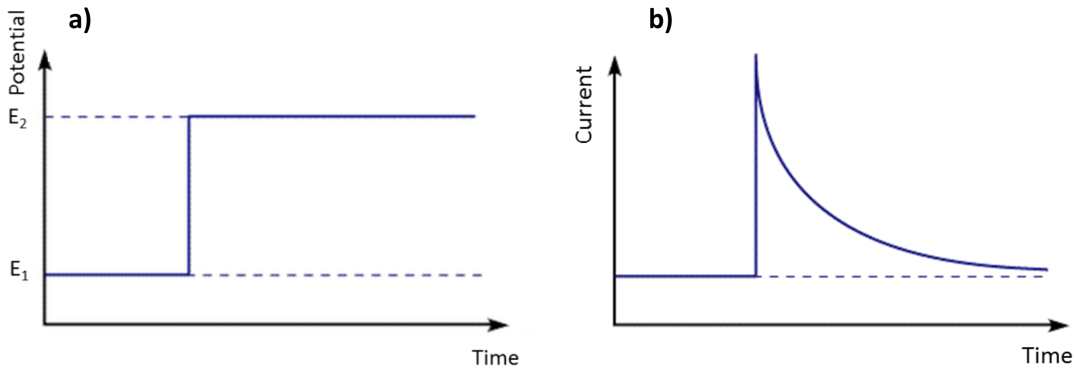

Figure 3-6: a) Potential step voltammetry. Potential is stepped instantaneously from E_1 to E_2. b) Typical current transient recorded during a potential step.

The change in the potential will lead to an instantaneous change in the concentration of the reactant at the surface, and result in a concentration gradient between the electrode surface and the bulk solution. This causes diffusion of reactant from the bulk to the surface, which in turn leads to an expansion of the diffusion layer length into the solution. With increasing time, the diffusion layer increases and the concentration gradients decrease, resulting in a reduced flux to the surface and hence a decrease in the measured current. With the considerations given here, and by use of Fick's second law, the current response from a potential step can be described mathematically by the Cottrell equation (3-13):

$$I = \frac{nF\sqrt{D}c}{\sqrt{\pi t}} \tag{3-13}$$

Where D is the diffusion coefficient of the reactant, c is the bulk concentration of the reactant and t is the time. The Cottrell equation can hence be used to find diffusion coefficients.

The theory behind the Cottrell equation applies only if the reaction rate can be controlled by mass transfer of the reactant. This is however not the case for oxygen evolution, as water is the reactant. The potential E_2 will typically be in the Tafel region of the polarisation curve for the OER, where the reaction rate is limited by charge transfer. The measured current density after the potential step should therefore be a constant value. However, the capacitive charging will still distort the transient, and a falling current over time will be observed. In addition, for gas evolving reactions, bubbles will block parts of the surface at times before they are released again, and this will result in a noisy current signal.

3.2.3 Polarisation curves (Linear sweep voltammetry)

Linear sweep voltammetry (LSV) is a technique used to obtain polarisation curves. It is similar to cyclic voltammetry in that a constant potential sweep rate is applied and the current response is recorded. However, the sweep rate is generally much lower in LSV, in order to obtain near steady-state conditions.[1]

The current-potential relationships obtained by linear sweep voltammetry is commonly represented as potential versus the logarithm of the current. These polarisation curves typically have one linear part, where the reaction kinetics obey the Tafel equation described in section 2.1.3. Thus, the Tafel slope can easily be determined from LSV.

3.2.4 Staircase voltammetry vs. analogue sweep voltammetry [73]

The theory of cyclic voltammetry and linear sweep voltammetry is based on true linear potential sweeps, which can be achieved only on analog potentiostats. Most modern potentiostats are, however, digital, and the potential is changed stepwise rather than swept continuously. The current is sampled at each of these potential steps, normally at one point which is close to the end of each step. This procedure can exclude the currents from any capacitive or surface-bound reactions in the obtained current curves, since the currents from such processes decays in the initial part of the step. However, many potentiostats allows for sampling throughout the duration of each potential step, and subsequently averaging this value. Thus, both capacitive and faradic effects are accounted for. It has also been shown that if the potential steps are small enough, the staircase voltammetry signal is similar to true CV.

The difference between true linear potential scans and staircase voltammetry is most important to have in mind when obtaining cyclic voltammograms. This is because the goal of this technique often is to study surface processes and how these are affected by changing sweep rates. For measurements to obtain polarisation curves, however, the aim is to approach near steady-state conditions. Thus, the capacitive currents are not studied. Polarisation curves are rather used to study faradaic processes, like the OER. However, for polarisation curves, it is important that the current is sampled closer to the end for each of the steps, in order to avoid the capacitive currents.

3.2.5 Ohmic loss compensation

As described in section 2.1.3 the total cell voltage is the sum of the reversible potential, the overpotentials and the ohmic losses. Ohmic losses arise between two electrodes when current is flowing, and increases linearly with the current, according to Ohm's law

$$\Delta V_{ohm} = IR_{Ohm} \qquad (3\text{-}14)$$

In principle, the ohmic losses arise both in the electrolyte and in the electrical conductors, but in practice, the latter is negligible compared to the ohmic drop in the electrolyte. The ohmic resistance of the electrolyte is a function of the electrolyte conductivity, κ, the distance between the electrodes, l, the surface area of the area of the electrodes, A, by the following relation:

$$R = \frac{l}{A\kappa} \qquad (3\text{-}15)$$

Where the conductivity of the electrolyte is given by:

$$\kappa \ = e_0(n^+z^+u^+ + n^-z^-u^-) \qquad (3\text{-}16)$$

Where the superscript '+' refers to cations and '–' to anions, e_0 is the elemental charge, n the number of ions per unit volume, z the elemental number of charges per ion, and u the mobility of the ions in the solvent. For strong 1:1 electrolytes, it is usually sufficient to employ the limiting ionic mobilities at infinite dilution as the mobility in this expression, as the mobilities in these electrolytes does not change significantly with concentration. [74]

Since there always will be some distance between the reference electrode and the working electrode, ohmic losses will result in a measured potential value that differs from the actual potential value at the working electrode. As mentioned above, this can lead to distortion of cyclic voltammograms, and it can be even more crucial when determining Tafel constants from polarisation curves. [55]

To avoid errors due to ohmic losses, the most important measure is to place the two electrodes as close as possible. Employing an electrolyte with high conductivity will also reduce the electrolyte resistance. However, it is often essential to correct for the ohmic losses by other methods in addition. A commonly used method is electrical impedance spectroscopy (EIS), where the ohmic resistance between the reference and working electrodes is measured prior to the experiment. The potentiostat can then automatically account for the electrolyte resistance in the preceeding experiments.[75]

The ohmic losses can also be corrected after the polarisation curve is obtained. This can be done by numerically fitting the linear equation given in equation (3-17) with the experimental data.

$$\eta = a + b \log i + IR_{Ohm} \qquad (3\text{-}17)$$

This is in principle the Tafel equation for the anodic reaction with an additional term that represents the contribution from the ohmic drop. The fit with experimental data can be extended only as far as this term increases linearly, thus ensuring that it follows Ohms law. The validity of this fitting procedure can thus be checked by plotting the uncompensated ohmic loss (i.e. the difference between the IR corrected curves and the raw data) as a function of current. For a good fit, this should give a straight line passing through the origin. This procedure for ohmic loss compensation has been successfully employed for extending the linear region of the polarisation curves of thermal iridium and mixed iridium-ruthenium oxides earlier.[31] An example of raw data and the IR corrected data are given in Figure 3-7 a), along with a plot of the uncompensated ohmic loss b). It can be seen that the corrected data extends the linear part of the polarisation curve from the low current regions, where the ohmic loss is low, towards higher currents, where ohmic loss contributes more to the total potential.

This correction procedure can, however, not be extended to very high potentials (typically above 1.6 V vs. RHE for IrO_2).[66] This has been ascribed to the large gas evolution rates at high potentials, resulting in an extra resistance term in equation (3-17). The resistance due to gas evolution does not follow ohms law, as bubbles gives a highly varying and complex contribution to ohmic losses, and the procedure described here does not apply in these regions. A change in reaction mechanism at the electrode can also account for the bad fit for higher potentials, as this will give a change in the Tafel slope at higher potentials. In such cases, two different fits must be executed. [76]

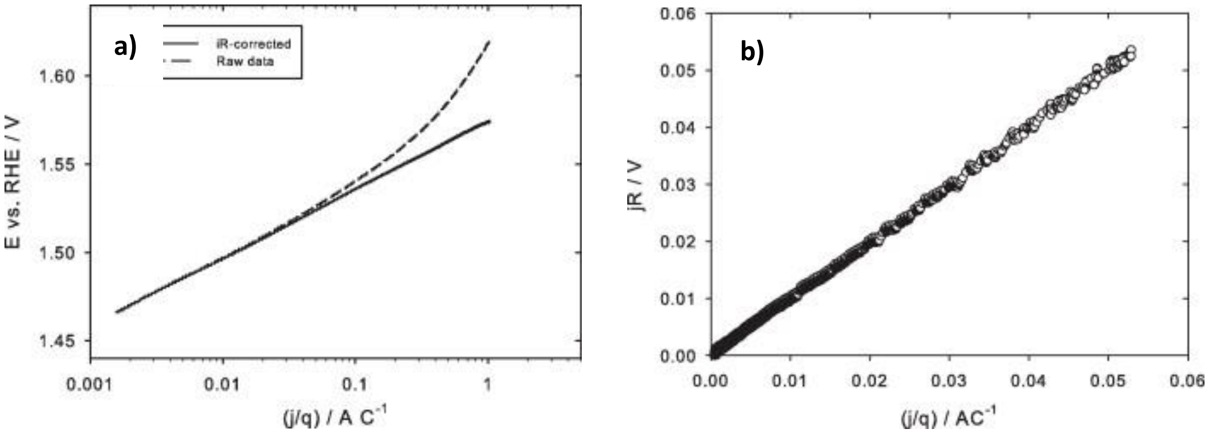

Figure 3-7: a) Example of raw data from polarisation experiments (dashed line) and the post-experimental IR corrected fit of these data (full line). Data are obtained from an iridium oxide electrode polarised at 5 mV/min. b) The uncompensated ohmic loss, calculated as the difference between the raw data and the fitted potential-current curves. Data are obtained from a sample of an atomic mixture of 75 % Ir and 25 % Ru oxide.[31]

3.2.6 Normalisation of current

For catalysts powders that are coated on electrodes, the coating is not identical from electrode to electrode. In addition, the powder size and physical properties can be different from synthesis to synthesis. In order to compare the electrochemical experiments of different catalyst coatings, one approach is to normalise the currents with relation to the electrochemically active surface area of the catalysts coating. This can in principle be done by dividing the current by mass of the catalyst if the powder particles for the different coatings are equal and well distributed. In practice, however, this is difficult to achieve.

A method for finding the “inner” and “outer” surface charges of oxide electrodes has been proposed in [62]. The outer surface charge is assumed to be proportional to the outer active area of the electrode, and can therefore be used for normalisation of the currents. By using this normalisation method, only the actually active surface area is accounted for, and coatings of slightly different powder distribution and particle sizes can be compared electrochemically.

This method is based on the principle that during cyclic voltammetry of oxide catalysts in acids, the catalyst exchange protons reversibly with the solution as described by the equations (3-10) and (3-11). The charge required for this process can be found by integration of the positive parts of the voltammogram where this reaction occurs (at potentials above the hydrogen region) with regards to time instead of potential.[28]

The total charge consumed or gathered during the reaction depends on the time, since the exchange of protons with the oxide requires diffusion. The charge found from integration of the voltammograms will therefore depend on the sweep rate. At low sweep rates, the protons has more time to diffuse further into each particle than at higher sweep rates. For an infinitely slow scan rate, the protons can diffuse into the less accessible areas, like pores and along grain boundaries. The charge required for this process is called the total charge, Q_T. For an infinitely high sweep rate, however, the process only has enough time to occur at the surface of the particles. The charge required for this process is called the outer charge, Q_S, and is proportional to the electrochemically active surface area. The total charge, Q_T is the sum of the inner and outer charges.[62]

The total charge has been found to be inversely proportional to the square root of the sweep rate, v:

$$q^*(v) = q^*_\infty + C\frac{1}{\sqrt{v}} \qquad (3\text{-}18)$$

Where q^*_∞ is the charge at infinitely high sweep rate, when there is no time for diffusion into the oxide. q^*_∞ is thus the charge related to the outer surface charge. This charge can thus be estimated by plotting the integrated charge as a function of $v^{-1/2}$, and extrapolating this line to the vertical axis where $v \rightarrow \infty$. The charge at zero sweep rate will analogously be related to the total charge that can be held by the oxide. The total charge can thus be found by plotting the inverse of the charge as a function of $v^{1/2}$, and extrapolating this to the the vertical axis where $v \rightarrow 0$.[62]

3.3 ROTATING DISC ELECTRODES (RDE) AND RING-DISK ELECTRODES UNDER HYDRODYNAMIC CONDITIONS

When studying electrochemical reactions that require mass transport, forced convection can be convenient for obtaining controlled conditions. A common way to obtain this is to rotate the electrode used. An alternative is to use a so-called flow cell where an electrolyte flow across the electrode is ensured by a pump. Controlled convection can also be employed for studying by-products of electrode reactions by ring-disk electrodes, where the flow from the disk to the ring is essential. The principles behind both the rotation disk electrode (RDE) and the ring-disk electrodes with controlled convection is described in this section.

3.3.1 Rotating disk electrodes

An electrochemical reaction involving solution species will depend on mass transport of reactants and products to/from the electrode. A constant flow regime will provide a controlled mass transport for the electrochemical reactions occurring at the electrodes, and thus mitigate mass transport limitation effects for the reactions. This is crucial for derivation of kinetic data from the electrochemical reactions, as these data would otherwise be time dependent. Forced convection also increases the currents on an electrode, and thus increasing detection limits. [56]

Rotating disk electrodes (RDE) can be employed to give a well-defined and steady-state mass-transport regime, as well as permitting for transportation calculations.[77] In a conventional RDE experiment, the electrode surface is facing down-wards in the electrolyte, and when the electrode starts to rotate, the electrolyte is pulled up to the centre of the electrode and flushed radially outwards across the surface of the disk.

When a reaction rate is under mass-transport control, a diffusion layer will arise in the electrolyte closest to the electrode surface. Inside this layer, the concentration of the species taking part in the electrode reaction varies. If the reaction rate is controlled by slow entry of reactants to the electrode surface, the concentration of the reactant will be equal to the bulk concentration at the starting point of the diffusion layer, and decreasing towards the electrode surface. If the reaction rate is controlled by mass-transport, then a maximum limiting current at the electrode is obtained when the concentration of species at the electrode surface is zero. This limiting current is given by[78]:

$$I_L = \frac{nFcD}{\delta} \tag{3-19}$$

Where n is the number of electrons transferred in the reaction, F is the Faraday constant, c the bulk concentration, D the diffusion coefficient of the reaction species in the electrolyte, and δ the diffusion layer thickness.

For a rotating disk electrode, the diffusion layer thickness is given by the following relation[78]:

$$\delta = \frac{1.61 v^{1/2} D^{1/3}}{\omega^{1/2}} \tag{3-20}$$

where v is the kinematic viscosity and ω the rotation rate of the electrode. As n, F, c, D and v are normally constant during most RDE experiments, the diffusion layer, and thus the limiting current, is dependent only on the rotation rate. The relation between the limiting current and the rotational speed is given by the Levich equation:

$$I_L = 0.62AnFD^{2/3}v^{-1/6}c^{\infty}\omega^{1/2} \tag{3-21}$$

Where A is the electrode area. This gives a linear relationship between the limiting current and the square root of the rotation rate. Thus, for entirely mass transport controlled reactions, a plot of the current as a function of $\omega^{1/2}$ should give a straight line that passes through the origin.[56]

Rotating an electrode is also an efficient method to remove products from the reaction, including gas. However, when there is a heavy gas evolution at the disk electrode, it can be more convenient to assemble the cell such that the working electrode is facing upwards to allow the gas to escape. Efficient gas removal is important as adhering gas bubbles can exert a substantial effect on mass and heat transfer, overpotential, limiting current and ohmic resistance, and deactivate parts of the electrode surface. In some cases with heavy gas evolution, it has been found that a flow cell can be a better alternative than conventional rotating electrodes.[9] In these cells, a pump system provides the constant electrolyte flow across the electrode surface. Flow cells of this type has also been found to ensure controlled mass transport and reproducibility.[9] It has been shown that even moderate flow velocities reduce the bubble coverage substantially, and that a velocity of 0.3 m/s is sufficient to reduce the bubble coverage to only a few percent of that in a stagnant electrolyte.[79]

3.3.2 Ring-disk electrodes with forced convection

A ring-disk electrode set-up consists of two electrodes, an inner disk electrode and an outer ring electrode, as shown schematically in Figure 3-8.[80] These electrodes are electrically insulated from each other, and can thus be controlled independently. Conventionally, these electrodes are used with the same set-up as the RDE to obtain controlled mass transport as well as to provide transport of products from the disk to the ring electrode. Flow cells can also provide these advantages. Both techniques will ensure that products and intermediates from the reaction occurring at the disk will flow towards the ring. If the products or intermediates are electrochemically active, these species can be detected electrochemically at the ring by oxidation or reduction. A ring-disk electrode can thus be used to obtain information about reaction intermediates from the disk electrode reaction very short after the reaction at the disk is taking place.

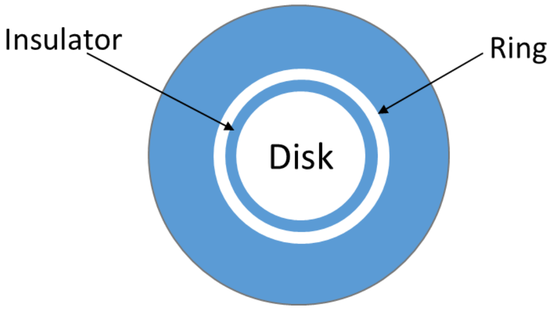

Figure 3-8: Schematic figure of a ring-disk electrode set-up.

Collection efficiency for the ring-disk electrodes

Not all off the species produced at the ring electrode will pass close to the surface of the ring. If species formed at the disk are completely stable, the fraction of the species that reaches the ring electrode and undergoes an electrochemical reaction there depends on the characteristics of the electrode geometry and the electrolyte flow.[80] A measure of this fraction is the collection efficiency, N, which is defined as the fraction of the completely stable species formed at the disk that can be detected at the ring.[77] This corresponds to the ratio between the current at the ring electrode, I_{ring}, and the current at the disk electrode, I_{disk}:

$$N = -\frac{I_{ring}}{I_{disk}} \qquad (3\text{-}22)$$

In principle, the collection efficiency can be calculated analytically for a rotating ring-disk electrode with perfect geometry.[77] Ideally, N is not a function of rotation rate for a RRDE since an increase in the rotation speed will increase the rate of transport both to the disc as well as to the ring.[80] However, the geometry of all electrodes are not completely identical and the collection efficiency is often determined experimentally. For a flow cell, the flow regime is complicated to predict and can change with flow rate, and the collection efficiency should then be determined experimentally.[81] The collection efficiency can be determined by using a well-behaved redox couple in solution. A typical redox couple used to determine the collection efficiency is the ferrocyanide/ferricyanide couple.[9, 77, 81-83] The ferrocyanide/ferricyanide half reaction is a simple, on-electron, reversible reaction:

$$\mathrm{Fe(CN)_6^{3-} + e^- \rightleftharpoons Fe(CN)_6^{4-}} \qquad \mathrm{E^0} = 0.28 \qquad (3\text{-}23)$$

The experiment is carried out by using a small concentration of the redox couple in question in combination with a so-called supporting electrolyte in a higher concentration. This keeps the ionic strength, and thus the ion activity, at an approximately constant level even when the reaction proceeds.[24, p. 51] Ideally, this experiment should be performed with the same electrode and cell, and with an identical flow regime as the experiment the collection efficiency is to be determined for, as small geometry variations as well as variation in flow regime influence N.

Initially, both the disk and the ring are held at potentials sufficiently positive to the reversible potential of reaction, to ensure that no reaction occurs. Then, the potential at the ring is kept constant at the same potential (above the reduction potential of the redox reaction) whilst the potential of the disk is slowly swept in the negative direction. After a while, a cathodic current can be observed at the disk. This corresponds to the reduction reaction (forward direction) of reaction (3-23). The ferrocyanide

($Fe(CN)_6^{4-}$) produced at the disk is then swept to the ring, and a fraction of it will be close enough to the ring surface to be oxidised back to ferricyanide ($Fe(CN)_6^{3-}$). It is common to use the current values when a limiting current is established at both the ring end disk electrodes, for calculating N. [81, 83]

A typical value for N of a rotating ring-disk electrode is 25 %, and a N value of approximately 10 % has been found for a flow cell with the similar arrangement as used for the flow cell experiments in this thesis.[9]

Detection of reaction intermediates with RRDE

The ring and disk electrodes can be controlled individually by a bipotentiostat. Typical experiments conducted with a RRDE are[80]:

- Keeping the disk electrode at a constant potential where the reaction to be studied can take place. The potential of the ring electrode is simultaneously scanned, and a current vs. potential diagram is recorded for this electrode. The variation of current with potential allows for identification of some intermediates from the reaction occurring at the disk.
- Scanning the potential on the disk electrode, while keeping the potential of the ring electrode constant at a value where a particular intermediate can be oxidised or reduced. Thus, information about the potential range (disk) where the intermediate is formed can be obtained.
- Keeping both disk and ring electrodes at constant potentials. The potential of the disk is such that the intermediate is formed, and the potential at the ring such that it can be detected. This is the most common method in order to determine *quantitative* kinetics of the reaction.

The RRDE has proved ideal for studying the oxygen reduction and evolution reactions, since the hydrogen peroxide intermediate itself is electroactive, and thus can be re-oxidised or re-reduced at the ring.[25, 84]

Potential step voltammetry can also be used in combination with rotating ring-disk electrodes to study the products and intermediates of a reaction. [85] If the potential at the ring is kept at a potential where reaction intermediates can react, the disk can be stepped between a potential where no reaction occurs and to a potential where the reaction studied does occur. Then the exact time of the start of the production at the disk is known, and this allows for quantitative treatment of the transit time, t'. The transit time is the time from the potential step into the region where a reaction can occur at the ring until a product can react at the ring. It comprises the time for reaching steady-state values at the disk and the time required for the product to travel from the gap between the outer radius of the disk and the inner radius of the ring. An approximate value for the transit time of redox species can be obtained by a formula proposed by Bruckenstein and Feldman[86]:

$$\omega t' = 3.58\left(\frac{v}{D}\right)^{1/3}\left(\log\frac{r_2}{r_1}\right)^{2/3} \qquad (3\text{-}24)$$

Where ω is the rotation rate of the electrode, *D* is the diffusion constant of the product of the disk, v is the kinematic viscosity, r_2 the inner radius of the ring electrode and r_1 the outer radius of the disk.[85]

The transit time is here a parameter defined for potential step voltammetry at the disk. A transit time is obviously also required for the product of the ring to reach the disk when cyclic voltammetry is performed at the disk. In that case, it is however, difficult to know the exact time of the start of the production at the disk, and the transit time is not easily obtained from experiments, especially if more than one product can be produced during the scan.

3.4 SYNTHESIS OF METAL OXIDE POWDERS BY HYDROLYSIS

Many different methods can be used to synthesise oxides based on iridium and ruthenium. The different methods results in materials that exhibit different physical, microstructural and electrochemical properties (e.g. surface area, stability, electrocatalytic activity).[13] Wet chemical methods can be employed to make nanosized particles with a chemical mixture of the oxides, as these are based on reactions with the metal ions in solution. Some of these methods are the hydrolysis, polyol and sol-gel methods. [9, 70, 87]

For hydrolysis methods, a metal precursor salt is dissolved in an aqueous NaOH solution to form a hydroxide. This is oxidised by addition of HNO_3 followed by increasing the temperature. Subsequent heat treatment of this precipitate converts it to a more or less crystalline phase, depending on the temperature.[88] The hydrolysis synthesis of IrO_2 can result in nanometer-sized powder with an average crystallite size of 20 nm.[70] The electrochemical stability of thermally prepared Ir oxide films during the OER is strongly dependent on the calcination temperature during the procedure. The stability generally increases with increased calcination temperature. This is proposed to be an effect of the oxide structure (amorphous or crystalline). However, the activity for the OER decreases with increased calcination temperature.[32]

Iridium oxide films obtained by hydrolysis synthesis are called anhydrous, as they are less hydrolysed than anodically formed iridium electrodes (AIROF), which is another commonly used method for making iridium oxide electrodes. Another important difference is that the AIROF electrodes are mainly amorphous, whereas the thermal treatment during hydrolysis synthesis ensures a much more crystalline structure. Both the crystallinity and the degree of hydration affect the electrochemical properties of the oxides.[71]

4 EXPERIMENTAL PROCEDURES

This chapter presents the experimental procedures employed in this thesis. First, general information about the equipment and chemical employed is given, followed by a description of procedure for preparing the reference electrodes employed. Then a description of the synthesis procedure is given. The last two subchapters concerns the experimental procedures employed for the determination of Tafel slopes and reaction orders, and for detection of by-products of the OER.

4.1 MATERIALS AND EQUIPMENT

All glass cell parts and equipment were cleaned in a hydrogen peroxide bath prior to each experiment (with an exception of the salt bridges, which were cleaned with this procedure only prior to filling with agar). The bath consisted of H_2O_2 and H_2O in the approximate ratio 1:3, with a small addition (1 V%) of H_2SO_4 as a catalyst, and was kept at the boiling point during the cleaning procedure.

All electrochemical measurements were performed at room temperature (24° C to 27 °C).

4.1.1 Chemicals

Water: Type 1 Milli-Q water (Merck Millipore) was used for all washing, synthesis and electrolyte purposes. This water is filtered and deionised to a purity characterised by a high resistivity (ca. 18.2 MΩ·cm).

Chemicals for catalyst synthesis: NaOH (Sigma-Aldrich, ≥ 97 %), $H_2IrCl_6 \cdot xH_2O$ (Alfa Aesar, 99.9 %), $RuCl_3 \cdot xH_2O$ (Sigma Aldrich, ReagentPlus), HNO_3 (pro analysi, Merck).

Other chemicals: KNO_3 (Merck, pro analysi), KCl (Merck, pro analysi, 99.5 %), $K_3Fe(CN)_6{\cdot}3H_2O$ (Merck, 99.0 %), Agar (VWR chemicals, technical grade)

Electrolytes:

- H_2SO_4 (0.5 M) prepared from (VWR chemicals, 95 %).
- $HClO_4$ (y M) + $NaClO_4$ (1-y M) (y = 1, 0.1, 0.01 and 0.001) prepared from $HClO_4$ (Merck, ACS, 60 %) and $NaClO_4$ (Sigma-Aldrich, ACS reagent, ≥ 98.0 %).

Polishing: Alumina suspension (Allied High Tech Products. Inc.), 5 µm, 0.3 µm and 0.05 µm on a microcloth.

4.1.2 Potentiostat

For all electrochemical experiments, a VMP3 Multi Potentiostat from BioLogic was used in combination with the EC-lab software.

4.1.3 Electrodes

Commercial rotating ring-disc electrodes with permanent gold and platinum rings, and interchangeable platinum and gold disks inserts from Pine Research Instrumentation was used for the ring-disk experiments [89]. Dimensions are given in Table 4-1 below. Commercial gold disk electrodes from the same supplier were also employed, and had the same electrode areas as the disk inserts of the RRDE.

As reference electrodes, a reversible hydrogen electrode (RHE), a laboratory-made Ag/AgCl electrode, a commercial Ag/AgCl (REF321, Radiometer Analytical) and a commercial Red Rod (REF201, Radiometer Analytical) electrode was employed. Preparation of the two first mentioned reference electrodes is described in the next subchapter, and data for the two commercial electrodes is given in Table 4-2 below.

Table 4-1: Pine Ring-disk electrode specifications.[89]

Electrode part	**Dimensions**
Ring Electrode	6.5 mm ID, 7.5 mm OD
Disk insert	5 mm OD x 4 mm thick

Table 4-2: Data for commercial reference electrodes from Radiometer Analytical.[90, 91]

	REF321	**REF201**
Reference system	Ag/AgCl	Red rod
Liquid junction	Porous pin	Porous pin
Salt-bridge solution	3 M KCl with sat. AgCl	Sat. KCl
E vs. SHE at 25°C [mV]	208	200

4.2 PREPARATION OF REFERENCE ELECTRODES

The preparations of the RHE and the “laboratory-made” Ag/AgCl reference are described below.

4.2.1 Reversible hydrogen electrode (RHE)

The reversible hydrogen reference electrode was prepared fresh prior to each experiment. A glass cylinder with a platinum wire inside (right in Figure 4-1) was the starting point. This cylinder was filled with the electrolyte solution and immersed in the electrolyte together with a platinum counter electrode in a beaker. These electrodes were connected with a 9 V battery, forming H_2 at the reference electrode and O_2 at the counter electrode, until approximately half of the reference electrode chamber was filled with hydrogen gas. Thus, a reversible hydrogen electrode with a known activity of H^+ and H_2 was obtained. This glass tube was contained in a glass compartment (left in Figure 4-1) filled with fresh electrolyte.

Figure 4-1: Reference electrode. To the right is the tube with platinum wire, and to the left is the outer compartment for this tube.

4.2.2 Silver/silver chloride electrode

Due to short mechanical robustness of these electrodes, several electrodes were prepared. Some of them were prepared during the preliminary project work, and some during this master thesis work.

For the laboratory-made Ag/AgCl reference, a silver wire (99.99 %) was used as the starting point. The wire was placed in a 1 M KCl solution, coupled with a Pt counter electrode and a RHE reference. The wire was electrochemically cleaned by cycling between -0.1 V and 0.5 V ten times with a sweep rate of 10 mV/s. The surface of the wire was then converted to silver chloride by first applying a potential of 0.1 V vs. RHE for 2 minutes, followed by 10 minutes at 0.3 V vs. RHE. The Ag/AgCl reference was thus obtained.

After the production, the electrode potential and stability were controlled by coupling the electrode with a RHE and studying the open circuit potential over time. For the first electrode made (during the preliminary project work), extra tests were performed to verify the preparation procedure. The potential of the electrode was checked as a function of Cl^- concentration, and a cyclic voltammogram of a Pt electrode in 0.5 M H_2SO_4 (not deaerated) was recorded against both the RHE and Ag/AgCl reference between 0 V and 1.2 V vs. RHE (Figure 4-2). These voltammograms are shown in Figure 4-2 and shows a good agreement between the shapes for the two electrodes, indicating that the Ag/AgCl reference has a stable potential of approximately 0.52 V positive to the RHE. The potential of these electrodes were found to be between 0.50-0.52 V positive to the RHE in the sulphuric acid.

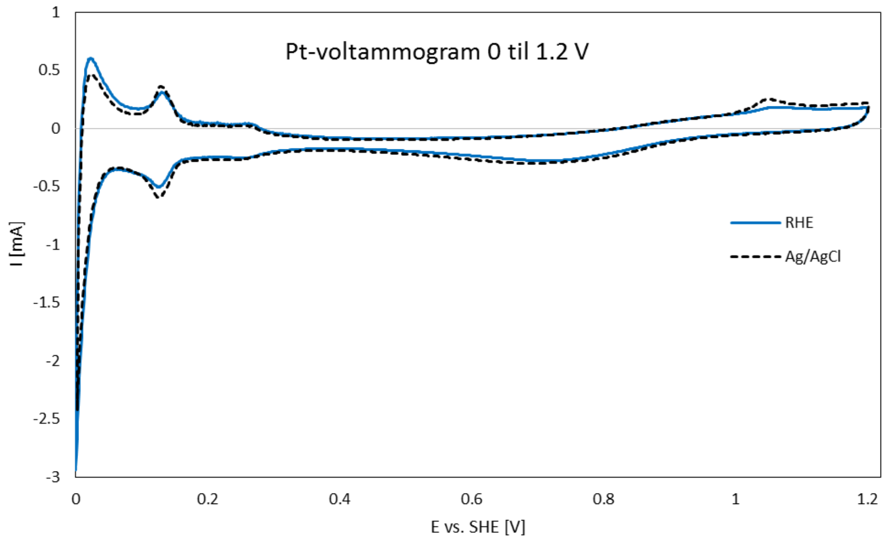

Figure 4-2: Voltammogram of platinum, recorded against RHE (blue line) and Ag/AgCl (black, perforated line).[12]

4.3 CATALYST PREPARATION

In this section, the synthesis procedure of the four different catalyst powders (IrO_2, $Ir_{0.6}Ru_{0.4}O_2$, $Ir_{0.3}Ru_{0.7}O_2$ and RuO_2) and the coating procedure is described. A description of the method for physical characterisation of the obtained powders is also included.

4.3.1 Synthesis of metal oxide powders

The four different catalysts (IrO_2, $Ir_{0.6}Ru_{0.4}O_2$, $Ir_{0.3}Ru_{0.7}O_2$ and RuO_2) were prepared by a hydrolysis method similar to what is described in [88] and [70]. IrO_2, $Ir_{0.6}Ru_{0.4}O_2$ were synthesised during the preliminary project work, whereas $Ir_{0.3}Ru_{0.7}O_2$ and RuO_2 were synthesised during this thesis work. NaOH solved in water was heated in a PTFE beaker in a water bath holding 90 °C for 70 minutes, during continuous stirring. The metal precursors ($H_2Cl_6 \cdot xH_2O$, $RuCl_3 \cdot xH_2O$) were weighted out in the desired proportions, solved in some water, added to the PTFE beaker, and the solution was left in the water bath at 90 °C for one hour. The molar ratio precursor ion:NaOH was 1:20, and the precursor concentration was in total 0.01 M.

After one hour, the PTFE beaker was transferred from the hot water bath to a water bath holding 0 °C, and kept there until the solution was at room temperature. The pH of the solution was then adjusted from approximately 12-12.5 to 8 by addition of HNO_3 (1 M). The mixture was then transferred to a glass Erlendmeyer flask, and heated by immersion in a water bath holding 80 °C for 30 minutes during continuous stirring. The mixture was subsequently cooled to room temperature. Then the mixture was transferred to centrifuge tubes (V_{tube} = 45 mL) and centrifuged at 11 000 rpm for 10 minutes. The liquid was then separated from the precipitated oxide, and new water was added to the tubes. The centrifuging at 11 000 rpm for 10 minutes was repeated four times in order to eliminate unreacted precursor or sodium hydroxide from the product. The precipitate was then dried at 80 °C and grinded by a mortar and pestle. It was then heated in a tube furnace with a flow of synthetic air at 500 °C for 30 minutes. After cooling, the powder was finally grinded again.

4.3.2 Preparation of thin film electrodes

Ink for coating the electrodes were prepared by mixing the metal oxide powders with a H_2SO_4 solution that had been adjusted to pH = 2 in advance. A concentration of 1 mg per mL was used, and this was mixed in an ultrasonic cleaner for 30 minutes. 20 µL of the ink was dripped onto the electrode substrate by a volumetric pipette and left to dry in a nitrogen atmosphere. Inks with different pH values were tested for this preparation procedure, but for all higher values of pH, the coating showed a typical "coffee stain" behaviour, leaving most of the powder on the outer parts of the electrode and almost nothing in the central parts after drying. By using a solution with pH = 2, the powder fell faster to the electrode surface, and a significantly more homogeneous layer was obtained. The resulting catalyst layer did not cover the disc perfectly homogeneously, but this will not affect the results, as these are normalised with respect to the active surface area of the electrodes (see section 3.2.6). Higher concentrations of powder in the ink was also tested to obtain a higher coverage of the disk substrate, but these did not have a good enough mechanical stability for use in the experiments with hydrodynamic electrolyte conditions.

Prior to the ink coating, the gold disc was polished to a mirror finish with 0.05 µm alumina paste. The disk electrode was also polished and washed in an ultrasonic bath between experiments with coatings of different catalyst powders.

4.3.3 X-ray diffraction of the catalyst materials

All oxide powders were characterised physically by X-ray diffraction. The oxide powders synthesised during the preliminary project work (IrO_2 and $Ir_{0.6}Ru_{0.4}O_2$) were characterised by use of the instrument AXS D8Focus with a Cu Kα radiation source, and the X-ray spectra were obtained by scanning in the 2θ range from 20° to 80°. Single crystalline silicon was used as the sample holder, and the samples were prepared by dissolving the powder in ethanol before transferring to the sample holder where they were left for evaporation of the solvent. A thin layer of catalyst powder was thus obtained prior to the diffraction measurements. The catalyst powders synthesised during this master thesis work (IrO_2 and

$Ir_{0.6}Ru_{0.4}O_2$) were prepared for X-ray diffraction in the same way, but were characterised by the use of a D8 DaVinci diffractometer equipped with a Cu Kα radiation source in the same 2θ range.

4.4 DETERMINATION OF TAFEL SLOPES AND REACTION ORDERS

For determination of Tafel slopes and reaction orders, polarisation curves for each of the four catalyst powders (IrO_2, $Ir_{0.6}Ru_{0.4}O_2$, $Ir_{0.3}Ru_{0.7}O_2$ and RuO_2) were recorded by linear sweep voltammetry at four different pHs. The nominal pH values of the electrolytes were 0, 1, 2 and 3. A constant ionic strength, and thus an approximately constant ion activity, was achieved by using a mix of y M $HClO_4$ and (1-y) M $NaClO_4$, where y equals 1, 0.1, 0.01 or 0.001. The pH of the four solutions were measured with a pH-meter (PHM210, Radiometer Analytical) using a Red Rod pH electrode (sat.KCl) and calibrating the pH meter with buffer solutions of pH 1.09 and pH 4.65 (Radiometer Analytical, Technical grade).

4.4.1 Cell design

A conventional downwards-facing RDE set-up was used in these experiments. A schematic drawing of the cell design is given in Figure 4-3. The commercial Ag/AgCl reference electrode was employed in these experiments, and was contained in a separate compartment from the WE. A salt bridge filled with agar saturated with KNO_3 (3.76 M) connected these compartments. The high concentration and the choice of ions with almost similar mobility ($76.2 \cdot 10^{-9} \frac{\boldsymbol{m^2}}{\boldsymbol{Vs}}$ for K^+ and $74.0 \cdot 10^{-9} \frac{\boldsymbol{m^2}}{\boldsymbol{Vs}}$ for NO_3^-) was done in order to reduce the liquid junction potentials between the two compartments as much as possible. The working electrode compartment contained the counter electrode in addition to the WE. The CE was a platinum electrode of much larger surface area than the WE. The RE compartment was filled with 3 M KCl, which eliminated the LJP between this solution and the inner solution of this RE. The large RDE shaft limited the location of the salt bridge in relation to the WE, and the minimum distance that could be obtained between the WE and the capillary tip of the salt bridge was approximately 2 cm. A Teflon lid was placed on top of the WE compartment, but was not completely tight. The RE compartment was sealed with cork and Parafilm.

The RDE was rotated by use of a Pine AFMSRX Rotator.

The salt bridges were prepared by firstly preparing a saturated solution of KNO_3. This solution was heated to 80 °C and agar was added until the mixture had a suitable consistency. The hot agar solution was then drawn into the salt bridge by the vacuum from a rubber pipette filler, carefully to avoid bubbles. The agar solution formed a more firm gel as it was cooled down to room temperature. To test the salt bridges, voltammograms in 1 M $HClO_4$ was recorded with the salt bridges and set-up shown in Figure 4-3. These voltammograms were compared with voltammograms recorded under otherwise similar experimental conditions, but employing a RHE contained in the WE compartment instead of the salt bridge and the Ag/AgCl reference. Figure 4-4 shows the voltammograms of IrO_2 between 0 and 1.5 V recorded with these two set-ups (cycled at 100 mV/s between 0 and 1.8 V vs. RHE in 1 M $HClO_4$), and it can be seen that they overlap very well.

The salt bridges could not be cleaned in the hydrogen peroxide bath between each experiment, and were instead rinsed thoroughly with Milli-Q water and flushed with the electrolyte to be used prior to each experiment. The salt bridges were stored in saturated KNO_3 solution.

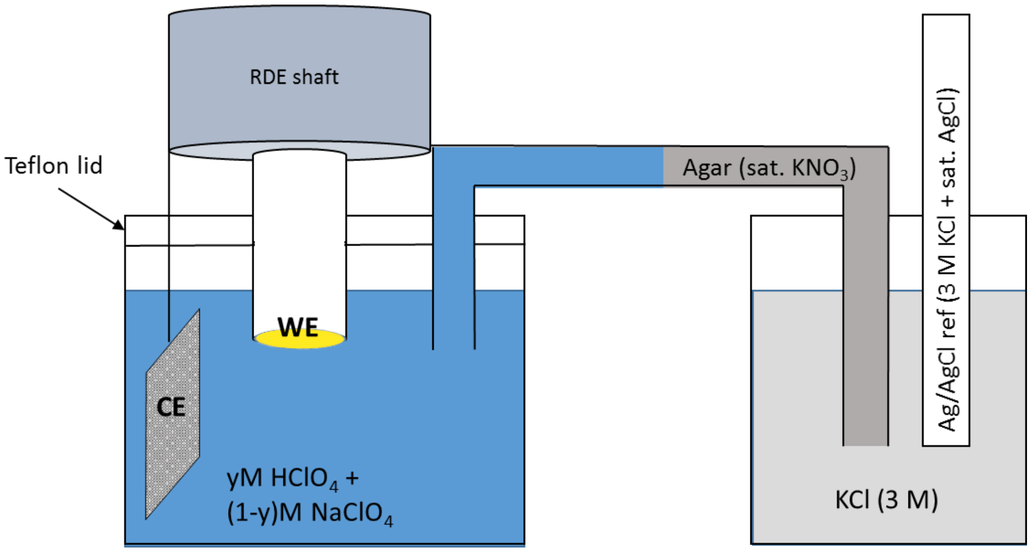

Figure 4-3: Schematic drawing of the cell design used for determination of Tafel slopes at different pHs and determination of reaction orders. To the left is the working electrode chamber, comprising the WE, CE, electrolyte and capillary tip end of the salt bridge. To the right is the reference electrode chamber, containing the agar end of the salt bridge and the RE in a 3 M KCl solution.

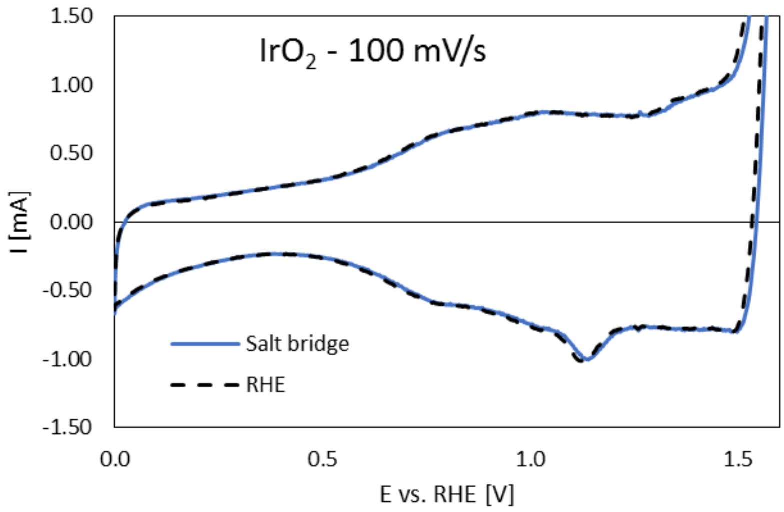

Figure 4-4: Cyclic voltammogram of IrO$_2$, recorded at 100 mV/s between 0 V and 1.8 V vs. RHE, in 1 M HClO$_4$.

4.4.2 Experimental procedure

For each catalyst at each pH (0, 1, 2 and 3), the following experimental procedure was employed:

1) The catalyst was cycled between 0 and 1.4 V vs. RHE at a scan rate of 350 mV/s until a stable voltammogram was obtained (normally 20 times).
2) The cell resistance was measured by impedance spectroscopy.
3) Cyclic voltammetry at seven different sweep rates were recorded in the following order: 20, 10, 100, 200, 20, 150, 50, 350, 20 mV/s, with 5 cycles for each scan rate. The voltammograms of 20 mV/s were recorded in between the other scans to see whether there was a development of the voltammograms over time.
4) The cell resistance was measured again by impedance spectroscopy.
5) The potential was held at 1.35 V vs. RHE for 30 seconds.

6) Linear sweep voltammetry from 1.35 V to 1.65 V vs. RHE (sometimes the upper limit was higher), with a scan rate of 0.083 mV/s. During this sweep the electrode was rotated at 1800 rpm to ensure efficient removal of bubbles.
7) Cyclic voltammetry at 350 mV/s (20 cycles) and 20 mV/s (5 cycles) to check the status of the voltammograms after the LSV.

The Ag/AgCl reference electrode was checked versus the Red Rod reference electrode prior to each experimental procedure. This was done since the Red Rod electrode was believed to be more reliable than the Ag/AgCl, since it was newer and it contained saturated KCl solution, which ensures a constant potential even if some of the filling solution should evaporate. The Red Rod electrode was, however, not available for the entire time of the experimental procedure, and could therefore not be used during the experiments. It was assumed that the potential of the Ag/AgCl electrode was +0.21 V vs. SHE in the settings of the programs for the potentiostat. Deviations from this was corrected for in the data obtained for the polarisation curves.

There are some exceptions from point number 1. Some of the voltammograms were recorded at slightly higher potentials than what is given here. This applies for IrO_2 in pH 1 and pH 2 solutions and $Ir_{0.6}Ru_{0.4}O_2$ in pH 1 solution. However, the upper limit was never higher than 1.5 V, and never high enough for oxygen evolution to occur. Thus, the catalyst properties in the subsequent LSV should not be affected.

During the LSV, the electrolyte resistance was compensated for. This was done by obtaining the electrolyte resistance at the starting potential of the LSV (1.35 V vs. RHE) by impedance, and the potentiostat automatically compensating for 85 % of this value in the subsequent LSV. This procedure is referred to as the ZIR technique later in this thesis. The cell resistance proved to be quite high for the solutions of pH $\neq$ 0, and it was found to influence the voltammograms slightly. Therefore, 85 % of the cell resistance was compensated for during the cyclic voltammetry for all solutions with pH $\neq$ 0. It is recommended that maximum 85 % of the electrolyte resistance is compensated to avoid oscillation of the instrument.[75]

In the electrolytes of pH 3, the shape of the voltammograms suddenly changed significantly compared to the other pH solutions. Forced convection in the electrolyte by rotation of the electrode was found to restore the typical shape of the voltammograms in the area to be used in normalisation. The electrodes were therefore rotated at 1800 rpm during the cyclic voltammetry at this pH. In addition, the electrolyte was purged with N_2 gas prior to and during the cyclic voltammetry at pH 3, since the electrode rotation caused a significant contribution from the oxygen reduction to distort the voltammograms in the low potential region. The origin of this problem is addressed in the discussion.

Voltammograms and polarisation curves for the pure gold substrates were also measured, to see whether the background current contribution from these could be significant. This was done for the lowest and the highest pHs, pH 0 and 3. In addition, IrO_2, $Ir_{0.6}Ru_{0.4}O_2$ and $Ir_{0.3}Ru_{0.7}O_2$ and were tested in 0.5 M H_2SO_4 by the same experimental procedure and set-up for comparison. This characterisation of IrO_2 and $Ir_{0.6}Ru_{0.4}O_2$ was carried out in the preliminary project work related to this master thesis.

To ensure that the proton intercalation areas of the voltammograms were not affected by the digital staircase voltammetry (see section 3.2.4), different settings of the potentiostat was tested. This was tested on an $Ir_{0.4}Ru_{0.6}O_2$ catalyst synthesised with the same procedure as the other catalyst. A quite slow scan rate was chosen for this testing, 50 mV/s. The parameters tested was the step size and the part of the current measured for each step (i.e. "50 %" implies that the current throughout the last 50 % of each potential step is averaged). The four different conditions tested are summarised in Table 4-3, and the results in Figure 4-5. As can be seen, only test no. 1 (step size of 305 µV and the last 50 % of each step) exhibited any significant deviation from the voltammograms recording the current during 100 % of the potential step. The settings applied for the CVs were as described in test no. 3, and should give correct charges, similar to those obtained by analog voltammetry.

Table 4-3: Parameters tested to ensure correct charge in voltammograms.

Test no.	Step size [µV]	Part of current measured
1	305	Last 50 % of each step
2	305	Last 100 % of each step
3	50	Last 50 % of each step
4	50	Last 100 % of each step

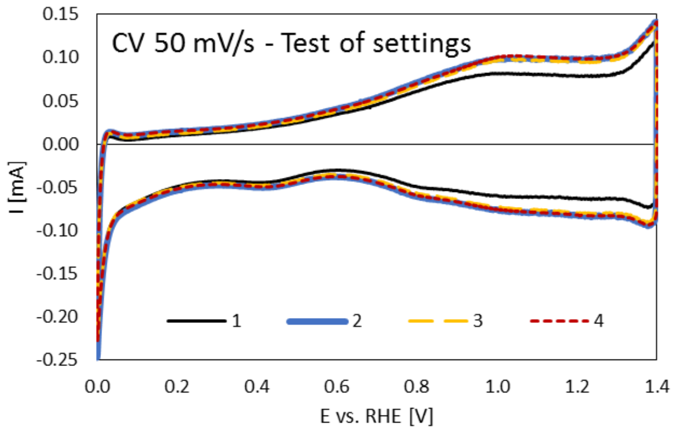

Figure 4-5: Cyclic voltammograms of $Ir_{0.4}Ru_{0.6}O_2$ at 50 mV/s. The four curves represents four different potentiostat settings, as shown in Table 4-3.

4.5 DETECTION OF BY-PRODUCTS OF THE OER BY RING-DISK EXPERIMENTS

This section gives a description of the experimental set-up and procedures and summarises the experiments carried out with the aim of identifying the by-products of the OER by the use of ring-disk electrodes.

The IrO_2 and $Ir_{0.6}Ru_{0.4}O_2$ catalyst powders employed in these experiments had already been characterised by cyclic voltammetry and linear sweep voltammetry in 0.5 M H_2SO_4 in the preliminary project work for this master thesis. The procedure for the characterisation was similar to what is described for the catalysts characterised in $HClO_4$ solutions for the experiments for determination of Tafel slopes and reaction orders (section 4.4.2). The LSV technique was compensated for the electrolyte resistance by the ZIR method (85 % compensation).

There were two main cell designs employed in these experiments, either a conventional RRDE set-up or a flow cell set-up similar to what was used in the preliminary project work. Both are described below. The flow cell was used in the beginning of this master work, as it had proved to be more suitable for efficient bubble removal at high potentials of the OER.[9] However, the conventional RRDE set-up was also tested in some experiments, and it proved to be equally or more suitable for the measurements in this master thesis.

4.5.1 Flow cell

The flow cell is similar to that used in the work of Kuznetsova et.al.[9] A schematic drawing of the flow cell employed in the ring-disk electrode experiments is shown in Figure 4-6. The cell is cylindrical, 6 cm in diameter, and consists of a PTFE bottom part, PTFE lid, and a cylindrical glass wall. The working electrode (WE) with both ring and disk is inserted into the middle of a PTFE cell bottom, and the counter electrode (CE) and hydrogen reference (RE) is placed as shown in the figure, through holes in the lid. Tubes for the electrolyte inlet and outlet flow also goes through the lid. A J-tube is used at the pump outlet in order to ensure coplanar electrolyte flow across the ring and disk electrode surfaces.

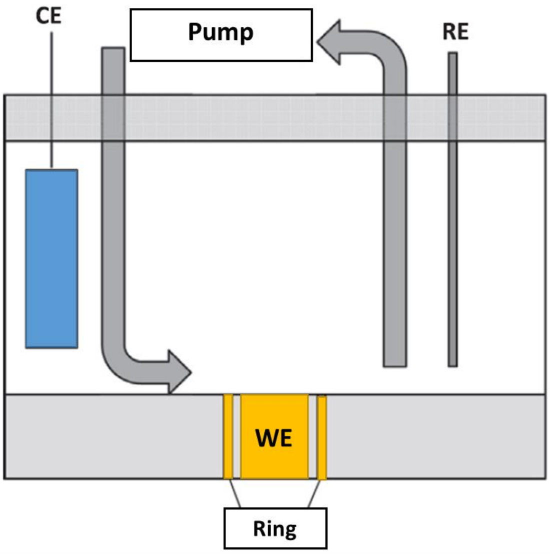

Figure 4-6: Flow cell design. Adopted from [9].

The electrolyte flow rate was controlled by a pulsation-free Ismatec ISM 901 REGLO-Z digital gear pump. A flow rate of 300 mL/min has been found to be optimal for removing gaseous products from the electrode and at the same time avoiding turbulence in the same arrangement in [9]. However, this proved not to be ideal for all measurements, and different flow rates were tested.

A platinum electrode of much larger surface area than the WE was used as counter electrode. This was placed in a glass tube, connected to the cell electrolyte through a glass frit in order to avoid mixing of the gaseous products from the counter and working electrodes. A RHE prepared as described in section 4.2.1 was used as reference electrode for all experiments using the flow cell set-up, except when determining the collection efficiency as described below.

The collection efficiency of the ring-disk electrode in this flow cell set-up has been determined in the preliminary project work, by the use of the $\mathrm{Fe(CN)_6^{4-}/Fe(CN)_6^{3-}}$ redox couple. The collection efficiency was then found to decrease with increasing flow rate. Values of 10.5 % to 7 % was found for flow rates between 200 and 450 mL/min, which is similar to the values given in [9]

4.5.2 Conventional RRDE cell

With this cell set-up, the RRDE was fastened to a conventional rotator (Modulated Speed Rotator, Pine Instruments), and the electrode surface faced down-ward in the electrolyte. The same CE as in the flow cell was used, but was not placed in a separate glass frit due to geometrical limitations of the cell. However, this did not seem to affect the measurements as long as the CE was not placed directly below the WE. Then the interaction from the hydrogen bubbles from the CE could be avoided. Different rotational speeds of the ring-disk electrode were tested.

4.5.3 Experiments for detection of by-products by the ring-disk electrode

Either the flow cell design or the conventional RRDE set-up was used for the ring-disk measurements for identification of by-products. If not otherwise stated, 0.5 M H_2SO_4 was used as electrolyte. The disk was coated with the catalyst (IrO_2 or $Ir_{0.6}Ru_{0.4}O_2$) powder, and was either cycled or stepped between E_1 and E_2, while the ring was held at a constant potential. E_1 was a potential lower than the reversible potential of the OER, and E_2 was normally high enough that the OER occurred (between 1.6 V and 1.9 V vs. RHE). The ring were held at either 0.6 V or 1.2 V vs. RHE. The effect of different scan rates at the disk was also studied. The ring material was either platinum or gold, whereas the substrate for the catalyst coating always was a gold disk electrode.

It proved to be hard to obtain interpretable and reproducible results, and different parameters therefore had to be adjusted during the time of the experimental work. This is why the flow cell was used for some experiments whereas the conventional RRDE set-up was used in other experiments. This also resulted in one experiment being preformed with the catalyst coating on the ring, and using the disk for detection, and one experiment where the near-neutral 0.5 M Na_2SO_4 solution was used as electrolyte.

In order to establish the method, ring-disk experiments were performed on the $\mathrm{Fe(CN)_6^{4-}/Fe(CN)_6^{3-}}$ redox couple, both in the flow cell and in the conventional RRDE set-up. The electrolyte was then 1 M KNO_3 + 10 mM $K_3Se(CN)_6$. Both potential step and potential sweep voltammetry experiments were performed with this redox couple. The method for detection of by-products of the OER by ring-disk electrodes was further tested by using only the plain disk electrode instead of the catalyst coating at the disk. The disk was used in combination with either a gold or platinum ring. The disk was cycled between E_1 and E_2, as described for the experiments with the coating on the disk.

A summary of the ring-disk experiments performed for establishing the experimental method are given in Table 4-4. The ring-disk experiments for studying the by-products of the OER at the two catalysts are summarised in Table 4-5. The current on both electrodes were recorded simultaneously by the bipotentiostat during all these experiments.

Table 4-4: Ring-disk experiments performed to establish the method for detection of by-products. Potentials in the ferricyanide solution are given vs. the laboratory-made Ag/AgCl reference, whereas the potentials in the sulphuric acid solution are given vs. a RHE.

Technique at disk	Cell design	Disk	Ring	Electrolyte
Potential step	FC	Au 0.3 V to -0.3 V	Au 0.3 V	1 M KNO_3 + 10 mM $K_3Fe(CN)_6$
Potential step	RRDE	Au 0.3 V to -0.3 V	Au 0.3 V	1 M KNO_3 + 10 mM $K_3Fe(CN)_6$
			Pt 0.3 V	1 M KNO_3 + 10 mM $K_3Fe(CN)_6$
Cyclic voltammetry	RRDE	Au 0.5 V to -0.3 V 200 mV/s	Au 0.3V	1 M KNO_3 + 10 mM $K_3Fe(CN)_6$
			Pt 0.3 V	1 M KNO_3 + 10 mM $K_3Fe(CN)_6$
			Au 0.3 V	1 M KNO_3 + 0.1 mM $K_3Fe(CN)_6$ (diluted solution)
Cyclic voltammetry	RRDE	Au 0.6 V to 1.9 V 200 mV/s	Pt 1.2 V	0.5 M H_2SO_4
			Au 1.2 V	0.5 M H_2SO_4

Table 4-5: Overview of the parameters in the different ring-disk experiments performed to identify by-products of the OER. Potentials are given vs. RHE.

Disk material, electrolyte and cell design	**Technique at disk**	**Ring**	**Electrolyte flow rates**
IrO_2 **0.5 M H_2SO_4** **Flow cell**	Potential step 0.6 V to 1.8 V	Pt 0.6 V	100 to 650 mL/min
		Pt 1.2 V	100 and 650 mL/min
IrO_2 **0.5 M H_2SO_4** **Flow cell**	Cyclic voltammetry 0.6 V to 1.9 V 100 and 50 mV/s	Au 0.6 V	0, 100 and 650 mL/min
	Cyclic voltammetry 0.6 V to 1.9 V 200 and 100 mV/s	Pt 0.6 V	0, 100, 300 and 600 mL/min
		Pt 1.2 V	0, 100, 300 and 600 mL/min
IrO_2 **0.5 M H_2SO_4** **RRDE**	Cyclic voltammetry 0.6 V to 1.9 V and 1.7 V 200 and 100 mV/s	Pt 0.6 V	0 to 2000 rpm
	Cyclic voltammetry 0.6 V to 1.8 V 200 mV/s	Pt 1.2 V	0 to 2000 rpm
Pt **0.5 M H_2SO_4** **RRDE**	Cyclic voltammetry at the ring 0.6 V to 1.9 V (200 mV/s)	IrO_2	500 and 1000 rpm
IrO_2 **0.5 M Na_2SO_4** **RRDE**	Potential step 0.6 V to 1.7 V	Pt 0.6 V	500 rpm
		Pt 1.2 V	0 to 1000 rpm
	Cyclic voltammetry 0.6 V to 1.7 V (200 mV/s)	Pt 0.6 V	0 to 2000 rpm
		Pt 1.2 V	0 to 2000 rpm
$Ir_{0.6}Ru_{0.4}O_2$ **0.5 M H_2SO_4** **RRDE**	Potential step 0.6 V to 1.7 V	Pt 0.6 V	0 to 500 rpm
	Potential step 0.6 V to 1.7 V and 1.9 V	Pt 1.2 V	0 to 500 rpm
	Cyclic voltammetry 0.6 V to 1.7 V	Pt 0.6 V	0 to 2000 rpm
	Cyclic voltammetry 0.6 V to 1.7 V (200 mV/s)	Pt 1.2 V	0 to 1000 rpm

5 RESULTS

Two approaches for obtaining insight into the OER has been preformed in this thesis, and the results from both are given in this chapter, but each approach has its own sub-chapter. The results from characterisation of the synthesised catalysts are given in the first section, as some of the prepared powders were used in both approaches. The results obtained for the Tafel slope and reaction order determination are given in the second subsection, whereas the results obtained from the ring-disk experiments for identification of by-products are collected in the last subchapter. The abbreviations Ir60 and Ir30 will be used for the two mixed oxides $Ir_{0.6}Ru_{0.4}O_2$ and $Ir_{0.3}Ru_{0.7}O_2$, respectively.

5.1 CHARACTERISATION OF THE METAL OXIDES

In this section the results from characterisation of the catalysts are given. The catalysts are characterised physically by XRD, and electrochemically by cyclic voltammetry and linear sweep voltammetry. The electrochemical characterisation is performed in both sulphuric and perchloric acid for the pure iridium oxide and the two mixed oxides. In addition, the background contribution from the gold substrates are presented. The potential of the voltammograms are as a rule referred to RHE, whereas the polarisation curves are as a rule given vs. SHE.

5.1.1 XRD of the metal oxides

The XRD spectra of the four catalysts are given in Figure 5-1. The graphs are displaced vertically in order to be distinguished. The position and relative intensity of the peaks for pure IrO_2 and pure RuO_2 are included in the figure by blue and yellow points, respectively. In addition to the entire spectra between the two 2θ values of 20 ° and 80 °, two of the peaks with higher intensity and showing the most difference between the two oxides are given at higher resolution. The main peaks of the IrO_2 powder coincide with the peaks expected for pure IrO_2, whereas the samples containing ruthenium exhibits peaks closer to the expected RuO_2 peaks the higher the ruthenium content.

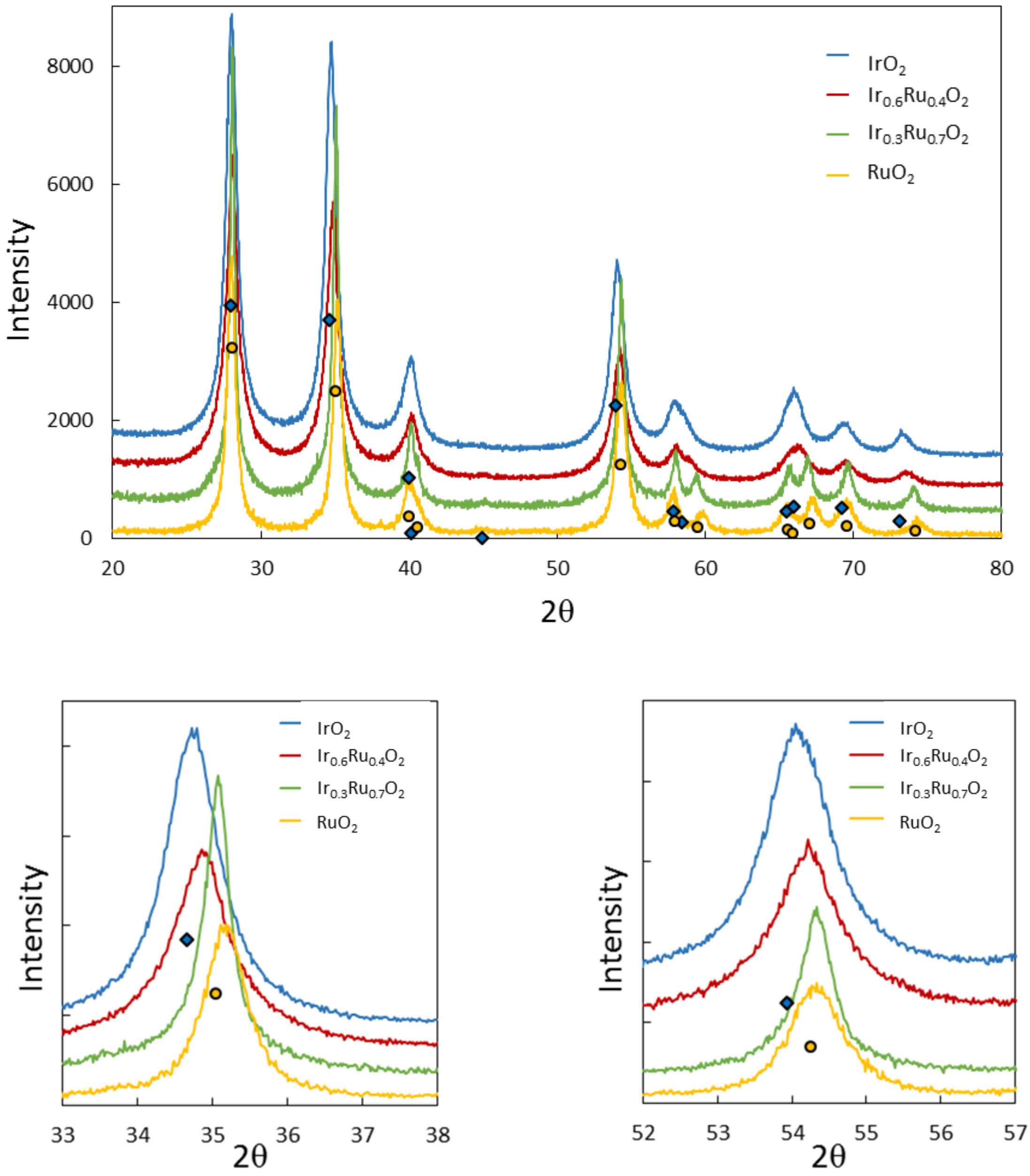

Figure 5-1: XRD spectra of IrO_2 (blue) and $Ir_{0.6}Ru_{0.4}O_2$ (red), $Ir_{0.3}Ru_{0.7}O_2$ (green) and RuO_2 (yellow), as well as points showing where peak of the pure phases of IrO_2 (blue) and RuO_2 (yellow) are expected to occur.

5.1.2 Characterisation of the metal oxides in 0.5 M H_2SO_4 and 1 M $HClO_4$

All catalysts used in this part of the thesis were characterised by cyclic voltammetry and linear sweep voltammetry in 1 M $HClO_4$. In addition, the mixed oxides and the pure iridium oxide were characterised by the same methods in 0.5 M H_2SO_4. The cyclic voltammograms of IrO_2 and $Ir_{0.6}Ru_{0.4}O_2$ in 0.5 M H_2SO_4 were recorded as a part of the preliminary project, but are included here for comparison. A RHE was used in these experiments. For the other experiments, however, the salt bridge set-up shown in Figure 4-3 was employed. The voltammograms are not corrected for the LJP, which was found to be ca. 16

mV (see section 5.2.3). For all catalyst coatings voltammograms were recorded at seven different sweep rates, as this was required for the normalisation procedure described in section 3.2.6.

As an example of the development of the voltammograms as a function of sweep rate, Figure 5-2 shows the cyclic voltammograms for IrO_2 recorded at seven different sweep rates: 10, 20, 50, 100, 150, 200 and 350 mV/s in 1 M $HClO_4$. The sweeps that are presented in the figure are the 4th sweeps recorded at each sweep rate. The voltammograms at each sweep rate exhibit broad and ill-defined peaks above 0.8 V. The inner curve represents the lowest sweep rate. The current increases as a function of sweep rate, and the outer curve represent the scan at 350 mV/s. The peak positions are found at approximately the same potentials for all sweep rates. The voltammogram of IrO_2 is compared to the voltammograms of the other catalysts below.

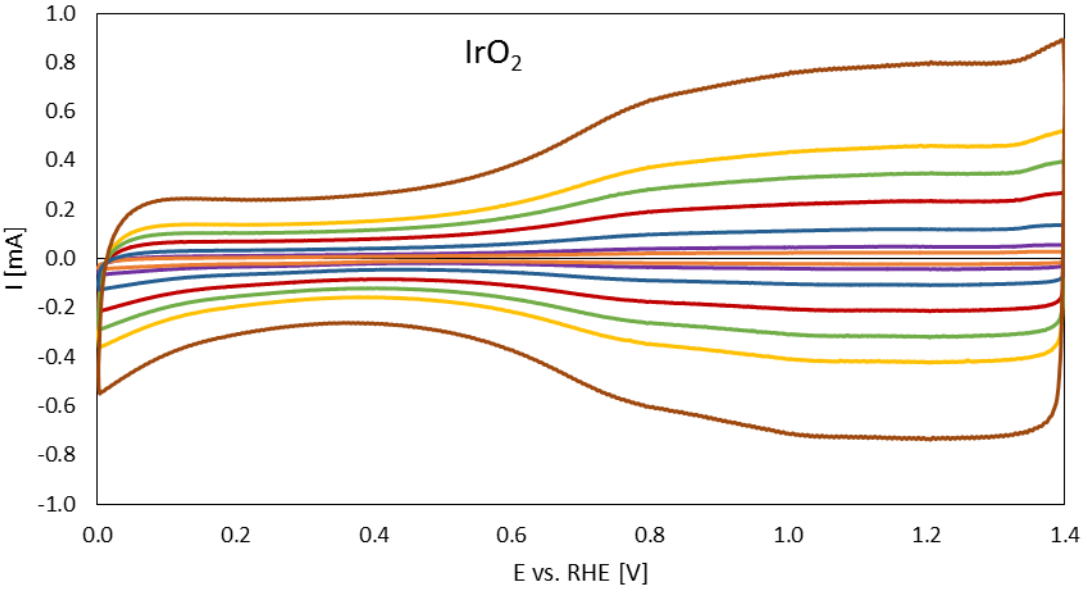

Figure 5-2: Cyclic voltammograms for IrO_2 for different sweep rates: 10, 20, 50, 100, 150, 200 and 350 mV/s obtained in 1 M $HClO_4$. The inner curve representing cyclic voltammogram for the lowest sweep rate, and the outer for the highest sweep rate.

Figure 5-3 presents the voltammograms obtained between 0 V and 1.4 V vs. RHE in 0.5 M H_2SO_4 (pH ≈ 0.24) for scan rates of 50 mV/s (a) and 350 mV/s (b). The current values in these figures are normalised with respect to the total surface charge at 350 mV/s. All three oxides show quite similar voltammograms. The major divagation is the higher charge observed in the hydrogen region (below 0.4 V) for Ir60 compared to the other oxides. The pure iridium oxide exhibits two reversible peaks, one at ca. 0.85 V and one at ca. 1.25 V. These two peaks can also be observed in the voltammograms of the two mixed oxides. However, the peak at about 0.85 V is shifted slightly down in potential for Ir60 at the slow sweep rate (50 mV/s). The two mixed oxides exhibit an extra peak at ca. 0.6 V. This peak is somewhat more prominent at 50 mV/s then at 350 mV/s, especially for Ir30.

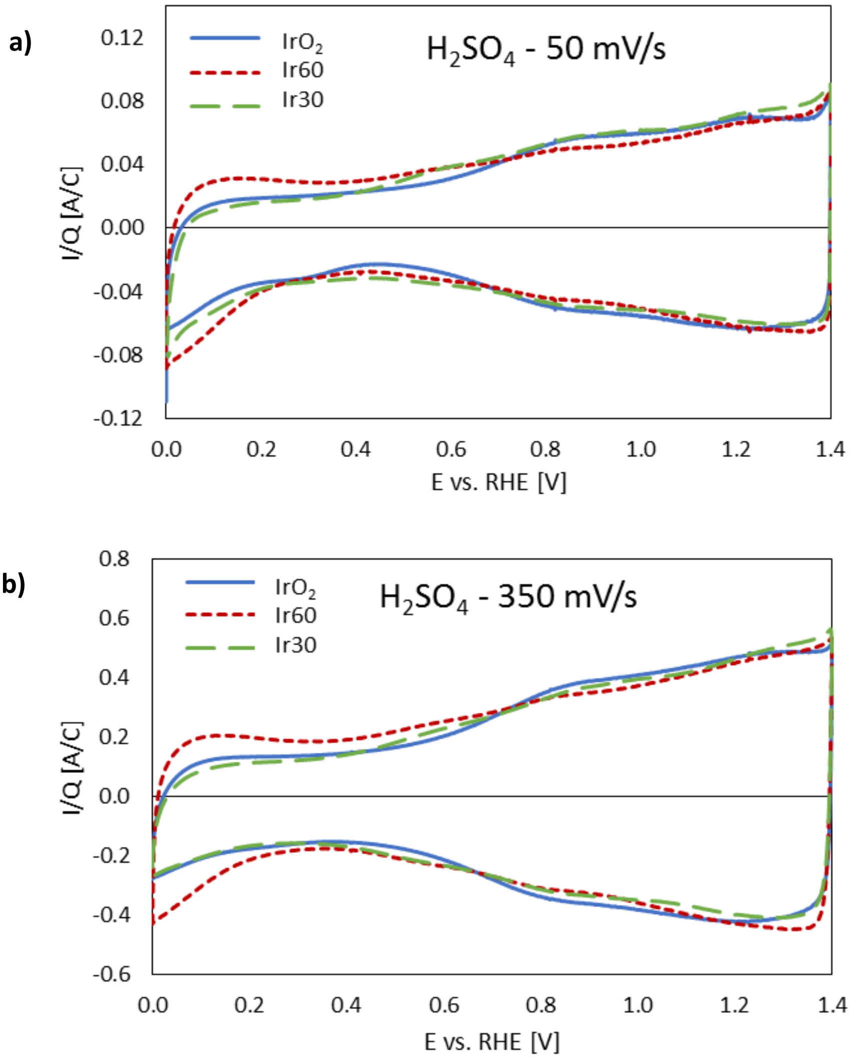

Figure 5-3: Cyclic voltammograms of IrO_2, Ir60 and Ir30 obtained at a) 50 mV/s and b) 350 mV/s, in 0.5 M H_2SO_4. The currents are normalised with respect to the surface charge at 350 mV/s.

The voltammograms of IrO_2, Ir60, Ir30 and RuO_2 in 1 M $HClO_4$ (pH ≈ 0) are presented in Figure 5-4 a) for a scan rate of 50 mV/s and b) for a scan rate of 350 mV/s. The vertical axes are scaled similar to those for the voltammograms in sulphuric acid above to make comparison between the two solutions easier. The voltammogram for pure iridium oxide is very similar to the one obtained in 0.5 M H_2SO_4, but the peaks are less pronounced and slightly shifted towards more negative potentials, with the lowest peak at ca. 0.8 V. It is perhaps possible to distinguish three peaks for IrO_2 in $HClO_4$, at 0.8 V, 1.0 V and 1.25 V, but the peaks are very ill-defined. A slight increase in the current above ca. 1.35 V can also be seen for this oxide in $HClO_4$.

Three anodic peaks can still be observed in the voltammograms of the mixed oxides. For Ir60 the peaks are located at ca. 0.55 V, 0.8 V and 1.2 V when the scan rate is 50 mV/s. The peaks at the two lowest potentials are less pronounced at the highest sweep rate, whereas the last peak is more pronounced. The latter is also shifted towards higher potentials at the high scan rate. The anodic peaks in the Ir30 voltammogram are located at approximately 0.55 V, 0.95 V and 1.2 V for a scan of 50 mV/s. When the scan rate is increased, the same trend as for Ir60 is observed, but to a greater extent. The lowest peak is almost absent at 350 mV/s. A slight increase in current at potentials above 1.35 is seen also for the mixed oxides.

Three peaks can be distinguished in the voltammogram of RuO_2, at ca. 0.55 V, 0.8 V and 1.2 V. The peak at 0.8 V is barely distinguishable and the peak at 1.2 V is somewhat disguised by a current commencing at ca. 1.2 V – 1.3 V.

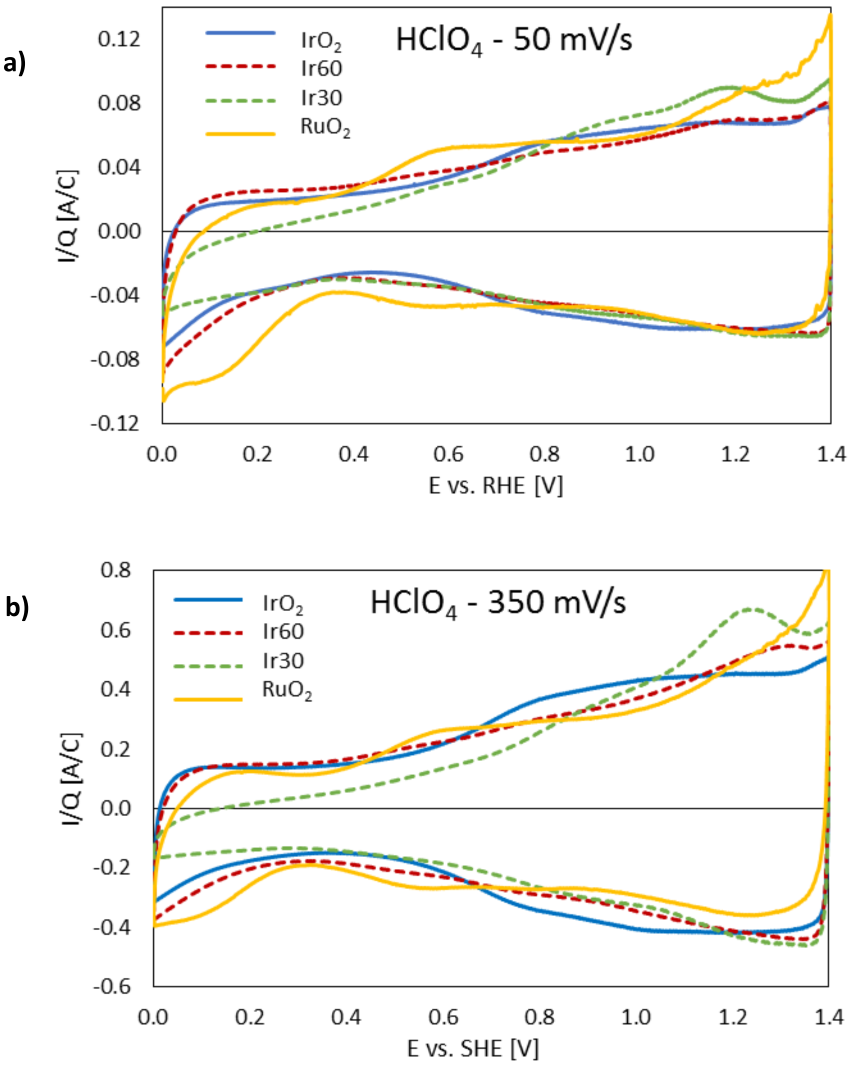

Figure 5-4: Cyclic voltammograms of IrO_2, Ir60, Ir30 and RuO_2 obtained at a) 50 mV/s and b) 350 mV/s, in 0.5 M H_2SO_4. The currents are normalised with respect to the outer surface charge.

Polarisation curves for all four catalysts in 1 M $HClO_4$ (unbroken lines) and IrO_2 and the two mixed catalysts in 0.5 M H_2SO_4 (dashed lines) are given in Figure 5-5. A scan rate of 0.083 mV/s was employed. The current is normalised by the charge found from the voltammograms obtained prior to the LSV. The ohmic losses are corrected for by use of the ZIR method, and the resistance values corrected for are between 2.73 Ohm and 2.87 Ohm. The activity of the catalysts increase with increasing ruthenium content in both acids. It is observed that the activity of the catalyst with 60 % iridium exhibits an activity closer to RuO_2 than IrO_2 at low overpotentials. It is also apparent that the activity in $HClO_4$ is higher than in H_2SO_4 for all catalysts compared here. The Tafel slopes are higher for the mixed oxides compared to the pure iridium and ruthenium oxides. Further comparison of the different catalysts in perchloric acid solutions and determination of the Tafel slopes are given in section 5.2.3.

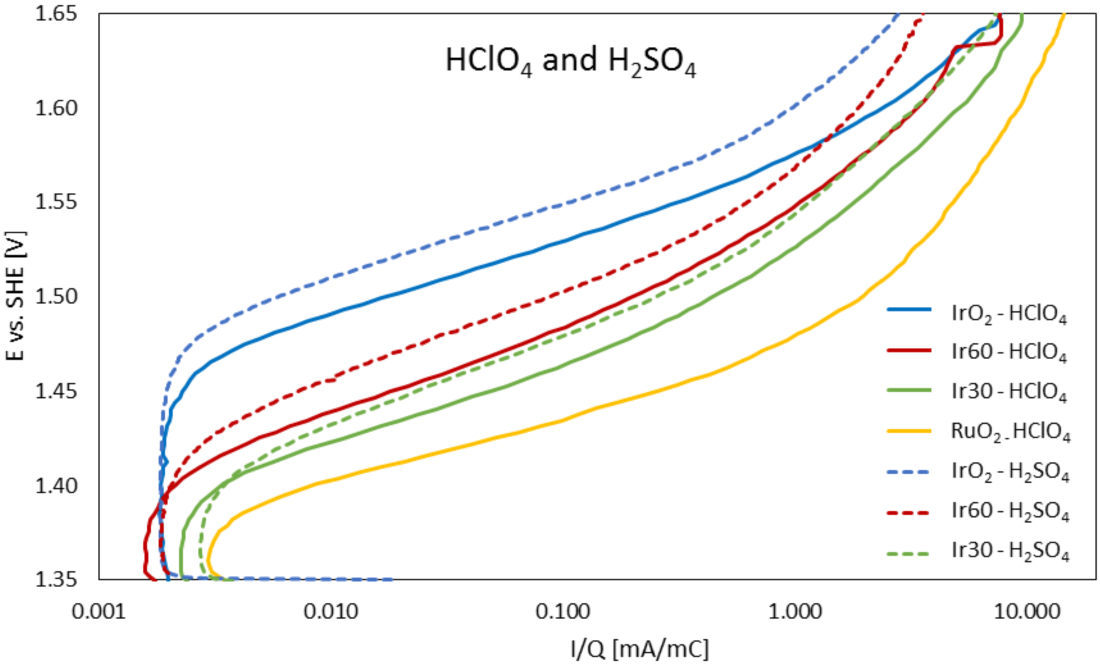

Figure 5-5: Polarisation curves for the four different catalysts in 1M $HClO_4$ (unbroken lines) and for IrO_2, $Ir_{0.6}Ru_{0.4}O_2$ and $Ir_{0.3}Ru_{0.7}O_2$ in 0.5 M H_2SO_4 (dashed lines), recorded at 0.083 mV/s. The ohmic loss in the electrolytes is compensated by the ZIR technique carried out prior to the polarisation experiment. The currents are normalised with respect to the surface charge from the CV at 350 mV/s, obtained prior to the LSV.

5.1.3 Au background

Cyclic voltammetry and linear sweep voltammetry of the pure gold disk electrodes were performed in the pH0 and pH3 solutions. The voltammograms obtained at 350 mV/s can be seen in Figure 5-6. The voltammogram of IrO_2 in the pH0 solution is included in the figure for comparison. The currents at the catalyst is about 10 to 20 times higher than the gold background. The polarisation curves of the pure gold disks are compared with the polarisation curves of IrO_2 in Figure 5-7 on a logarithmic current scale.

The voltammogram at a pure gold disk was also recorded in 0.5 M H_2SO_4 solution. This is given in Figure 5-8 together with the voltammogram of IrO_2 in the same solution and at the same sweep rate, 20 mV/s.

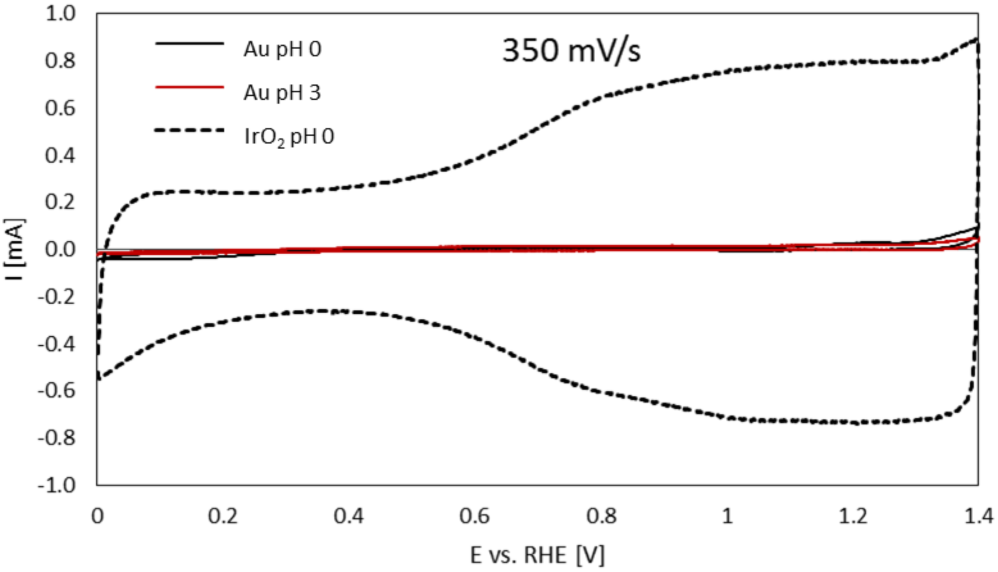

Figure 5-6: Voltammograms of the pure gold disk in the pH0 and pH3 solutions at a scan rate of 350 mV/s. The voltammogram of IrO_2 in the pH0 solution is included for comparison.

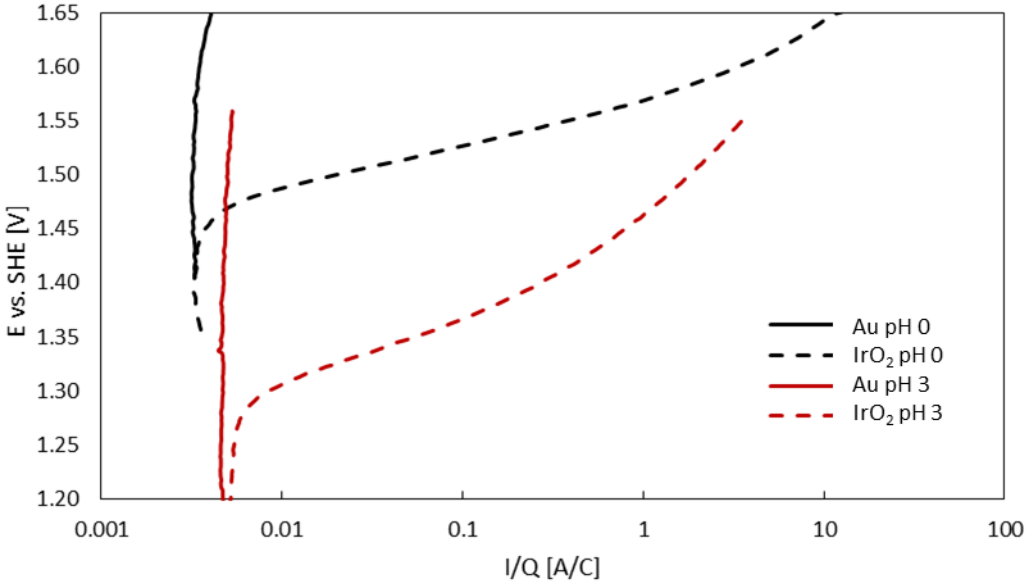

Figure 5-7: Polarisation curves of the pure gold disks in the pH0 and pH3 solutions, obtained with a scan rate of 0.083 mV/s. The corresponding curves of IrO_2 are included for comparison.

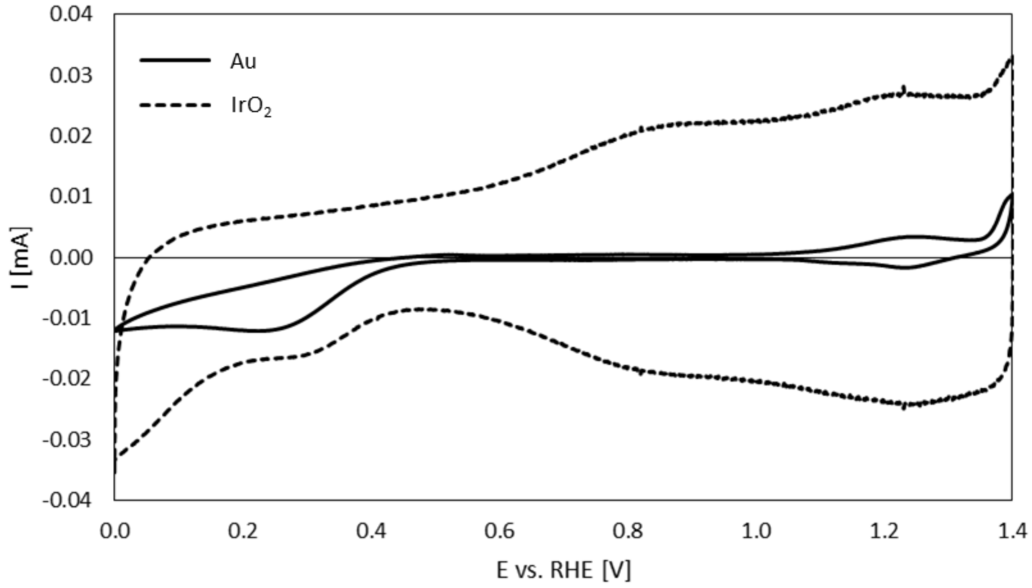

Figure 5-8: Voltammogram of pure gold in 0.5 M H_2SO_4 (full line). The voltammogram of IrO_2 (stippled line) is included for comparison. Both voltammograms are recorded at a sweep rate of 20 mV/s.

5.2 DETERMINATION OF TAFEL SLOPES AND REACTION ORDERS

In this subchapter, the results from all experiments related to finding the Tafel slopes and reaction orders of the four different oxide compositions (IrO_2, $Ir_{0.6}Ru_{0.4}O_2$, $Ir_{0.3}Ru_{0.7}O_2$ and RuO_2) are given. The abbreviations Ir60 and Ir30 will be used for the two mixed oxides $Ir_{0.6}Ru_{0.4}O_2$ and $Ir_{0.3}Ru_{0.7}O_2$, respectively.

First, the voltammograms in the four solutions of pH 0, 1, 2 and 3 are given as well as the obtained outer surface charges. After this, the polarisation curves of all catalysts in the four electrolytes are given, and the reaction orders for each catalyst are calculated. The potential of the voltammograms are as a rule referred to RHE, whereas the polarisation curves are as a rule given vs. SHE.

The polarisation curves are corrected for the contribution form the liquid junction potential, and the calculations of these are also given in the section representing the polarisation curves.

5.2.1 Cyclic voltammograms for the mixed oxides at different pHs

Figure 5-9 and Figure 5-10 present the cyclic voltammograms of the four catalysts at different pHs, for three selected scan rates: a) 20 mV/a, b) 50 mV/s and c) 350 mV/s. The voltammograms of the different catalyst coatings were used to obtain the outer surface charge of the catalyst coatings for normalisation of the polarisation curves, as explained in section 3.2.6. The voltammograms are, however, already normalised with respect to the outer surface charge in figures Figure 5-9 and Figure 5-10 to accommodate comparison of the different materials and comparison between the different pHs. Blue voltammograms correspond to CVs recorded in solution of pH 0, red to pH = 1, green to pH = 2 and yellow to pH = 3. The voltammograms obtained in the solutions with pH 0, 1 and 2 were performed at a stationary electrode and without gas purging, while the voltammogram in the pH 3 solution is rotated at 1800 rpm and purged with N_2. The potentials are given with respect to the RHE.

The majority of the voltammograms were recorded between 0 V and 1.4 V vs. RHE. However, there are some exceptions. This applies for IrO_2 in pH 1 and pH 2 solutions and $Ir_{0.6}Ru_{0.4}O_2$ in pH 1 solution. These were recorded between 0 V and 1.4 V vs. SHE. However, the upper limit was never high enough for oxygen evolution to occur. Only the parts between 0 V and 1.4 V vs. RHE are given here, as these parts can be compared for all pHs. The anodic curve between 0.4 V and 1.4 V was the part used to obtain the outer surface charge to be used for normalisation.

In general, each of the oxides show the same features in the anodic region above 0.4 V in all solutions. The two peaks at ca. 0.85 V and 1.25 V for IrO_2 are found at approximately the same potential in all solutions. For RuO_2, the three peaks are located at ca. 0.55 V, 0.8 V and 1.2 V in all solutions, the peak at 0.8 V being barely distinguishable. The voltammograms of the mixed oxides have three peaks at approximately the same potentials as RuO_2, but with the peak at ca. 0.8 V being larger and more defined. The voltammograms of the mixed oxides are also similar in all solutions, with one exception for each. For the Ir60 oxide at 350 mV/s, it seems like some of the charge related to the peak at 0.5-0.6 V is absent. Therefore, this voltammogram was excluded from the normalisation procedure. All other voltammograms obtained for Ir60 in the pH3 solution (10 mV/s to 200 mV/s), did not show this discrepancy from the voltammograms obtained in the other solutions, and could thus be used for normalisation. The other exception is the voltammogram of Ir30 in the pH0 solution. Three peaks can be extinguished in the voltammograms obtained at all pHs, but the location is slightly shifted for the pH0 solution compared to the other solutions. The middle peak is more pronounced and shifted to higher potentials in the pH0 solution, whereas the lowest peak is smaller. This shift of charges from lower to higher potentials in the voltammogram was less pronounced in the first cycles obtained (not included here), but rather developed after a few (ca. 10-20) cycles.

For the pH3 solution, the cathodic scan at high sweep rates differs significantly from the voltammograms obtained in the other solutions. Some of the charge at higher potentials seems to be moved towards lower potentials, compared to the other voltammograms.

In the area below 0.4 V in the voltammograms, the curves are slightly shifted up or down as the pH is varied. The largest deviation is observed in the curve at 350 mV/s for Ir60, where there is no net anodic current until ca. 0.3 V is reached. However, as mentioned above, this curve was excluded when obtaining the outer surface charge used for normalisation.

Figure 5-11 is included to demonstrate the effect of rotation of the electrode and nitrogen purging in the pH3 electrolyte. The voltammogram obtained without rotation deviates significantly from the voltammograms obtained with rotation. For the positive scan, there is a somewhat higher current at lower potentials for this curve. However, as the potential is scanned in the anodic direction, the current does not increase until approximately 0.8 V is reached. This results in a considerably lower charge from the voltammogram when the electrode is not rotated. The effect of nitrogen purging in combination with rotation can also be seen in this figure. When the electrolyte is purged with N_2, the curve is shifted slightly upwards for potentials below ca. 0.5 V.

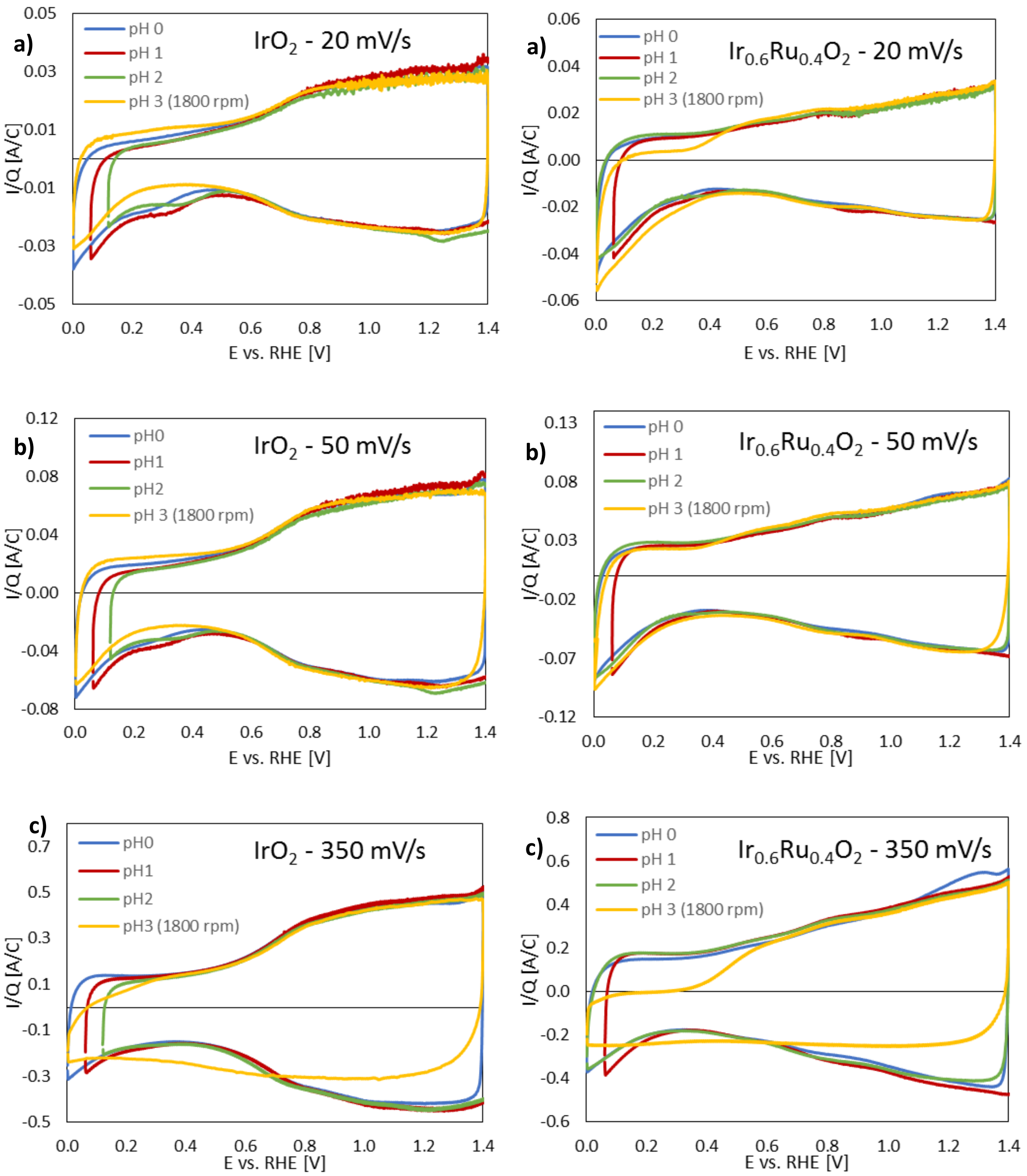

Figure 5-9: Voltammograms of IrO_2 (left column) and $Ir_{0.6}Ru_{0.4}O_2$ (right column) in the different pH solutions obtained at a) 20 mV/s, b) 50 mV/s and c) 350 mV/s. The voltammograms in the solutions with pH 0, 1 and 2 are recorded at a stationary electrode and without gas purging, while the voltammogram in the pH 3 solution is rotated at 1800 rpm and purged with N_2. The currents are normalised with respect to the outer surface charge.

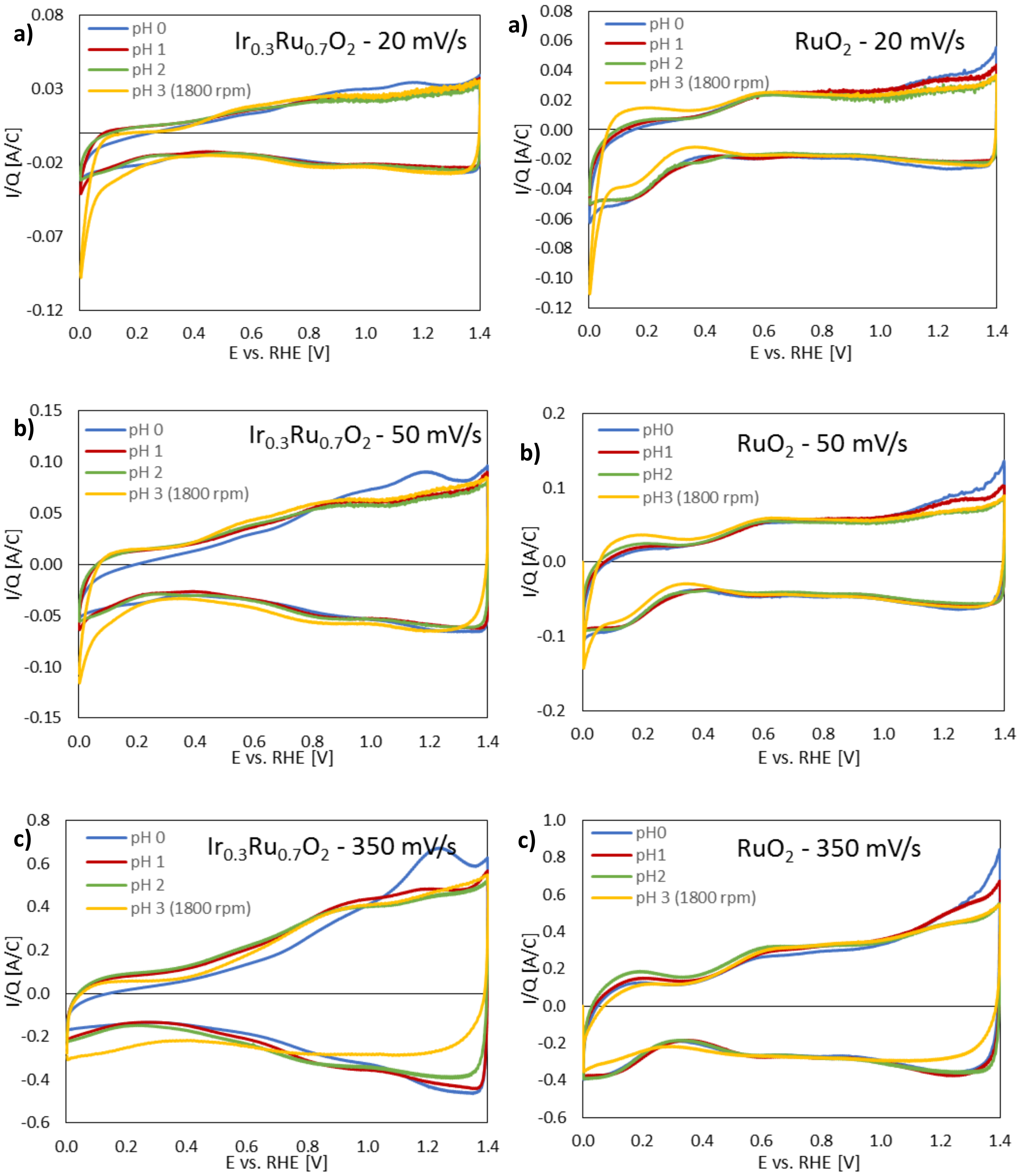

Figure 5-10: Voltammograms of $Ir_{0.3}Ru_{0.7}O_2$ (left column) and RuO_2 (right column) in the different pH solutions obtained at a) 20 mV/s, b) 50 mV/s and c) 350 mV/s. The voltammograms in the solutions with pH 0, 1 and 2 are recorded at a stationary electrode and without gas purging, while the voltammogram in the pH 3 solution is rotated at 1800 rpm and purged with N_2. The currents are normalised with respect to the outer surface charge.

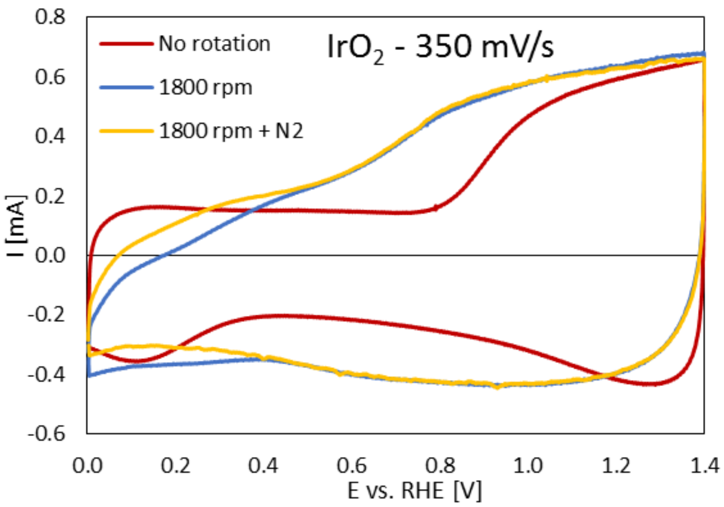

Figure 5-11: Voltammogram of IrO_2 at 350 mV/s with and without rotation of the electrode. Voltammograms with the rotating electrode are recorded both with and without N_2 purging.

5.2.2 Normalisation

The charge at each scan rate (10 mV/s to 350 mV/s) was calculated by numerical integration of the anodic current between 0.4 V and 1.4 V as a function of time. The outer surface charge for each catalyst coating was thereafter found from graphs where the charge was plotted as a function of the inverse of the square root of the sweep rate. Graphs showing the total charge at each sweep rate, as well as the plots for finding the outer and total surface charges are given in Figure 5-12 a), b) and c), respectively. These data were obtained from IrO_2 in the four different pH solutions. The shape of the graphs obtained for the other catalysts were qualitatively similar. For the graph of Q vs. v (a), it can be seen that the charge at slow sweep rates for pH 2 does not increase like that seen for pH 0, 1 and 3. Similarly, the curves for obtaining the outer surface charge (Figure 5-12 b) at pH 2 and 3 were generally further from a straight line than the curves obtained at lower pHs.

The obtained surface charges for each catalyst coating are given in Table 5-1. All coatings of the same catalyst are made from the same ink. There is some variation in charge from coating to coating, but in general the variation is larger between materials. For the pH3 solution, the outer charge of three catalysts found when the point at 350 mV/s was excluded from the normalisation procedure is also included in the table. For Ir60 this was the value used due to the inconsistent voltammogram obtained at 350 mV/s, as described in the previous section. It can be seen that the charge found with and without this point is very similar for IrO_2 and Ir30. The total charges for IrO_2 at 350 mV/s are also included for comparison with the normalisation executed in the H_2SO_4 solution, as described in section 5.1.2.

Table 5-1: Outer surface charge for the different catalysts in the different pH solutions, given in millicoulombs. The total charge of IrO_2 at a scan rate of 350 mV/s is also included.

pH	**IrO_2**	**IrO_2 (Q_{350})**	**Ir60**	**Ir30**	**RuO_2**
0	1.76	1.78	2.39	1.56	1.29
1	1.59	1.65	2.39	1.13	1.28
2	1.66	1.65	1.41	1.64	1.00
3	1.40	1.11	2.25	1.12	0.85
3 (without 350 mV/s)	1.42	-	2.16	1.17	-

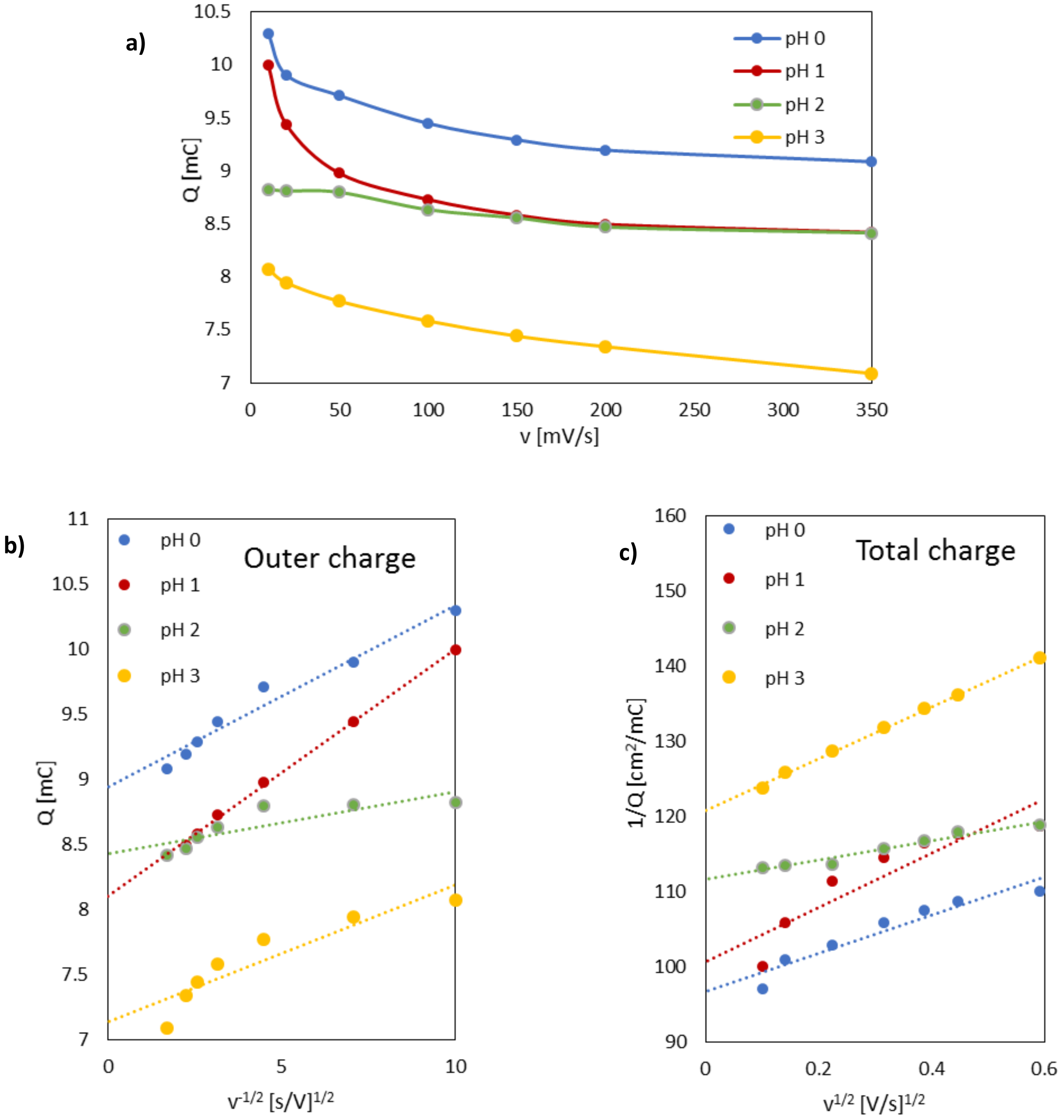

Figure 5-12: Curves from the normalisation procedure of IrO_2 at the three different pHs. a) total charge at each sweep rate, and b) plots for finding the outer charge and c) plots for finding the total charge.

5.2.3 Polarisation curves in the different pH solutions

In this section the polarisation curves of the four catalysts in the four different pH solutions are given. The curves were obtained by linear sweep voltammetry at a scan rate of 0.083 mV/s while the RDE was rotated at 1800 rpm. The electrolyte resistance was compensated for by the ZIR technique during the polarisation. Post-experimental correction of the electrolyte resistance was also carried out by numerically fitting the raw data to equation (3-17), as explained in section 3.2.5. Both the raw data (only compensated by the ZIR technique) and the fitted curve are presented. The potentials are given vs. SHE, and the currents are normalised with respect to the outer surface charge obtained from voltammetry of the same catalyst coating in the same solution prior to the linear sweep voltammetry.

Since different electrolytes were used in the WE and RE compartments, the liquid junction potential between these compartments were calculated and the potentials values corrected accordingly.

Liquid junction potential correction

The four electrolytes with different pHs $(yM\ HClO_4 + (1-y)M\ NaClO_4)$ inevitably contains very different proton concentrations. Due to the exceptionally high mobility of protons compared to the mobilities of the other ions in the electrolyte, the total liquid junction potential (LJP) between the WE compartment and the RE compartment can be quite different when electrolytes of different pHs are used. Therefore, the LJP between these two compartments are calculated for each of the four electrolytes, by employing the Henderson equation (3-8) and the limiting ionic mobilities given in Table 5-2. Since the electrolytes employed here are strong 1:1 electrolytes, were the molar conductivity depends only weakly on concentration, the mobilities in the Henderson equation are approximated by the limiting ionic mobilities.

The LJPs between the WE compartment and the salt bridge (sat. KNO_3 = 3.76 M KNO_3), and between the salt bridge and the reference compartment (3 M KCl) are calculated separately and are given in Table 5-3. The total LJP between the RE and WE is the sum of these, and is also given in this table. For the experiments performed in the pH 0 solution, the LJP contributes significantly to the measured potential, whereas the LJPs between the RE and WE for the other electrolytes are negligible. Therefore, the potentials of the polarisation curves recorded in 1 M $HClO_4$ are corrected for the LJP, whereas the potentials in the other solutions are not corrected for the LJP.

The calculated LJP between the RE and WE electrode chambers is calculated to be negative since the protons will diffuse faster into the salt bridge than K^+ diffuses the other way, giving a too positive potential at the RE side of the salt bridge. The potential in the WE chamber is thus in reality 16 mV lower than the measured value, and the obtained data should thus be moved 16 mV in the positive direction:

$$E_{real} = E_{measured} - LJP = E_{measured} - (-16\ mV)$$

The Ag/AgCl reference was checked before the start of the experiment vs. a Red Rod (sat. KCl) reference electrode. The liquid junction potential between these two reference electrodes was calculated to 0.2 mV, and thus negligible.

Table 5-2: Limiting ionic mobilities of the ions found used in the set-up when obtaining the polarisation curves. [92]

Ion	Limiting mobility $[\frac{m^2}{Vs}]$
H^+	$362 \cdot 10^{-9}$
Na^+	$51.9 \cdot 10^{-9}$
K^+	$76.2 \cdot 10^{-9}$
ClO_4^-	$69.8 \cdot 10^{-9}$
NO_3^-	$74.0 \cdot 10^{-9}$
Cl^-	$79.1 \cdot 10^{-9}$

Table 5-3: Calculated liquid junction potentials between the WE chamber and the salt bridge and between the salt bridge and the RE chamber. The total LJP between the WE and RE chambers are also given.

Electrolyte (pH)	LJP (WE-salt bridge) [mV]	LJP (salt bridge-RE) [mV]	Total LJP [mV]
0	-15	-0.84	-16
1	-0.4	-0.84	-1
2	2	-0.84	1
3	2	-0.84	1

Polarisation curves in the different pH solutions

The polarisation curves of IrO_2 obtained in the four different pH solutions are given Figure 5-14. The raw data are represented by the full lines, whereas the results from the post-experimental ohmic drop corrections are given as dotted lines with corresponding colour coding. Figure 5-15, Figure 5-16 and Figure 5-17 present the corresponding data for $Ir_{0.6}Ru_{0.4}O_2$, $Ir_{0.3}Ru_{0.7}O_2$ and RuO_2, respectively. The polarisation curves of the four different catalysts have already been plotted together in the solution of pH 0 in Figure 5-5. As all the catalysts respond in the same way with respect to the changing pH, it was not seen necessary to make further plots for comparison.

For all polarisation curves of all materials and pHs, a linear region is observed at low overpotentials. The curves then start to bend upward at higher potentials. The linear region shortens as the pH of the solution is increased, since the curves start to bend upward at lower potentials. The remaining linear region at pH 3 is thus very short, and sometimes hard to identify. All catalysts exhibit significant increase in activity as the pH is increased, and the polarisation curves are shifted approximately 59 mV downward per pH unit. This is illustrated in Figure 5-18 to Figure 5-21, where the polarisation curves of the oxides in the four different solutions is given with respect to the RHE instead of the SHE. The linear region observed in the solutions of pH 0, 1 and 2 overlap quite well for more low overpotentials. This figure also illustrates how the curves start to bend upwards at lower potentials for higher pH values, as described above. The activity as a function of pH is analysed more thoroughly by finding the reaction order with respect to H^+ from the obtained Tafel slopes in the next subsection.

For the high potential regions in Figure 5-14 to Figure 5-17, all curves bend considerably upwards. Since the curves starts to bend earlier the higher the pH of the solution, the OER seem to exhibit more similar activities in all solutions at high potentials. Some of the curves also intersect at high potentials. This is seen for IrO_2, where the curve from pH 3 intersects the curve of pH 2, and for RuO_2 where the curve of pH 1 intersects the curve at pH 0.

The starting potential of the linear Tafel region for the different catalysts (at all pHs) with respect to RHE are given in Table 5-4. It can be seen that Tafel kinetics for the OER commences at lower potentials the more ruthenium the catalyst contains, and that there is a larger decrease in this onset potential from IrO_2 to Ir60, than from Ir60 to RuO_2.

Table 5-4: Approximate onset potential of region with linear reaction kinetics in the polarisation curves for the different catalysts at all pHs.

Material	IrO_2	$Ir_{0.6}Ru_{0.4}O_2$	$Ir_{0.3}Ru_{0.7}O_2$	RuO_2
E vs. RHE [V]	1.48	1.43	1.42	1.41

The Tafel slopes were found as the constant *b* in equation (3-17) after the curves were numerically fitted to this equation, i.e. after the post-experimental ohmic loss correction. The *b*, *a* and resistance values obtained from this fitting for all catalysts in all pH solutions are given in Table 5-5, and the Tafel slopes are also presented as a function of solution pH in Figure 5-13.

Table 5-5: a and b values obtained from fitting the raw data from the polarisation curves with equation (3-17) for all four catalysts in the four solutions of pH 0, 1, 2 and 3. a given in V, b in mV and R in mΩ.

	IrO_2			**$Ir_{0.6}Ru_{0.4}O_2$**			**$Ir_{0.3}Ru_{0.7}O_2$**			**RuO_2**		
pH	b	a	R	b	a	R	b	a	R	b	a	R
0	38	1.57	8	42	1.53	31	37	1.51	36	32	1.47	13
1	41	1.52	13	47	1.49	36	45	1.47	34	34	1.43	22
2	42	1.46	25	47	1.43	54	42	1.41	74	36	1.37	36
3	53	1.42	78	54	1.38	152	58	1.37	92	44	1.32	59

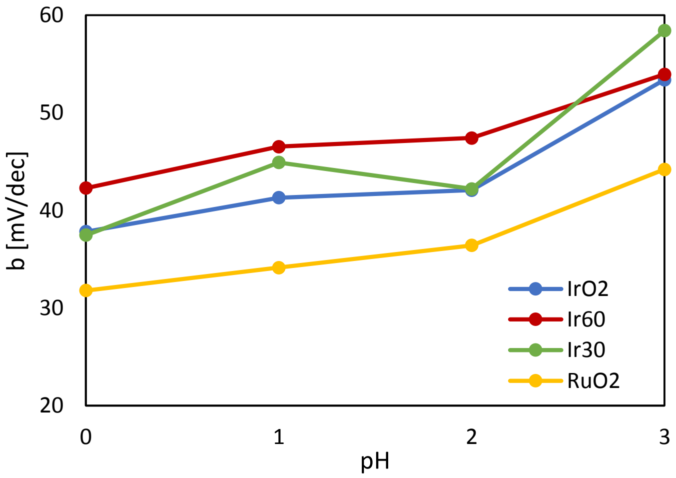

Figure 5-13: Tafel slopes for the four different catalysts as a function of solution pH.

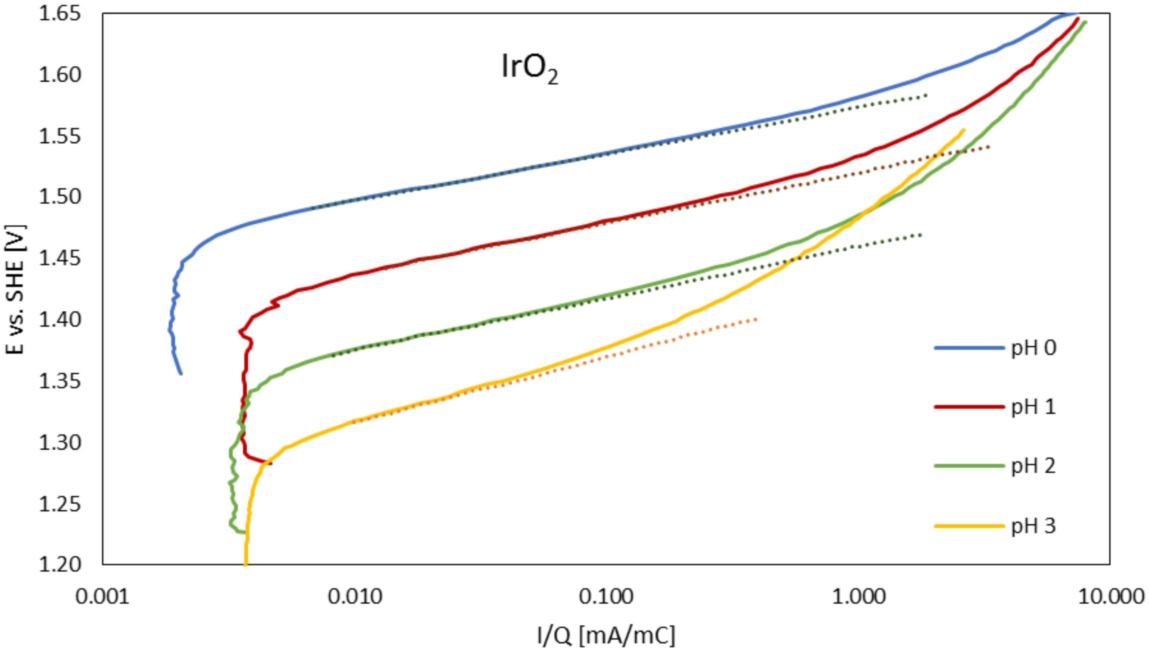

Figure 5-14: Polarisation curves of IrO_2 in the four different solutions of pH 0, 1, 2 and 3 obtained at a scan rate of 0.083 mV/s. Full lines represent raw data from the potentiostat, whereas the dotted lines are the curves obtained from fitting the raw data to equation (3-17) in the region where the ohmic losses increases linearly with current. Currents are normalised with respect to the outer surface charge.

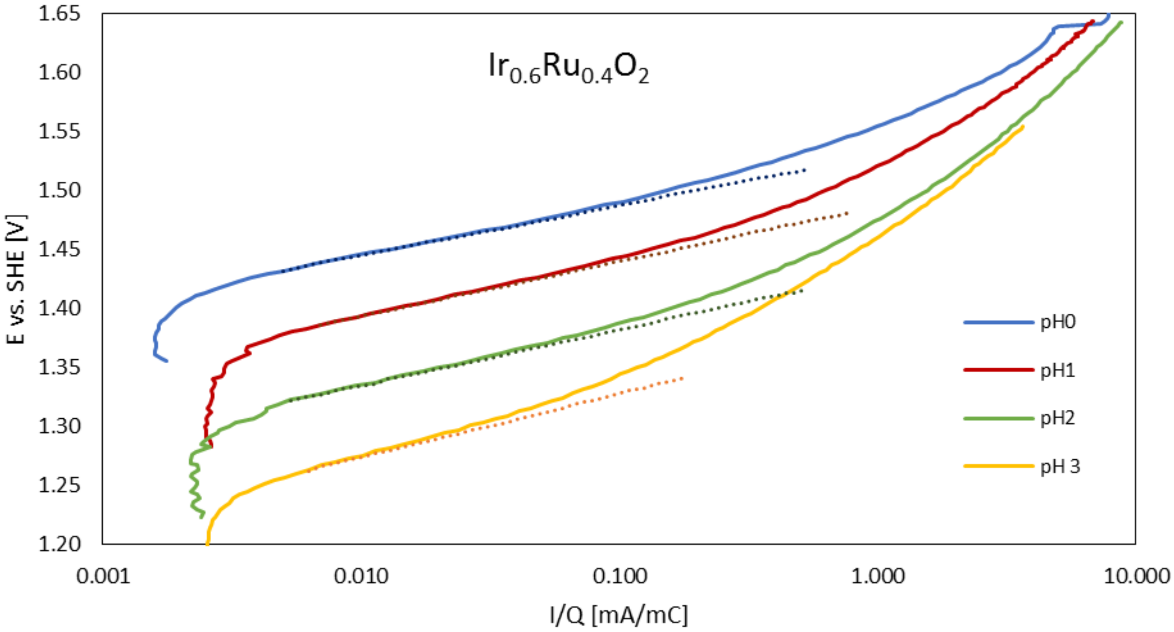

Figure 5-15: Polarisation curves of $Ir_{0.6}Ru_{0.4}O_2$ in the four different solutions of pH 0, 1, 2 and 3 obtained at a scan rate of 0.083 mV/s. Full lines represent raw data from the potentiostat, whereas the dotted lines are the curves obtained from fitting the raw data to equation (3-17) in the region where the ohmic losses increases linearly with current. Currents are normalised with respect to the outer surface charge.

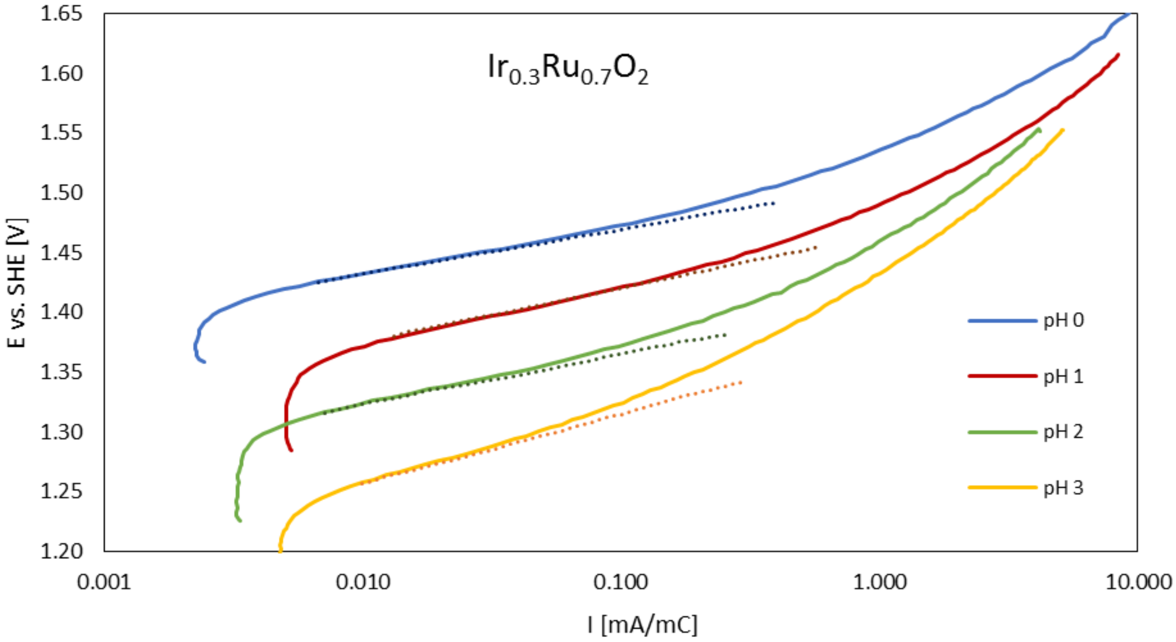

Figure 5-16: Polarisation curves of $Ir_{0.3}Ru_{0.7}O_2$ in the four different solutions of pH 0, 1, 2 and 3 obtained at a scan rate of 0.083 mV/s. Full lines represent raw data from the potentiostat, whereas the dotted lines are the curves obtained from fitting the raw data to equation (3-17) in the region where the ohmic losses increases linearly with current. Currents are normalised with respect to the outer surface charge.

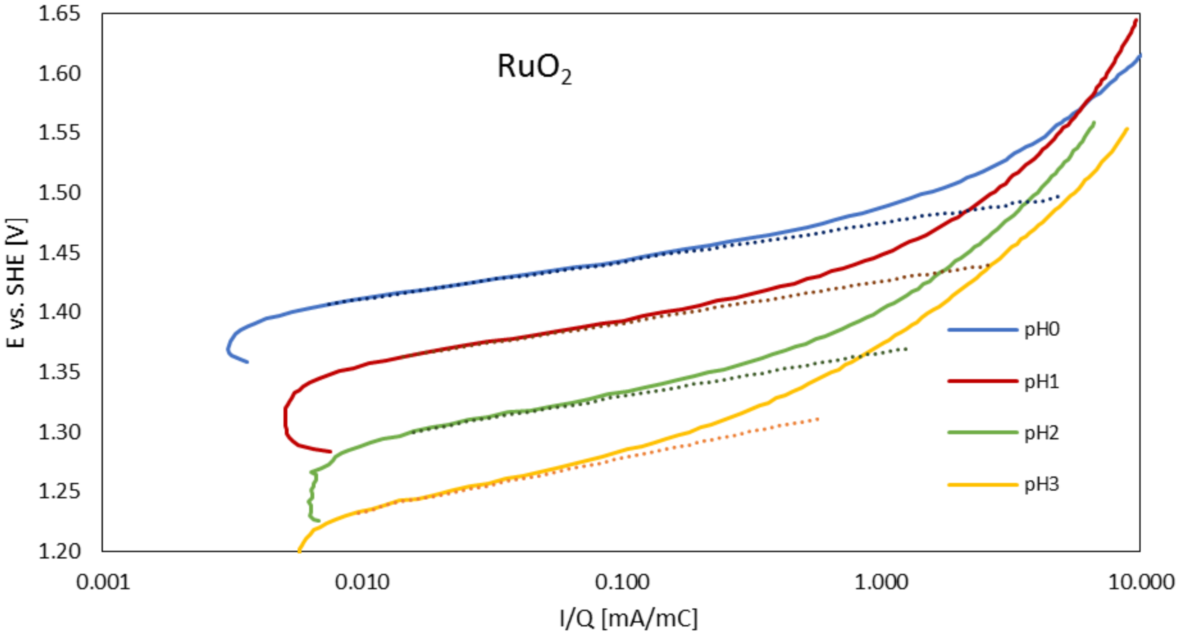

Figure 5-17: Polarisation curves of RuO_2 in the four different solutions of pH 0, 1, 2 and 3 obtained at a scan rate of 0.083 mV/s. Full lines represent raw data from the potentiostat, whereas the dotted lines are the curves obtained from fitting the raw data to equation (3-17) in the region where the ohmic losses increases linearly with current. Currents are normalised with respect to the outer surface charge.

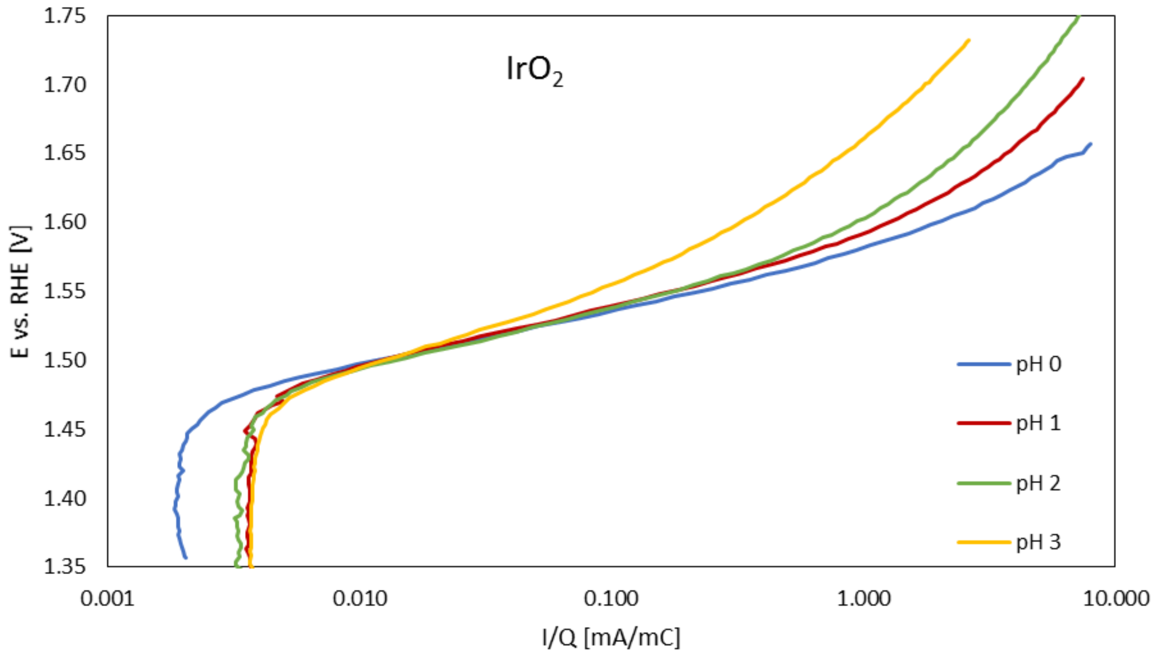

Figure 5-18: Polarisation curves of IrO_2 in the solutions of pH 0, 1, 2 and 3 obtained at a scan rate of 0.083 mV/s. The currents are normalised with respect to the outer surface charge. Potentials are given vs. RHE.

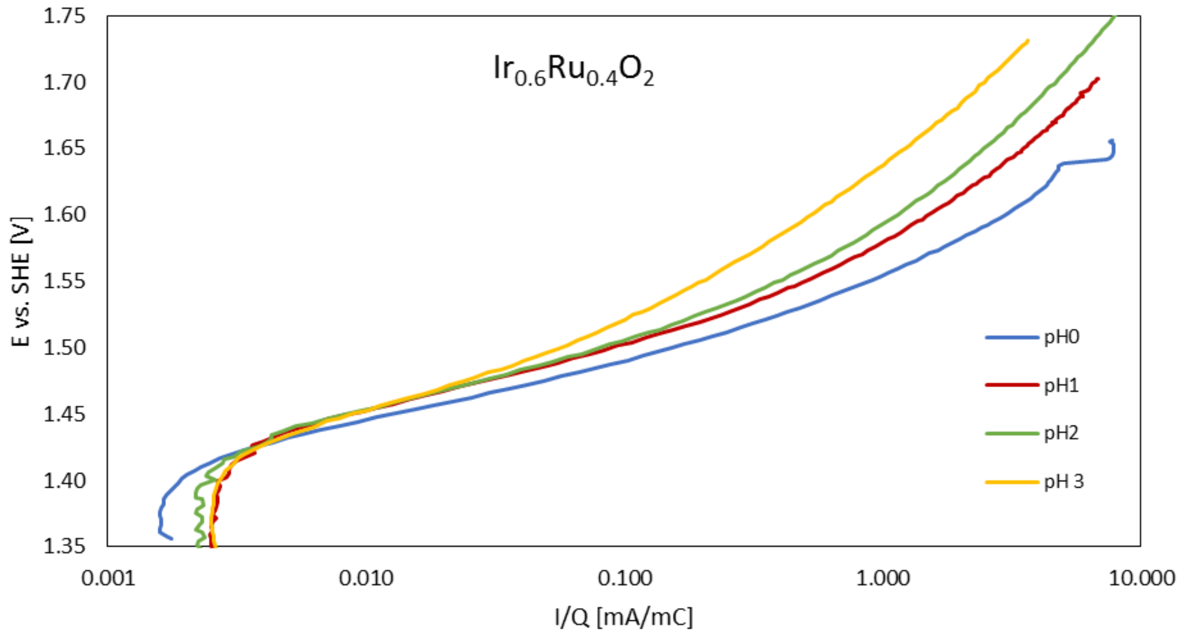

Figure 5-19: Polarisation curves of $Ir_{0.6}Ru_{0.4}O_2$ in the solutions of pH 0, 1, 2 and 3 obtained at a scan rate of 0.083 mV/s. The currents are normalised with respect to the outer surface charge. Potentials are given vs. RHE.

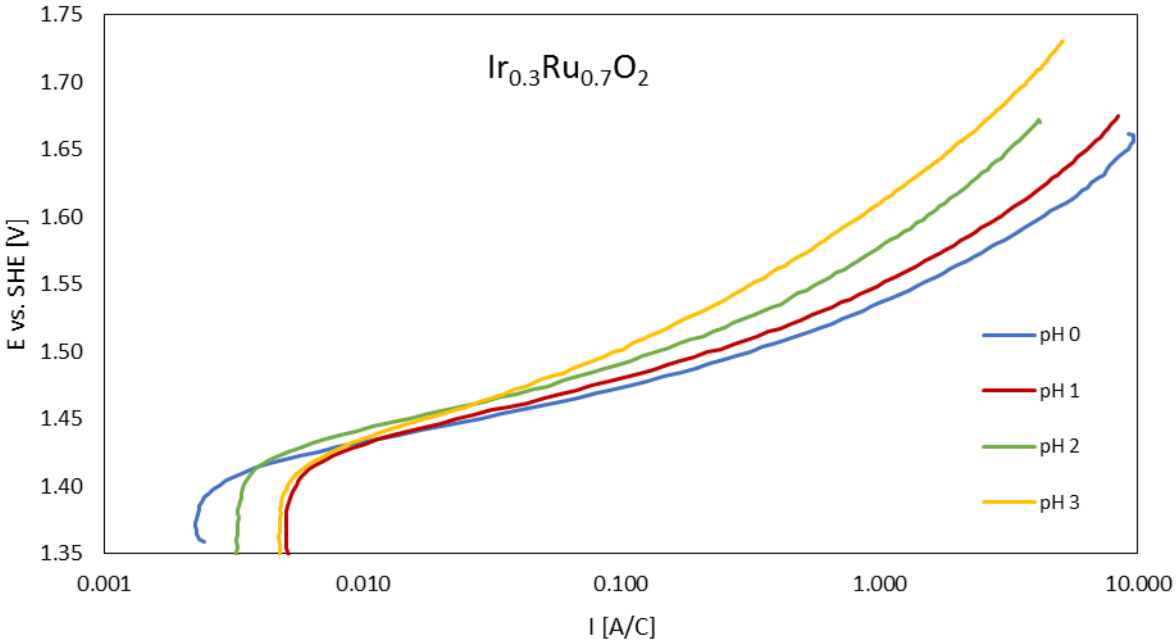

Figure 5-20: Polarisation curves of $Ir_{0.3}Ru_{0.7}O_2$ *in the solutions of pH 0, 1, 2 and 3 obtained at a scan rate of 0.083 mV/s. The currents are normalised with respect to the outer surface charge. Potentials are given vs. RHE.*

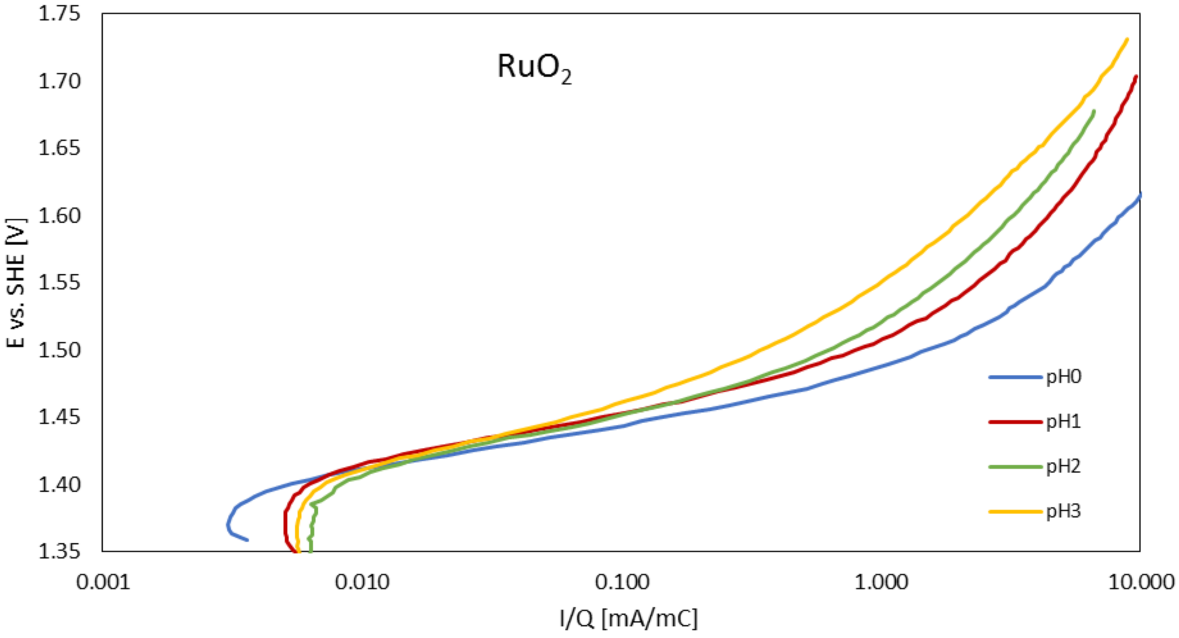

Figure 5-21: Polarisation curves of RuO_2 *in the solutions of pH 0, 1, 2 and 3 obtained at a scan rate of 0.083 mV/s. The currents are normalised with respect to the outer surface charge. Potentials are given vs. RHE.*

5.2.3.1.1 Ohmic losses measured in the electrolytes

Mean values for the electrolyte resistance in each electrolyte (pH 0, 1, 2 and 3) measured by the ZIR method prior to the electrochemical experiments are given in Table 5-6. The electrolyte resistance is significant for solutions with pH > 0. Employing the equations for the electrolyte resistance given in section 3.2.5, values close to the experimentally obtained values are obtained by using a cell constant (l/A) of 170 m^{-1}, which is a probable value for the experimental setup. The mobilities used in these calculations are the limiting ionic mobilities at infinite dilution (Table 5-7), and the calculated values are given in Table 5-6 along with the measured values

Table 5-6: Mean electrolyte resistance values obtained by the ZIR method for the solutions of pH 0, 1, 2 and 3, and theoretical values for the same solutions.

Solution pH	Mean $R_{measured}$ [Ω]	$R_{calculated}$ [Ω]
0	3	4
1	10	12
2	16	14
3	15	14

Table 5-7: Limiting ionic mobilities used for calculating the ohmic resistance in the electrolytes.[92]

Ion	Limiting mobility $[\frac{m^2}{Vs}]$
H^+	$362 \cdot 10^{-9}$
Na^+	$51.9 \cdot 10^{-9}$
ClO_4^-	$69.8 \cdot 10^{-9}$

Example of post-experimental ohmic loss compensations by the numerical fitting procedure

An example of curves obtained from the fitting procedure described in section 3.2.5 is given here. The currents were normalised with respect to the outer surface charge prior to this procedure. Applying this method extended the linear regions of the polarisation curves to some extent, but generally the linear regions are more limited in electrolytes with high pH and for the mixed oxides. The a, b and resistance values of equation (3-17) for all polarisation curves were found by this procedure. The validity of this IR correction was checked for every data set by plotting the uncompensated ohmic losses as a function of current. An example of the raw data polarisation curve and the linear fit are given in Figure 5-22 (a), along with the uncompensated ohmic loss (difference between IR corrected curve and raw data) (b). These data were obtained from the polarisation of RuO_2 in the electrolyte with pH 2. It was generally more difficult to obtain good fits of the data obtained at higher pH due to shorter linear regions in the polarisation curves.

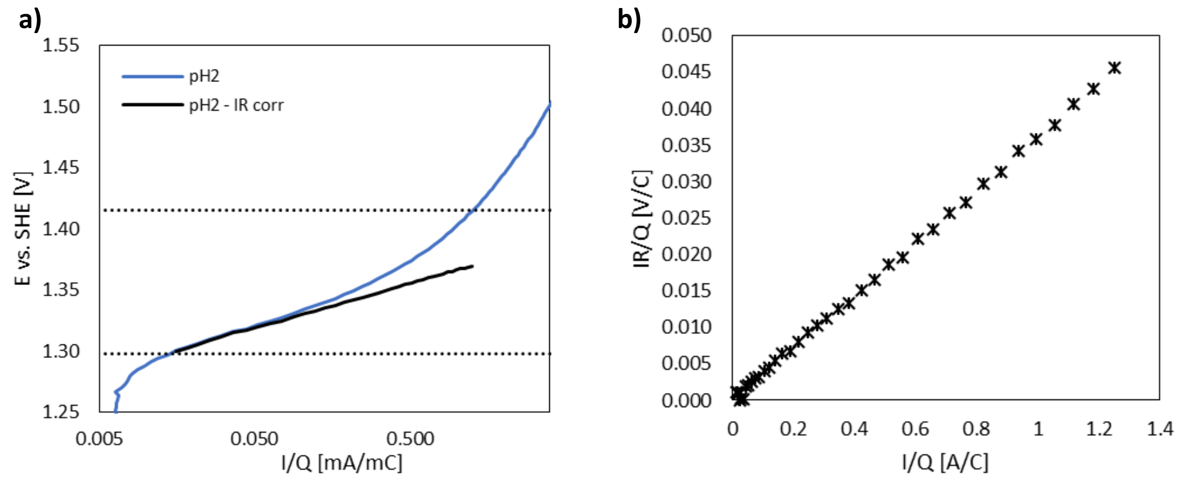

Figure 5-22: a) Raw data polarisation curve (blue) and the post-experimental IR corrected fit of these data (black). b) The uncompensated ohmic loss, calculated as the difference between the raw data and the fitted potential-current curves. Data are obtained for polarisation of RuO2 at 0.083 mV/s in the electrolyte of pH 2. Currents are normalised with respect to the outer surface charge.

5.2.4 Anodic reaction order with respect to H^+

The anodic reaction orders with respect to H^+ were obtained from the linear curves obtained from the numerical fitting of the polarisation curves with equation (3-17). The reaction orders were found by plotting $\ln(\frac{I}{Q_S})$ as a function of $\ln[\mathrm{H}^+]$, and subsequently obtaining the slope of these curves by the least squares fit in excel. These plots were made for three different potentials, 1.35 V, 1.40 V and 1.45 V, and the reaction orders were thus found at each of these potentials. Figure 5-23 present these plots for all four catalysts, and includes the trend lines found in excel. The reaction orders at each potential as well as the average value are summarised in Table 5-8. For reasons given in the discussion, the reaction orders were also found with a basis in only the solutions of pH 0, 1 and 2. These are summarised in Table 5-9.

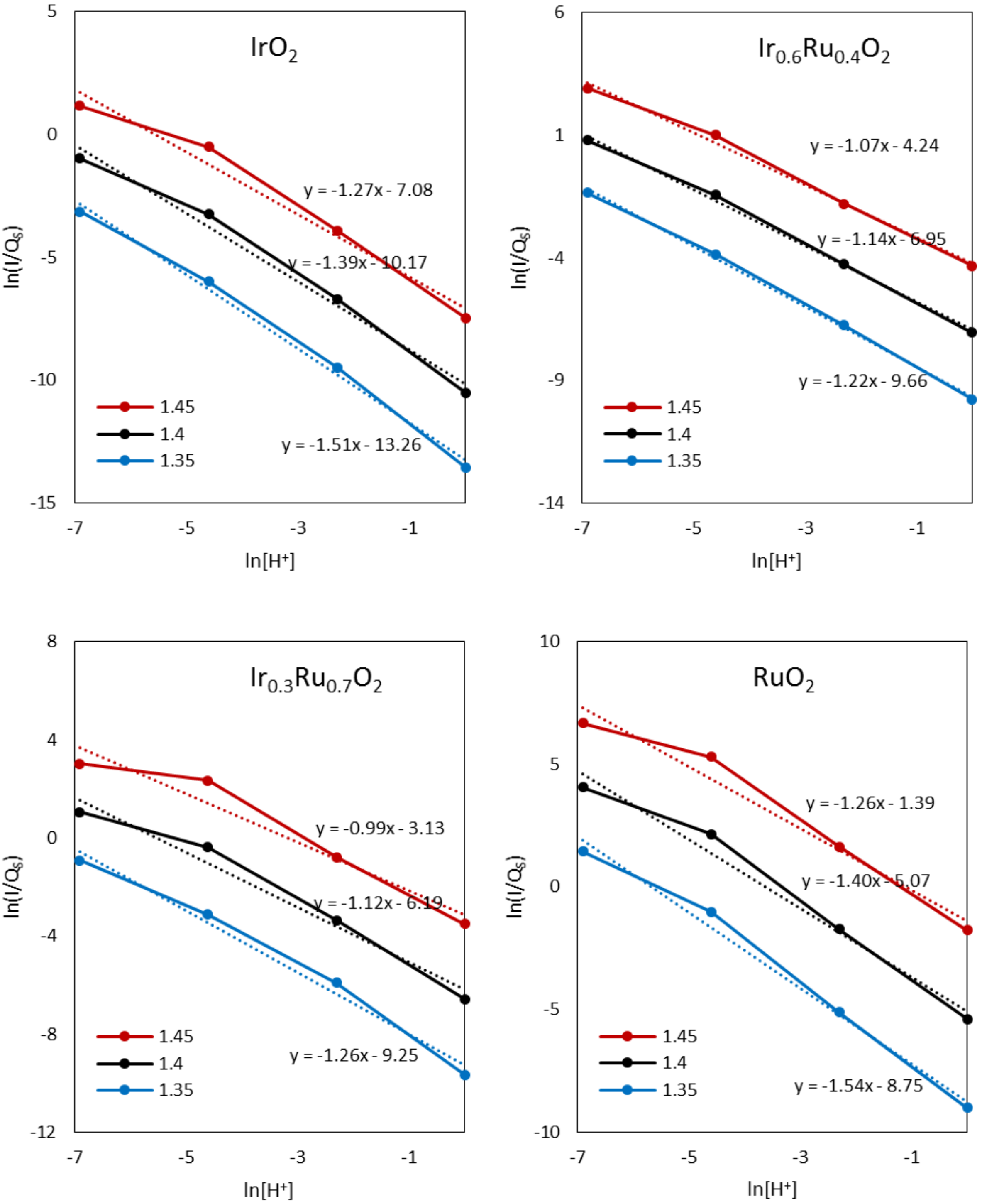

Figure 5-23: Reaction order plots for the four different oxide compositions. The curves present the logarithm of the normalised current as a function of the logarithm of proton concentration.

Table 5-8: Anodic reaction orders with respect to [H^+] for the four different catalysts, obtained from polarisation curves in solutions of pH 0, 1, 2 and 3.

	IrO_2	**$Ir_{0.6}Ru_{0.4}O_2$**	**$Ir_{0.3}Ru_{0.7}O_2$**	**RuO_2**
1.45 V	-1.27	-1.07	-0.99	-1.26
1.40 V	-1.39	-1.14	-1.12	-1.4
1.35 V	-1.51	-1.25	-1.26	-1.54
Average	**-1.39**	**-1.15**	**-1.12**	**-1.4**

Table 5-9: Anodic reaction orders with respect to [H^+] for the different materials, obtained from polarisation curves in solutions of pH 0, 1 and 2.

	IrO_2	**$Ir_{0.6}Ru_{0.4}O_2$**	**$Ir_{0.3}Ru_{0.7}O_2$**	**RuO_2**
1.45 V	-1.51	-1.16	-1.27	-1.54
1.40 V	-1.58	-1.22	-1.34	-1.64
1.35 V	-1.64	-1.28	-1.42	-1.74
Average	**-1.58**	**-1.22**	**-1.34**	**-1.64**

5.3 DETECTION OF BY-PRODUCTS OF THE OER BY RING-DISK EXPERIMENTS

In this section, the results from the experiments aimed at identifying by-products of the OER at IrO_2 and $Ir_{0.6}Ru_{0.4}O_2$ are given. The first section presents results aiming to establish the method. Then the results from IrO_2 in sulphuric acid solution are given, followed by similar experiments at IrO_2 in sodium sulphate solution. The last section presents the results from the ring-disk experiments at $Ir_{0.6}Ru_{0.4}O_2$.

5.3.1 Establishment of method

The method for detection of by-products of the OER by ring-disk electrodes was tested by using only a plain disk electrode in combination with either a gold or platinum ring. All results from these test are given in this section. First the results from potential step voltammetry in ferricyanide solution are given, both for the flow cell set-up and the conventional set-up. This is followed by results form cyclic voltammetry of the disk in the same solution with a conventional RRDE set-up. Then, the results form cyclic voltammetry of the disk in 0.5 M H_2SO_4 in the conventional RRDE set-up are given.

The reference used in the experiments with the ferricyanide solution was the laboratory-made Ag/AgCl reference, and potentials in the results from these experiments are therefore given with respect to this electrode (this reference is approximately 0.51 V positive to the SHE). The reference used in the solutions of 0.5 M H_2SO_4 was the RHE, and potentials in these graphs are given with respect to this electrode.

Potential step voltammetry in ferricyanide solution

Potential step measurements with a gold ring and a gold disk electrode were performed with the ferricyanide solution in the flow cell set-up. The observed ring currents when the gold ring was held at 0.3 V and the disk was stepped from 0.3 V to -0.3 V are given in Figure 5-24. It can be seen that the ion reduced at the disk travels faster to the ring when the flow rate is higher, as the oxidation currents are more delayed for low flow rates. The observed transit times, t', for each flow rate are summarised in Table 5-10.

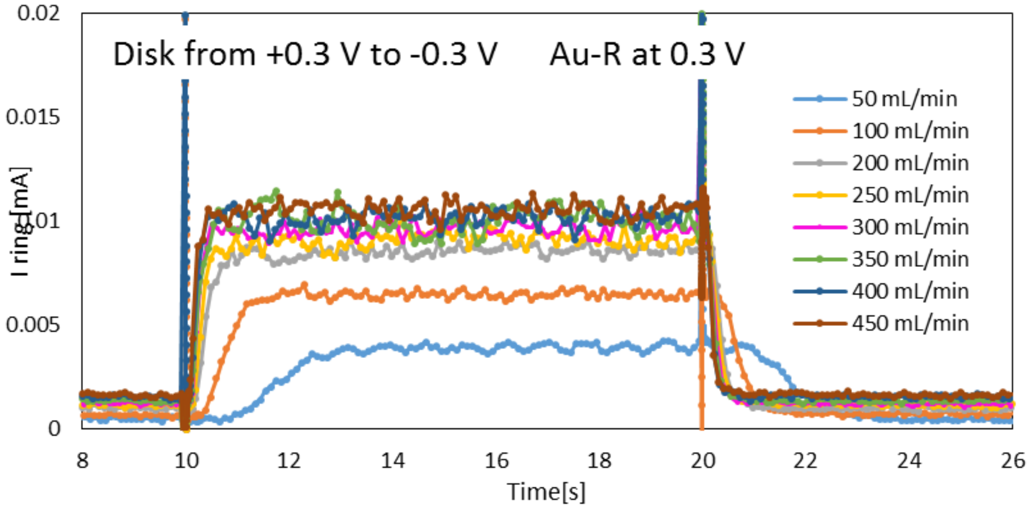

Figure 5-24: Ring current response when the gold ring was held at 0.3 V vs. Ag/AgCl while the disk was stepped from -0.3 V to 0.3 V at different electrolyte flow rates. The electrolyte was 1 M KNO_3 + 10 mM $K_3Fe(CN)_6$.

Table 5-10: Transit times observed for $Fe(CN)_6^{4-}$ at different electrolyte flow rates.

Flow rate	**450**	**400**	**350**	**300**	**250**	**200**	**100**	**50**
Observed t' $Fe(CN)_6$ [s]	0.07	0.08	0.09	0.1	0.14	0.15	0.4	1

Equivalent potential step experiments were performed in the conventional RRDE set-up with both a gold and a platinum ring. The ring current responses are given in Figure 5-25 for a) the Pt ring and b) the Au ring. Higher rotation speeds at the electrode results in a faster response at the ring electrode., as the $Fe(CN)_6^{4-}$ ion travels faster at these speeds. The transit times observed at the different rotational speeds are compared with the theoretically calculated values from (3-24) and are summarised in Table 5-11. Transit times found from the experiments with both the Pt and Au ring electrodes are quite similar. However, the values in the table are obtained from the RRDE experiments with the Pt electrode. A viscosity of 0.00893 cm^2/s for water and a diffusion coefficient of $7 \cdot 10^{-6}$ cm^2/s for $Fe(CN)_6^{4-}$ were employed in these calculations.[92]

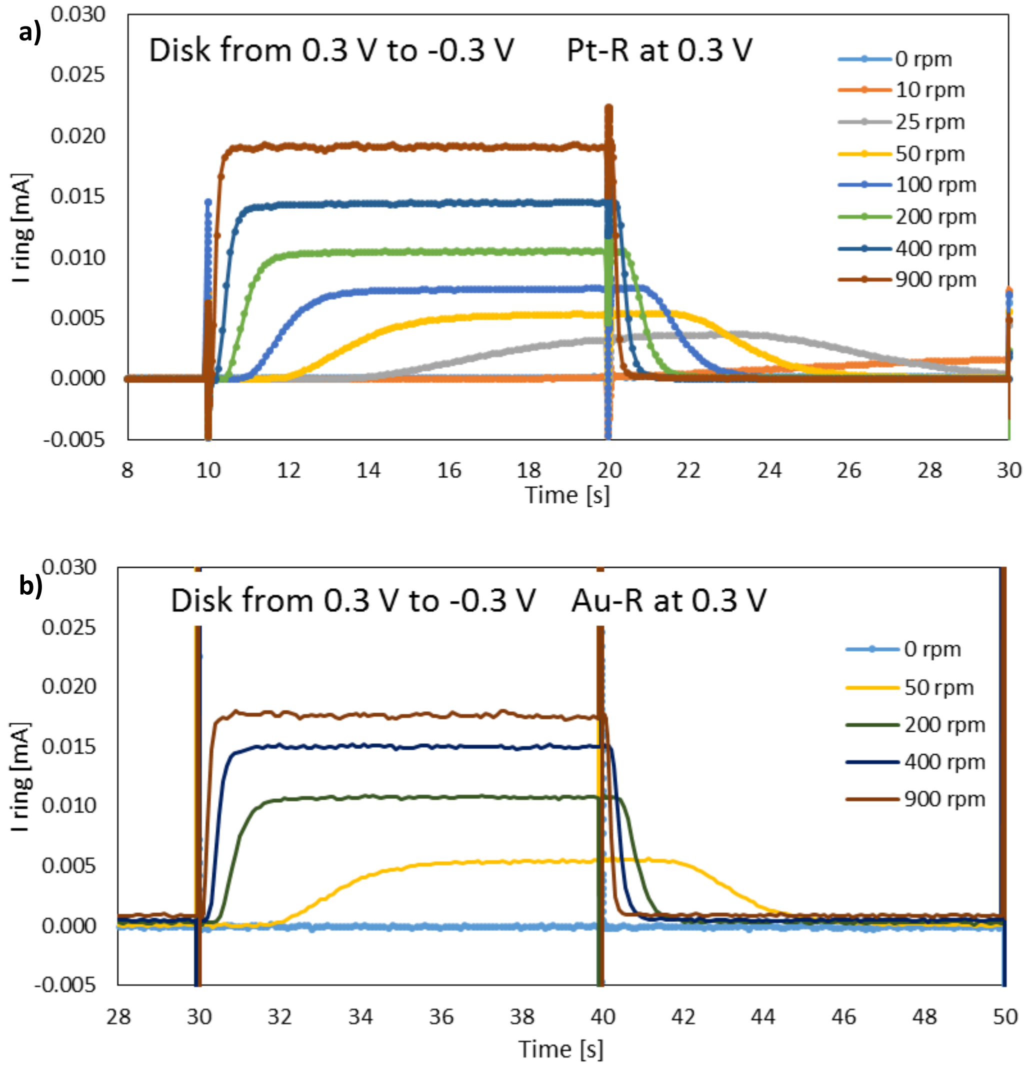

Figure 5-25: Ring current response when ring is held at 0.3 V vs. Ag/AgCl while the disk is stepped from -0.3 V to 0.3 V at different electrode rotational speeds, for a) the Pt ring and b) the Au ring. The electrolyte was 1 M KNO_3 + 10 mM $K_3Fe(CN)_6$.

Table 5-11: Calculated and observed transit times for different rotational speeds at the RRDE in ferricyanide solution by the use of viscosity and diffusion coefficients given in the text.

Rpm	**900**	**400**	**200**	**100**	**50**	**25**	**10**
Calculated t' $Fe(CN)_6$ [s]	0.097	0.218	0.436	0.871	1.743	3.486	8.714
Observed t' $Fe(CN)_6$ [s]	0.1	0.2	0.4	1	2	4	-

The collection efficiency of the RRDE with a Au disk and Pt ring in the conventional RRDE set-up is also estimated by the potential step measurements. Figure 5-26 presents the current response of both the ring and the disk electrodes when the ring is held at 0.3 V while the disk is stepped from 0.3 to -0.3 V. The collection efficiency is calculated from the observed currents at the four different rotational speeds: 100 rpm, 200 rpm, 400 rpm and 900 rpm. The calculated collection efficiencies are summarised in Table 5-12, and the average collection efficiency was found to be 23 %.

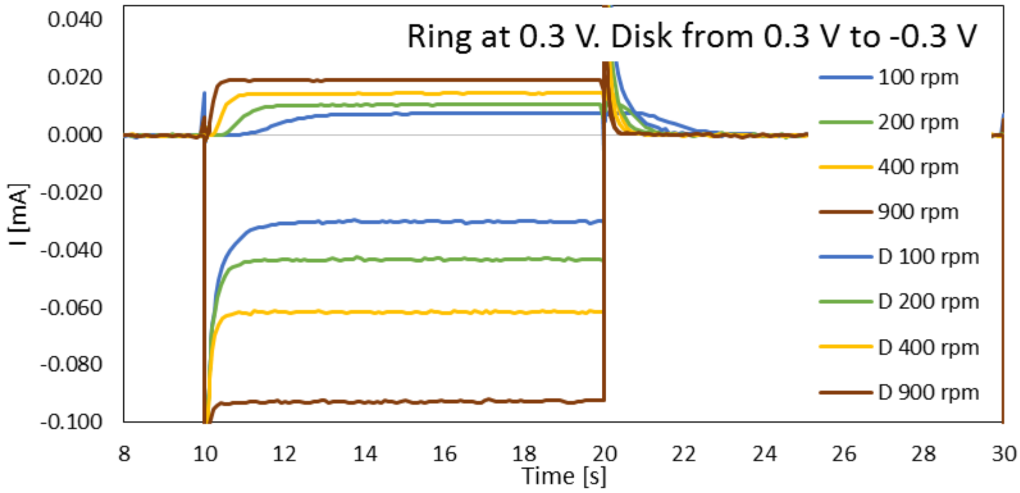

Figure 5-26: Ring and disk current responses as the disk was stepped from 0.3 V to -0.3 V while the Pt ring was held at a constant potential of 0.3 V, for electrode rotational speeds of 100, 200, 400 and 900 rpm. The electrolyte was 1 M KNO_3 + 10 mM $K_3Fe(CN)_6$.

Table 5-12: Collection efficiencies calculated at four rotational speeds of the RRDE (100, 200, 400 and 900 rpm), using the data presented in Figure 5-26.

	I ring	**I disk**	**Collection efficiency**
100 rpm	0.007	0.03	23 %
200 rpm	0.0105	0.043	24 %
400 rpm	0.015	0.062	24 %
900 rpm	0.019	0.092	21 %

Potential sweep in ferricyanide solution

Results from cycling the disk at 200 mV/s between -0.3 V and 0.3 V while the ring was held constantly at 0.3 V are given in Figure 5-27 a) with a platinum ring and b) with a gold ring. The 10 mM $K_3Fe(CN)_6$ solution was used in these experiments. These experiments were repeated in a solution with 0.01 mM $K_3Fe(CN)_6$, and the currents obtained in this solution is given in Figure 5-28. The disk currents are represented by the lower curves and are given by the right axis, whereas the ring currents are presented by the upper curves and are given by the left axis. Sweeps in directions towards more positive potentials are marked “positive” and are given by the dotted lines, whereas sweeps in the negative direction are marked “negative” and are given by full lines.

In all figures both the disk and the ring currents increase as the rotational speed of the RRDE increases. The time from the onset of the disk current until the onset of the ring current is higher when the electrode is rotated at 200 rpm vs. 900 rpm. No ring response is observed in either of the curves when the electrode is not rotated. In the 10 mM $K_3Fe(CN)_6$ solution, no ring currents are observed as the disk potential reaches the upper potential limit and starts to scan in the negative direction. In this solution, no significant background currents are seen at the ring.

In the diluted solution (0.1 mM $K_3Fe(CN)_6$) the ring currents are ca. 1/100 of the currents in the 10 mM $K_3Fe(CN)_6$ solution, whereas the disk currents are reduced to ca. 1/20. For these small faradaic currents, a significant contribution of capacitive currents can be seen for the gold disk. A background current is observed at the ring when the electrode is rotated. Small deviations from the baseline current can be seen at the ring close to the upper potential of the disk. However, these deviations are positive when the electrode is rotated at 200 rpm and negative when the electrode is rotated at 900 rpm.

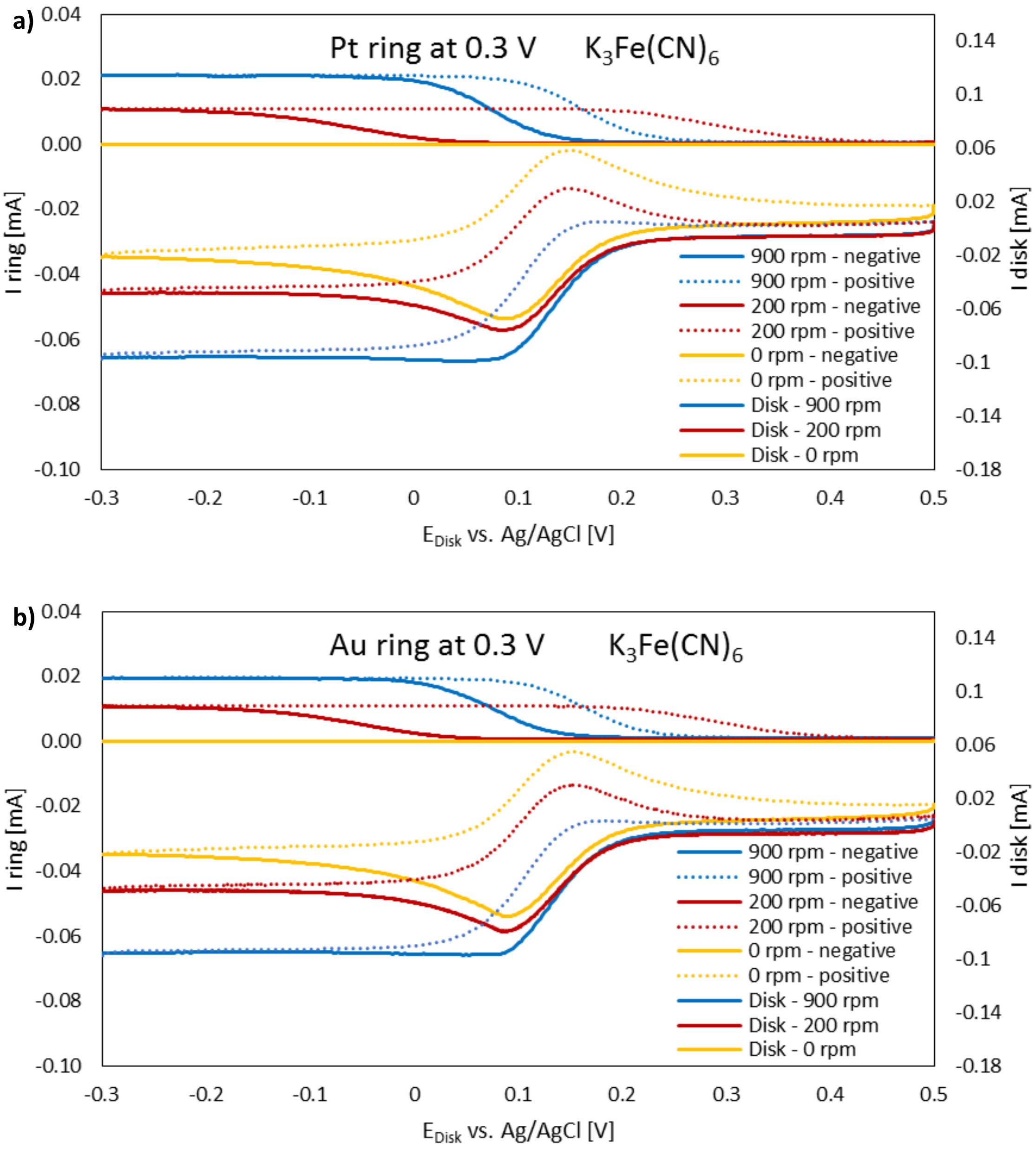

Figure 5-27: Current response of ring (upper curves) and disk (lower curves) when the disk was cycled at 200 mV/s, while the ring was held constantly at 0.3 V, for a) a Pt ring and b) a gold ring. Electrolyte: 1 M KNO_3 + 10 mM $KFe(CN)_6$.

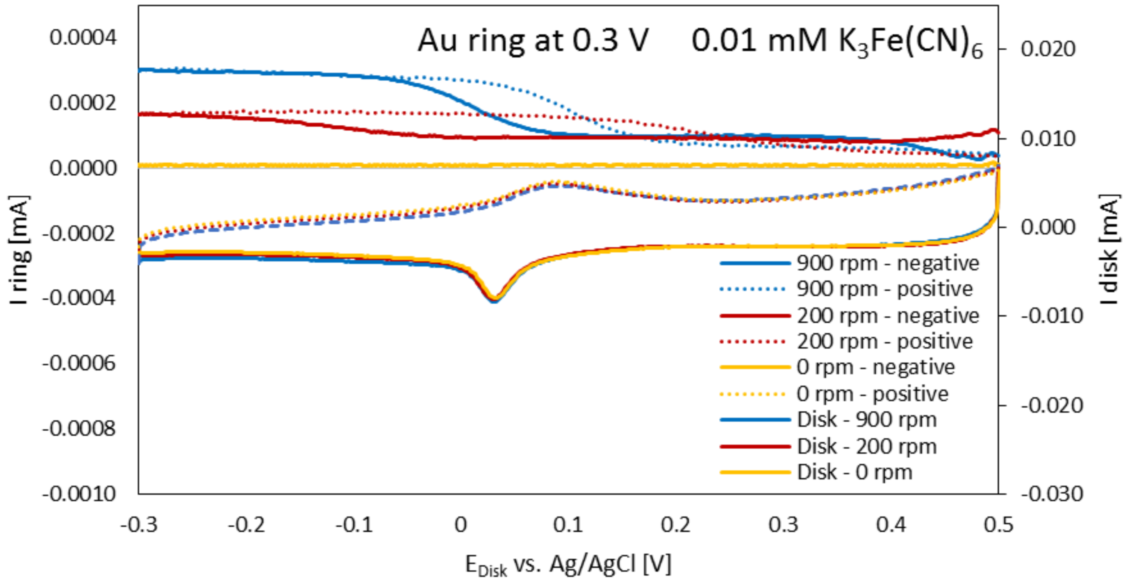

Figure 5-28: Current response of ring (upper curves) and disk (lower curves) when the disk was cycled at 200 mV/s, while the gold ring was held constantly at 0.3 V. Electrolyte: 1 M KNO_3 + 0.1 mM $KFe(CN)_6$.

Uncoated Au disk electrode in combination with a Pt or Au ring electrode, conventional RRDE set-up

The results from the experiments with the plain gold disk in combination with a platinum or gold ring are given below. These experiments were carried out in the conventional RRDE set-up with 0.5 M sulphuric acid as electrolyte.

The ring currents (upper curves) and disk currents (lower curves) for the plain Au disk in combination with the Pt ring are given in Figure 5-29. The disk was cycled at 200 mV/s between 0.6 V and 1.9 V while the ring was held at 0.6 V in figure a) and 1.2 V in figure b). Background currents were observed at the ring at all times, i.e. the baseline was shifted from zero. The ring currents were corrected for this by subtracting the baseline current from all the recorded values (i.e. the graphs of the ring currents were moved vertically such that the baseline corresponded to zero current), assuming the baseline corresponded to zero current at 0.6 V at the disk. Scans performed in the positive direction are referred to as “forward” scan, whereas scan from higher to lower potentials are referred to as “reverse” scans.

At 2000 rpm when the Pt ring is held at 0.6 V, reduction starts at the ring when disk potentials are above 1.75 V. The reduction increases as the disk potential is increased further, and a peak in the reduction current is observed at ca. 1.88 V at the start of the reverse scan of the disk. A reduction peak is observed at the gold disk at ca. 1.12 V at the reverse scan. This is followed by a reduction peak at the ring. The current response at the ring during the experiments at 1000 rpm is qualitatively similar to the response at 2000 rpm. However, the reduction currents are shifted towards later times. The peak reduction current at high potentials is larger at 1000 rpm, whereas the peak reduction at ca. 1.1 V is smaller for 1000 rpm. At no electrode rotation, the ring current is constant at all times.

When the Pt ring was held constantly at 1.2 V, no significant reduction or oxidation could be observed at the ring as the disk was cycled. However, there might be a very small reduction current at the ring for potentials above 1.75 V.

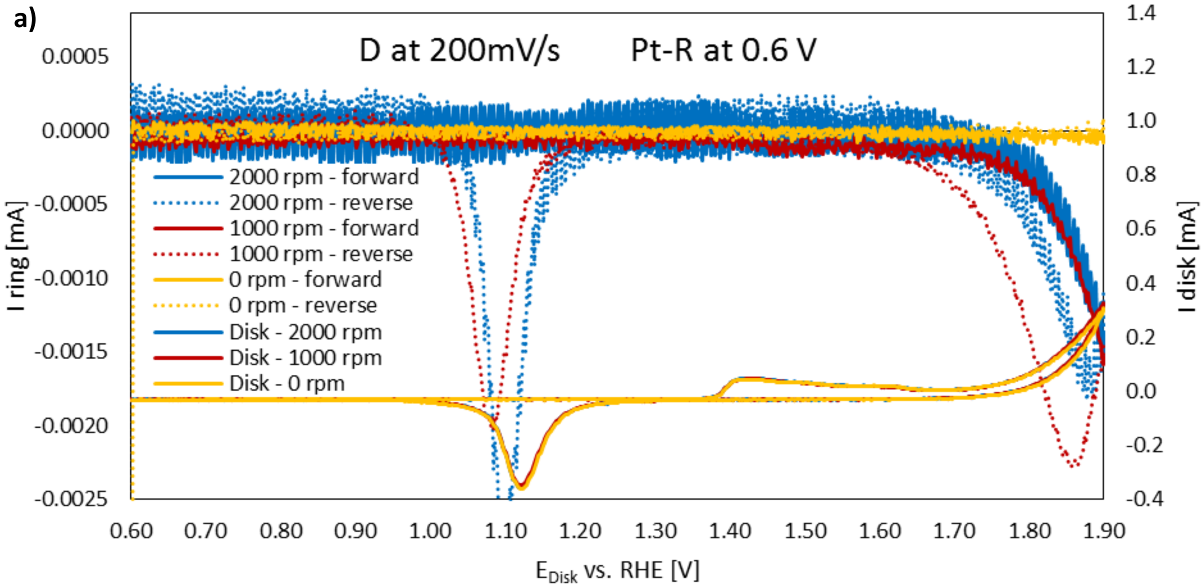

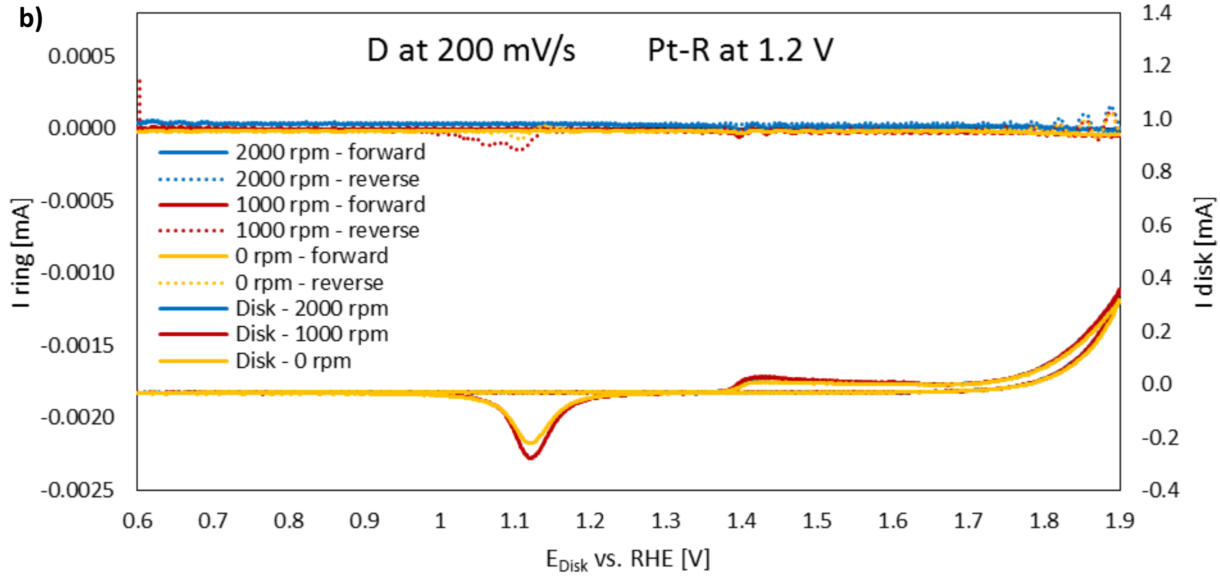

Figure 5-29: Current response from gold disk (lower curves) and platinum ring (upper curves) when the disk was cycled at 200 mV/s between 0.6 V and 1.9 V and the ring was held constantly at a) 0.6 V or b) 1.2 V. The experiments were performed in 0.5 M H_2SO_4 and at an RRDE rotated at 0, 1000 and 2000 rpm.

Figure 5-30 shows the results from the analogous experiments, but with a gold ring instead of a platinum ring. When the ring is held at 0.6 V, the only feature of the ring current curve is a reduction peak at ca. 1.1 V at the reverse scan of the disk. This peak is later in time and smaller when the electrode is rotated at 1000 rpm compared to 2000 rpm. At 0 rpm, no current is detected at the ring. When the Au ring is held at 1.2 V, the current is very similar to that of the Pt ring at 1.2 V. No significant current is detected at the ring, but a slight reduction might be observed during the forward scan of the disk at potentials above 1.75 V.

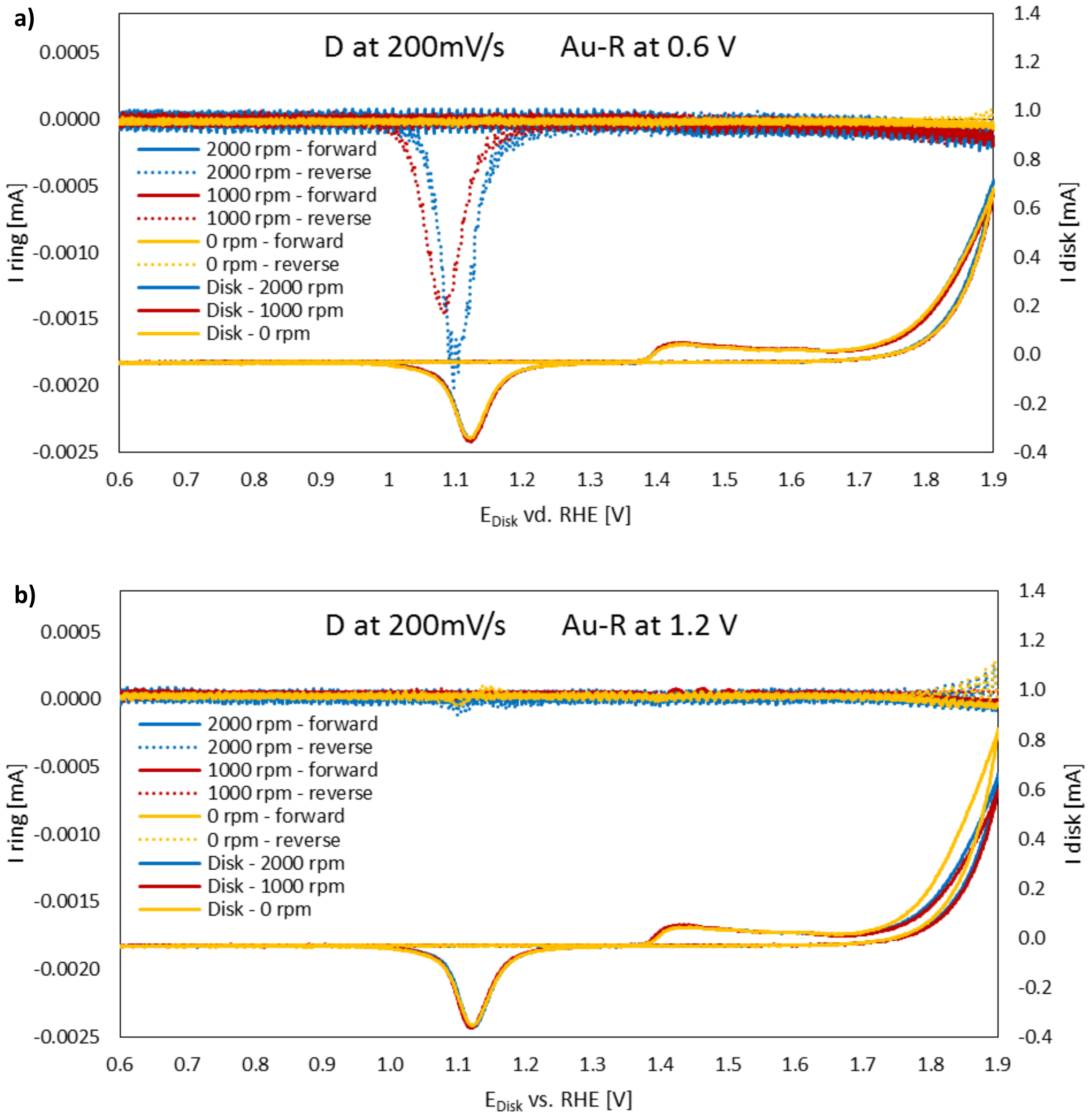

Figure 5-30: Current response from gold disk (lower curves) and gold ring (upper curves) when the disk was cycled at 200 mV/s between 0.6 V and 1.9 V and the ring was held constantly at a) 0.6 V or b) 1.2 V. The experiments were performed in 0.5 M H_2SO_4 and at an RRDE rotated at 0, 1000 and 2000 rpm.

5.3.2 Cyclic voltammetry at the IrO_2 combined with a Pt or Au ring in 0.5 M H_2SO_4

In this section, all results obtained for the IrO_2 catalyst in 0.5 M H_2SO_4 are presented. Firstly, the results obtained in the flow cell set-up are presented, starting with experiments with cyclic voltammetry at the disk before the results from the potential step voltammetry at the disk are given. Then the results obtained with the conventional RRDE set-up are given, and at last the results from the experiments with the catalyst coating on the ring.

The ring currents are plotted for all these experiments. In some cases, this is convenient to present as a function of the disk potential. However, when the ring currents are less reproducible or difficult to interpret, it is believed that a plot of ring current vs. time is a more correct presentation. Thus, both types of graphs are given in this section.

Varying the electrolyte flow rate in the flow cell set-up

Figure 5-31 shows the ring current response (full lines, left axis) and the disk current (stippled line, right axis) for the gold ring held at 0.6 V while the disk is scanned between 0.6 V and 1.9 V, at a) 100 mV/s and b) 5 mV/s. The detected ring currents at three different flow rates (0, 100 and 600 mL/min) are shown, whereas only one disk current (at no flow) is included in each figure. The ring currents are normalised with respect to the peak disk current at 1.9 V (e.g. all ring current values are divided by 30 mA for the measurements at 100 mV/s and no flow), hence the µA/mA unit at the ring current axis. Background currents were observed at the ring at all times, i.e. the baseline current was shifted from zero. The ring currents were corrected for this by subtracting the baseline current from all the recorded values.

This background current was different for each of the recordings (even for the exact same measurement recorded some minutes later), and were therefore believed to be an artefact of the potentiostat when the bipotentiostat mode was employed. However, the background currents had a random nature. As no by-products can be produced when the OER is not occurring, i.e. at disk potentials below ca. 1.4 V, it is believed that it is legitimate to correct the ring currents such that the constant current values observed between the disk potentials 0.6 V and 1.4 V equals zero. All deviations from this value are assumed to be reduction or oxidation processes occurring at the electrode.

The reduction currents observed in Figure 5-31 were recorded at the positive scan at the disk. The start of the reduction current on the ring corresponds to the onset of the OER on the disk, and both ring and disk currents increases until the upper potential limit at the disk is reached. There is an immediate increase in the ring current as soon as the disk starts the negative scan, and a net positive current is soon established at the ring.

Figure 5-31 shows that the ring currents at different electrolyte flow rates are similar. The same ring current is observed even when the pump is turned off. The ring currents are however, affected by the scan rate of the ring. Both the anodic and cathodic currents are larger for 100 mV/s than for 50 mV/s. The ratio of net cathodic vs. net anodic current also seems to be higher for the lowest scan rate at the disk.

Results from similar experiemnts, but with a platinum ring electrode instead of the gold ring, are shown in Figure 5-32. The disk is still scanned between 0.6 V and 1.9 V, while the ring is held at 0.6 V. The currents are normalised and corrected for background currents as described above for the experiments with the gold ring.

A net reduction current is observed at the ring for both the positive and negative scan at the disk. The onset of the observed reduction coincides with the onset of the OER, and the ring current increases as the OER current at the disk increase. At the reverse scan of the disk, the reduction at the ring gradually decreases until it stops at the same time as the OER at the disk stops. The ring signal is quite noisy, and the observed size of the reduction peak at the ring varied considerably from cycle to cycle. It is therefore difficult to compare the reduction peaks at the ring for the different electrolyte flowrates, and also for the two different disk scan rates. The variation in current from cycle to cylce is demonstrated in Figure 5-33, which shows the current at the ring and potential of the disk as a function of time. However, looking at this figure, it can be seen that the first cycles for all flow rates is unlike the later cycles. In the first cycle, the reduction peak is larger than for later cycles, and the onset of the reduction is earlier for the highest flow rates. The disk current are equal in size for all experients and all cycles.

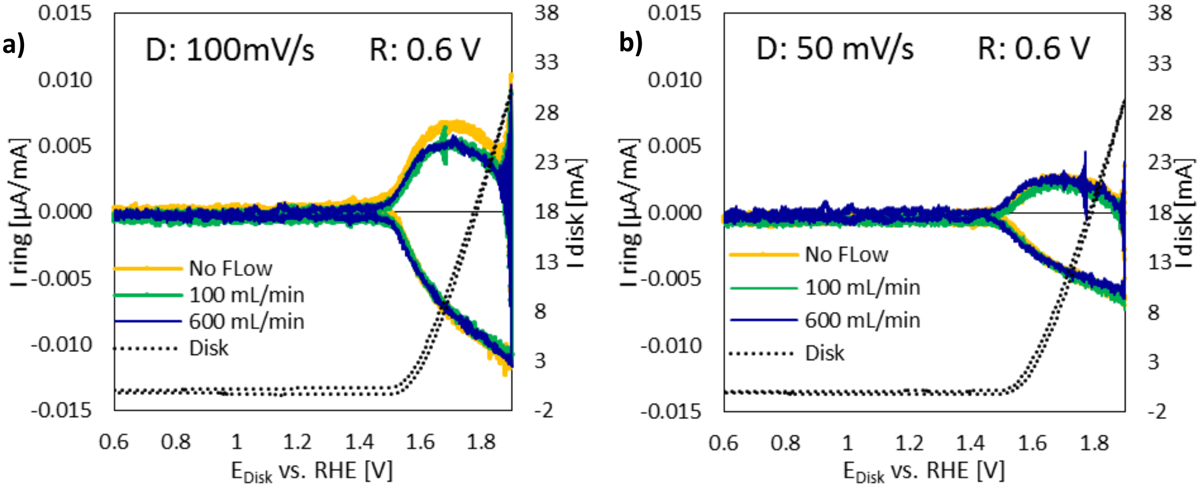

Figure 5-31: Ring current (full line, left axis) and disk current (stippled lines, right axis) as a function of disk potential when the gold ring is held at 0.6 V while the IrO_2 coated disk is cycled between 0.6 V and 1.9 V at a) 100 mV/s and b) 50 mV/s. The ring currents at three different electrolyte flow rates are shown (0, 100 and 600 mL/min). Only on disk current is included in each figure, i.e. at no flow. Ring currents are normalised with respect to the peak disk current, and corrected for the background current as described in the text.

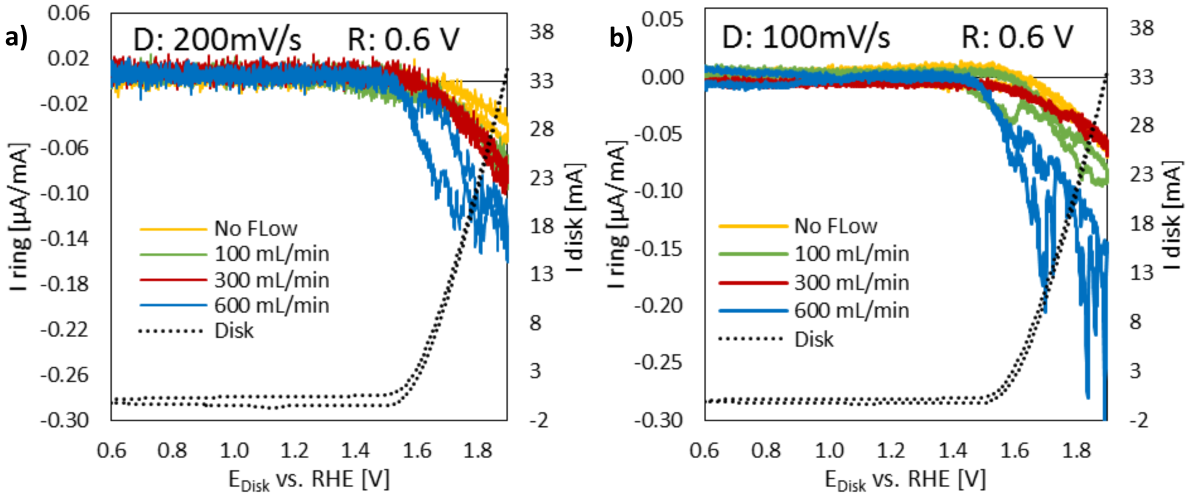

Figure 5-32: Ring current (full line, left axis) and disk current (stippled lines, right axis) as a function of disk potential when the platinum ring is held at 0.6 V while the IrO_2 coated disk is cycled between 0.6 V and 1.9 V at a) 200 mV/s and b) 100 mV/s. The ring currents at four different electrolyte flow rates are shown (0, 100, 300 and 600 mL/min). Only on disk current is included in each figure, i.e. at no flow. Ring currents are normalised with respect to the peak disk current, and corrected for the background current as described in the text.

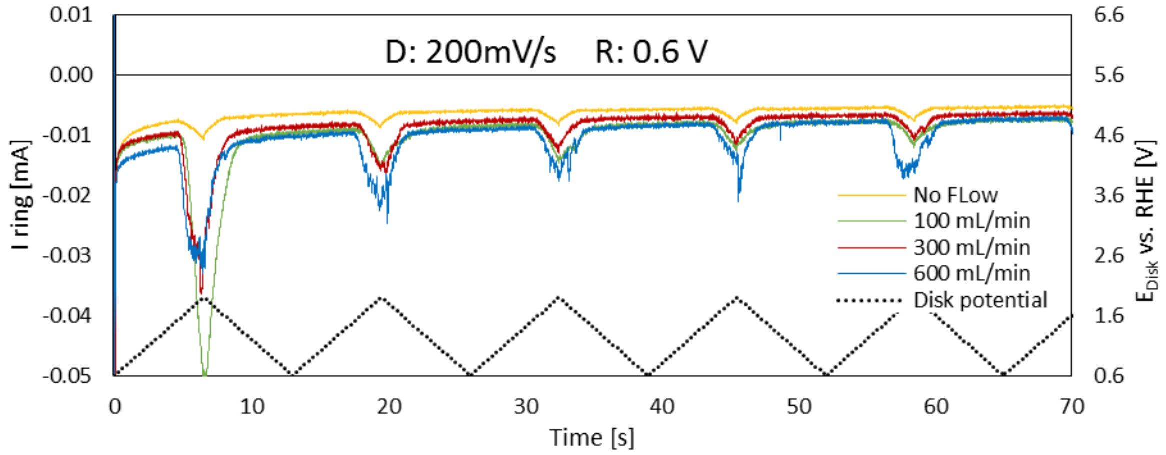

Figure 5-33: Ring current (full line, left axis) and disk potential (stippled line, right axis) as a function of time when the platinum ring is held at 0.6 V while the IrO_2 coated disk is cycled between 0.6 V and 1.9 V at 200 mV/s. The ring currents at four different electrolyte flow rates are shown (0, 100, 300 and 600 mL/min). These are raw data, and are not normalised or adjusted for background current.

The same experiments as above were in addition performed with the ring electrode potential at 1.2 V instead of 0.6 V. The recorded currents from these measurements are given in Figure 5-34, for a disk scan rate of a) 200 mV/s and b) 100 mV/s. The detected ring currents are qualitatively similar to the currents detected at the gold ring at 0.6 V. Reduction at the ring coincides with the OER at the disk at the positive scan, and the oxidation current at the ring is observed on the reverse sweep at the disk. No effect of varying the electrolyte flow rate can be seen, as all four ring current curves overlap quite well. Again it is observed that the normalised ring current decreases as the disk scan rate is reduced.

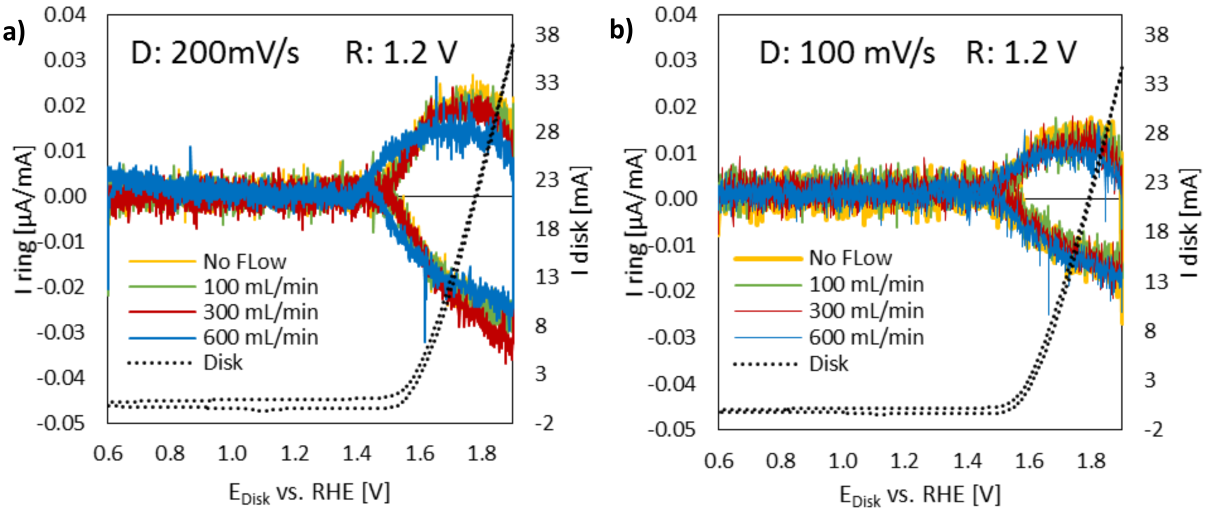

Figure 5-34: Ring current (full line, left axis) and disk current (stippled lines, right axis) as a function of disk potential when the platinum ring is held at 1.2 V while the IrO_2 coated disk is cycled between 0.6 V and 1.9 V at a) 200 mV/s and b) 100 mV/s. The ring currents at four different electrolyte flow rates are shown (0, 100, 300 and 600 mL/min). Only on disk current is included in each figure, i.e. at no flow. Ring currents are normalised with respect to the peak disk current, and corrected for the background current as described in the text.

Potential step voltammetry was also attempted at the IrO_2 disk in combination with the Pt ring. The disk was stepped between 0.6 V and 1.8 V. Figure 5-35 presents the current responses of the ring when the ring was held at 0.6 V. A background reduction current is observed all the time. However, it is clear that stepping the disk to 1.8 V results in an increased reduction current at the ring. The ring current response is quite noisy when the disk is at 1.8 V. The increased ring current ceases almost instantly when the disk is stepped down to 0.6 V again. However, at the lowest flow rate, 100 mL/min, approximately a second passes until the reduction current is down at the background current level again.

Figure 5-36 presents the ring current response when the ring was held at 1.2 V. Only a few micro amperes separate the ring current when the disk is at 0.6 V vs. 1.8 V. There seems to be a constant background current at the ring. If it is assumed that this current equals zero when disk is held at 0.6 V, a small reduction can perhaps be detected when the disk is at 1.8 V. However, the difference at the ring is very small when the disk is at 0.6 V vs. 1.8 V.

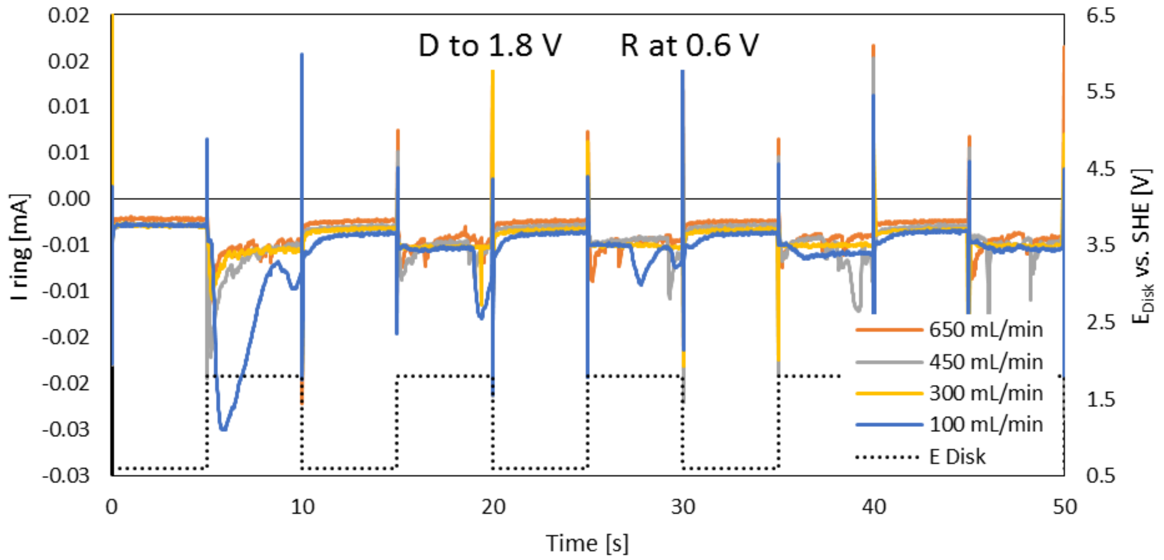

Figure 5-35: Current response at the Pt ring when the ring was held at 0.6 V while the disk was stepped between 0.6 V and 1.8 V. The different colours correspond to different electrolyte flow rates. The black stippled line shows the disk potential. The electrolyte was 0.5 M H_2SO_4.

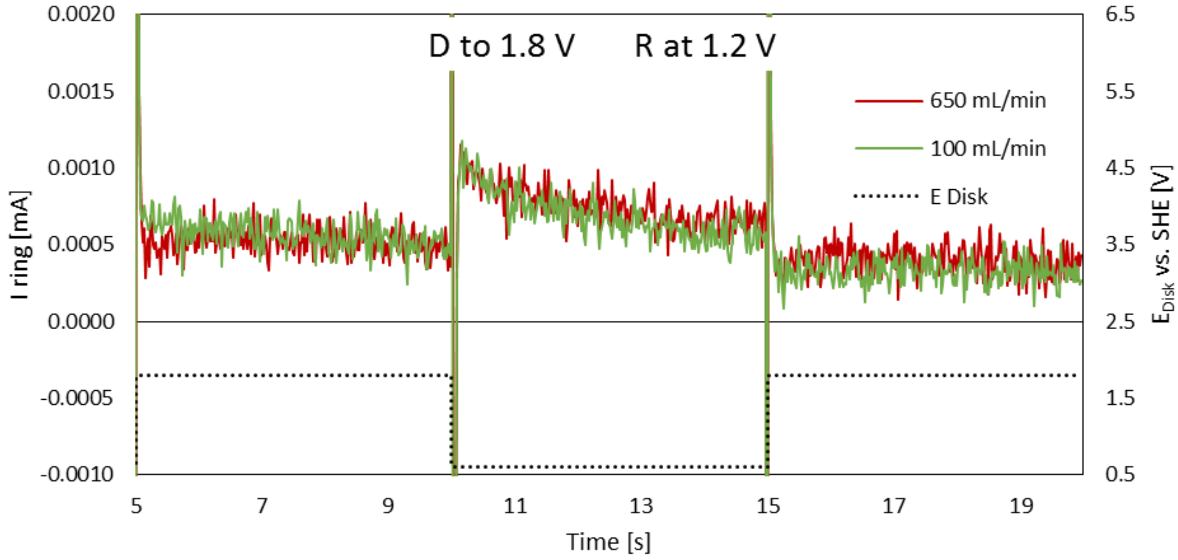

Figure 5-36: Current response from Pt ring held at 1.2 V while the IrO_2 coated disk was stepped between 0.6 and 1.8 V in 0.5 M H_2SO_4. The two different curves are recorded at 650 mL/min (red) and 100 mL/min (green). The black stippled line shows the potential at the electrode.

Varying the electrolyte flow rate (RRDE rotational speed) in the conventional RRDE set-up

An IrO_2 coated disk electrode in combination with a Pt ring were tested in a conventional RRDE set-up, with the ring held at both 0.6 V and 1.2 V while the disk potential was scanned up and down. The results from these experiments are given in this section.

Due to the large variation in ring current from cycle to cycle, it was found to be more convenient to present the ring and disk currents as functions of time, thus allowing more than one cycle to be shown. The disk current is also included as stippled lines, since the ring currents cannot be normalised when more than one cycle is included.

Figure 5-37 shows ring currents (full lines, left axis) and disk currents (stippled lines, right axis) as a function of time when the platinum ring is held at 0.6 V while the IrO_2 coated disk is cycled between 0.6 V and 1.9 V at a) 200 mV/s and b) 100 mV/s. The ring currents at four different RRDE rotational speeds are shown (0, 500, 1000 and 2000 rpm). These are raw data, and are not normalised or adjusted for background current. Similar to the flow cell, only reduction currents are observed when the electrode is rotated. However, at no rotation, the reduction current at the ring is much smaller than the reduction currents obtained in the flow cell. There is also possibly a net oxidation current at the ring as the disk is swept in the negative direction. This is perhaps more evident in figure b), and also in Figure 5-38, which shows the ring and disk currents for the same experiments, except that the maximum potential of the disk sweep is only 1.7 V.

In Figure 5-38 the reduction peak at the peak disk potential is much smaller than when the disk was cycled up to 1.9 V. In addition, another reduction peak can be observed further down the reverse scan. There is much less noise in this figure compared to cycling to 1.9 V, and it is possible to distinguish a slight shift of the reduction peaks towards later times for 1000 rpm vs. 2000 rpm.

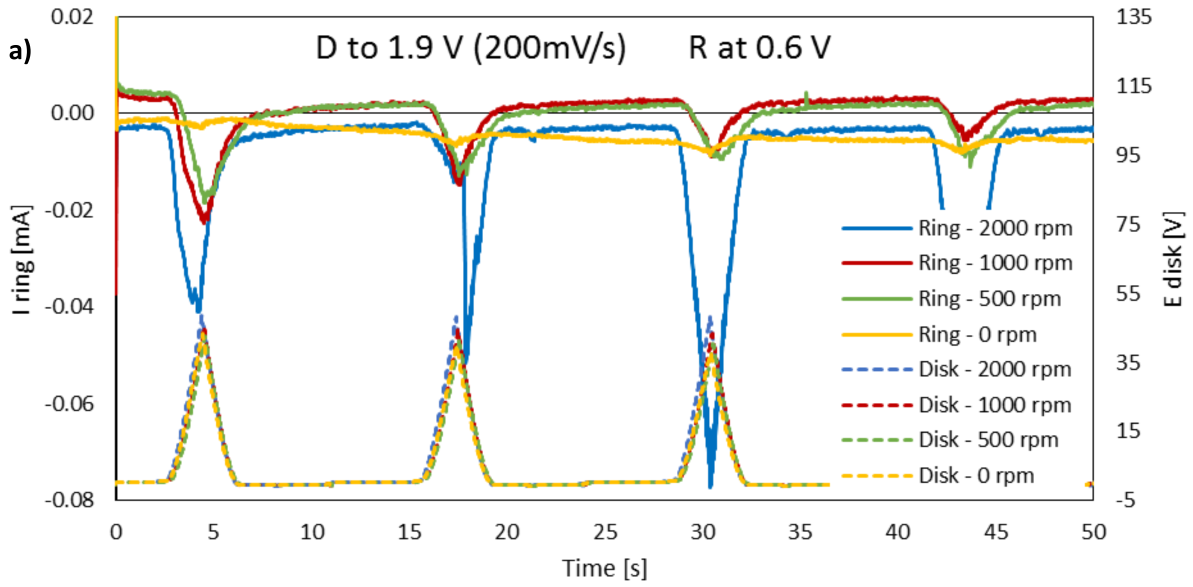

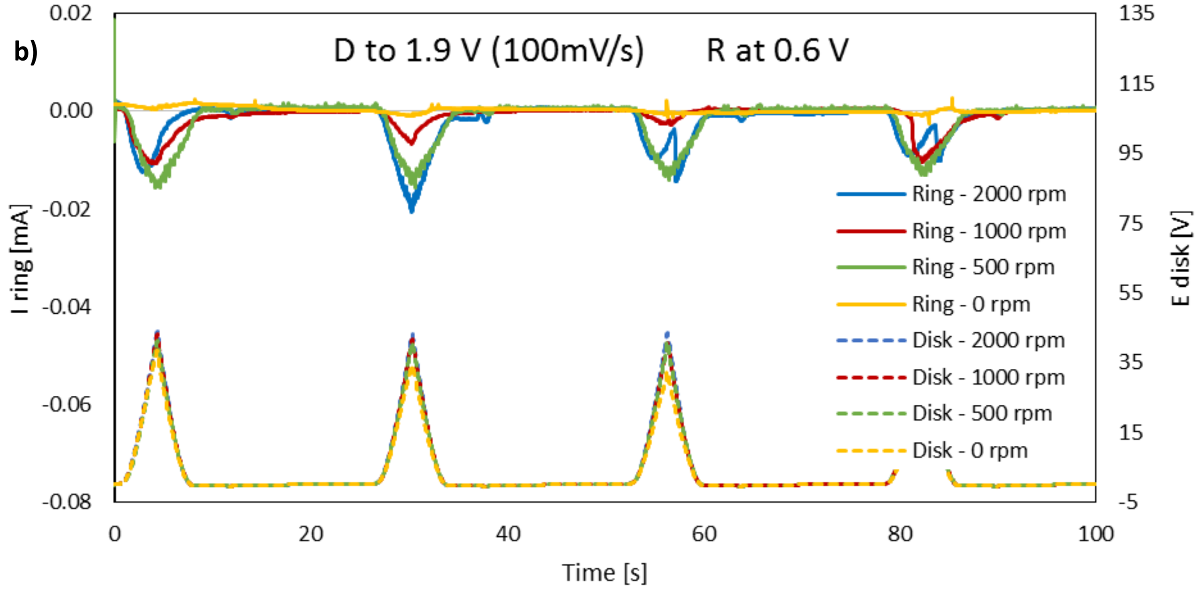

Figure 5-37: Ring currents (full lines, left axis) and disk currents (stippled lines, right axis) as a function of time when the platinum ring is held at 0.6 V while the IrO_2 coated disk is cycled between 0.6 V and 1.9 V at a) 200 mV/s and b) 100 mV/s. The ring currents at four different RRDE rotational speeds are shown (0, 500, 1000 and 2000 rpm). These are raw data, and are not normalised or adjusted for background current.

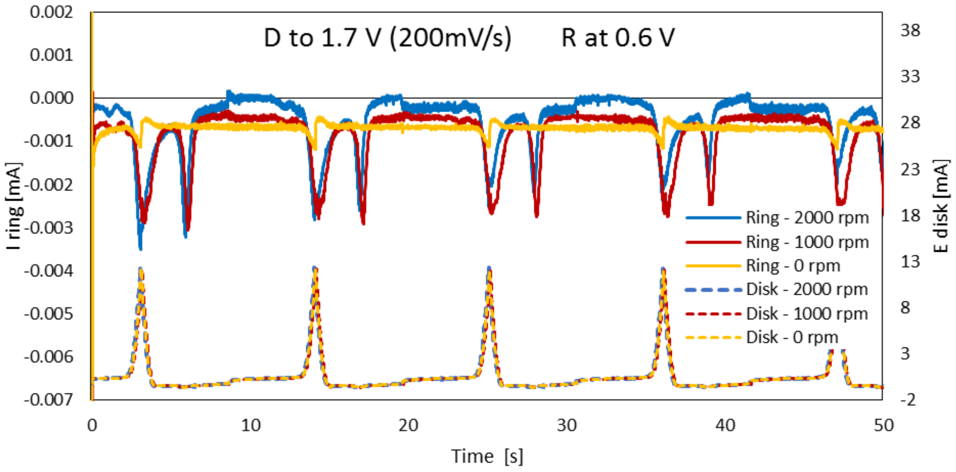

Figure 5-38: Ring currents (full lines, left axis) and disk currents (stippled lines, right axis) as a function of time when the platinum ring is held at 0.6 V while the IrO_2 coated disk is cycled between 0.6 V and 1.7 V at a) 200 mV/s. The ring currents at four different RRDE rotational speeds are shown (0, 500, 1000 and 2000 rpm). These are raw data, and are not normalised or adjusted for background current.

Figure 5-39 shows the ring currents at different electrode rotation rates (full lines, left axis) as a function of time when the Pt ring was held at 1.2 V while the IrO_2 coated disk is cycled between 0.6 V and 1.8 V at 200 mV/s. In figure a), the raw data is presented, whereas the currents in b) and c) are adjusted for background currents to allow for easier comparison. As is apparent from the figure a), a significant offset is present in the current values. No systematic variations with any of the parameters of the experiment could be found, and the variations are believed to be due to artefacts associated with the instrumentation. Two different attempts of an interpretation of the figures were therefore performed. The feature marked “Feature X” in figure a) is the feature that is always observed at the Pt ring at 1.2 V when there is no electrolyte flow. It consists of a small downwards peak at the ring at the positive scan of the disk that is followed by a sudden shift to an upwards peak when the disk potential scan is reversed. This feature proved to be flow-independent, and it is therefore assumed that it is most likely an artefact related to the instrumentation.

In the first attempt of an interpretation of the ring currents observed in figure a) it is assumed that the current related to “Feature X” balances out around zero. Shifting all the currents so that it does gives the currents presented in Figure 5-39 b). With these assumptions and additionally assuming that the baseline current at 0 rpm is equal to zero, it is possible to distinguish an oxidation current at the ring after “Feature X” has occurred. This oxidation is observed when the rotational speed is 300 rpm or higher. At 300 and 800 rpm, is seems like this current is occurring instantaneously after the feature, whereas there is some time before this oxidation is observed at the ring when a rotation rate of 300 rpm is employed. The currents are, however very small. This assumption is also used for interpretation of curves later in the results section and will then be referred to as “Assumption 1”.

The other attempt at an interpretation was to assume that ring currents were zero at the lower disk potentials. Figure 5-39 c) displays the ring currents correspondingly shifted. With this assumption, the observed reduction peaks are slightly larger for higher rotational speeds. Perhaps some small changes can also be observed for the size of the oxidation peak. This assumption is also used for interpretation of curves later in the results section and will then be referred to as “Assumption 2”.

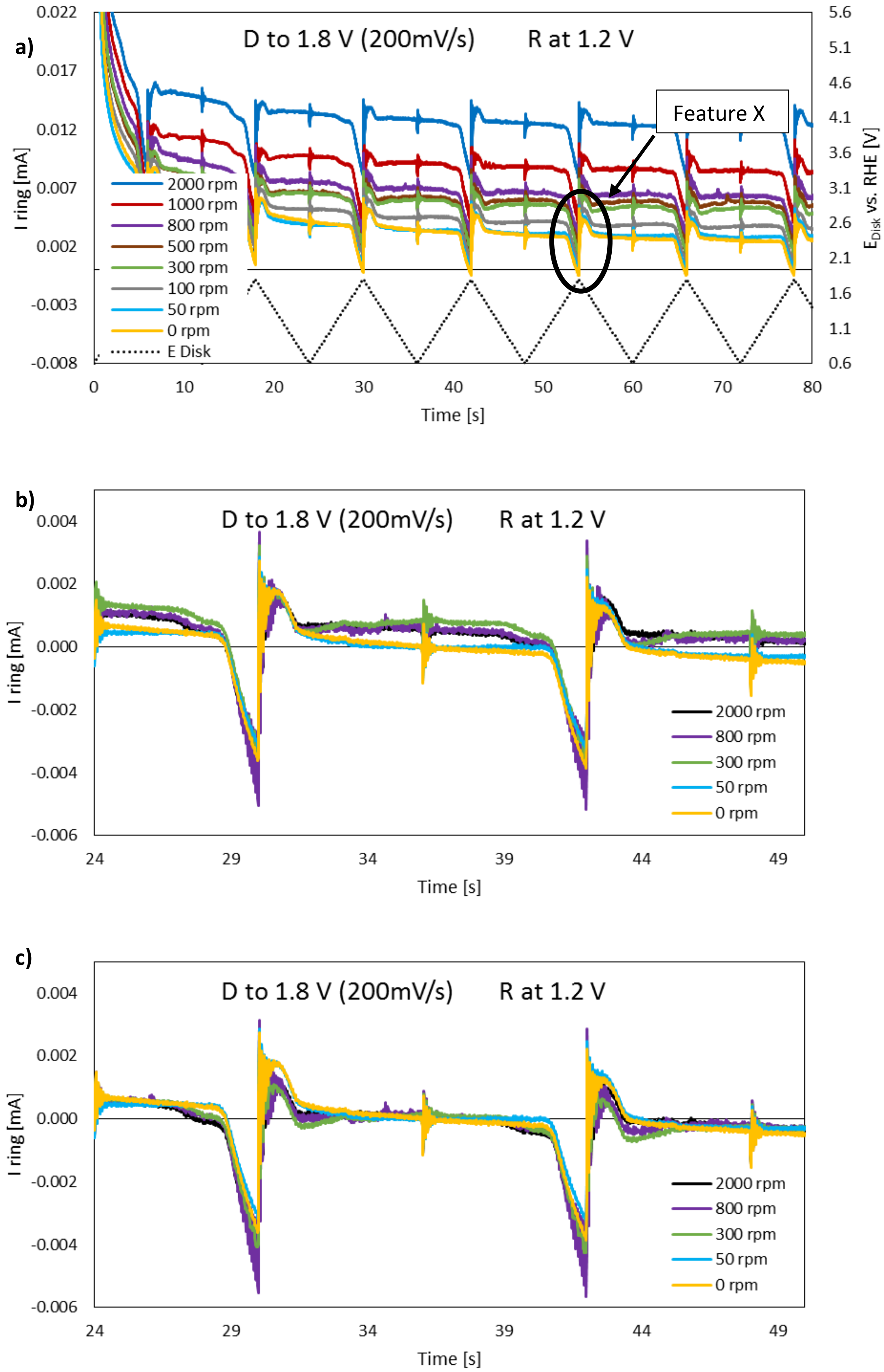

Figure 5-39: Ring currents (full lines, left axis) and disk potential (stippled line, right axis) as a function of time when the platinum ring is held at 1.2 V while the IrO_2 coated disk is cycled between 0.6 V and 1.8 V at 200 mV/s. a) The raw data ring currents at eight different RRDE rotational speeds are shown (from 0 rpm to 2000 rpm). b) and c) show two different attempts at background correction of the currents obtained at five selected rotational speeds.

IrO_2 at the ring and Pt disk

An experiment where the role of the ring and the disk were exchanged was also carried out, in order to reverse the electrolyte flow compared to the usual experimental procedure. The ring was coated with the catalyst and cycled between 0.6 and 1.9 V, while a Pt disk was held at a constant potential throughout the experiment.

The currents detected at the disk held constant at 1.2 V at 500 rpm and 1000 rpm (full lines, left axis) are given as a function of time in Figure 5-40, along with the potential at the ring as a function of time. Compared to the corresponding experiments with catalyst on the disk and by-product detection on the ring (Figure 5-34), the cathodic and anodic peaks occur at the same time during the cycle and are in the same order of magnitude (a few µA).

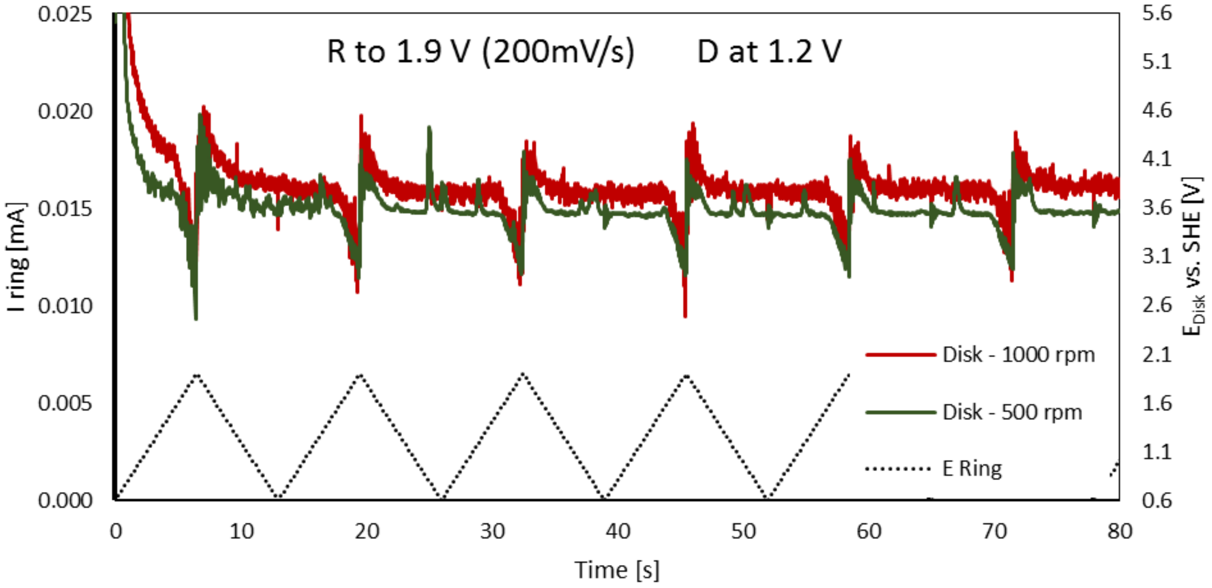

Figure 5-40: Disk currents response over time (full lines, left axis) at 500 and 1000 rpm, when the disk is held at 1.2 V while the ring is cycled between 0.6 V and 1.9 V at 200 mV/s. The ring potential is included as the stippled line (right axis).

5.3.3 IrO_2 disk and Pt ring in 0.5 M Na_2SO_4

The IrO_2 coated disk was cycled in a near neutral solution (0.5 M Na_2SO_4) in combination with the Pt ring in the conventional RRDE set-up. The RRDE was rotated at different speeds to see whether the ring response would be affected by the electrolyte flow rate. As reference electrode, the laboratory made standard hydrogen reference electrode was prepared from 0.5 M H_2SO_4 solution. The liquid junction potential between the reference chamber and the electrolyte was calculated by the Henderson equation to be ca. -30 mV, using the mobilities given in Table 5-13. This is not considered significant in these experiments, as this gives a constant contribution to the potential, and it is the difference between the different electrolyte flow rates that is investigated in these experiments.

In this neutral solution, the onset of the OER is expected to be moved towards lower potentials, as the standard reduction potential of the OER is moved 0.059 mV downwards per pH unit. It was therefore believed to be sufficient to set the highest potential at the disk to 1.7 V vs. SHE.

Table 5-13: Limiting mobilites at infinite dilution for ions involved in the LJP between the WE and RE compartments. [92]

Ion	Limiting mobility [m^2/Vs]
H^+	$3.62 \cdot 10^{-7}$
Na^+	$5.19 \cdot 10^{-8}$
SO_4^{2-}	$8.29 \cdot 10^{-8}$

The recorded ring currents (full lines) and disk current (stippled line) when the IrO_2 coated disk was cycled between 0.6 V and 1.7 V while the ring was held at 0.6 V are given in Figure 5-41. The electrode was rotated at 300, 500, 1000 and 2000 rpm, and in addition the experiment was repeated with no rotation. For all the experiments with rotation, only reduction currents are observed. The onset of the reduction coincides with the onset of the OER at the disk. The reductions cease faster for the two highest rotational speeds compared to the two lowest. The peak value is shifted towards later times for lower rotational speeds. The size of the reduction peaks does not seem to vary systematically with rotational speed.

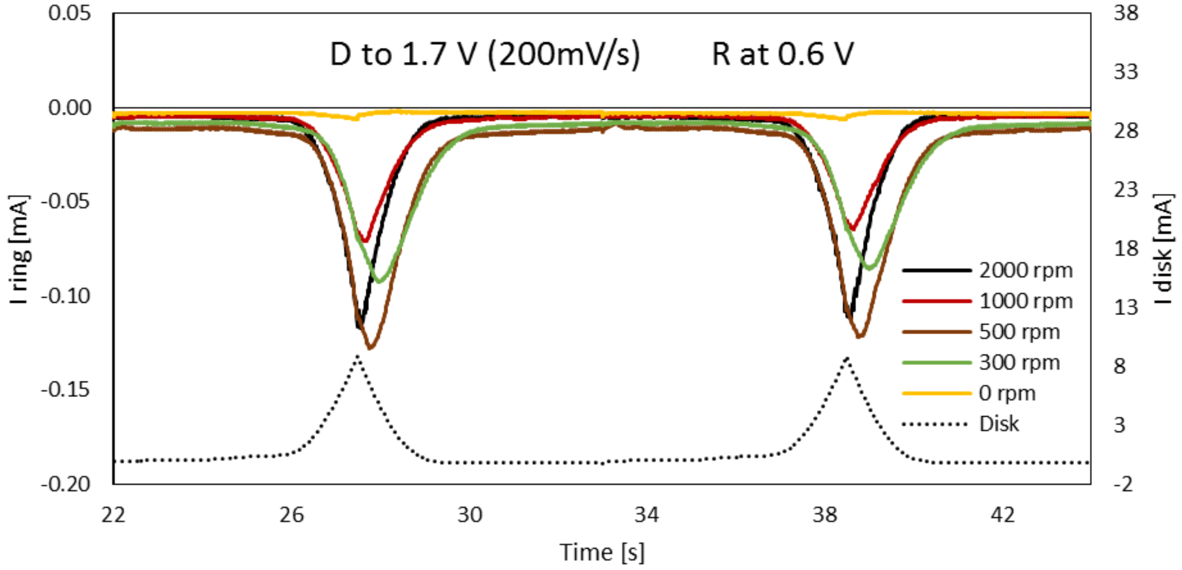

Figure 5-41: Ring current (full lines, left axis) detected at a Pt ring electrode surrounding an IrO_2 coated disk electrode in 0.5 M Na_2SO_4, as the disk was cycled between 0.6 V and 1.7 V while the ring was held constantly at 0.6 V. The different coloured curves represent different electrode rotational speeds. The disk current response is included as the stippled line (right axis).

The ring current detected at 0 rpm is given separately in Figure 5-42. From this figure it can be seen that this curve bears similarities to the ring current detected at the Pt ring at 1.2 V in the sulphuric acid solution (Figure 5-39).

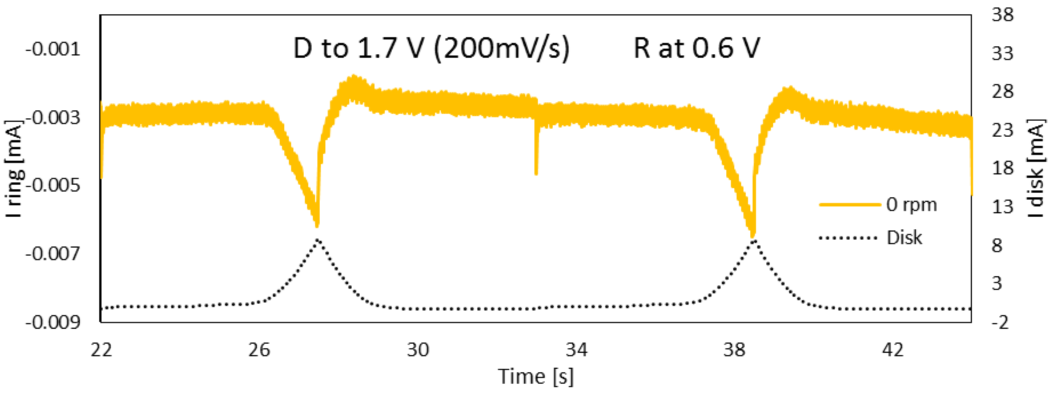

Figure 5-42: Ring current (left axis) detected at a stagnant Pt ring electrode surrounding an IrO_2 coated disk electrode in 0.5 M Na_2SO_4, as the disk was cycled between 0.6 V and 1.7 V while the ring was held constantly at 0.6 V. The disk current response is included as the stippled line (right axis).

Figure 5-43 shows the ring current (left axis) and the disk current (right axis) as a function of time when the disk is cycled at 200 mV/s between 0.6 V and 1.7 V while the ring was held at 1.2 V. The different curves represent different rotational speed of the RRDE, from 0 rpm to 2000 rpm.

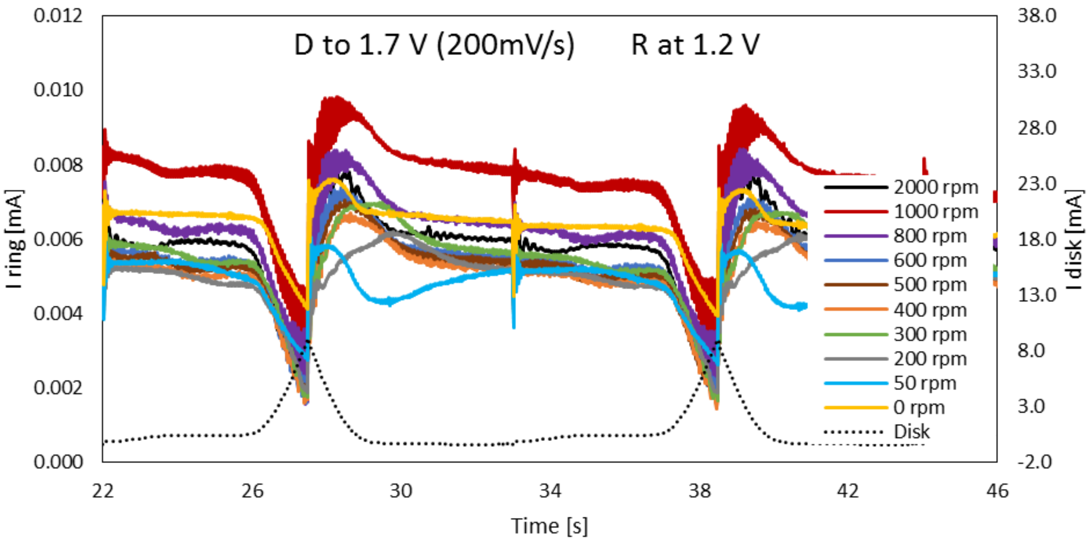

Figure 5-43: Ring current (full lines, left axis) detected at a Pt ring electrode surrounding an IrO_2 coated disk electrode in 0.5 M Na_2SO_4, as the disk was cycled between 0.6 V and 1.7 V while the ring was held constantly at 1.2 V. The different coloured curves represent different electrode rotational speeds. The disk current response is included as the stippled line (right axis).

In Figure 5-44 "Assumption 1" as explained above is used to correct for the background currents observed in Figure 5-43. The currents detected at the five slowest rotational speeds (0, 50, 200, 300 and 500 rpm) are compared in Figure 5-44 a. The main difference between the different rotations is observed as the disk is scanned in the negative direction. For the currents recorded at 200, 300 and 500 rpm, the oxidation peak is shifted towards later times and the peak current is reduced for lower rotation rates. At 0 rpm, the ring response is very similar to, and in the same order of magnitude as, the ring current detected in H_2SO_4 at a Pt ring at 1.2 V, as well as to the ring current detected at the Pt electrode at 0.6 V in the Na_2SO_4 solution at 0 rpm. The ring current at 50 rpm shows a similar potentiostat feature as the current obtained at 0 rpm. However, after a couple of seconds a net reduction is observed before the current again starts to increase.

The currents recorded at higher rotational speeds (500, 800, 1000 and 2000 rpm) are compared with the ring current at 0 rpm in Figure 5-44 b. Here it can be seen that higher rotational rates results in higher oxidation currents, and that the oxidation currents at 800 rpm to 2000 rpm are equal in size. Further, is seems like the oxidation current endures for the entire cycle of the disk.

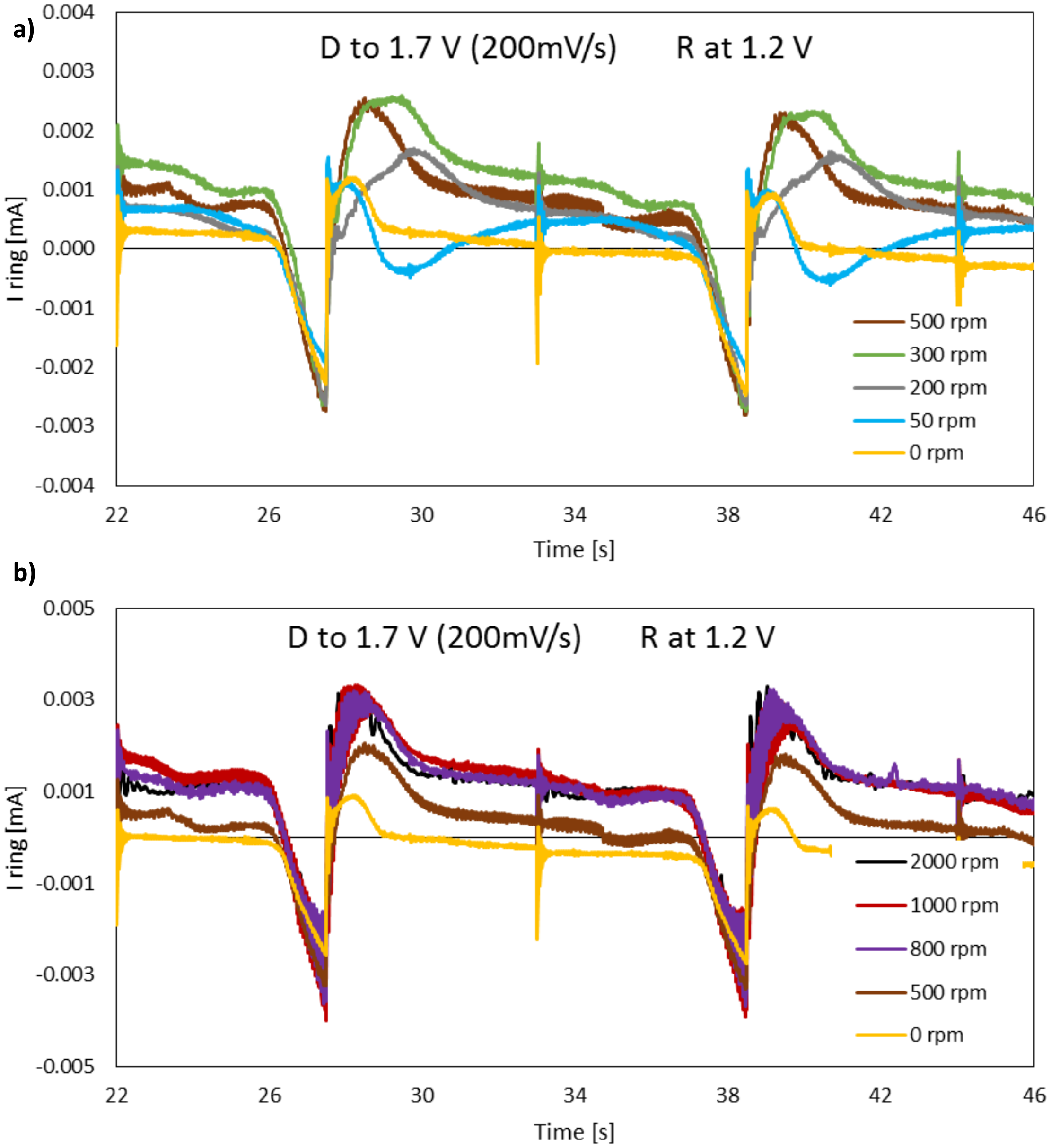

Figure 5-44: Current response at the Pt ring electrode held at 1.2 V while the IrO_2 disk was cycled between 0.6 V and 1.7 V in 0.5 M Na_2SO_4. The ring currents are adjusted for background currents by assuming the reduction peak current is equal for all curves. The response at 0, 50, 200, 300 and 500 rpm are presented in a), and the current at 0, 500, 800, 1000 and 2000 rpm are given in b).

In Figure 5-45 "Assumption 2" as explained above, was used to interpret the ring currents of Figure 5-43. Using this interpretation, both the reduction peak and following oxidation peak at high disk potentials increase as a function of rotation rate. The curve obtained at 50 rpm seems to exhibit a net reduction current right after the oxidation peak, until it rises to zero again at the lowest disk potential.

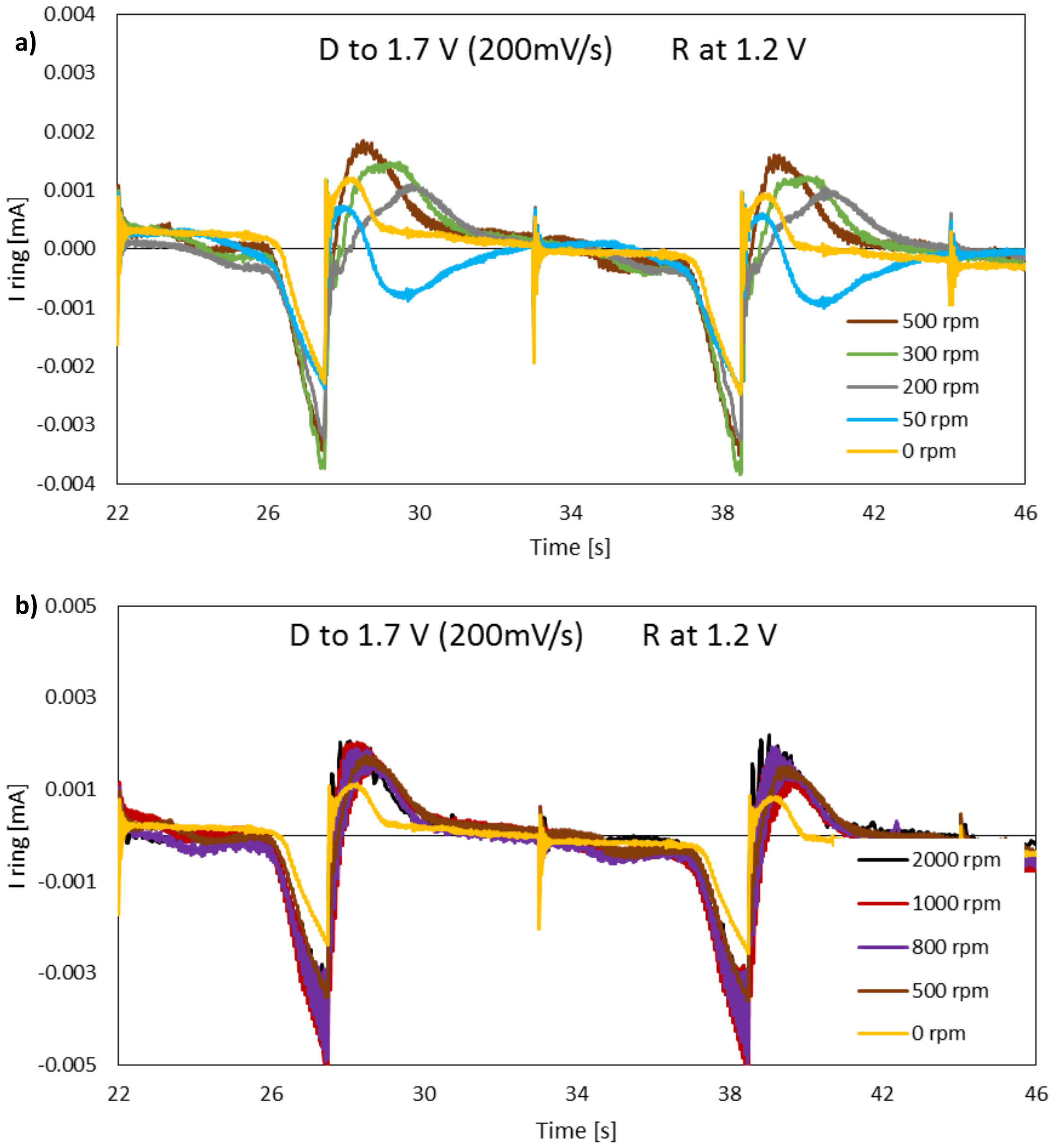

Figure 5-45: Current response at the Pt ring electrode held at 1.2 V while the IrO_2 disk was cycled between 0.6 V and 1.7 V in 0.5 M Na_2SO_4. The ring currents are adjusted for background currents by assuming the current at the ring at low disk potentials is zero. The response at 0, 50, 200, 300 and 500 rpm are presented in a), and the current at 0, 500, 800, 1000 and 2000 rpm are given in b).

Potential step voltammetry was also tested in the 0.5 M Na_2SO_4 electrolyte. In Figure 5-46 is a comparison of the detected ring currents when the IrO_2 coated disk was stepped from 0.6 to 1.7 V while the ring was held constantly at either 1.2 V (blue line) or 0.6 V (red line). The RRDE was rotated at 500 rpm. When the ring was held at 0.6 V, a reduction current could be observed at the ring after ca. 0.2 s. The reduction current at the ring made a positive jump as the disk was stepped down to 0.6 V again, and then decreased gradually. For the ring held at 1.2 V, the observed currents were very close to zero compared with the ring at 0.6 V.

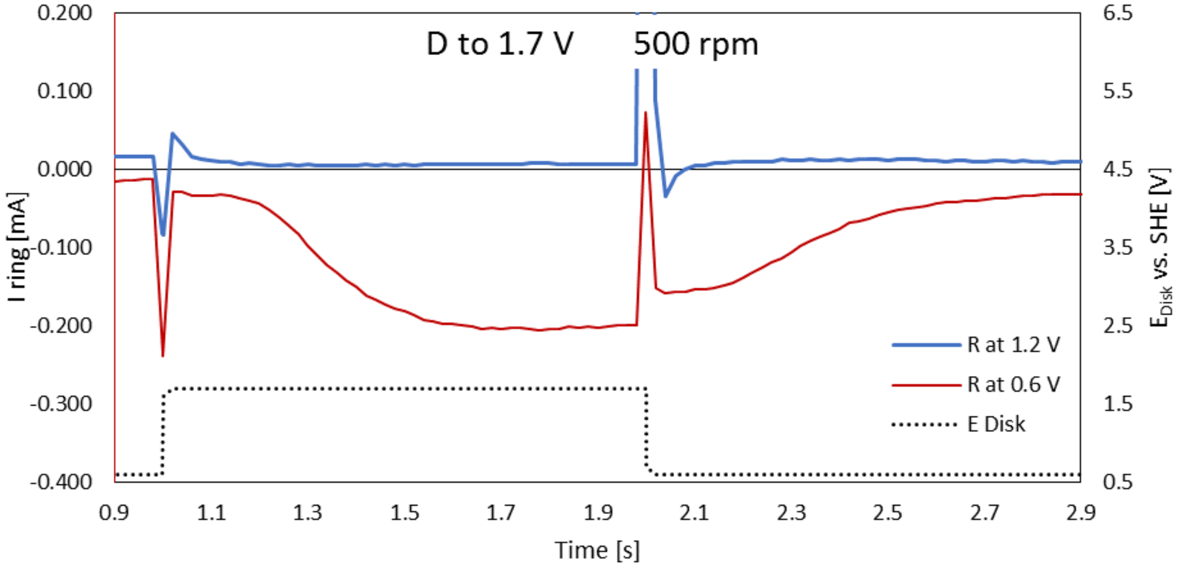

Figure 5-46: Detected ring currents at the Pt ring when the IrO_2 coated disk was stepped from 0.6 V to 1.9 V while the ring was held at 1.2 V (blue line) or 0.6 V (red line). The disk potential is also included as the stippled line.

Potential steps at the disk were performed at different electrode rotational speeds while the Pt ring was kept at 1.2 V. The ring current responses from these experiments are given in Figure 5-47. The potential of the disk is also included in this figure. The disk was stepped between 0.6 and 1.7 V. If the current at the ring is assumed to be equal to the background current when the disk is at 0.6 V (i.e. no reduction or oxidation of by-products), a reduction current is observed at the ring when the disk is at 1.7 V. This only occurs when the electrode is rotated. At 800 rpm, there might also be an oxidation peak observed right after the potential of the disk is stepped down to 0.6 V again.

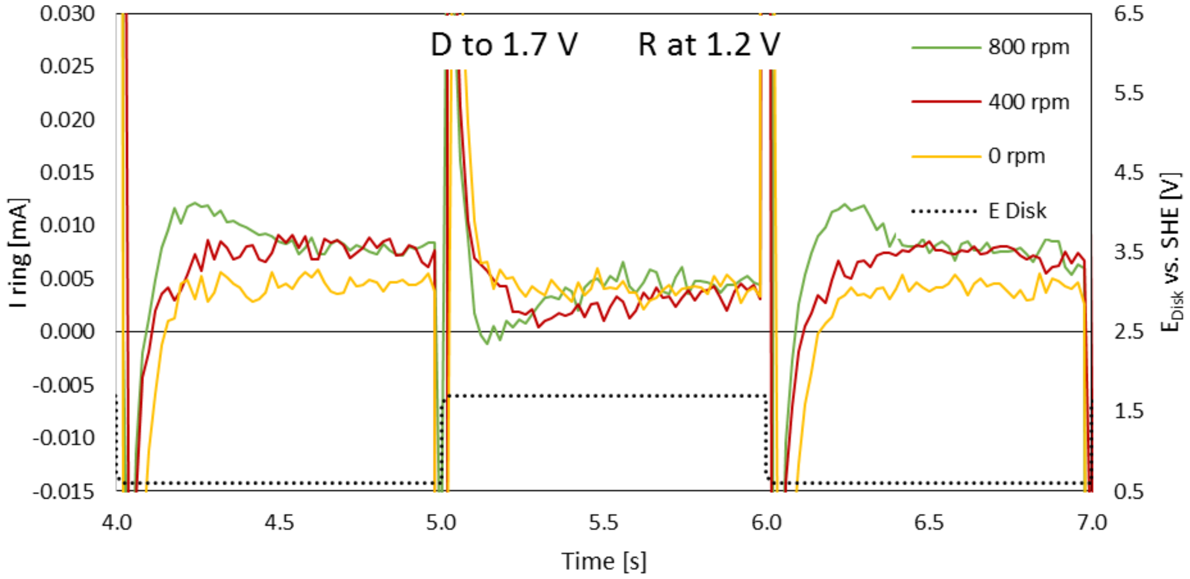

Figure 5-47: Ring current response at different rotational speeds, when the IrO_2 coated disk was stepped from 0.6 to 1.7 V while the ring was held at 1.2 V. Electrolyte: 0.5 M Na_2SO_4. The disk potential is included as the stippled line.

5.3.4 $Ir_{0.6}Ru_{0.4}O_2$ disk and Pt ring in conventional RRDE cell

Cyclic voltammetry at the disk

Experiments with the $Ir_{0.6}Ru_{0.4}O_2$ catalyst on the disk in combination with a Pt ring were performed in the conventional RRDE set-up. The ring current response when it was held at 0.6 V while the disk was cycled between 0.6 V and 1.7 V at 200 mV/s are presented in Figure 5-48. No evident reduction or oxidation current response can be observed at 0 rpm. From 25 rpm to 300 rpm, the peak current increases with increasing rotational speed. This was observed for all cycles. As the rotational speed is increased further, the peak current decreases again. The start of the peak is shifted to later times for lower rotational speeds.

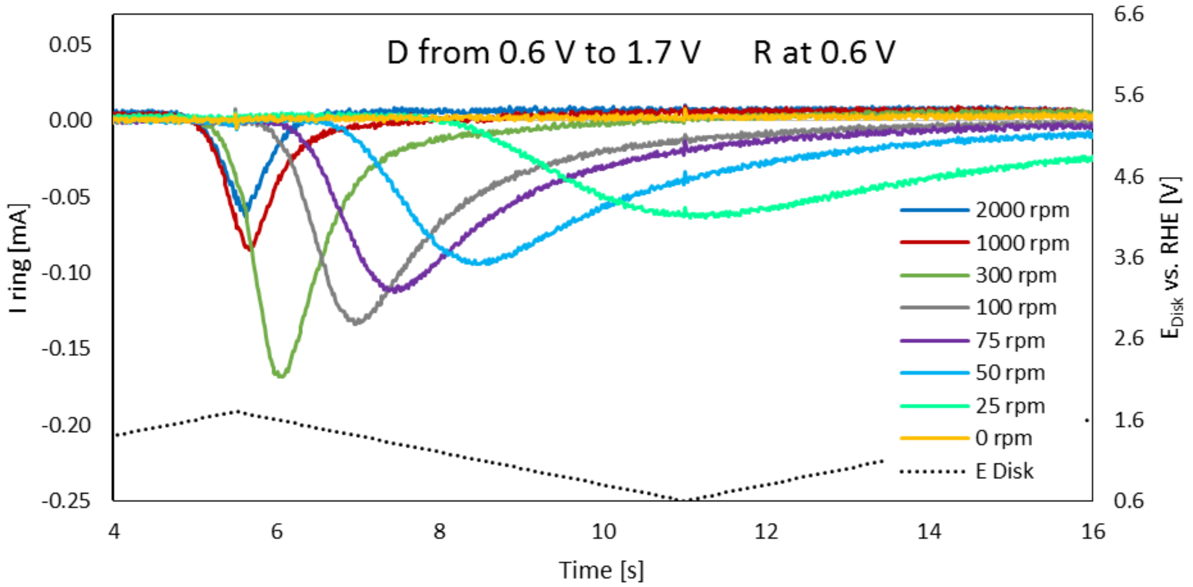

Figure 5-48: Current response at the Pt ring held at 0.6 V while the disk was scanned between 0.6 V and 1.7 V at a rate of 200 mV/s.

The recorded ring currents when the Pt ring was held at 1.2 V while the disk was cycled at 200 mV/s between 0.6 V ant 1.7 V are presented in Figure 5-49. Again, a significant offset is present in the detected currents. In Figure 5-50, the currents are adjusted for this background current by a) applying “Assumption 1”, and b) applying “Assumption 2” as described earlier.

Applying “Assumption 1”, a small reduction current is observed at the top potentials of the disk. When the disk sweep is reversed, oxidation currents occur at the ring. The onset of the oxidation occurs later for lower rotation rates. The oxidation then ceases before the next peak potential of the disk. The ring current obtained at 2000 rpm seems to give a high oxidation current during all the time between the peaks potentials of the disk. At 50 rpm, a net reduction follows “Feature X” and endures for the entire reverse scan of the disk. As the end of the positive disk scan, however, this ring current response is positive.

Applying "Assumption 2", a cathodic ring current commences when the disk is at ca. 1.2 V for high rotation rates. At 50 rpm, the ring current is however positive at the end of the positive scan at the disk. Another dissimilarity with this ring current, is the reduction that commences at the same time as the reduction at the other curves cease.

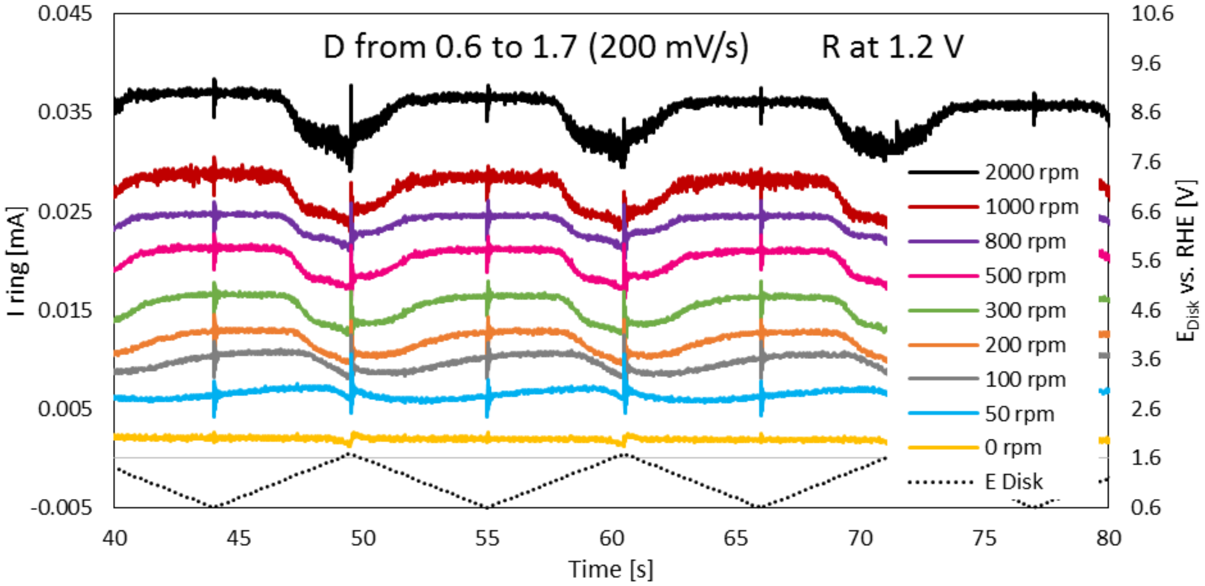

Figure 5-49: Ring current response when the disk coated with $Ir_{0.6}Ru_{0.4}O_2$ was cycled between 0.6 V and 1.7 V. The potential at the disk is included as the stippled line The electrolyte was 0.5 M H_2SO_4.

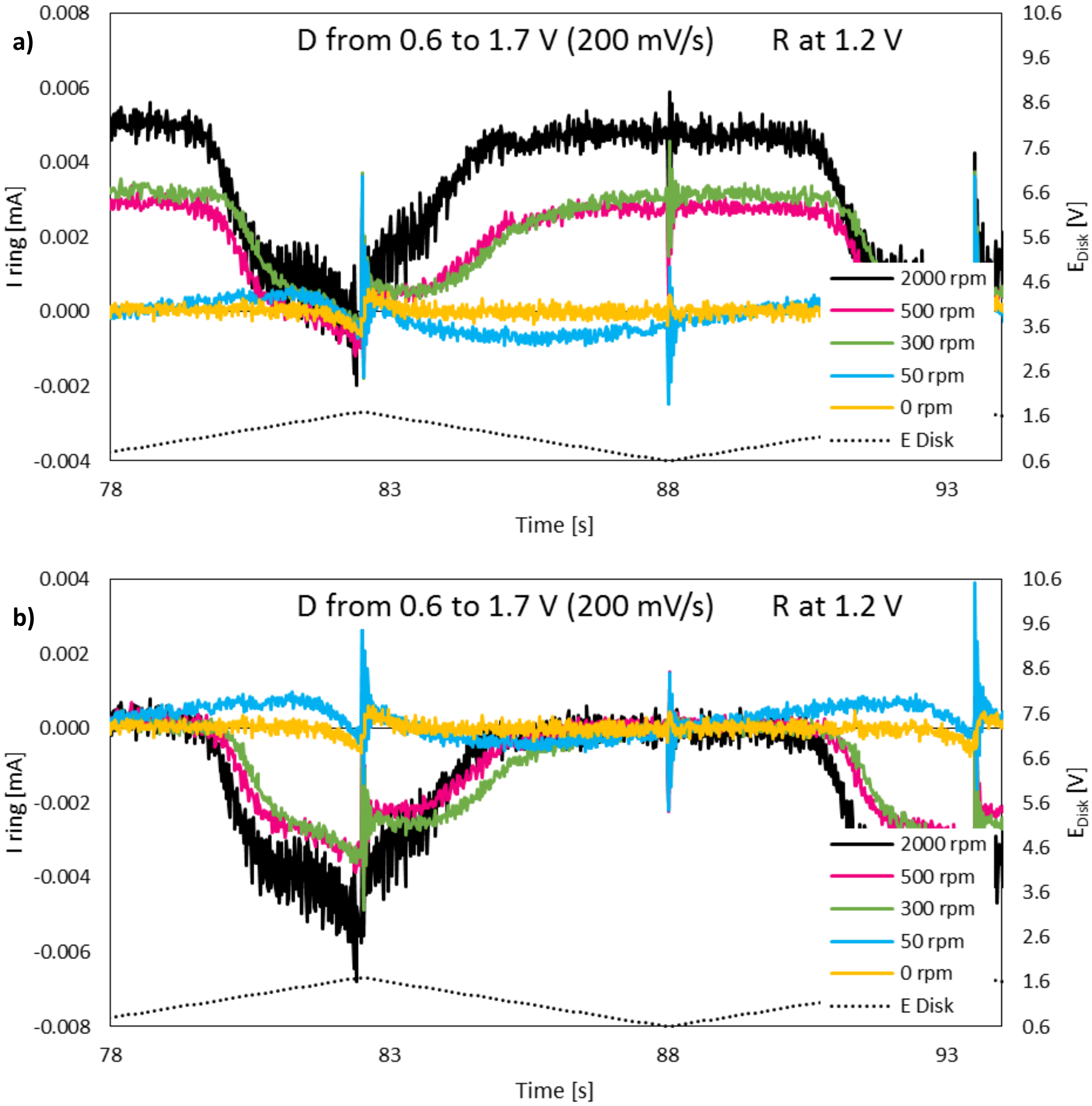

Figure 5-50: Ring current response when the disk coated with $Ir_{0.6}Ru_{0.4}O_2$ is cycled between 0.6 V and 1.7 V. The potential at the disk is included as the stippled line The electrolyte is 0.5 M H_2SO_4. The ring currents are adjusted for background currents by applying a) "Assumption 1" and b) "Assumption 2" as described in the text.

Potential steps at the disk

Potential step measurements at the disk were performed for the disk coated with $Ir_{0.6}Ru_{0.4}O_2$ in combination with the Pt ring. The ring was held at a constant potential of 0.6 V or 1.2 V. The electrolyte flow over the electrode was controlled by rotation of the ring-disk electrode in the conventional RRDE set-up, and the electrolyte was 0.5 M H_2SO_4.

The detected ring currents for the ring held at 0.6 V, at six different rotational speeds are presented in Figure 5-51. When the ring is stepped from 0.6 to 1.7 V, a reduction current is observed for all cases. The reduction is moved towards later times for lower rotational speeds. Some reduction is observed also for the electrode without rotation, but no defined starting point is seen. There seems to be a peak at the beginning of the reduction before the current decrease slightly again.

The transit times for the different electrode rotational speeds, taken as the time from the potential step at the disk and until the reduction starts at the ring, are summarised in Table 5-14. The calculated transit times for oxygen under the same conditions are included in this table for comparison. These values are calculated based on a viscosity of 0.00893 cm^2/s for water and a diffusion coefficient of 2.26 · 10^{-6} cm^2/s for O_2.[92]

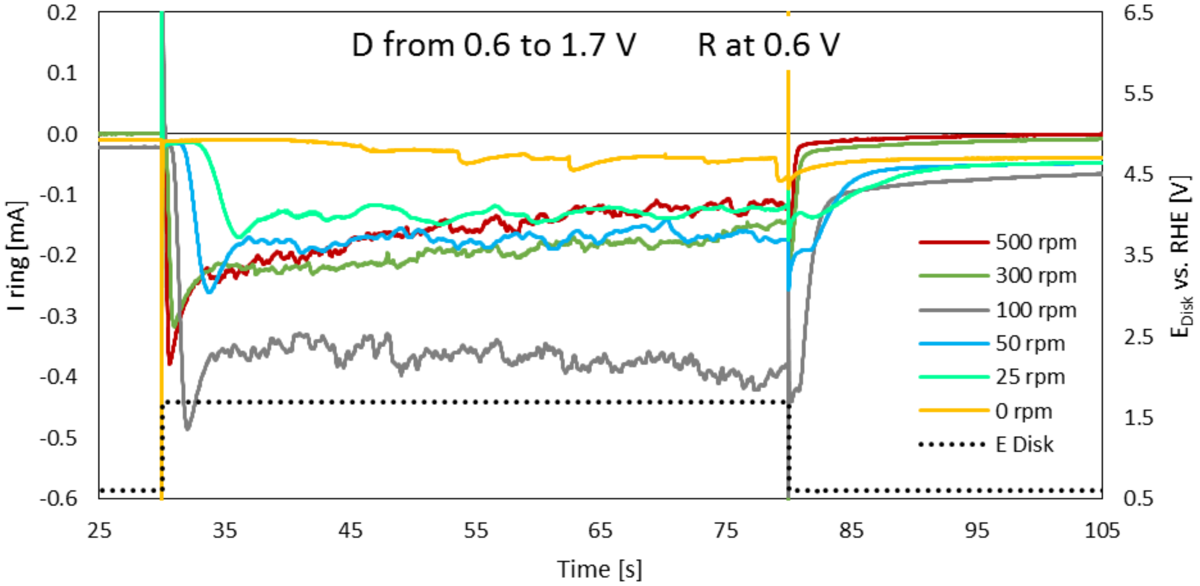

Figure 5-51: Current response at the Pt ring held at 0.6 V while the $Ir_{0.6}Ru_{0.4}O_2$ coated disk was stepped from 0.6 V to 1.7 V in 0.5 M H_2SO_4. The ring current recorded at six different rotational speeds are shown (full lines) in addition to the ring potential (stippled line).

Table 5-14: Calculated transit times for O_2 at the RRDE employed and observed transit times for the RRDE with $Ir_{0.6}Ru_{0.4}O_2$ at the disk and Pt at the ring at different rotational speeds.

Rpm	**500**	**300**	**100**	**50**	**25**
Omega	52.4	31.4	10.5	5.2	2.6
Calculated t' O_2 [s]	0.1	0.2	0.6	1.2	2.4
Observed t' [s]	0.2	0.3	0.6	1.5	3

The ring current response for the corresponding experiments, but with the ring held at 1.2 V, are presented in Figure 5-52. As for the Pt ring at 0.6 V, a reduction is observed shortly after the potential is stepped from 0.6 V to 1.7 V, and it endures until the disk is stepped down to 0.6 V again. The observed reduction current is, however, only ca. five µA for the electrode at 1.2 V, which is only a few percent of the reduction current observed when the electrode was held at 0.6 V.

When the disk is stepped down from 1.7 V to 0.6 V, this is followed by an oxidation peak at the ring. The oxidation peaks recorded after the first potential step from 1.7 V to 0.6 V at the different rotational speeds can be seen in more detail in Figure 5-53. It is clear that the time before the reduction occurs, the transit time, is longer for currents recorded at lower rotational speeds. The reduction current also lasts longer for lower rotational speeds. In general, the peak currents increased for increasing rotational speeds between 10 and 50 rpm. Further increase in the rotational speed resulted in a decrease in peak current again. However, the peak size could change from time to time when the electrode was stepped from 1.7 V to 0.6 V, so the relationship between the sizes of the peaks in these figures are not definite. The transit times observed for the start of the reduction at the ring when the disk is stepped up to 1.7 V, and the times observed for the start of the oxidation on the ring when the disk is stepped down to 0.6 V are summarised in Table 5-15. The calculated values for O_2 at the same electrode is included in the table for comparison.

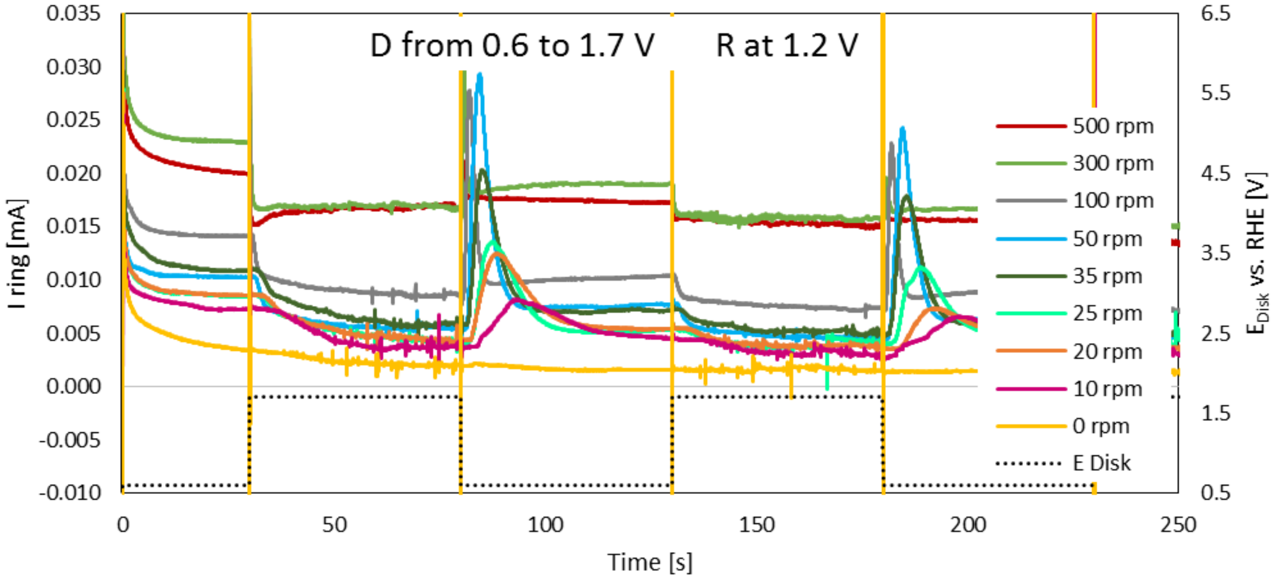

Figure 5-52: Current response at the Pt ring held at 1.2 V while the $Ir_{0.6}Ru_{0.4}O_2$ coated disk was stepped from 0.6 V to 1.7 V in 0.5 M H_2SO_4. The ring current recorded at nine different rotational speeds are shown (full lines) in addition to the ring potential (stippled line).

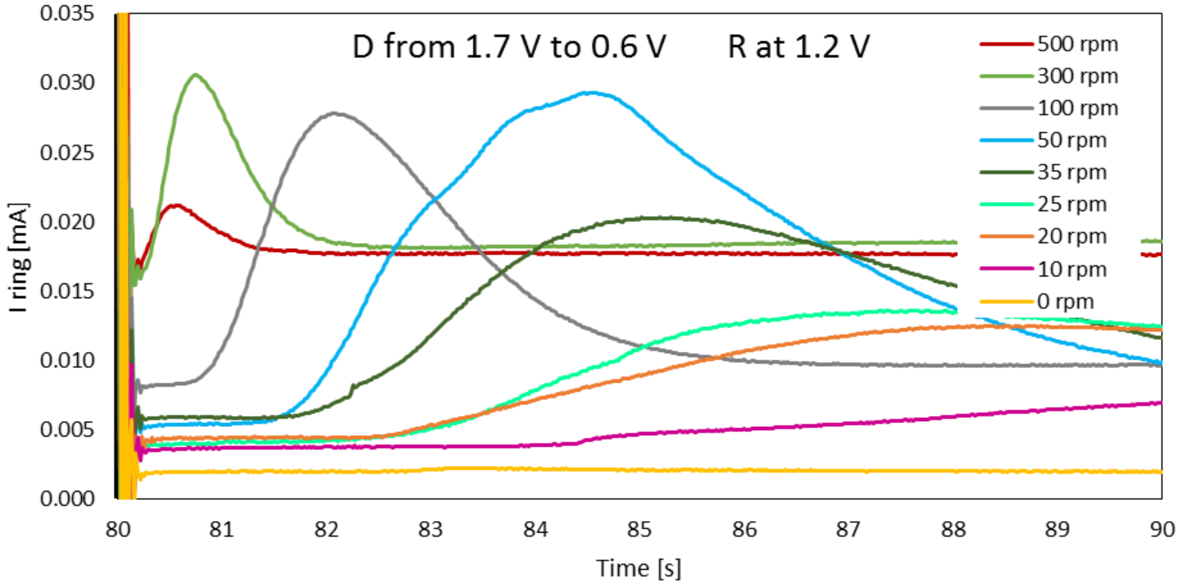

Figure 5-53: Current response at the Pt ring held at 1.2 V while the $Ir_{0.6}Ru_{0.4}O_2$ coated disk was stepped from 1.7 V to 0.6 V in 0.5 M H_2SO_4. The ring current recorded at nine different rotational speeds are shown (full lines). The step at the disk occurs at t = 80 s.

Table 5-15: Observed transit times until the start of reduction and oxidation at the ring as the disk is stepped up to 1.7 V or down to 0.6 V, respectively. The calculated transit time for O_2 is included for comparison with a typical value.

Rpm	**500**	**300**	**100**	**50**	**10**
Calculated t' O_2 [s]	0.1	0.2	0.6	1.2	5.9
Observed t' reduction [s]	< 0.2	< 0.3	0.8	1.8	8
Observed t' oxidation [s]	0.1	0.2	0.8	1.6	4.5

To investigate the observed currents at the potential step voltammetry further, the disk was also stepped between 0.6 V and 1.4 V. The currents recorded at the ring for these experiments at different rotational speeds are given in Figure 5-54. The value axis for the ring current is equal to that in Figure 5-52. The reduction current as the electrode is stepped up to 1.4 V is somewhat smaller than the reduction currents observed when the disk was stepped to 1.7 V. When the disk potential is stepped down to 0.6 V again, no clear oxidation peaks can be seen.

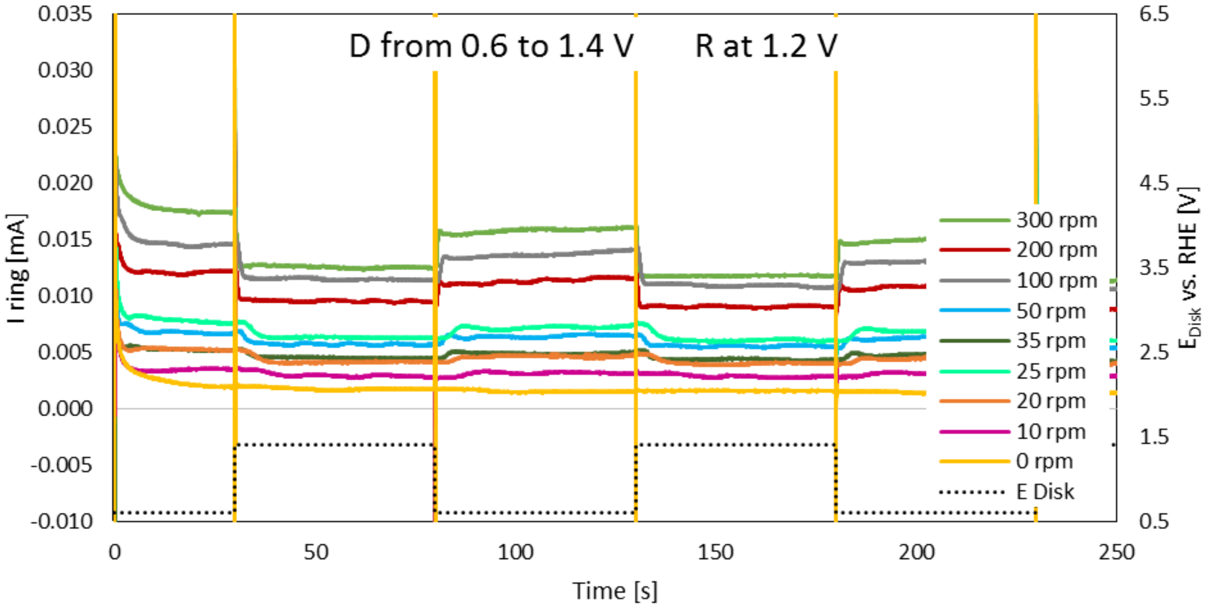

Figure 5-54: Current response at the Pt ring held at 1.2 V while the $Ir_{0.6}Ru_{0.4}O_2$ coated disk was stepped from 0.6 V to 1.4 V in 0.5 M H_2SO_4. The ring current recorded at nine different rotational speeds are shown (full lines) in addition to the ring potential (stippled line).

6 DISCUSSION

In this chapter, the results obtained in this thesis will be discussed. First, the results from the characterisation of the catalysts are discussed as it is relevant for both approaches. Then a separate section is given for the part regarding the determination of Tafel slopes and reaction orders. At last, the results from the ring-disk experiments are discussed and relations between the two sections are considered. The abbreviations Ir60 and Ir30 will be used for the two mixed oxides $Ir_{0.6}Ru_{0.4}O_2$ and $Ir_{0.3}Ru_{0.7}O_2$, respectively.

6.1 CHARACTERISATION OF THE CATALYSTS

6.1.1 XRD of the metal oxides

The XRD patters in Figure 5-1 show that phase pure crystalline IrO_2 and RuO_2 oxides were obtained through the hydrolysis synthesis procedure. The mixed oxides exhibited peak values intermediate of these two pure phases. The mixed oxide containing the highest amount of iridium exhibited peaks closer to IrO_2 than the sample with the least amount of iridium did. Thus, this shows that the bulk composition of the mixed oxides develop as expected with increasing ruthenium content. However, it is not possible to obtain information of the level of mixing or the size of the crystallites from XRD spectra with this resolution. Further, the XRD spectra cannot give information about any surface segregation of one of the components.

6.1.2 Characterisation of the catalysts in 0.5 M H_2SO_4 and 1 M $HClO_4$

The voltammograms in sulphuric acid were normalised with respect to the total surface charge at 350 mV/s instead of the outer surface charge. This was done for all catalyst in this acid since this had been the normalisation procedure for the catalysts characterised in the preliminary project work, and it was preferred to use the same normalisation procedure for all catalysts. The surface charge at 350 mV/s is believed to be related to the surface area, since the scan rate is very high and the surface regions taking part in the proton exchange with the solution will be close to the outer surface charge. The charge at 350 mV/s can thus give some reference point for normalisation. For catalysts where both the outer surface charge and the surface charge at 350 mV/s were calculated, the charges were within 5 % of each other, indicating that this approximation is sufficient for comparing the catalysts at the level done below.

The catalysts were characterised in 0.5 M H_2SO_4 since this is more commonly encountered in the literature for catalysts prepared by similar hydrolysis syntheses. The iridium oxide voltammograms in Figure 5-3 are similar to voltammograms of iridium oxide powders prepared by hydrolysis in the literature.[9, 31, 70] The peaks are broad and located around 0.8 V and 1.2 V. For the mixed catalysts, the extra peak at ca. 0.6 V can be ascribed to ruthenium, which exhibits a peak around these potentials. At 350 mV/s, the current at Ir60 is slightly higher than the current at Ir30 around this peak, contrary to what is expected since the ruthenium associated peak should be more pronounced when the content of ruthenium increases. For the two higher peaks ascribed to iridium, the peak size of Ir60 is smaller than for Ir30. Both these observations means that the oxide containing the least amount of iridium thus resembles the pure IrO_2 more than the mixed oxide containing most iridium. This is further observed in the region below 0.4 V, where the Ir30 and IrO_2 voltammograms are much more similar than the Ir60 voltammogram. This means that the Ir30 sample behaves more like IrO_2 than Ir60 does. However, when the scan rate is decreased to 50 mV/s (Figure 5-3 a), the ruthenium peak in the Ir30 voltammogram is the same size as the peak of Ir60. Since a lower scan rate allows the less accessible surface regions of the oxides to take part in the proton exchange reaction (equation (3-10)), this behaviour can be ascribed to a surface segregation of iridium in the Ir30 sample, which has been found to occur for mixed Ir-Ru oxides prepared by hydrolysis.[31] However, the polarisation curves of the four different oxides (Figure 5-4) show that the OER activity is higher at the Ir30 catalyst than at the Ir60 catalyst both in sulphuric and perchloric acid, and thus that the higher ruthenium content has increased the activity of this catalyst.

The voltammograms obtained in perchloric acid show a larger difference between the three iridium containing oxides than what was observed in the sulphuric acid. The pure iridium oxide voltammogram is very similar to that obtained in sulphuric acid, exhibiting the same peaks and similar currents. Ir60 is similar to IrO_2, but with the extra ruthenium peak as seen also in the sulphuric acid. Further, the highest peak is also shifted to slightly higher potentials. The voltammogram of Ir30 is the one that is most different in perchloric vs. sulphuric acid. The ruthenium peak at 0.6 V is barely distinguishable at 50 mV/s and absent at 350 mV/s. The total charge of the Ir30 voltammogram seems to be unaltered, but a portion of the charge is shifted to higher potentials. A shift of the peaks in the voltammogram for iridium oxides in perchloric contra sulphuric acid has been observed for AIROF electrodes in [66]. The effect was then suggested to be caused by differences in the interaction between the different anions and the bulk of the oxide, causing a change in the intercalation reaction given by equation (3-12). The peak shifts were however, much more prominent for the AIROF electrode, compared to what is observed here. On the other hand, the voltammograms of Ir30 obtained in the perchlorate solutions of higher pH (Figure 5-10) did not show this behaviour and were more similar to the voltammograms obtained in sulphuric acid. Therefore, this behaviour is probably not caused simply by different adsorption of the anions. The origin remains unknown, but is not considered to cause any major influence for the normalisation procedure as it seems like the total charge remains unaltered.

The peaks seen in the pure ruthenium oxide voltammogram are in agreement with voltammograms obtained in sulphuric acid in the literature.[60, 61] The anodic currents at RuO_2 does not increase as much as for IrO_2 with the increase in sweep rate. This might also account for the less distinguishable ruthenium peaks for the mixed oxides when the scan rate is increased.

The polarisation curves in Figure 5-5 show that the activity of the OER increases with the ruthenium content of the oxide in both acids. The sample containing 60 % iridium exhibits an activity closer to RuO_2 than IrO_2 in $HClO_4$, even though the oxide contains more iridium than ruthenium. This might indicate electronic interactions between iridium and ruthenium. However, the actual surface composition of the two mixed oxides is not known, and is expected to influence the activity.[31] The Ir30 catalyst, on the other hand, exhibits an activity closer to Ir60 than RuO_2. The differences in the effect of ruthenium addition to the catalysts on the voltammograms and polarisation curves can be a result of different surface segregation in the two samples. It can also be a result of ruthenium oxide being less stable than iridium oxide, and thus that the ruthenium oxide is less stabilised when the iridium content is low, resulting in more dissolution of the ruthenium on the Ir30 catalyst.

For the three catalysts that were polarised in both acids, the activities at all potentials are higher in perchloric acid than in sulphuric acid. This was also observed for iridium oxide in [66], and can be ascribed to HSO_4^- adsorbing to a higher extent than ClO_4^- and thus blocking active surface sites for intermediates for the OER.

From the voltammograms and polarisation curves obtained in sulphuric and perchloric acid, it is clear that four different oxides of different composition and electrochemical properties has been obtained through the hydrolysis synthesis. As described in section 3.4 the synthesis procedure might affect the electrochemical properties of the oxides significantly. Slight deviations in the synthesis might affect the crystallinity, particle size and surface segregation of the oxides. The surface composition of the mixed oxides was not determined in this work, but from the voltammograms at different sweep rates and the polarisation curves, it is suggested that the extent of iridium surface segregation is higher at Ir30 than Ir60 relative to the nominal iridium composition. Regardless of this, four different catalysts are obtained, and the activity the OER increases as a function of nominal ruthenium content.

6.1.3 Gold background

Cyclic voltammetry and linear sweep voltammetry at the pure gold surfaces showed that the current of the substrate without any catalyst coating was only a few percent of the current observed at the catalyst coating. When the gold is coated, the gold surface will be partly blocked and the contribution from the gold will then be even lower. Evidently, it is acceptable to neglect any contribution from the substrate when analysing the voltammograms of the catalysts. For the polarisation curves, the contribution of the gold substrate was also very small compared to the currents observed at IrO_2, which is the least active catalyst. At the start of the linear region of IrO_2, the current from the gold is about 10 % of the current at IrO_2, and the contribution decreases fast as the potential increases. Again, most of the surface area of the gold surface is blocked by the catalyst coating, and the contribution from the gold substrate to the total current is difficult to predict. However, due to the low current of pure gold and the expected decrease of current at the gold when the catalyst is coated, it is reasonable to neglect the contribution form gold during LSV of the catalysts.

6.2 DETERMINATION OF TAFEL SLOPES AND REACTION ORDERS

The results obtained in relation to determination of Tafel slopes and reaction orders will be discussed in this section. This includes the voltammograms and polarisation curves obtained in the four different pH solutions, the Tafel slopes and reaction orders.

6.2.1 LJP correction

The liquid junction potential was calculated to be less than ± 1 mV for the solutions of pH 1 to 3. This is considered negligible and a correction of the potential in these solutions are not necessary. However, LJP of -16 mV calculated between the solution of pH 0 and the reference chamber is substantial and must be corrected in the presentation of the polarisation curves as this will influence the location of the polarisation curves in relation to each other, and thus the reaction order.

The voltammograms were, however, not corrected with respect to the LJP. A wrong potential in the voltammograms can affect the charge which is later used for normalisation, and can through this affect the reaction order. However, the 16 mV shift does not affect the voltammograms substantially, at least not in the region between 0.4 V and 1.4 V where the charge is evaluated. The peaks observed in the voltammograms are very broad and the exact peak potential is not easy to distinguish. The 16 mV LJP contribution will thus be insignificant when the location of the peak potentials are interpreted. The shift of 16 mV is actually less than the differences observed in the voltammograms from pH to pH and will therefore not be a major source of error in this respect.

6.2.2 Ohmic losses in the electrolytes

The electrolyte resistance values obtained by the ZIR technique were quite high. This can be ascribed to a combination of limitations in the cell design (the electrode shaft hindered the RE capillary tip to be close to the WE) and the considerably reduced electrolyte conductivity as the concentration of the high mobility protons is significantly reduced compared to the pH0 electrolyte. Calculation of the electrolyte resistance values required a value of 170 m^{-1} to be employed as the cell constant. This is a reasonable value for the employed experimental set-up. It is therefore believed that the values obtained by the ZIR technique are reliable, and that the majority of the ohmic contribution was corrected by this procedure. However, as only 85 % of the resistance was corrected for, the contribution of uncorrected resistance is higher in the electrolytes with higher resistivities. This can result in higher Tafel slopes as a function of pH. However, the polarisation curves were also corrected by the post-experimental procedure described in section 3.2.5, which is expected to reduce the effect of these errors. The use of this post-experimental fitting procedure is discussed more thoroughly in section 6.2.5 in relation with the obtained Tafel slopes.

6.2.3 Cyclic voltammograms for the four oxides at different pHs

The anodic part of the voltammograms obtained in the solutions of different pHs are very similar for each material, with two minor exceptions being the Ir60 voltammogram at 350 mV/s in pH 3 and the Ir30 voltammograms obtained in the pH0 solution. The peak potentials shifted as a rule -59 mV per unit increase in pH. This is consistent with the literature for thermally prepared iridium oxides.[71] This relationship indicates that one H^+ is intercalated per electron in the intercalation processes described by equation (3-10), and thus that the anion does not play a significant part in these reactions.[93]

The fact that the voltammograms obtained at different pHs overlap well indicates that the same process is occurring in all solutions, and that the normalisation procedure is valid. The anomalous behaviour of Ir30 in the pH 0 solution was discussed in section 6.1.2, but the reasons for this is not known. However, the total charge of the anodic part of the voltammograms seems to be ca. the same value as for those obtained in the other pH solutions, even though some of the charge is shifted to higher potentials. This is therefore not expected to affect the normalisation procedure to a large extent.

Rotation of the electrodes in the pH 3 solutions

The voltammograms obtained in the solutions of pH 3 were significantly different depending on whether the electrodes were rotated or not, as exemplified by IrO_2 in Figure 5-11. Without rotation, the anodic charge between 0.4 V and 1.4 V was considerably smaller than with rotation. In addition, the peak at 0.8 V was absent. When rotation was employed in combination with nitrogen purging, the anodic part of the curve between 0.4 V and 1.4 V was similar to the curves obtained at the other pHs. As this occurs only for the solution with the highest pH and the charges in this part of the voltammogram are related to exchange of protons with the surface, it is probable that the limited charge in this region is a result of the low proton concentration.

The limiting current of protons (as an electrochemical reactant) can be calculated by equation (3-9). For pH 3 and assuming that the electrode surface area is equal to the geometrical surface area of the disk electrode (d = 5 mm), using a diffusion coefficient of $9.8\cdot10^{-5}\frac{cm^2}{s}$ and a viscosity of $0.45\frac{V}{s}$:[92]

$$I_p = 2.69\cdot10^5 n^{3/2} A D^{1/2} c v^{1/2}$$

$$I_p = 2.69\cdot10^5 1^{\frac{3}{2}}\pi\left(\frac{0.5}{2}\right)^2\left(9.8\cdot10^{-5}\frac{cm^2}{s}\right)^{\frac{1}{2}}\left(10^{-6}\frac{mol}{cm^3}\right)\left(0.45\frac{V}{s}\right)^{\frac{1}{2}} = 0.31\text{ mA}$$

It is evident that the limiting current of protons is in the same order of magnitude as the currents in the voltammograms obtained at 350 mV/s in the pH3 solutions. As seen from this equation, the limiting current of protons increase ten times per unit decrease in pH, and this can explain why this problem occurs only for the solution of pH 3.

At higher pH values, the proton concentration can vary locally within the coating, especially when the electrode is not rotated.[94] As mentioned above, the peak positions observed due to the intercalation reaction (equation (3-9)) depends on pH. The peak potentials of the voltammograms can therefore be distorted by local change of pH within the electrode coating.[94] Furthermore, the pH will change during the potential scan, as protons are inserted or ejected into/from the oxide material. The net result of this effect and the fact that the proton intercalation process is probably mass transport limited in the solution, seem to be (from Figure 5-11) that the intercalation process that is normally observed at 0.8 V is substantially reduced. Thus, the total amount of protons intercalated is decreased, and the anodic charge is reduced correspondingly. At lower potential scan rates, this problem is less pronounced since the currents are smaller, and thus not limited by mass transfer to the same extent. At lower pHs this problem is not observed, as the limiting current is ten times higher.

When the electrode is rotated, the cathodic region of the voltammogram is still distorted. The limiting current of protons for pH 3 and a rotation rate of 1800 rpm is given by the Levich equation:

$$I_L = 0.62 A n F D^{2/3} v^{-1/6} c^{\infty} \omega^{1/2}$$

$$I_L = 0.62\pi\left(\frac{0.5cm}{2}\right)^2\cdot 96485\frac{C}{mol}\left(9.8\cdot10^{-5}\frac{cm^2}{s}\right)^{\frac{2}{3}}\left(0.45\frac{V}{s}\right)^{-\frac{1}{6}}\left(10^{-6}\frac{mol}{cm^3}\right)188^{\frac{1}{2}} = 0.41\text{ mA}$$

This indicates that the proton intercalation reaction might still be mass transport limited during rotation, and can be the cause of the distortion of the cathodic curve of the voltammograms obtained when rotating the electrode. However, the charge is more spread out over a wider potential range, and the total cathodic charge seems to be in the same order of magnitude as the voltammograms obtained in the solutions of lower pHs.

The limiting current of protons observed in the voltammograms at pH 3, may cause a miscalculation of the outer surface charge used for normalisation. However, the problem with mass transport limitation of protons is reduced for lower sweep rates, and it can be seen from Table 5-1 that the outer surface charges calculated with and without the charge form the voltammogram at 350 V/s are very similar. This suggests that the total amount of protons intercalated in the voltammograms at 350 mV/s is at least not far from what would be obtained in solutions without mass transport limitations.

Rotation of the electrode caused the voltammograms to be shifted slightly down in the region below ca. 0.5 V. In this region, the oxygen reduction reaction (ORR) is thermodynamically possible. For IrO_2 nanoparticles prepared by thermal decomposition at 500 °C, ORR has been found to occur at potentials below 0.62 V vs. RHE.[95] Therefore, the ORR is expected to contribute to the shape of the voltammograms in this region, and to be more pronounced when the electrode is rotated since this will increase the limiting current of O_2. The electrolyte was therefore purged with nitrogen, which resulted in a slight upwards shift of this region of the voltammograms. However, the effect of this was lower than expected. This might be because the distortion of the voltammogram in this area was caused by additional processes. This distortion, however, only affected the area used for normalisation slightly, as it occurred below 0.5 V. The voltammograms were improved when the electrolyte was purged with nitrogen, but it cannot be known whether this was sufficient to get the correct charge for normalisation. For Ir60 at 350 mV/s, there still seemed to be some limitations of the charge when the electrode was rotated and the electrolyte purged with N_2. It was thus regarded reasonable to exclude this voltammogram from the normalisation procedure, especially since the outer surface charge with and without this voltammogram was generally found to be similar, as discussed above.

6.2.4 Validity of the normalisation procedure

The correct calculation of the outer surface charge is highly important since this is used for normalisation of the current of the polarisation curves, and thus determines the exact location of the polarisation curves in relation to each other. The reaction order depends on the relative locations of these curves as a function of pH. Therefore, it is important that the outer surface charge does not change as a function of pH.

From the curves of Q vs. $v^{-1/2}$ the linear fit was generally worse for pH 2 and 3 than for pH 0 and 1, as seen by the example in Figure 5-12 b). This can indicate that the normalisation procedure is not ideal for high pHs. This might be an effect of the lower proton concentrations, that might result in more difficulties of intercalation into the less accessible areas (i.e. a lower inner charge), which has been proposed in [62]. However, from Figure 5-12 a) the charges at higher sweep rates at pH 2 does not seem to be affected to the same extent, since this part of the curve follow the same trend as that observed at pH 0 and 1. Therefore, the charge at 350 mV/s can be expected to be more reliable at pH

2. The charge at 350 mV/s is compared with the outer surface charge for IrO_2 in Table 5-1, and it can be seen that the difference between these values obtained at pH 0 to 2 is very small for all these solutions. This suggests that the Q_S values obtained in these solutions are valid for normalisation.

The surface charges obtained in solutions of pH 3 are, however, still questionable. This is probably related to the currents approaching the value of the mass limited current of protons as discussed in the previous section.

It should be stressed that a new coating was used for each catalyst at each pH. The catalyst loading will therefore probably be different from pH to pH in Figure 5-12, and only the quantitative behaviour of the curves at each pH can be compared, and not the quantitative charge values. However, the effect of pH is not expected to be very high for solutions with pH between 0 and 3, as the difference between pH 0 and pH 14 has been found to be only 25 %.[62] This is an extreme case, as the intercalation reaction in alkaline solution requires intercalation of OH^-, which has a much lower mobility than H^+. The 25 % difference at pH 0 and 14 applies only when there is no mass transport limitations from the bulk to the electrode as seen for the solution of pH 3 in this thesis. The conclusion should thus be that the normalisation procedure used in this master thesis is adequate for the solutions of pH 0 to pH 2. For the solution of pH 3, however, the normalisation is questionable due to mass transport limitations. Further evidence of the uncertainties at pH 3 can be seen in Table 5-1 where the total surface charge at 350 mV/s is significantly lower than the outer surface charge for IrO_2 at pH 3.

6.2.5 Polarisation curves of the four oxides in the solutions of pH 0, 1, 2 and 3

The polarisation curves for all four mixed oxides in the different solutions, showed that increased ruthenium content resulted in an increase in activity of the OER at all pHs. This is in accordance with ruthenium oxide being the most active material for the OER, as shown in the volcano plot in Figure 2-3 and by the DFT calculations of Rossmeisl.

The onset potential of the OER on Ir60 is closer to the onset potential at pure ruthenium oxide than pure iridium oxide, which suggest that addition of some ruthenium to the iridium oxide will lowers the activation barrier for the OER more than what is expected by interpolating between the two pure oxide values. This drop in the onset potential for the OER could therefore indicate synergistic interactions between iridium and ruthenium, which has been observed in [6].

The Tafel slopes of all oxides in the solutions of pH 0 to pH 2 was around 40 mV, corresponding to the second step in the mononuclear path being the rds, which is equivalent to the second step in the electrochemical oxide path. These values agrees with values found by [31] for mixed iridium-ruthenium oxides prepared by hydrolysis synthesis and characterised at pH 0, but disagrees with the 60 mV/dec Tafel slope found for thermally prepared IrO2 by [96] and [97] for thermally decomposed iridium and ruthenium precursors. The two latter references also found a gradual increase from 40 mV to 60 mV from pure ruthenium oxide to pure iridium oxide. In general, pure ruthenium oxide exhibited the lowest Tafel slopes in all solutions, followed by pure iridium oxide, whereas the Tafel slopes of the two mixed oxides showed the highest slopes. This trend was also observed for the mixed iridium-ruthenium hydrolysis powder in [31]. The Tafel slopes obtained for all oxides studied in this thesis are in any case quite similar and generally closer to 40 mV than 60 mV or 15 mV, and thus suggests that the same mechanism take place on all oxides. The differences between the Tafel slopes for the different oxides can be explained by different reaction intermediate coverage at the materials.[22] This means that some of the materials adsorb intermediates stronger than others, which is analogous to the materials having different electrocatalytic activities.

For all oxides, the linear region of the polarisation curves, corresponding to Tafel kinetics, was longest in the solutions of high pH, and gradually decreased as the pH increased. This left only a short linear region in the pH 3 solutions. This resulted in a shorter region for fitting by the procedure described in section 3.2.5, and can result in less reliable results for the Tafel slope even though the curves of IR vs. I (as exemplified by Figure 5-22 b) give a linear line through the origin. The resistance values found from the fitting procedure increased when the solution pH increased, and for most oxides the increase was considerably higher from pH 2 to pH 3 than between the other solution pHs. This can also be an indication of a less reliable fit at pH 3.

The higher resistance in the solutions of higher pH is expected since the solution resistance increases as the proton concentration is reduced. This is because only 85 % of the solution resistance could be accounted for by the ZIR method, thus leaving a higher uncorrected resistance contribution in the solutions with initially higher electrolyte resistance. However, the difference in electrolyte resistance decreases as the pH increases due to the logarithmic decrease in proton concentration. This is contrary to the trend observed in the resistance values from the numerical fitting, suggesting that the resistance is not only a result of the electrolyte resistance.

The obtained Tafel slopes also increased consistently from the lowest to the highest pH, with the only exception of Ir30 that exhibited a higher Tafel slope at pH 1 than at pH 2. The increase in the obtained resistance values for higher pHs can be related to the higher Tafel slopes obtained as the solution pH increases. Both phenomena could be ascribed to a more uneven current distribution on the electrode as the conductivity decreases and/or by the fact that the reaction mechanism changes at higher potentials. Both possibilities are discussed further in the following.

On an electrode where the electrode reaction is controlled by Tafel kinetics, the current distribution is generally characterised by a secondary current distribution with concentration variations near the electrode surface.[98] Electrode geometry, the charge transfer overpotential and the electrolyte conductivity are parameters that influence this current distribution. As the conductivity of the electrolyte decreases, the current distribution will be less uniform.[98] The polarisation resistance at the electrode pulls in the other direction, and tries to make the secondary current distribution more uniform. As the overpotential at the electrode is increased, the polarisation resistance decreases, and consequently the current distribution will be more inhomogeneous.[99] A change in the current distribution, and thus the potential distribution, as the overpotential increases will obviously affect the Tafel slopes. In [100] it was found that the Tafel slopes were significantly altered by this phenomenon in solutions of low conductivity, whereas those obtained in higher conductivity electrolytes was not much affected. This higher sensitivity of the Tafel slopes on the inhomogeneous current distribution at high pH might thus offer an explanation to the increase in Tafel slopes as a function of pH, and might also account for the higher resistance values obtained in the numerical fitting to equation (3-17).

An iterative procedure for correcting the Tafel slopes for the problem addressed above has been proposed by Estaban et. al.[100] This is based on the fact that the additional potential drop caused by the more inhomogeneous current distribution is a function of the average current density of the electrode and that it varies radially from the centre of the electrode. However, the current distribution assumed for this correction procedure requires that the electrode is a planar disk. The oxide powder electrode coatings employed in this master thesis cannot be approximated by planar surfaces. The current distribution will therefore vary in each point, and not only radially as a function from the centre of the electrode. The proposed iterative correction procedure is therefore not believed to be appropriate for the electrodes this thesis, and cannot be used here.

The explanation given above ascribes the deviation in Tafel slopes to the increase in electrolyte resistance. This might give a contribution to the increase in Tafel slopes as the pH increases, but again, this does not account for the large jump in Tafel slope values from the solution of pH 2 to pH 3, seeing that the electrolyte resistance changes less from pH 2 to pH3, than between the other solutions.

As the solution pH increases, the length of the linear Tafel region decreases, mainly because the curves start to bend upwards at lower overpotentials for each increase in pH. Some of the curves obtained in the solutions of higher pH might also seem to approach another linear region when the potential is increased sufficiently. However, the LSV is not extended to high enough potentials to see whether this actually occurs. On the other hand, dual Tafel behaviour has been observed on thermally prepared iridium, ruthenium and mixed iridium-ruthenium oxides in sulphuric acid in [97]. The Tafel slope at high potentials was then found to be 120 mV for all oxides and was not affected by pH changes (i.e. a reaction order of 0). However, the transition from the lower to higher Tafel slope region was more marked in this reference. This suggest that the strong bending of the polarisation curves found in this thesis can be caused partly by a transition to a higher Tafel slope (e.g. 120 mV) and partly by resistive effects caused by blocking of the electrode surface due to the vigorous gas bubble evolution at these high potentials. The effect of the increased resistance due to gas bubbles might explain both the slow bending as opposed to a marked transition, and the fact that the curves seems to approach slightly different slopes at high potentials. However, it must be stressed that the data in this thesis is not sufficient to determine Tafel slopes at high overpotentials, and the development at these potentials can only be guessed.

The transition from a low slope Tafel region where the current increases with pH to a higher Tafel slope region where the current is unaffected by pH can offer an explanation as to why the lower Tafel slope region analysed in this thesis is shortened when the pH increases. When the pH is increased the curves in the low potential region will be shifted down, whereas the curves in the high potential region ideally has a fixed location. Thus, the intersection of the two linear regions will occur at lower current values when the pH is increased and the lower Tafel slope region is consequently shortened. This hypothesis can further explain why the polarisation curves obtained at pH 3 was hard to fit to equation (3-17) as well as the high resistance value obtained by this equation at this pH. The fit to equation (3-17) is only valid for compensation of a resistance following Ohm's law. If the bending of the curve is caused by a transition to a higher Tafel slope value, the increased current is clearly not an effect of ohmic resistance. Thus, the fitting procedure is not appropriate in the region when a substantial contribution of the second Tafel slope is significant. This might well be the case for the pH 3 solutions as the bending occurs early and leaves only a short linear region at low overpotentials. The Tafel slopes in the pH 3 solutions might therefore be estimated to too high values in these solutions. The contribution from this error might be problematic in the other solutions as well, but is expected to be less significant as the linear regions in the low Tafel regions are much more extended, making the fitting procedure more reliable.

Dual Tafel slopes with 120 mV at high overvoltages are commonly encountered for the OER at oxide electrodes.[76, 97, 101, 102] A Tafel slope of 120 mV in combination with a reaction order of 0 (i.e. the current is unaffected by the pH) corresponds to the first step of all reaction mechanisms proposed in section 2.2.2 being the rds. A transition from a low to a high Tafel slope can be caused by a change in the reaction step that dominates the reaction rate (rds). This can be ascribed to the potential dependence of the surface coverage of adsorbed intermediates.[97] At higher overpotentials the surface is saturated with regard to adsorbed intermediates. Another rds that occurs on the less active regions of the oxide will thus predominate at higher potentials. This can also explain why the transition from the low to high Tafel slope occurs gradually, since the rds at higher potentials gradually becomes of greater importance as the potential is increased.

From the discussion above it is clear that the Tafel slopes obtained at higher pHs are less reliable than those obtained at lower pHs, and that this applies especially for the solution of pH 3 where the linear Tafel region at low overpotentials is very short. This adds to the uncertainties of the voltammograms obtained in this solution, which might cause a wrong estimation of the active surface area and thus of the electrocatalytic activity. As a consequence of the added sources of error for the solution of pH 3, it was considered that the results obtained when excluding the results from this solution would give more reliable results.

6.2.6 Anodic reaction orders with respect to H^+

The reaction orders obtained from Figure 5-23, which are based on the polarisation curves, varies depending on the potential at which they are obtained. The reaction order decreases consistently with increasing potential. This is caused by the consistent increase in Tafel slopes as a function of pH, causing the polarisation curves to converge towards higher potentials. As discussed above, it is believed most appropriate to exclude the results obtained in the solutions of pH 3. The reaction orders are then found to be approximately -1.5 for the pure iridium and ruthenium oxides, whereas the reaction orders of the mixed oxides are between -1 and -1.5. From Figure 5-23, it can be seen that the curves used for obtaining the reaction orders exhibit a very close to linear behaviour for the three points obtained at pH 0 to 2, and that the point obtained at pH 3 deviates from this line. This clearly demonstrates how the very different results obtained at this pH affects the reaction order.

Due to the uncertainties regarding the increasing Tafel slopes for higher pHs, another approach for finding the reaction order might be used. If the polarisation curves are evaluated against the RHE (Figure 5-18 to Figure 5-21), it can be seen that the curves overlap quite well for the lower potentials of the linear Tafel area. Here, the curves are not yet much affected by the differences in value the Tafel slopes. An overlap of the polarisation curves when plotted vs. RHE corresponds to a reaction order of -1.5 if the Tafel slope is 40 mV. This therefore further indicates that the reaction order is -1.5.

A reaction order of -1.5 in combination with at Tafel slope of 40 mV agrees with that found for thermally prepared RuO_2 in [97, 103]. One of these references [97] also found the reaction order to decrease with addition of iridium to the oxide, similar to what is found in this thesis. However, in this reference, the reaction order of pure IrO_2 was -1, and the intermediate values between -1.5 and -1 could be justified by a combination of iridium and ruthenium oxide sites.

As seen in section 2.2.2 reaction orders should in theory be integer values. However, fractional reaction orders are often encountered for the OER at oxide electrodes.[76, 104] A number of reasons for the fractional reaction orders are given by Carugati et. al.[103] The most encountered explanation is that a fractional reaction order is related to double layer effects caused by the surface charge of the oxides being a function of pH due to the acid-base properties of metal oxide surface in aqueous solutions.[104, 105] Oxide surfaces are high-energy surfaces that interact strongly with water, and become covered by OH groups in aqueous media. These groups behave as weak acids or bases, and acid-base equilibria at the oxide surface give rise to surface charging according to the following reactions:

$$S-OH_2^+ \rightleftharpoons S-OH+H^+$$

Or:

$$S-OH \rightleftharpoons S-O^- + H^+$$

The dissociation of the OH groups is a function of the solution pH. When the reaction order with respect to H^+ is investigated, the proton concentration is necessarily changed, and therefore the free charge of the oxide changes as well. As a consequence, the potential at the reaction site also changes with pH.

For a Tafel slope of ca. 40 mV, the most likely rds is the second step of the electrochemical reaction path (or equivalently the second step of the mononuclear path). If the potential at the reaction site is φ^*, the rate expression for the rds is given by (see section 2.2.2):

$$i_{2,a} \propto a_{OH_{ads}} e^{\frac{\alpha_a F(E-\varphi^*)}{RT}}$$

Where α_a is used instead of $(1-\beta)$.

The reaction site is in this case equal to the adsorption plane, and therefore the potential at the reaction site is given by the potential at the adsorption site. The potential at the adsorption site is further proportional to the pH as a consequence of the acid-base equilibria according to[105]:

$$\varphi^* = \frac{RT}{F} \ln a_{H^+}$$

Inserting this into the equation for the current of the rds:

$$i_{2,a} \propto a_{OH_{ads}} e^{\frac{\alpha_a FE}{RT}} e^{-\frac{\alpha_a F\varphi^*}{RT}} \quad \rightarrow \quad i_{2,a} \propto a_{OH_{ads}} e^{\frac{\alpha_a FE}{RT}} e^{-\frac{\alpha_a FRT}{RT\ F} \ln a_{H^+}}$$

$$i_{2,a} \propto a_{OH_{ads}} e^{\frac{\alpha_a FE}{RT}} a_{H^+}^{-\alpha_a}$$

When step 2 is the rds, it is assumed that step one is in quasi-equilibrium, and this can be used to express the activity of OH as a function of the activity of H$^+$:

$$r_{1,a} = r_{1,c}$$

$$k_{1,a} a_s c_{H_2O} e^{\frac{(1-\beta)FE}{RT}} = k_{1,c} a_{OH_{ads}} a_{H^+} e^{\frac{-\beta FE}{RT}}$$

$$a_{OH_{ads}} \propto a_{H^+}^{-1} e^{\frac{FE}{RT}}$$

Inserting this into the expression for the current of the rds:

$$i_{2,a} \propto a_{H^+}^{-1} e^{\frac{FE}{RT}} e^{\frac{\alpha_a FE}{RT}} a_{H^+}^{-\alpha_a}$$

$$i_{2,a} \propto a_{H^+}^{-(1+\alpha_a)} e^{\frac{(\alpha_a+1)FE}{RT}}$$

From this expression for the total current, it is evident that the anodic reaction order of protons equals $-(1+\alpha_a)$, thus justifying a fractional reaction order. Often $\alpha_a \approx 0.5$, and the resulting reaction order expected from reaction step 2 being rds is -1.5.

The explanation of the reaction order of -1.5 given above requires step 2 in the electrochemical reaction path to be the rds. Thus, a reaction order of -1.5 is more likely linked to the second step being the rds, rather than the third step in the mononuclear path, seeing that the third step does not involve OH groups. The lower reaction orders for the mixed iridium ruthenium oxides can by this model be explained by a lower α_a value at these oxides.

Fractional reaction orders has also been explained by two competing or parallel reaction pathways occurring at the electrode. The observed values of the Tafel slopes and reaction orders are then a combination of the values expected for the competing pathways, and depends on the fraction of the catalytic sites that follow each individual pathway.[106, 107] The surface sites available for each pathway can also change as a function of pH, since OH groups still are important in the second step proposed as rds above, and the reaction order can thus change with pH. The explanation of competing pathways can also be used to justify intermediate values of Tafel slopes.[106] This can explain the Tafel slopes of RuO_2 that were found to lie between 32 mV and 36 mV. These values are intermediate values between the Tafel slopes expected if step 2 of the chemical oxide path (30 mV) and step 2 of the electrochemical oxide path (39 mV) are parallel. A reaction order of -1.5 is also supports this hypothesis. However, with regards to IrO_2 the reaction order of -1.5 is more likely to be caused by the first explanation as the Tafel slopes at IrO_2 are very close to 40 mV, and not intermediate values between steps 2 and 3 being rds. The explanation relying on the double layer correction explained above thus seems to be a more likely explanation for the fractional reaction order.

In view of the discussion above, the second step of the electrochemical path is expected to result in Tafel slopes of 40 mV and reaction orders close to -1.5. The reaction order could deviate from -1.5 as it depends on the value of α_a. The Tafel slopes can deviate from 40 mV due to different surface coverage of the intermediates. These two kinetic parameters are close to what is observed for all the oxides examined in this thesis. Taking into account the effects on the Tafel slope discussed in the previous section, the Tafel slopes at the lowest pH are most reliable. This makes the reaction orders obtained from the lowest part of the polarisation curves plotted vs. RHE more reliable than the reaction orders found from Figure 5-23, where the higher parts of the linear Tafel region are considered. The conclusion is thus that the reaction order and Tafel slopes of all the examined oxides correspond well with step two of the electrochemical oxide path being the rate determining step.

6.3 DETECTION OF BY-PRODUCTS OF THE OER BY RING-DISK EXPERIMENTS

The results obtained in relation to detection of by-products by the ring-disk electrodes will be discussed in this section. Firstly, the results from establishment of the method are discussed, then the results of the different two catalyst materials on the disk are discussed. In the end a comparison of the results are given, and the identity of the ring currents are discussed.

6.3.1 Establishment of method

Experiments in ferricyanide solutions

The potential step experiments performed with the $\mathrm{Fe(CN)_6^{4-}/Fe(CN)_6^{3-}}$ redox couple and the ring-disk electrode with a gold disk and a platinum or gold ring behaved as expected. The collection efficiency of the Au ring-Pt disk electrode in the conventional RRDE set-up was slightly lower than the theoretical value of 25 %, but similar to the value obtained for the same type of electrode in [9]. The collection efficiency does not vary significantly with rotation rate. The ring-disk electrode has an interchangeable disk, and small changes in height of the disk each time the electrode is assembled can affect the flow regime. Slight variations are therefore expected to occur between different experiments. The collection efficiency is approximately twice as high for the conventional RRDE set-up compared to the flow cell arrangement [12], which is expected, as approximately half of the ring electrode surface is upstream to the disk in the flow cell.

A transit time was observed in both the flow cell and the conventional RRDE cell. Further, no products were detected at the ring when no flow or electrode rotation was employed. Since the conventional RRDE cell is well established in the literature, employing this set-up allowed to compare the observed transit times with expected theoretically calculated values, as seen in Table 5-11. The theoretical values were in good agreement with the observations. This also allowed for comparison of the two cell set-ups used in this thesis. It can be seen that the flow rate of 300 mL/min resulted in approximately the same transit time as a rotation rate of 900 rpm, and 50 mL/min to approximately the same flow as at 100 rpm.

Cyclic voltammetry at the disk in the 10 mM ferricyanide solution also gave expected ring current responses. Again, a transit time that decreased with increasing rotation rate could be observed. This is not strictly the transit time as defined in section 3.3.2 as these are potential sweep and not potential step experiments. As the potential increases continuously from a potential where no reaction occurs to potentials where ferricyanide is reduced, it is more difficult to know the exact time of the start of the reduction. However, the product still has to travel from the disk to the ring, and this is expected to go faster with higher rotational speed of the electrode, which is in agreement with Figure 5-27. The current at the ring when the electrode is not rotated is constantly zero, indicating that no disk products are able to reach the ring for these conditions. The RRDE with the Au ring electrode and the Pt ring electrode give very similar results, which is a further indication that these electrodes behave exemplary.

In the diluted ferricyanide solution (0.1 mM $K_3Fe(CN)_6$) the disk currents are quite different than those obtained in the 10 mM $K_3Fe(CN)_6$) solution. At these low concentrations, the currents caused by the redox couple are so small that the capacitive processes occurring at the electrode surface gives a significantly higher contribution to the total current at the disk. As the ring currents are in the range of 0.0002 mA and the collection efficiency is ca. 23 %, the disk current due to the redox reaction is probably about 0.0008 mA, which is only 10-20 % of the currents observed at the disk. The rest of the currents thus presumably correspond to double layer charging at the electrode. Background currents at the ring caused the currents to be shifted slightly upwards when the electrode was rotated. However, the currents are very low in this solution(ca. 0.3 µA), and even a very small background current is sufficient to detect a deviation from zero. If the constant background current is subtracted from the ring response, it seems like the expected behaviour is still obtained from the ring.

In summary, the experiments performed in the ferricyanide solutions showed that the ring-disk electrode worked as expected, both in the flow cell and in the conventional RRDE set-up. A relation was also found between the transit times in the flow cell and the conventional RRDE.

Experiments without catalyst coating in 0.5 M H_2SO_4

The main features of the detected ring currents at the Pt electrode are the reductions observed when the disk was at approximately 1.1. V and 1.9 V while ring was held at 0.6 V. The reduction at 1.9 V is unique for the Pt ring at 0.6 V, whereas the reduction at 1.1 V is also observed at the Au ring at 0.6 V. This is in agreement with oxygen reduction that is only expected to occur at the Pt disk at 0.6 V, as described in section 2.3. The fact that the reduction current is a product from the ring is further demonstrated by the increasing transit time as the rotation rate decreases.

The reduction current observed at both the Pt and Au ring after the reduction at the ring at ca. 1.1 V is probably linked to the reduction process at the disk, since it is detected at the ring right after the reduction occurs at the disk, and it is observed earlier at the ring when the flow rate is higher. Similar behaviour has been observed at Au and Pt ring electrodes combined with a gold disk electrode in sulphuric acid earlier, and was found to be caused by dissolution of the gold disk during the reduction peak at 1.1 V.[108] In this reference different ring potentials of the gold ring were studied. It was found that the reduction peak at the ring decreased when the ring potential was increased, until finally oxidation currents could be detected when the ring potential was > 1.24 V vs. SHE. This can explain why no ring current is observed when the ring is held at 1.2 V, as this is close to the potential where no oxidation or reduction of the gold dissolution product occurs. Gold dissolution products are thus a plausible explanation of the detected reduction currents at the ring close to a disk potential of 1.1 V on the reverse scan.

Small reduction currents are observed at the Au ring at both 0.6 V and 1.2 V, when the disk potential is above 1.75 V at the positive scan. This is possibly also seen at the Pt ring at 1.2 V, but the currents are very small. When the Au ring is at 1.2 V, this reduction seems to occur at the same time whether the electrode is rotated or not. This is therefore not likely to be caused by any physical process that would require the transport of species from the disk to the ring. These currents might therefore be ascribed to artefacts of the potentiostat or to build-up of species in the solution resulting in a background current. Since this only occurs for disk potentials above 1.75 V, these phenomena are probably linked to higher disk currents.

In summary, the experiments performed in 0.5 M H_2SO_4 with only the gold substrates at the disk suggest that the detection of by-products of the OER at ring-disk electrodes can be done with Pt and Au rings. Dissolution of the gold substrate may contribute to the detected ring currents by a reduction peak after the reduction of the gold disk at ca. 1.1 V vs. SHE. However, when the disk is coated by catalyst, this current contribution is expected to decrease. Artefacts of the potentiostat could possibly result in small deviations from the baseline current at potentials above 1.75 V at the disk.

6.3.2 IrO_2 disk and Au or Pt ring in H_2SO_4

Experiments in the flow cell

The experiments with the Au and Pt ring performed in the flow cell are similar to those performed in the preliminary project work [12], but in addition the electrolyte flow rate is varied. The response if the gold and platinum ring electrodes are similar as those obtained in the preliminary project. For the Au ring at 0.6 V and the Pt ring at 1.2 V, a reduction is observed at the positive scan of the disk and an oxidation at the reverse scan. Reducing the disk scan rate has the effect of lowering the normalised ring currents, and possibly giving less oxidation in relation to oxidation currents at the ring. These effects were also observed in the work of Kuznetsova et.al. in a similar flow cell set-up with an IrO_2 disk in combination with a Pt ring at 1.2 V.[9] The size of the ring and disk currents are also in the same order of magnitude as those obtained in these references.

If the ring currents obtained at the Au and Pt rings at a scan rate of 100 mV/s are compared, it is interesting that they exhibit almost the same shape and size. This means that if the currents arise from by-products of the OER, these by-products must be equally electrocatalytic at both Pt and Au. This is not the case for ozone, as described in section 2.3, and probably not the case for any intermediate requiring adsorption to the electrode surface to react. The similar currents at the Pt and Au electrode thus indicates that these currents might not be caused by OER by-products.

When the Pt ring is held at 0.6 V, oxygen reduction is expected to occur at the ring when the OER commences at the disk. This is in accordance with Figure 5-32. However, unlike the experiments with the uncoated gold disk (Figure 5-29) it is difficult to distinguish the location of the peak potentials of the ring currents, and therefore impossible to see the effect of different electrolyte flow rates.

The new finding from the discussed in this section compared to the results of the preliminary project work is that the current at the ring is unaffected by the electrolyte flow rate. This is unexpected, as all products produced at the ring will require some time to travel from the disk to the ring. However, the ring currents observed when the Pt ring is held at 0.6 V are unaffected by flow rate as well. The latter experiment can be regarded as a reference experiment, as it is known that oxygen reduction will occur at the Pt ring at 0.6 V. When these experiments result in a reduction current at the ring even when the electrode is not rotated, this indicates that oxygen, and thus also other products from the disk, can travel from the disk to the ring without enforcing electrolyte flow by the pump. An explanation to this can be that the vigorous gas evolution due to the ORR at the IrO_2 disk causes strong convection. The currents at the IrO_2 disk are approximately 40 times higher than those observed at the uncoated Au disk, and this can explain why the gas bubbles causes this effect when the disk is coated with the catalyst as opposed to when the disk electrode was the plain gold electrode. These results suggest that the vigorous gas evolution at the IrO_2 disk complicates the ring-disk measurements for the high current values obtained at the disk.

Experiments in the conventional RRDE set-up

Similar experiments to those discussed above were executed in a conventional RRDE set-up. This set-up has a different flow pattern and the gas bubble removal is therefore also expected to be different. The experiments with the Pt ring at 0.6 V exhibited a more promising nature in this set-up compared to the flow cell. When the disk was scanned to 1.9 V, the ring currents at no rotation were significantly lower than when the electrode was rotated. It is unclear why the gas evolution should give less disturbances in this cell set-up.

The currents obtained in the conventional set-up when scanning the disk to only 1.7 V are less noisy than those where the disk is scanned to 1.9 V. The results are also more reproducible, possibly because the flow is less disturbed by gas bubbles. This enables a more reliable interpretation of the ring current response as a function of flow rate (Figure 5-38). When the electrode is rotated, two reduction peaks are observed at the ring for each cycle at the disk. These are similar to those obtained for the Pt ring in combination with the gold disk (Figure 5-29 a). One reduction peak is located right after the OER peak at the disk, whereas the other peak is located right after the reduction at the disk (at 1.1 V of the negative scan). The observations suggest that there might be some gold areas exposed at the electrode. Then the reduction currents can be explained in the same way as those observed at the Pt electrode in combination with the gold disk. The higher currents at the reduction related to oxygen reduction can be explained by the disk being more active for the OER when it is (partly) coated by IrO_2.

Another interesting feature observed in Figure 5-38 is the ring current response at 0 rpm. It does not seem like the response is a result of oxygen reduction, since both a cathodic and an anodic response is observed. This indicates that the gas evolution is not high enough to disturb the convection significantly when the potential is scanned only to 1.7 V. The curve at 0 rpm exhibits exactly the same behaviour as the Pt ring at 1.2 V in the flow cell (or equivalently the Au ring at 0.6 V). At the positive scan, a small reduction occurs, before it suddenly shifts to positive currents when the disk scan is reversed. The size of the peaks are also approximately similar for all these cases. This is further proof that this feature, observed at the ring when the electrode is not rotated, cannot be explained physically by products travelling from the disk to the ring. This feature is observed in all other experiments when the rotation rate is zero, and will hereafter be referred to as "Feature X".

The experiments with the catalyst coating applied on the ring instead of the disk, and using the plain Pt disk for detection gives further evidence of this feature being attributed to something other than the products of the disk. When rotation is employed for this configuration, it is expected that all products will be flung out from the ring, and thus not be able to reach the disk which is located upstream of the ring in the conventional RRDE experiments. However, the ring current response in these experiments were still quantitatively similar to those obtained in the flow cell and at the Pt ring at 0.6 V and 0 rpm (Figure 5-38), i.e. exhibiting only “Feature X” in the ring current response. This is a strong indication that this feature is most likely an artefact related to the instrumentation, and will therefore in all following interpretations be regarded as such. The resulting ring currents when “Feature X” is subtracted from the ring current response will therefore present the true ring current arising from products originating from the ring. It should, however, be noted that “Feature X” is a function of the disk scan rate and of the upper potential of the disk. However, the current response at 0 rpm is included in all figures and can thus easily be compared with the curves obtained at other rotation rates.

The results from cyclic voltammetry at the IrO_2 disk in combination with the Pt ring electrode at 1.2 V were interpreted in two ways. First with the basis of “Assumption 1”[1] and subtracting “Feature X”, small oxidation currents were detected at higher rotation rates. However, these oxidation currents endured for the entire period when the disk was scanned to low potentials. This is not expected if the species giving rise to the reduction currents are by-products of the OER. On the contrary, it would then be expected that the oxidation would cease after some time, and faster when the rotation rate was increased. This is not the case when ”Assumption 1” is used. It might therefore be more correct to employ “Assumption 2”[2]. When “Feature X” is subtracted, “Assumption 2” results in a net reduction at the ring at higher rotation rates. A further indication of a net reduction when “Feature X” is neglected, is the small shoulder of the reduction currents observed at high rotation rates. The reason for this being absent in the curves obtained at slow rotation rates can be because the transit time is longer than the time until “Feature X” commences, and is thus disguised by this. If the reduction ceases later at the slow scan rates, this can also explain why it takes longer time before the ring currents at these experiments reach zero current again after “Feature X” has occurred.

The most plausible interpretation seems to be based on “Assumption 2”, and thus that only reduction currents results from the products produced at the ring. This is in accordance with the potential step measurements performed on the same catalyst with the Pt ring at 1.2 V in the flow cell (Figure 5-36). In these experiments, holding the disk at 1.8 V also resulted in net reduction currents. These are also in the same order of magnitude as the reduction currents observed in the potential sweep experiments if “Feature X” is subtracted from the net current (< 0.5 µA). If the net reduction current is caused by by-products of the OER, the most plausible specie is ozone, as this is the only product with long enough lifetime that can cause reduction currents at the ring, as outlined in section 2.3. The assumptions underlying this conclusion will be further addressed in section 6.3.5.

The collection of experiments performed for the IrO_2 catalyst has resulted in valuable insight into the results obtained during the preliminary project work. It seems that the conventional RRDE set-up is superior for removal of gas bubbles, especially when low electrolyte flow rates are desired. Lowering the upper potential limit of the disk is also useful to ensure less disturbances of convection due to vigorous gas evolution. It was found that an upper disk potential of 1.7 V to 1.8 V is sufficient to obtain ring current responses. Further, it has been valuable to study the effect of varying the electrolyte flow

---

[1] “Assumption 1” involves shifting all the currents such that “Feature X” balances for all ring curves.

[2] “Assumption 2” involves shifting all ring currents such that they are zero when the disk potential is at 0.6 V.

rate, especially in relation to the conventional RRDE set-up. Varying the rotation rate allows for comparison of calculated values with observed transit times. Thus, this can be used to see whether a current is likely to be a result of a species with a probable transit time, or not. A feature in the ring current curves referred to as "Feature X" was found to be flow-independent and therefore ascribed to the instrumentation rather than to products originating from the ring. Further analysis of ring currents should therefore be based on subtracting this current contribution from the recorded ring currents. However, the origin of this feature is unknown, and the analysis is thus somewhat dubious. During the time of this thesis, the origin of this feature could not be established, but further work should attempt to identifying this.

6.3.3 IrO_2 disk and Pt ring in 0.5 M Na_2SO_4

Changing the electrolyte from 0.5 M H_2SO_4 to the near-neutral 0.5 M Na_2SO_4 solution had an effect on the Pt ring currents detected at both 0.6 V and 1.2 V. The results were also less noisy and more reproducible in this solution, which might be a result of the smaller disk currents, and thus less bubbles, obtained in this solution.

The results from the Pt disk at 0.6 V can again be used as a reference as it is known that oxygen reduction will occur at this electrode when the disk is scanned to potentials where the OER occurs. From these experiments it is obvious that the results are more reproducible and reliable in this solution. Evidence for this is that the onset of the oxygen reduction at the ring start earlier and cease earlier as the electrode rotation rate is increased. In addition, the ring current at 0 rpm does not seem to be a result of oxygen reduction. As seen in the H_2SO_4 solution, the ring current at 0 rpm again seems to be mainly a result of the potentiostat feature close to the maximum potential of the disk.

The ring currents obtained when the Pt disk is held at 1.2 V are somewhat similar to those obtained by the corresponding experiments in sulphuric acid. Here as well, the ring current obtained at 0 rpm includes only "Feature X". Applying "Assumption 1" (Figure 5-44) it can be seen that the oxidation currents at the ring commences earlier when the electrode is rotated faster. Comparing the transit times in Table 5-14 with the start of the oxidation current, it is probable that the specie resulting in the oxidation is produced close to the peak potential at the disk. This applies for all small molecular species, as the transit times for other small oxygen containing species are in the same range. This indicates that the positive contributions to the ring currents are probably caused by by-products of the OER. From the ring current obtained at 50 rpm, it seems to be a reduction process occurring at the ring electrode, as well. This process can be disguised by the high oxidation currents at larger rotational speeds. This finding suggests that there might be two processes, one reduction and one oxidation, occurring at the ring simultaneously. For most rotation rates, the oxidation seems to be the dominating process.

However, as pointed out for the results in sulphuric acid, a problem with "Assumption 1" is that the oxidation currents endures the entire time between the peak potentials of the disk. Thus "Assumption 2" might give a more reliable interpretation. If "Feature X" is subtracted from the curves in (Figure 5-45) a small reduction is observed at the forward scan of the disk, and it is followed by an oxidation after the disk scan is reversed. The fact that the reduction and oxidation responses commences faster when the rotation rate is increased is a strong evidence that the currents are caused by products originating from the ring.

It is useful to compare the potential sweep experiments with the results from the potential step experiments given in Figure 5-47. For the potential step measurements it is assumed that the ring current when the disk is at 0.6 V is equal to the background, and can thus be subtracted. This results in a reduction at the ring when the disk is at 1.7 V. This fits best wit "Assumption 2", as no reduction is seen if "Assumption 1" is applied. After the step down to 0.6 V at the disk, a small oxidation peak might be observed at the ring at 800 rpm. This can indicate that the oxidation current is not originating from the disk while the OER is occurring, but rather that it is an effect of reducing the potential again. Further, this peak occurs in the beginning of the step down to 0.6 V and does not endure until the potential is stepped up again. This means that the small oxidation peak must be linked to species being present at the surface at the time when the potential is stepped from 1.7 V to 0.6 V, rather than being produced continuously at the disk at 0.6 V. However, this feature is barely visible in the ring current and it is therefore not certain that it results from species from the ring. Therefore, it will not be discussed further here. However, a similar feature but with significantly higher currents were seen in the experiments with $Ir_{0.6}Ru_{0.4}O_2$ at the disk. This feature will therefore be discussed in relation to that material below.

Either of the assumptions used to interpret the results of the potential sweep voltammetry results in both oxidation and reduction currents. This is also seen in the potential step voltammetry. Thus, the processes occurring at the disk seem to result in at least two different by-products, one giving rise to reduction at the ring and the other to oxidation. Comparing the results from potential sweep and step voltammetry at the disk, "Assumption 2" seems to be the most plausible. The most likely situation is thus that the by-product causing a reduction current is produced while the OER occurs at the disk (and possibly also at somewhat lower potentials). This specie dominates the ring current until the disk starts to scan in the negative direction. Then, a specie resulting in oxidation at the ring is released at the disk surface, and after some time (depending on the rotation rate), oxidation dominates. Again, this is based on assumptions about the background current that will be discussed further in section 6.3.5.

The experiments performed in the sodium sulphate solution resulted in more activity at the ring compared to the experiments in the sulphuric acid solution. The reason for this is difficult to predict as the disk currents in the two solutions are different, and the differences in gas evolution might affect the currents detected at the ring. The experiments in the sodium sulphate solution does anyway provide more insight into the by-products produced at the IrO_2 disk since higher by-product currents provide more reliable results. With higher currents at the ring it is more evident that some of these currents are in fact originating from the disk, still excluding "Feature X" as concluded in the last section.

6.3.4 $Ir_{0.6}Ru_{0.4}O_2$ disk and Pt ring in 0.5 M H_2SO_4

The results from the experiments with $Ir_{0.6}Ru_{0.4}O_2$ at the disk are discussed in this section. The discussion is divided into two, where the results from holding the Pt ring at 0.6 V are discussed in the first, and the results from holding the Pt ring at 1.2 V in the second.

Pt ring at 0.6 V

For $Ir_{0.6}Ru_{0.4}O_2$ at the disk, experiments with the Pt ring at 0.6 V were again performed as reference measurements. A more thorough series of experiments was performed, both with potential step and sweep voltammetry at the disk. This allowed for comparison with calculated transit times. As seen from Table 5-14 the transit times observed in the potential step measurements are close to the calculated values for oxygen. It is not surprising that there is more deviation between the calculated and observed transit times for O_2 as compared to the $Fe(CN)_6^{4-}$/ $Fe(CN)_6^{3-}$ couple, since the equation for transit time is derived for simple redox species that do not require adsorption and desorption at the disk. This is more correct for the $Fe(CN)_6^{4-}$/ $Fe(CN)_6^{3-}$ couple than for the OER. In addition, the gas evolution at the oxygen electrode can disturb the electrolyte flow.

For the experiments with cyclic voltammetry at the disk, the currents recorded at the Pt ring at 0.6 V showed smooth reduction current peaks for each of the rotational speeds (Figure 5-48). The transit time is similar for the potential sweep and step voltammetry, if the transit time for the sweep voltammetry is taken as the time between the start of the OER and until any reduction is observed at the ring.

The experiments with Pt at 0.6 V thus behave as expected, and suggest that a maximum disk potential of 1.7 V is a good choice for low noise levels.

Pt ring at 1.2 V

For the experiments with the ring potential at 1.2 V and cyclic voltammetry at the disk, the same problem with large background currents as observed for IrO_2 was encountered. Thus, it was necessary to apply the two assumptions used for the experiments for IrO_2 here as well. As before, "Assumption 1" is insufficient to explain why the oxidation current endures for the entire time when the disk is at low potentials.

However, "Assumption 2" and subtraction of "Feature X" results in a large reduction current commencing at the disk potential of 1.2 V for high rotation rates. This is long before the onset of the OER, and is contradictory to the results obtained by Kuznetsova et.al.[9] where the reduction commenced concurrently with the onset of the OER. This was possibly also the case for the IrO_2 catalyst both in sulphuric acid and in the sodium sulphate solution when "Assumption 2" was applied. However, the currents resulting from those experiments were much smaller, and thus less reliable. For $Ir_{0.6}Ru_{0.4}O_2$ these currents are so large that it can be assumed that the currents are not mere instrumental artefacts, but rather results of products originating from the disk. None of the possible by-products that can cause reduction at the ring at 1.2 V (HO_2 and O_3) proposed in section 2.3 can be produced electrochemically at the disk at 1.2 V. This implies that either "Assumption 2" is incorrect or that the reduction at the ring results from something other than HO_2 and O_3 form the disk.

Comparing with the potential step measurements it is more evident that a reduction current can indeed be observed at the ring at lower disk potentials than those required for the OER. Stepping the potential up to 1.7 V results in a net reduction at the ring. The reduction is likely to be a result of a specie originating from the ring since the transit time depends on rotation rate and is close to what is expected for species with diffusion constants similar to O_2. When the disk was stepped from 0.6 V to 1.4 V, a qualitatively similar reduction response is observed at the ring. This suggest that the reduction current at the ring in the potential sweep experiments can in fact be caused by a process at the disk that commences before the onset of the OER. According to this, "Assumption 2" still holds.

When the potential is stepped down from 1.7 V to 0.6 V oxidation peaks are observed at the ring. The onset of the oxidation is shifted towards later times for lower rotational speeds. Again, the transit times are similar to what is expected for small molecules traveling from the disk to the ring, indicating that these peaks are results of species produced at the disk as soon as the potential is stepped down to 0.6 V. The observed oxidation current has the shape of a peak, and is not present throughout the entire step at 0.6 V. This suggests that the species that are oxidised are present in a certain amount, as opposed to being continuously produced throughout the time at this potential. Therefore, it is probable that the species causing the oxidation peak is related to surface species present at the electrode during the polarisation at 1.7 V, and not related to species continuously produced at 0.6 V. The potential step voltammetry between 0.6 V and 1.4 V does not result in this oxidation peak, and it is thus probable that the species causing the oxidation currents at the ring are produced only at high potentials, suggesting that these are related to the OER.

As the oxidation of the specie commences only after the potential is stepped down from 1.7 V, the specie is probably not a by-product of the OER under constant potential conditions, but rather a product produced due to fluctuating potential conditions. A possible mechanism for this behaviour is attempted in the following.

If the same reaction mechanism applies for the OER both during the potential sweep and potential step voltammetry, the same intermediates will be present at the electrode. However, the amount of the intermediates is a function of potential and can therefore result in different by-product yield depending on how fast the potential is varied. When the OER occurs at the disk, all reaction intermediates are consumed in the OER (and possibly also for a by-product causing the reduction currents at the ring). When the potential is stepped suddenly down to 0.6 V the OER abruptly stops, and unreacted intermediates of the OER are left on the surface. At 0.6 V these cannot react further to oxygen. Instead they can desorb from the disk electrode or possibly react to form other products. These can then be detected as oxidation current at the ring held at 1.2 V. During the sweep voltammetry, however, the OER does not abruptly stop but rather ceases gradually. Thus, both the surface concentration of intermediates and the oxygen evolution ceases gradually, and less or no intermediates will result in the specie giving oxidation currents at the ring. This can explain why the large oxidation currents are observed as the potential is stepped from 1.7 V to 0.6 V as opposed to what is observed during the potential sweep. This is also in accordance with the results from Kuznetsova et.al.[9] where the ring currents at Pt at 1.2 V decreased with decreasing scan rate of the disk (i.e. more gradual decrease of the OER).

The reduction currents at the ring are of another nature, and seems to be related to a specie that is produced continuously at high disk potentials, resulting in ring currents that endure as long as the disk is at high disk potentials both during potential step and potential sweep voltammetry.

6.3.5 Summary of the ring-disk experiments with IrO_2 and $Ir_{0.6}Ru_{0.4}O_2$

The ring current responses in the ring-disk experiments where the Pt ring is held at 1.2 V while the disk is scanned to potentials equal to or higher than 1.7 V are found to exhibit certain features that are flow-independent. These features are referred to as “Feature X” and are assumed to be related to the instruments employed. When the ring currents are interpreted, the contribution from “Feature X” is therefore subtracted from the observed current response. Due to large and inconsistent background currents, certain assumptions had to be done in order to compare the current responses at different rotation rates. Based on the combination of potential step and potential sweep voltammetry at both catalysts, it has been found that the results are more likely to be explained by "Assumption 2" than by "Assumption 1". However, the analysis presented is somewhat dubious due to the fact that the origin of "Feature X" *and* the origin of the background currents are unknown.

Applying the assumptions above, only small reduction currents were observed for IrO_2 in sulphuric acid. The measurements with the same catalyst in the sodium sulphate solution did however result in higher activity at the ring. The results suggest that at least two species other than oxygen is produced at the ring, one giving rise to oxidation at the ring and the other to reduction. A combination of both a reduction current and an oxidation current was also the case for $Ir_{0.6}Ru_{0.4}O_2$ in sulphuric acid. For the potential sweep experiments, oxidation dominates the current response for IrO_2 in the sodium sulphate solution, whereas reduction dominates for $Ir_{0.6}Ru_{0.4}O_2$. This is in accordance with the work of Kuznetsova et.al.[9] where mainly net reduction currents were detected for $Ir_{0.6}Ru_{0.4}O_2$, whereas both oxidation and reduction currents were detected at IrO_2.

If the current responses are compared to the size of "Feature X" it seems like the amount of by-products is significantly higher for $Ir_{0.6}Ru_{0.4}O_2$ than for IrO_2. This can explain why no net oxidation is observed for this material, as it can be disguised in the large reduction. The potential step measurements revealed significantly higher oxidation currents for $Ir_{0.6}Ru_{0.4}O_2$ as opposed to IrO_2. This can indicate a higher amount of surface coverage of intermediates at the mixed oxide. This is in line with the higher Tafel slopes observed at the mixed oxide. However, comparison of the quantity of by-products for the two materials is difficult due to different conditions (disk potential and electrolyte), and no conclusions can be done in this respect. It would be interesting to test other oxide compositions by the similar ring-disk measurements to see whether this is indeed a function of composition.

It can be concluded that the ring current response is a result of three contributions: the feature ascribed to the instrumentation ("Feature X"), reduction currents and oxidation currents. From the potential step measurements it can be suggested that the reduction current is occurring concurrently with the OER, and can thus be regarded as a by-product of the OER. However, both the potential sweep and potential step voltammetry suggest that this product is produced already at potentials lower than the onset of the OER. None of the candidate species presented in section 2.3 can explain this behaviour. A candidate for the oxidation current at the ring is H_2O_2. This specie cannot be produced by oxidation at the disk at the low potentials when the oxidation is observed at the ring. However, it can be produced by recombination of the hydroperoxyl radical (see section 2.2.3). This can thus suggest that this specie is present at the electrode. This is in line with the work of Kuznetsova et.al. where $HOO^{\cdot}$ was identified at the surface of IrO_2 by potential modulated reflectance spectroscopy.[9] However, further investigation of the specie causing the oxidation at the ring must be done before any conclusion can be made.

Since there are at least one reduction and one oxidation process occurring at the ring, it is vital to know when the current is zero. As long as the nature of "Feature X" and the background currents are uncertain, it is not possible to conclude regarding the position of the current curves along the y-axis, and it cannot be known for certain when reduction or oxidation currents starts or ceases during the potential sweep experiments. The experiments performed during establishment of the method could unfortunately not elucidate these complications, possibly due to considerably lower disk currents. In the absence of a resolution to the cause of these artefacts, we therefore refrain from further interpretation here. Further work would, however, have to resolve these artefacts and possibly involve iodometry and/or spectroscopic methods such as FTIR and UV-vis spectroscopies, as well.

As no conclusions could be drawn concerning the identity of the by-products, the results from the ring-disk experiments cannot elucidate the reaction mechanism occurring at the disk. The same reaction mechanism was found to occur at all four oxides based on the Tafel slopes and reaction orders. Thus, the intermediates at the surfaces of IrO_2 and $Ir_{0.6}Ru_{0.4}O_2$ are expected to be of the same identity. However, based on the slight differences in Tafel slopes, the intermediate coverage at these two oxides possibly exhibits slightly different potential dependency, and thus by-product yield under dynamic potential control. From the Tafel slopes and reaction orders, the rate limiting step of the OER at these oxides appears to be the transition of OH_{ads} to O_{ads}, which suggests that OH_{ads} is available at the surface during the reaction. However, the Tafel slopes and reaction orders were determined only at low overpotentials and under near steady-state conditions, and might therefore not apply under the conditions applied during the ring-disk experiments.

The different ratios of the cathodic and anodic contributions to the ring currents in the potential step vs. potential sweep measurements illustrates the potential dependence of the intermediate production. This is demonstrates the importance of investigating the by-products of the OER under fluctuating conditions in relation to operation of a PEM water electrolyser. It seems that some operating conditions and catalyst material compositions can favour less by-product yield and thus longer life-time of the electrolyser.

7 CONCLUSIONS AND FURTHER WORK

In this work, four different compositions of rutile oxide powder was obtained through a hydrolysis synthesis procedure, IrO_2, $Ir_{0.6}Ru_{0.4}O_2$, $Ir_{0.3}Ru_{0.7}O_2$ and RuO_2. The syntheses resulted in powders with crystalline oxide phases. The catalytic activity for the OER at the oxides increased with increasing ruthenium content in both sulphuric and perchloric acid. Characterisation by cyclic voltammetry proved that the mixed oxides exhibited voltammograms intermediate of those obtained for the two pure iridium and ruthenium oxides. Indications of surface segregation of iridium were found for $Ir_{0.3}Ru_{0.7}O_2$.

The Tafel slopes and reaction orders of the four oxides were established in perchlorate solutions of pH 0, 1, 2 and 3. Tafel slopes of approximately 40 mV and reaction orders of -1.5 were established for all oxides. The fractional reaction order was ascribed to double layer effects caused by the acid-base properties of the metal oxide surfaces in aqueous solutions. Thus, the reaction order of -1.5 in combination with the Tafel slopes of 40 mV can be ascribed to step 2 in the mononuclear path being the rate determining step of the OER at these oxides. This means that it is the transition of the surface adsorbate OH_{ads} to adsorbed oxygen O_{ads} that is limiting the rate of the OER at these materials. The Tafel slopes varied somewhat with the composition of the oxide, which indicates that the intermediate coverage, and thus the stability of reaction intermediates depends on the composition.

A ring-disk electrode was used for electrochemical detection of by-products of the OER. Two different set-ups were employed, either a flow cell with a pump providing the electrolyte flow or a conventional rotating ring-disk electrode. The conventional RRDE set-up seemed superior for experiments with vigorous gas evolution when a low electrolyte flow rate was desired. Varying the rotation rate of the electrode revealed that parts of the detected ring current originated from features probably caused by the instrumentation. These features and a variable background current contribution at the ring complicated the interpretation of the ring-disk measurements. The identity of the products produced at the ring could therefore not be established. However, a combination of potential step and potential sweep voltammetry at the disk strongly suggests that at least two products other than oxygen were produced at the disk, one giving rise to a reduction at the ring and the other giving rise to an oxidation. As no conclusion could be drawn concerning the identity of the by-products, the results from the ring-disk experiments could not elucidate the reaction mechanism further.

Potential sweep and potential step voltammetry at the disk resulted in different ratios of the two by-products. This demonstrates that the production of by-products depends on the potential dynamics of the oxygen electrode, and thus the importance of investigating the by-products of the OER under fluctuating conditions in relation to operation of a PEM water electrolyser. It seems that different operating conditions favour different by-products and also different amounts of these products.

7.1 FURTHER WORK

In this study the Tafel slopes and reaction orders with respect to protons were determined at low overpotentials. However, the reaction order was determined on the basis of the polarisation curves in only three solutions due to mass transport limitations of H^+ in the solution of pH 3. Furthermore, the reaction order was found to vary with the potential. Thus, it would be valuable to improve the accuracy of the measurements by obtaining the polarisation curves in one or two more solutions with different pH. Furthermore, the polarisation curves at high potentials are uncertain in the results presented in this thesis. It would be interesting to extend the polarisation measurements into higher potential regions to see whether this would actually yield Tafel slopes of 120 mV or not.

For the ring-disk experiments, it is obvious that the artefacts that were ascribed to the instrumentation in this thesis must be resolved before further experiments of this type can be performed. If these are resolved, it would be interesting to investigate the relationship between the oxide composition and by-product yield at all four oxide compositions synthesised in this work. This can give further information about how the intermediate-to-by-product ratio depends on composition. This can then be related to the determined reaction mechanisms. Possible relations between differences in surface coverage and by-product yield at the different oxides could also be analysed.

The ring-disk experiments with IrO_2 suggested that the by-product yield was different in the sodium sulphate and sulphuric acid solutions. It would be interesting to investigate this further by performing similar experiments in solutions of different pH. This can then be compared to the development of Tafel slopes as a function of pH, and might yield information about the development of by-product yield, and thus intermediate coverage, as a function of pH.

Non-electrochemical methods like FTIR and UV-vis spectroscopy, and possibly iodometry, in situ or ex situ, will also be important to conclude on the identity of the by-products of the OER.

8 REFERENCES

1. Bontempelli, G. and R. Toniolo, *MEASUREMENT METHODS | Electrochemical: Linear Sweep and Cyclic Voltammetry*, in *Encyclopedia of Electrochemical Power Sources*, J. Garche, Editor. 2009, Elsevier: Amsterdam. p. 643-654.
2. Abbott, D., *Keeping the energy debate clean: How do we supply the world's energy needs?* Proceedings of the IEEE, 2010. **98**(1): p. 42-66.
3. Marshall, A., *Electrocatalysts for the Oxygen Evolution Electrode in Water Electrolysers using Proton Exchange Membranes: Synthesis and Characterisation*, in *Department of Materials Technology*. 2005, Norwegian University of Science and Technology: Trondheim. p. 231.
4. Carmo, M., et al., *A comprehensive review on PEM water electrolysis.* International Journal of Hydrogen Energy, 2013. **38**(12): p. 4901-4934.
5. Trasatti, S., *Physical electrochemistry of ceramic oxides.* Electrochimica Acta, 1991. **36**(2): p. 225-241.
6. Kötz, R. and S. Stucki, *Stabilization of RuO2 by IrO2 for anodic oxygen evolution in acid media.* Electrochimica Acta, 1986. **31**(10): p. 1311-1316.
7. Bockris, J.O.M., *Kinetics of activation controlled consecutive electrochemical reactions: Anodic evolution of oxygen.* The Journal of Chemical Physics, 1956. **24**(4): p. 817-827.
8. Valdés, Á., et al., *Oxidation and Photo-Oxidation of Water on TiO2 Surface.* The Journal of Physical Chemistry C, 2008. **112**(26): p. 9872-9879.
9. Kuznetsova, E., et al., *Identification of the byproducts of the oxygen evolution reaction on Rutile-type oxides under dynamic conditions.* Journal of Electroanalytical Chemistry, 2014. **728**(0): p. 102-111.
10. Okada, F. and K. Naya, *Highly efficient and long-lifetime ozone water production system realized using a felt separator.* Journal of the Electrochemical Society, 2009. **156**(8): p. E125-E131.
11. Yu, T.H., et al., *Mechanism for degradation of nafion in PEM fuel cells from quantum mechanics calculations.* Journal of the American Chemical Society, 2011. **133**(49): p. 19857-19863.
12. Thuv, H., *Characterisation of Catalysts for Oxygen Evolution in PEM Water Electrolysis*, in *Department of Materials Science and Engineering*. 2014, NTNU: Trondheim.
13. Kuznetsova, E., *Structure, selectivity and electrocatalytic activity of Iridium-based oxides for oxygen evolution*, in *Department of Materials Science and Engineering*. 2014, NTNU: Trondheim. p. 130.
14. Borup, R., et al., *Scientific aspects of polymer electrolyte fuel cell durability and degradation.* Chemical Reviews, 2007. **107**(10): p. 3904-3951.
15. Qiao, J., et al., *Degradation of perfluorinated ionomer membranes for PEM fuel cells during processing with H 2 O 2.* Journal of the Electrochemical Society, 2006. **153**(6): p. A967-A974.
16. Vielstich, W., H.A. Gasteiger, and A. Lamm, *Handbook of fuel cells: fundamentals, technology and applications*. 2003, Chichester: Wiley. 6 b. : ill.
17. Burlaststky, S.F., et al., *MEMBRANE ELECTRODE ASSEMBLIES WITH HYDROGEN PEROXIDE DECOMPOSITION CATALYST*, in *U. S. Patent Application U.S.A*, U.S.P.A. U.S.A, Editor. 2004, U. S. Patent Application U.S.A: U.S.A.
18. Bard, A.J., R. Parson, and J. Jordan, *Standard potentials in aqueous solution*, ed. A.J. Bard, R. Parson, and J. Jordan. 1985, New York and Basel: International Union of Pure and Applied Chemistry.
19. Hamann, C.H., A. Hamnett, and W. Vielstich, *Chapter 3: Electrode Potentials and Double-Layer Structure at Phase Boundaries*, in *Electrochemistry*. 2007, Wiley: Weinheim. p. 77-155.
20. *JANAF THERMOCHEMICAL TABLES Third Edition.* Analytical Chemistry, 1991. **63**(4): p. 252A-252A.
21. Hamann, C.H., A. Hamnett, and W. Vielstich, *Chapter 4: Electrical Potentials and Electrical Current*, in *Electrochemistry*. 2007, Wiley: Weinheim. p. 157-250.

22. Trasatti, S., *ELECTROCHEMICAL THEORY | Oxygen Evolution*, in *Encyclopedia of Electrochemical Power Sources*, J. Garche, Editor. 2009, Elsevier: Amsterdam. p. 49-55.
23. Guerrini, E. and S. Trasatti, *Electrocatalysis in Water Electrolysis*, in *Catalysis for Sustainable Energy Production*. 2009, Wiley-VCH Verlag GmbH & Co. KGaA. p. 235-269.
24. Hamann, C.H., A. Hamnett, and W. Vielstich, *Electrochemistry*. 2007, Weinheim: Wiley. XVIII, 531 s. : ill.
25. Pletcher, D., et al., *7 - Electrocatalysis*, in *Instrumental Methods in Electrochemistry*, D.P.G.P.M.P. Robinson, Editor. 2010, Woodhead Publishing. p. 229-250.
26. Trasatti, S., *The oxygen evolution reaction*, in *Electrochemical Hydrogen Technologies: Electrochemical production and combustion of hydrogen*, H. Went, Editor. 1990, Elsevier: Amsterdam. p. 104-135.
27. Savadogo, O., *Chapter 50: Synergetic Effects of Surface Active Sites on the Hydrogen Evolution Reaction*, in *Interfacial electrochemistry: theory, experiment, and applications*, A. Wieckowski, Editor. 1999, Marcel Dekker: New York. p. XVIII, 966 s. : ill.
28. Trasatti, S., *Electrocatalysis in the anodic evolution of oxygen and chlorine.* Electrochimica Acta, 1984. **29**(11): p. 1503-1512.
29. Pourbaix, M., *Atlas of electrochemical equilibria in aqueous solutions*. 1974, Houston, Tex.: National Association of Corrosion Engineers. 644 p. : fig.
30. Rossmeisl, J., et al., *Electrolysis of water on oxide surfaces.* Journal of Electroanalytical Chemistry, 2007. **607**(1–2): p. 83-89.
31. Owe, L.-E., et al., *Iridium–ruthenium single phase mixed oxides for oxygen evolution: Composition dependence of electrocatalytic activity.* Electrochimica Acta, 2012. **70**(0): p. 158-164.
32. Cherevko, S., et al., *Stability of nanostructured iridium oxide electrocatalysts during oxygen evolution reaction in acidic environment.* Electrochemistry Communications, 2014. **48**(0): p. 81-85.
33. Rogers, D.B., et al., *Crystal chemistry of metal dioxides with rutile-related structures.* Inorganic Chemistry, 1969. **8**(4): p. 841-849.
34. Matsumoto, Y. and E. Sato, *Electrocatalytic properties of transition metal oxides for oxygen evolution reaction.* Materials Chemistry and Physics, 1986. **14**(5): p. 397-426.
35. Oldham, K.B., J.C. Myland, and A.M. Bond, *13 The Electrode Interface*, in *Electrochemical science and technology: fundamentals and applications*

2011, John Wiley: Chichester. p. XII, 405 s. : ill.

36. Bockris, J.O.M. and Z. Nagy, *Symmetry factor and transfer coefficient: A source of confusion in electrode kinetics.* Journal of Chemical Education, 1973. **50**(12): p. 839-843.
37. Krasil'shchikov, A.N., Zh. Fiz. Khim., 1963. **37**.
38. Busch, M., E. Ahlberg, and I. Panas, *Hydroxide oxidation and peroxide formation at embedded binuclear transition metal sites; TM = Cr, Mn, Fe, Co.* Physical Chemistry Chemical Physics, 2011. **13**(33): p. 15062-15068.
39. Busch, M., E. Ahlberg, and I. Panas, *Electrocatalytic oxygen evolution from water on a Mn(iii-v) dimer model catalyst - A DFT perspective.* Physical Chemistry Chemical Physics, 2011. **13**(33): p. 15069-15076.
40. Yeo, B.S., et al., *Identification of Hydroperoxy Species as Reaction Intermediates in the Electrochemical Evolution of Oxygen on Gold.* ChemPhysChem, 2010. **11**(9): p. 1854-1857.
41. Sivasankar, N., W.W. Weare, and H. Frei, *Direct observation of a hydroperoxide surface intermediate upon visible light-driven water oxidation at an Ir oxide nanocluster catalyst by rapid-scan FT-IR spectroscopy.* Journal of the American Chemical Society, 2011. **133**(33): p. 12976-12979.
42. Sawyer, D.T. and J.S. Valentine, *How super is superoxide?* Accounts of Chemical Research, 1981. **14**(12): p. 393-400.

43. Michaud, P.A., et al., *Electrochemical oxidation of water on synthetic boron-doped diamond thin film anodes.* Journal of Applied Electrochemistry, 2003. **33**(2): p. 151-154.
44. De Smedt, F., et al., *The Application of Ozone in Semiconductor Cleaning Processes: The Solubility Issue.* Journal of the Electrochemical Society, 2001. **148**(9): p. G487-G493.
45. Kinoshita, K., *Electrochemical oxygen technology*. 1992, New York: Wiley. XIV, 431 s. : ill.
46. Lenntech. *Ozone decomposition*. [cited 2014 10.12.14]; Available from: http://www.lenntech.com/library/ozone/decomposition/ozone-decomposition.htm.
47. Sehested, K., et al., *On the mechanism of the decomposition of acidic O3 solutions, thermally or H2O2-initiated.* Journal of Physical Chemistry A, 1998. **102**(16): p. 2667-2672.
48. Kwon, B.G. and J.H. Lee, *Determination of hydroperoxyl/superoxide anion radical (HO2 center dot/O-2(center dot)-) concentration in the decomposition of ozone using a kinetic method.* Bulletin of the Korean Chemical Society, 2006. **27**(11): p. 1785-1790.
49. Katsounaros, I., et al., *Hydrogen peroxide electrochemistry on platinum: Towards understanding the oxygen reduction reaction mechanism.* Physical Chemistry Chemical Physics, 2012. **14**(20): p. 7384-7391.
50. Knake, R. and P.C. Hauser, *Sensitive electrochemical detection of ozone.* Analytica Chimica Acta, 2002. **459**(2): p. 199-207.
51. Johnson, D.C., D.T. Napp, and S. Bruckenstein, *Electrochemical reduction of ozone in acidic media.* Analytical Chemistry, 1968. **40**(3): p. 482-488.
52. Adachi, T. and H. Suzuki, *Dynamic feedback regulation of the potential of a microfabricated liquid-junction Ag/AgCl reference electrode.* Sensors and Actuators B: Chemical, 2011. **156**(1): p. 228-235.
53. Ehahoun, H., M. Stratmann, and M. Rohwerder, *Ag/AgCl/KCl micro-electrodes as O2-insensitive reference tips for dynamic scanning Kelvin probe measurement.* Electrochimica Acta, 2005. **50**(13): p. 2667-2674.
54. Bockris, J.O.M., A.K.N. Reddy, and M. Gamboa-Aldeco, *Chapter 8: Transients*, in *Fundamentals of electrodics*

2000, Plenum Press: New York. p. XXVIII, S. 771-1534, XXIX-LII.
55. Hamann, C.H., A. Hamnett, and W. vielstich, *Chapter 5: Methods for the Study of the Electrode/Electrolyte Interface*, in *Electrochemistry*. 2007, Wiley: Weinheim.
56. Pletcher, D., *Chapter 7: Techniques for the study of electrode reactions*, in *A first course in electrode processes*. 2009, RSC Publ.: Cambridge. p. 154-221.
57. Jerkiewicz, G., et al., *Surface-oxide growth at platinum electrodes in aqueous H2SO4: Reexamination of its mechanism through combined cyclic-voltammetry, electrochemical quartz-crystal nanobalance, and Auger electron spectroscopy measurements.* Electrochimica Acta, 2004. **49**(9–10): p. 1451-1459.
58. Rand, D.A.J. and R. Woods, *Cyclic voltammetric studies on iridium electrodes in sulphuric acid solutions: Nature of oxygen layer and metal dissolution.* Journal of Electroanalytical Chemistry and Interfacial Electrochemistry, 1974. **55**(3): p. 375-381.
59. Pletcher, D., et al., *6 - Potential sweep techniques and cyclic voltammetry*, in *Instrumental Methods in Electrochemistry*, D.P.G.P.M.P. Robinson, Editor. 2010, Woodhead Publishing. p. 178-228.
60. Rasten, E., *Electrocatalysis in Water Electrolysis with Solid Polymer Electrolyte*, in *Department of Materials Technology and Electrochemistry*. 2001, Norwegian University of Science and Technology: Trondheim.
61. Michell, D., D.A.J. Rand, and R. Woods, *A study of ruthenium electrodes by cyclic voltammetry and x-ray emission spectroscopy.* Journal of Electroanalytical Chemistry, 1978. **89**(1): p. 11-27.
62. Ardizzone, S., G. Fregonara, and S. Trasatti, *"Inner" and "outer" active surface of RuO2 electrodes.* Electrochimica Acta, 1990. **35**(1): p. 263-267.

63. Koetz, R., H. Neff, and S. Stucki, *ANODIC IRIDIUM OXIDE FILMS: XPS-STUDIES OF OXIDATION STATE CHANGES AND O//2-EVOLUTION.* Journal of the Electrochemical Society, 1984. **131**(1): p. 72-77.
64. Kötz, R., et al., *Oxygen evolution on Ru and Ir electrodes: XPS-studies.* Journal of Electroanalytical Chemistry and Interfacial Electrochemistry, 1983. **150**(1–2): p. 209-216.
65. Wen, T.-C. and C.-C. Hu, *Hydrogen and oxygen evolutions on Ru-Ir binary oxides.* Journal of the Electrochemical Society, 1992. **139**(8): p. 2158-2163.
66. Owe, L.-E., M. Tsypkin, and S. Sunde, *The effect of phosphate on iridium oxide electrochemistry.* Electrochimica Acta, 2011. **58**(0): p. 231-237.
67. Birss, V.I., C. Bock, and H. Elzanowska, *Hydrous Ir oxide films: The mechanism of the anodic prepeak reaction.* Canadian Journal of Chemistry, 1997. **75**(11): p. 1687-1693.
68. McIntyre, J.D.E., et al., *Cation insertion reactions of electrochromic tungsten and iridium oxide films.* Physical Review B, 1982. **25**(12): p. 7242-7254.
69. Ardizzone, S., A. Carugati, and S. Trasatti, *Properties of thermally prepared iridium dioxide electrodes.* Journal of Electroanalytical Chemistry, 1981. **126**(1-3): p. 287-292.
70. Lervik, I.A., et al., *Electronic structure vs. electrocatalytic activity of iridium oxide.* Journal of Electroanalytical Chemistry, 2010. **645**(2): p. 135-142.
71. Yao, S., M. Wang, and M. Madou, *A pH Electrode Based on Melt-Oxidized Iridium Oxide.* Journal of the Electrochemical Society, 2001. **148**(4): p. H29-H36.
72. Burke, L.D., J.K. Mulcahy, and D.P. Whelan, *Preparation op an oxidized iridium electrode and the variation of its potential with pH.* Journal of Electroanalytical Chemistry, 1984. **163**(1-2): p. 117-128.
73. *Gamry Instruments: Cyclic Voltammetry: Measuring Surface Related Currents using Digital Staircase Voltammetry*. [cited 2015; Available from: http://www.gamry.com/application-notes/energy/cyclic-voltammetry-measuring-surface-related-currents/.
74. Hamann, C.H., A. Hamnett, and W. Vielstich, *Chapter 2: Electrical Conductivity and Interionic Interactions*, in *Electrochemistry*. 2007, WILEY-VCH Verlag: Weinheim. p. 13-75.
75. *EC-Lab Software: Techniques and Applications*. Version 10.1x 2011.
76. De Pauli, C.P. and S. Trasatti, *Composite materials for electrocatalysis of O2 evolution: IrO2+SnO2 in acid solution.* Journal of Electroanalytical Chemistry, 2002. **538–539**(0): p. 145-151.
77. Albery, W.J. and M.L. Hitchman, *Ring-disc electrodes*. 1971, Oxford: Clarendon Press.
78. Pletcher, D., *Chapter 1: Introduction to Electrode Reactions*, in *A first course in electrode processes*, D. Pletcher, Editor. 2009, Royal Society of Chemistry: Cambridge. p. 1-47.
79. Eigeldinger, J. and H. Vogt, *The bubble coverage of gas-evolving electrodes in a flowing electrolyte.* Electrochimica Acta, 2000. **45**(27): p. 4449-4456.
80. Pletcher, D., et al., *4 - Covective diffusion systems - the rotationg disc and ring-disc electrodes*, in *Instrumental Methods in Electrochemistry*, D.P.G.P.M.P. Robinson, Editor. 2010, Woodhead Publishing. p. 113-148.
81. Instrumentation, P.R. *Section 10 - Theory*. Hydrodynamic voltammetry theory 2011 [cited 2014 14.10.14]; Available from: http://wiki.voltammetry.net/pine/rotating_electrode/theory#rotating_ring-disk_electrode_rrde_theory.
82. Albery, W.J. and C.M.A. Brett, *The wall-jet ring-disc electrode: Part II. Collection efficiency, titration curves and anodic stripping voltammetry.* Journal of Electroanalytical Chemistry and Interfacial Electrochemistry, 1983. **148**(2): p. 211-220.
83. Paulus, U.A., et al., *Oxygen reduction on a high-surface area Pt/Vulcan carbon catalyst: A thin-film rotating ring-disk electrode study.* Journal of Electroanalytical Chemistry, 2001. **495**(2): p. 134-145.
84. Hamann, C.H., A. Hamnett, and W. Vielstich, *Chapter 6: Electrocatalysis and reaction mechanisms*, in *Electrochemistry*. 2007, Wiley: Weinheim. p. 339-379.

85. Bard, A.J. and L.R. Faulkner, *Methods involving forced convection - hydrodynamic methods*, in *Electrochemical methods: fundamentals and applications*. 2001, Wiley: New York. p. 331-367.
86. Bruckenstein, S. and G.A. Feldman, *Radial transport times at rotating ring-disk electrodes. Limitations on the detection of electrode intermediates undergoing homogeneous chemical reacti.* Journal of Electroanalytical Chemistry, 1965. **9**(5-6): p. 395-399.
87. Marshall, A., et al., *Iridium oxide-based nanocrystalline particles as oxygen evolution electrocatalysts.* Russian Journal of Electrochemistry, 2006. **42**(10): p. 1134-1140.
88. Marshall, A.T., et al., *Performance of a PEM water electrolysis cell using electrocatalysts for the oxygen evolution electrode.* International Journal of Hydrogen Energy, 2007. **32**(13): p. 2320-2324.
89. *E6 Series ChangeDisk RRDE Tips*. 2014 [cited 2014 09.10.14]; Available from: https://www.pineinst.com/echem/viewproduct.asp?ID=45651.
90. *REF321, Reference Electrode, Operating Instructions*. 2004, Radiometer Analytical SAS

France.
91. *REF201, Reference Electrode, Operating Instructions*. 2004, Radiometer Analytical SAS: France.
92. Oldham, K.B., J.C. Myland, and A.M. Bond, *Appendix*, in *Electrochemical science and technology: fundamentals and applications*. 2011, John Wiley: Chichester. p. 365-392.
93. Bock, C. and V.I. Birss, *Anion and water involvement in hydrous Ir oxide redox reactions in acidic solutions.* Journal of Electroanalytical Chemistry, 1999. **475**(1): p. 20-27.
94. Pickup, P.G. and V.I. Birss, *Chemical analysis of the ionic content of hydrous iridium oxide films.* Journal of Electroanalytical Chemistry, 1988. **240**(1-2): p. 171-183.
95. Yoshinaga, N., W. Sugimoto, and Y. Takasu, *Oxygen reduction behavior of rutile-type iridium oxide in sulfuric acid solution.* Electrochimica Acta, 2008. **54**(2): p. 566-573.
96. Angelinetta, C., et al., *Effect of preparation on the surface and electrocatalytic properties of RuO2 + IrO2 mixed oxide electrodes.* Materials Chemistry and Physics, 1989. **22**(1–2): p. 231-247.
97. Lyons, M.E.G. and S. Floquet, *Mechanism of oxygen reactions at porous oxide electrodes. Part 2-Oxygen evolution at RuO2, IrO2 and IrxRu1-xO2 electrodes in aqueous acid and alkaline solution.* Physical Chemistry Chemical Physics, 2011. **13**(12): p. 5314-5335.
98. Wendt, H. and G. Kreysa, *Mass transfer by fluid flow, convective diffusion and ionic electricity transport in electrolytes and cells*, in *Electrochemical engineering: science and technology in chemical and other industries*. 1999, Springer: Berlin. p. 81-127.
99. Newman, J.S. and K.E. Thomas-Alyea, *Applications of potential theory*, in *Electrochemical systems*. 2004, Wiley: Hoboken, N.J. p. 419-458.
100. Esteban, J.M., M. Lowry, and M.E. Orazem, *Correction of experimental data for the ohmic potential drop corresponding to a secondary current distribution on a disk electrode*, in *The measurement and correction of electrolyte resistance in electrochemical tests*, Scribner and Taylor, Editors. 1990, American Society for Testing and Materials. p. 127-141.
101. Doyle, R.L. and M.E.G. Lyons, *Kinetics and mechanistic aspects of the oxygen evolution reaction at hydrous iron oxide films in base.* Journal of the Electrochemical Society, 2013. **160**(2): p. H142-H154.
102. Lyons, M.E.G. and M.P. Brandon, *The oxygen evolution reaction on passive oxide covered transition metal electrodes in aqueous alkaline solution. Part 1-Nickel.* International Journal of Electrochemical Science, 2008. **3**(12): p. 1386-1424.
103. Carugati, A., G. Lodi, and S. Trasatti, *Fractional reaction orders in oxygen evolution from acidic solutions at ruthenium oxide anodes.* Materials Chemistry, 1981. **6**(4–5): p. 255-266.
104. Angelinetta, C., M. Falciola, and S. Trasatti, *Heterogenous acid-base equilibria and reaction order of oxygen evolution on oxide electrodes.* Journal of Electroanalytical Chemistry and Interfacial Electrochemistry, 1986. **205**(1–2): p. 347-353.
105. Trasatti, S., *SURFACE-CHEMISTRY OF OXIDES AND ELECTROCATALYSIS.* Croatica Chemica Acta, 1990. **63**(3): p. 313-329.

106. Carugati, A., G. Lodi, and S. Trasatti. *FRACTIONAL REACTION ORDERS IN OXYGEN EVOLUTION AT OXIDE ELECTRODES*. in *Extended Abstracts, Meeting - International Society of Electrochemistry*. 1981.
107. Doyle, R.L., et al., *Redox and electrochemical water splitting catalytic properties of hydrated metal oxide modified electrodes.* Physical Chemistry Chemical Physics, 2013. **15**(33): p. 13737-13783.
108. Cadle, S.H. and S. Bruckenstein, *Ring-disk electrode study of the anodic behavior of gold in 0.2M sulfuric acid.* Analytical Chemistry, 1974. **46**(1): p. 16-20.